Diffusion of light adsorbates on transition metal surfaces

Peter Stephen Morris Townsend
Gonville and Caius College
Surfaces, Microstructure and Fracture Group
Department of Physics

A dissertation submitted to the University of Cambridge
for the degree of Doctor of Philosophy

March 14, 2018

Abstract

Helium-3 surface spin echo spectroscopy (HeSE) has been used to measure the diffusive dynamics of adsorbates on close-packed metal surfaces, namely hydrogen on Cu(111), Pd(111) and Ru(0001), carbon and oxygen on Ru(0001), and oxygen on Cu(111). Chapter 2 reviews the HeSE technique and describes the relevant dynamical models and statistical methods used to interpret data in later chapters. The performance of the ionizing detector is analysed, with a focus on the signal-to-noise ratio.

In Chapter 3 expressions for the classical intermediate scattering function (ISF) are introduced for open and closed systems. The effects of corrugation and surface-perpendicular motion on the amplitude of different components in the ISF are modelled analytically and compared with simulation. The exact ISF for a particle on a flat surface, obeying the Generalized Langevin Equation with exponential memory friction, is calculated analytically. In Chapter 4 the analytical ISF is calculated for quantum Brownian motion and for coherent tunneling dynamics in a tight binding system. The bounce method for calculating quantum mechanical hopping rates in dissipative systems is applied to model diffusion of hydrogen on Ru(0001).

Chapter 5 presents the first HeSE measurements of carbon and oxygen diffusion. C/Ru(0001) diffusion is assigned to a small carbon cluster. The jump rate has an activation energy $E_A = 292 \pm 7\,\mathrm{meV}$ in the temperature range $550\,\mathrm{K} \leq T \leq 1300\,\mathrm{K}$. Oxygen diffusion is significantly slower. By comparison of literature data with the new HeSE results, the activation energy for oxygen diffusion at low coverage is estimated as $650 \pm 10\mathrm{meV}$. Oxygen measurements at high coverage $\theta \approx 0.22\,\mathrm{ML}$ are consistent with strong mutual O-O interactions. Surface diffusion is also observed after exposing Cu(111) to oxygen.

Chapter 6 presents low-coverage measurements of protium (H) and deuterium (D) diffusion on Ru(0001), Pd(111) and Cu(111). In the quantum activated regime there is evidence for multiple jumps in all three systems, suggesting a low dynamical friction. The measurements on Ru(0001) indicate that the deep tunneling rate is much slower for D than for H.

Declaration

This dissertation is the result of my own work and includes nothing which is the outcome of work done in collaboration except where specifically indicated in the text. It does not exceed the word limit prescribed by the Degree Committee for the Faculty of Physics and Chemistry and has not been submitted in whole or part for a degree, diploma or other qualification at this or any other university.

Peter Stephen Morris Townsend

March 14, 2018

Acknowledgements

Firstly, I would like to thank the many Drs who have helped me to navigate the field and perform meaningful investigations. My supervisor Dr John Ellis for helpful input at all stages of the project. Dr Alex Chin for helping me to get started with Open Quantum Systems. Dr Bill Allison for invaluable advice throughout. Dr Toni Tamtögl for my initial hands-on education on the spin echo instrument, and helping with measurements presented in Chapter 6. Dr Nadav Avidor for helping with measurements presented in Chapters 5 and 6, and encouraging me to think more critically about the instrument and surface science in general. Dr David Ward for frequent experimental assistance and in depth discussions about the work in Chapter 3. Bill, Nadav and David for helpful feedback on draft Chapters. Dr Irene Calvo Alamzán, Dr Andy Jardine, Dr Holly Hedgeland and Prof Gil Alexandrowicz for helpful practical and conceptual discussions. Dr Marco Sacchi for collaboration on the palladium work.

Secondly I would like to acknowledge the University staff who have helped with practical aspects of completing the work, including Nigel Palfrey for lending his mechanical expertise, the Cavendish workshop technicians for producing the stream of parts needed to keep the spin echo instrument running and Dr Filippo Spiga for assistance with the High Performance Computing service.

I would also like to thank everyone who has made my time in Cambridge a rich experience outside the lab. My contemporaries Jianding Zhu, Matt Bergin and Fulden Eratam, a number of other students to pass through the group, and most of the aforementioned Drs, for enjoyable social times. CUH&H and CUAC for memorable experiences involving running and otherwise. UCCB for a friendly and rewarding music-making environment.

I gratefully acknowledge a studentship from the EPSRC, and additional funding from Gonville and Caius College.

Finally I thank my parents Penny and Steve for their love and support.

Publications and presentations

- Submitted for review in Journal of Physical Chemistry C: "Structural Evolution of a Cyclooctatetraene Adlayer on Cu(111) During Isothermal Desorption". Lau, Jascha; Calvo Almazán, Irene; Townsend, Peter; Ward, David; Jardine, Andrew; Allison, William; Ellis, John; Hinch, B. Jane; Avidor, Nadav. Manuscript ID jp-2018-00482s
- Submitted for review in New Journal of Physics: "The intermediate scattering function for quasi-elastic scattering in the presence of memory friction". Townsend, Peter; Ward, David. Article reference NJP-108234
- The diffusion of H/Cu(111) has been presented at the Gordon Conference *Dynamics at Surfaces* 2015, ECOSS-31 (Barcelona) and the UK Vacuum Symposium 2016 (Coventry).
- The diffusion of H/Pd(111) has been presented at ECOSS-32 (Grenoble) and SAMS-3 (Bergen).

Contents

Chapter 1

Introduction

Surface and interface properties are critically important in modern technology, including chemical synthesis, nanotechnology, electronic devices and energy applications. One classic application of surface science is heterogeneous catalysis [1], which remains an extremely active field of research as well as a dominant industrial application. In parallel, the blooming field of nanotechnology interacts with traditional surface science in at least two different ways. Firstly, surfaces provide templates on which to grow nanoscale structures such as clusters, tubes and arrays [2, 3, 4]. Secondly, the lack of a bulk region, or the change in effective dimensionality in nanoscale objects, can lead to modified surface properties which feed back into other areas of application such as catalysis [5]. Another notable way in which material properties change with dimensionality is the electronic bandstructure and resulting electrical properties [6], which has stimulated intensive research into two-dimensional materials such as graphene with potential device applications. More conventional devices depend on the control of surfaces and interfaces, either to exploit their electronic properties [7], or for efficient synthesis via surface-mediated chemical reactions [8]. An especially motivating final area of application is the development of technologies for efficient and sustainable energy storage and distribution, including batteries and fuel cells where interface properties are critical in performance and long-term stability [9, 10]. Figure 1.1 illustrates some of the applications just mentioned.

The above examples illustrate that a base of fundamental understanding derived from controlled experiments on well-defined surfaces is vital for the discovery and refinement of surface-based applications. However, even for the simplest possible surfaces, a microscopically exact description of its behaviour would not be conceptually helpful even if it was technically possible. Instead, simple systems can be more usefully cast as model systems, describable with a limited number of param-

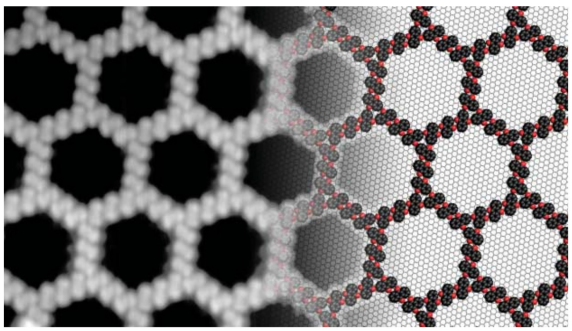

(a) Atomic-scale image and model of a molecular network with nanoscale pores [4].

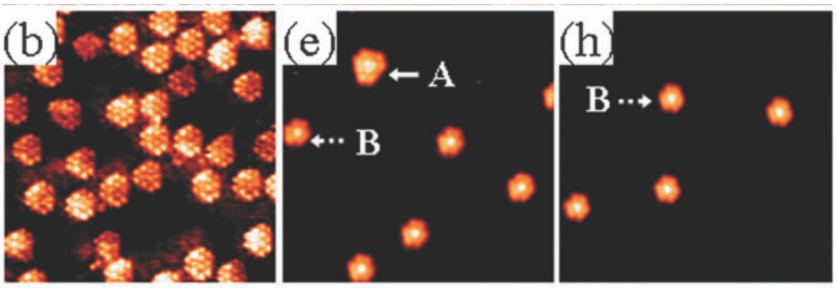

(b) Atomic-scale images of coronene molecules (left) deposited on Ru(0001), which decompose to form carbon clusters (centre and right).

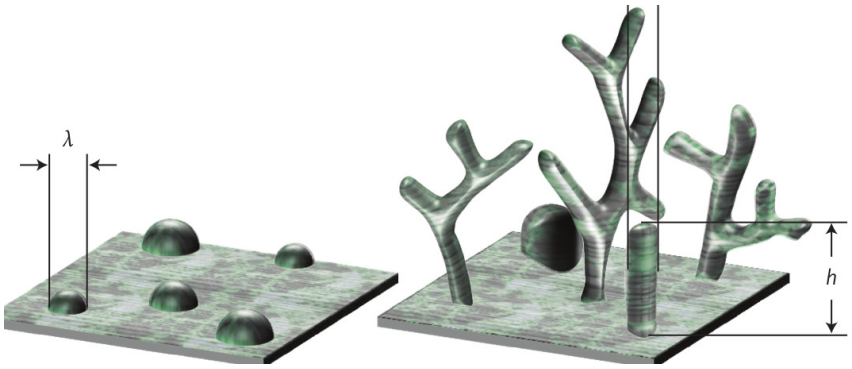

(c) Illustration of lithium dendrites nucleating at imperfections on an electrolyte/metal interface.

Figure 1.1: Illustration of the application of surface science to the growth of nanostructured materials and refinement of energy technologies. 1.1a: scanning tunneling microscopy image of a porous network formed by self-assembly of organic molecules deposited on a Cu(111) surface. Reprinted from reference [4] with permission from AAAS. 1.1b: formation of carbon clusters by decomposition of coronene molecules on Ru(0001). Reproduced in part from reference [2] with permission of The Royal Society of Chemistry. 1.1c: illustration of the growth of lithium dendrites at the metal/electrolyte interface, a potential failure mechanism, during battery operation. Reprinted in part from reference [9] with permission from Springer Nature, Copyright (2016).

eters. The kind of questions that fundamental surface science experiments address can then include:

- Phenomenology: what kinds of model systems exist?
- What are their key parameters?
- Can the parameters be predicted reliably from first principles?
- Can simple models be combined to understand more complex systems?

The experimental study of well-defined model surface systems relies on several technological developments, notably vaccuum techniques allowing experiments to be carried out in ultra-high vacuum (UHV). Due to the extremely high flux onto any surface from a gas at atmospheric pressure (1 bar) and temperature [11], pressures of $\leq 10^{-10}$ mbar are required to perform extensive stable measurements on uncontaminated surfaces, especially at low temperatures. Today the generation and measurement of UHV is routine thanks to inventions such as the turbomolecular pump [12] and the ionization gauge [13]. Other technological developments considered to be crucial [14] in enabling the modern experimental understanding of surfaces include advances in microelectronics, electron-scattering techniques and scanning probe techniques (such as scanning tunneling microscopy [15]) whose results are illustrated in Figure 1.1. Another particularly important development for the atom-scattering field was the development of high-intensity atomic and molecular beam sources [16]. A further key aspect is atom detection technology, which is discussed extensively in Chapter 2. Despite the long-term value of the knowledge acquired by UHV methods, applications will generally involve additional complexity, particularly in chemical applications where the aim is a high turnover requiring large pressures and temperatures. A recent trend in surface science is the development of techniques which bridge the "pressure gap" between UHV behaviour and ambient pressure [17, 18, 19]. Ambient or near-ambient experiments are valuable as they can reveal the development of complex phenomena as the pressure is increased [20]. However, if the aim is to make rigorous comparisons with theory then reducing complexity as far as possible is preferable. The UHV and ambient approaches are individually valuable and mutually complementary.

The experimental technique central to the present Thesis is helium-3 surface spin echo spectroscopy (HeSE), which is explained in detail in Chapter 2. HeSE is a UHV, nondestructive, equilibrium, surface-sensitive technique. The method is ideally suited to studying the fast diffusion of adsorbates, with unique access to the fundamental processes of surface diffusion on the picosecond-nanosecond, nanometre-$\mathring{A}$ scales. Surface diffusion is important practically since,

- nanoscale-synthesis applications, such as the examples mentioned in the opening paragraph, are facilitated by surface diffusion;

- surface chemical reactions can be diffusion-limited in certain regimes.

The methods and theoretical inputs needed to predict surface diffusion dynamics accurately are also needed for the accurate modelling of other dynamical surface processes. Therefore, experimental methods such as HeSE that can benchmark the theoretical methods for well-defined model systems are a very important building block in the development of theory and the modelling of more complex systems. Some key theoretical concepts in surface diffusion that can be probed with HeSE measurements include the static adsorbate-surface interaction quantified by the potential energy surface (PES), the dynamical dissipative coupling quantified by a friction, and the influence of nuclear quantum effects. Density functional theory (DFT) [21] has been the dominant theoretical backdrop to the interpretation of surface dynamics measured with HeSE, providing a means to calculate the PES [22, 23, 24] and more recently to obtain a handle on the friction [25]. The remainder of the present Thesis consists of investigations which are either HeSE experiments, or theoretical investigations motivated by data available from HeSE.

Noise and dissipation play a crucial role in adsorbate dynamics. The frictional coupling between a diffusing adsorbate, and the heat bath degrees of freedom of the substrate, can be quantified in terms of the frequency-dependent response function of the bath. Both the absolute coupling strength and the frequency-dependence have an impact on surface diffusion rates, but within HeSE they are also detectable in the detailed short-time behaviour of experimental lineshapes [26, 27, 28]. The effect of memory in the bath response is examined analytically in Chapter 3. Previously it has been established by numerical simulation that memory effects in the heat bath can reduce the amplitude associated with the slowest decaying component in HeSE lineshapes [28]. In Chapter 3 I derive analytical lineshapes for an adsorbate on a flat surface subject to the simplest possible model of a thermal environment with memory, which explains the numerically derived phenomenology.

The interaction of quantum systems with their environment is hugely important in condensed matter and other areas of Physics [29, 30, 31]. A well known example is the fact that environmental interaction induces dephasing in condensed-phase qubits [32]; the subject is therefore highly relevant in the field of quantum technologies. From a different perspective, predicting the rates of chemical processes such as electron transfer [33] or surface diffusion of light atoms at low temperatures [23] requires a realistic formulation involving both the quantum particle of interest and the thermal environment to which it is coupled. The difficulties involved in simulat-

ing large quantum systems arise from the exponential growth of the number of basis states of a quantum system with the number of degrees of freedom [29]. The field of open quantum systems (OQS) deals with how to calculate properties of a small subsystem of interest without having to treat the evolution of the entire quantum environment explicitly. Particularly relevant here are semiclassical methods that can describe quantum tunneling in the presence of a heat bath [31]. The OQS field also relates to foundational issues in Physics such as decoherence and the relationship between classical and quantum mechanical descriptions of the world [34]. However, the application of OQS techniques in the present work is focussed on the calculation of dynamical properties of adsorbates. In Chapter 4 I derive exact lineshapes for the quantized version of the classical Generalized Langevin Equation (GLE) model considered in Chapter 3, and for a particle tunneling coherently in a periodic tight-binding system. Finally I present calculations of the dissipative quantum escape rate over realistic first-principles potential energy barriers. The quantum escape rate methods are compared critically with bandstructure-based methods recently proposed for the analysis of HeSE experiments [35, 36]. The results of the dissipative calculations are used to place bounds on the strength of frictional coupling that could apply in HeSE experiments, which is important for the interpretation of experimental hydrogen diffusion results presented in Chapter 6, including absolute rates and isotope effects.

In Chapter 5 I present the first HeSE studies of carbon and oxygen diffusion. The purposes of studying the systems was not to search for the theoretical effects of Chapters 3 and 4, but because they are of far-reaching interest in their own right. Graphene is a well-known example of a material with special electronic properties as a result of its two-dimensional structure [6]. Growth at transition metal surfaces such as Ru(0001) is a promising method for preparing high quality graphene for devices, for example via chemical vapour deposition [37]. The new HeSE measurements demonstrate a rapidly diffusing graphene precursor during precipitative growth. The high temperatures achievable on Ru(0001) also facilitate the study of oxygen diffusion. It is difficult to overstate the importance of oxygen-metal interactions in nature and technology. Crucial gas-phase oxidation reactions are catalysed by metal surfaces [11]. Additionally, oxide surfaces themselves frequently act as catalysts [38, 39], and are potentially affected strongly by finite thickness effects [40], which places a special importance on the oxygen-metal interaction near surfaces. HeSE allows the oxygen/surface interaction to be quantified at high temperature which complements previous room-temperature scanning tunneling microscopy (STM) studies of dynamics in the literature. Meanwhile, the interaction of oxygen with Cu(111) is qualitatively different and altogether more complicated. Preliminary measurements of surface diffusion on Cu(111) after dosing oxygen suggest the

formation of a non-equilibrium structure upon initial dosing at 550 K, and a change in the diffusing species at different temperatures.

In Chapter 6, HeSE measurements of hydrogen diffusion on Ru(0001), Pd(111) and Cu(111) are presented. Hydrogen atoms adsorbed on metals are an experimental realisation of quantum particles diffusing in a dissipative periodic environment. As such, the surface diffusion displays a crossover from thermally activated behaviour to an approximately temperature-independent rate under experimentally accessible conditions [41]. Meanwhile, considerable theoretical work has led to a range of analytical and numerical methods for predicting quantum diffusion rates, subject to various assumptions or approximations. In some cases, diffusion in the presence of barriers to tunneling has been modelled in terms of 'quantum escape rates', governed either by semiclassical theories such as the Wolynes model [42, 43], or deep-tunneling extensions based on instantons [23]. In other cases, a more direct modelling of the system dynamics has been attempted, for example through stochastic wavefunction evolution [44] or approximating the dynamical structure factor via Lorentzian broadening of the system energies [45]. In Chapter 6 the rate theory methods from Chapter 4 are used to provide a consistent rationalization of the absolute rates and isotope effects.

In the course of Chapters 2 to 6, some questions are answered definitively. However, many questions are either left open or opened up. Chapter 7 highlights some important questions raised, and outlines possible routes to their solution.

Chapter 2

Experimental methods

The experimental technique central to the present Thesis is helium-3 surface spin echo spectrometry (HeSE), which allows the measurement of surface processes on atomic length and time scales. Section 2.1 presents an overview of the principles of the technique, the measurement possibilities, and the important features that HeSE inherits as a flavour of helium atom scattering (HAS).

To make sense of HeSE experiments, the data must be compared to models of surface dynamics. In principle HeSE allows surface dynamics to be characterized down to the very smallest atomic scales including continuous motion at adsorption sites. However, the technique is particularly well suited to investigations of jump dynamics, in which the model of adsorbate motion can be coarse-grained to a discrete description. The experimental adsorbate dynamics presented in Chapters 5 and 6 falls into the jump diffusion category. In Section 2.2 I describe the models applicable to the experimental results, and the statistical methods used to make the model-data comparison.

A key component of the instrumentation is an efficient and stable helium atom detector. Although the efficiency is important and one of the key challenges in the detector design, the bottom line in terms of measurement quality is the signal-to-noise ratio (SNR). It is therefore important to know what factors limit the SNR in different regimes of helium intensity, in order to optimize operating conditions in the short term, and inform instrumentation developments in the long term. In Section 2.3 I analyse the scaling of noise with signal under a range of conditions including the HeSE experiments presented in later Chapters. It was suspected beforehand that the majority of experimental data were limited by a noise originating before the detector. Under almost all practical experimental conditions the noise scales linearly with the mean intensity (signal). Linearly scaling noise would be consistent with

noise originating before the detector (for example, in the beam source or scattering chamber), but measurements performed in the absence of a helium beam suggest that the noise could be intrinsic to the detector.

2.1 Experimental methods overview

I describe the principles and key features of the helium-3 spin echo technique, the classes of measurement presented throughout the Thesis, and the relevant practical details.

2.1.1 Helium atom scattering (HAS)

Many experimental surface science techniques are based on a probe that scatters from a surface, either elastically or inelastically. The type of information available from the scattering experiment depends on the nature of the probe/surface interaction, and the energy and wavelength of the probe. Table 2.1 illustrates some standard types of scattering experiment, in order to broadly set the context for helium atom scattering, which underpins all of the experimental work in the present Thesis. Figure 2.1 illustrates helium atom scattering from a solid surface, showing specular scattering (B), and off-specular scattering or diffraction (C). The distinctive features of thermal energy helium atoms as scattering probes are:

- chemically inert (closed-shell);
- no physisorption (binding to the surface due to attractive van der Waals interactions) under any practical conditions;
- low incident energy (mean value 63 meV at room temperature, $\frac{5}{2}k_B T_{\text{nozzle}}$ in general [46]) and therefore non-destructive;
- classical turning point far above metal surfaces (nominally around 3 Å) due to strong repulsion by conduction electrons [47] implying surface specificity;
- sufficient off-specular scattering cross-sections from typical adsorbates [48], including hydrogen, to study them at low coverage (one adsorbate per many unit cells of substrate);
- Not-too-large amplitude for phonon exchange with transition metal substrates [48], which reserves intensity for the study of quasielastic processes (especially true of ^{3}He where the mass mismatch with the substrate is greater).

Chemical inertness and the low incident energy enables the study of delicate systems which might otherwise be disturbed (disordered, desorbed) by more energetic techniques such as low-energy electron diffraction (LEED) [49]. The low energy of helium atoms with wavelength $\mathcal{O}(1)$Å is related to the large mass of atoms compared to electrons and photons. Surface specificity makes HAS a powerful complement to techniques which are surface sensitive but do not straightforwardly distinguish between surface and near-surface scattering.

Much of the background information reported in Chapter 6 about the structure of hydrogen overlayers is taken from LEED studies. Therefore it is relevant to discuss the particular limitations associated with studying hydrogen with LEED. In HAS, ordered hydrogen structures are not especially difficult to detect: the increase in helium-surface potential corrugation induced by the overlayer typically produces diffraction peaks orders of magnitude larger than the clean surface diffracted intensity. In contrast, the electron scattering cross-section of hydrogen atoms in LEED experiments is very low, which has led to cases of ordered hydrogen overlayers going undetected in LEED but subsequently detected with HAS [48]. Examples include the close-packed surface Rh(111), where within LEED "no evidence for the formation of an ordered hydrogen overlayer" was found at $100\,\mathrm{K} \leq T_s \leq 400\,\mathrm{K}$ [50] but a (1×1) overlayer was later observed in HAS via the strong enhancement of the (1×1) clean surface diffraction peaks [51]. Another striking illustration of hydrogen sensitivity in HAS over LEED is seen in the lateral oxygen ordering but proton disordering in adsorbed water layers [52, 53]. Apart from occasionally discovering well-defined long-range structures missed by LEED, the high hydrogen sensitivity of HAS enables more subtle structures such as small islands (Section 6.5) to be investigated.

Inertness and hydrogen-sensitivity are separate advantages of HAS as a structural technique. Electron-induced disordering in LEED experiments can apply to any adsorbate system, not just hydrogen. However, the damage to the adsorbate overlayer is often slow enough to be disentangled from the thermal equilibrium behaviour of the surface in the absence of the beam. For example, in measurements of the geometry of (2×1)H/Ru(0001) by LEED [54], the diffracted intensities varied by 10 % over 30 minutes when the system was measured at 60 K. Electron-stimulated disordering becomes less severe when the adsorbate mobility is high, as electron-induced defects are quickly repaired by annealing [49]. Therefore, under conditions directly relevant to HeSE measurements where the adsorbate mobility is very high, relevant LEED measurements are most likely probing the thermal equilibrium structure. However, if the intensity of a hydrogen overlayer diffraction feature is very low then it will not be detected even if the overlayer is stable against electron damage.

Table 2.1: A comparison of scattering techniques in surface science: low energy electron diffraction (LEED), high-resolution electron energy loss spectroscopy (HREELS), surface x-ray diffraction (SXRD), quasi-elastic neutron scattering (QENS) and helium atom scattering (HAS). At room temperature the wavelength λ of a helium atom is $\mathcal{O}(1)$Å, comparable with lattice spacings on typical surfaces, allowing structure and dynamics to be measured on the crystallographic lengthscale. Lighter probes with comparable wavelength have higher energy E_i, are potentially destructive, and typically penetrate to a non-negligible depth below the surface of a sample. In contrast, the classical turning point for thermal energy helium atoms is a few Å above the surface. Neutrons penetrate straight through the bulk sample under most incident conditions, and so surface diffusion experiments are performed on layered samples with a high specific surface area [55].

Technique	**Probe**	**m(amu)**	**E$_i$ (meV)**	λ(Å)	**Depth**(Å)	**Info**
LEED	Electron	5×10^{-4}	> 2000	< 1	5-10[56]	Structure
HREELS	Electron	5×10^{-4}	4000[57]	< 1	10	Vibrations
SXRD	Photon	0	10^7 [58]	1	$10 - 5000$[59]	Structure
QENS	Neutron	1	25[60]	1	Bulk	Struct & dy
HAS	He atom	$3 - 4$	< 63	1	-3	Struct & dy

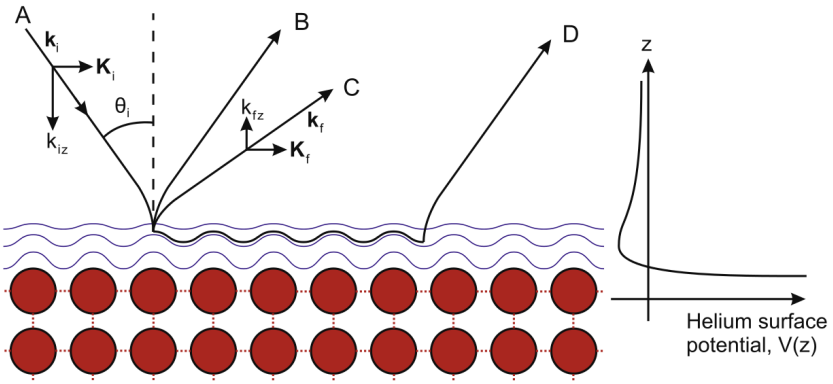

Figure 2.1: Schematic illustration of helium atom scattering from a solid surface. Reprinted from reference [61], Copyright (2009), with permission from Elsevier. Incident atoms are represented by the ray **A** with wavevector $\mathbf{K}_i$ in the plane of the surface, and k_{iz} perpendicular to the surface. The scattering processes shown include specular scattering (B) and off-specular scattering or diffraction (C). The outgoing wavevectors are $\mathbf{K}_f$ and k_{fz} which define the surface parallel momentum transfer $\Delta\mathbf{K} = \mathbf{K}_f - \mathbf{K}_i$ and the perpendicular momentum transfer Δk_z. **D** represents a bound-state resonance, which is not directly relevant to the remainder of the present work and will not be discussed further.

HAS without energy resolution can be used to study adsorption and structure [48]. Historically, energy resolution was first introduced via time-of-flight (TOF) methods, which have been used extensively to study surface phonons [62] and rapid diffusion of adsorbates [63]. The energy resolution in TOF methods is limited by the velocity spread of the incident beam, a difficulty which is circumvented in HeSE.

2.1.2 Helium-3 surface spin echo spectroscopy (HeSE)

HeSE is an experimental probe of surface dynamics, with the crucial feature that energy spread in the incident beam is largely mitigated, allowing very small energy exchanges to be measured. Figure 2.2 illustrates the principle of the technique and schematically indicates the experimental layout. The principles were first laid out in the context of neutron scattering [64]. The presentation here follows a similar path except that I describe the evolution of the probe's spin degree of freedom as state evolution via the Schrödinger equation

$$i\hbar\,\partial t\,|\Psi\rangle = H|\Psi\rangle\,, \tag{2.1}$$

rather than through an operator equation of motion.

The quantitative details of the experimental principle can be described using the quantum mechanical evolution of a spin wavefunction in a magnetic field. A ^{3}He atom is a spin-$\frac{1}{2}$ particle. The quantum operator describing its spin degree of freedom can therefore be written as

$$\mathbf{S} = \mathbf{x}S_x + \mathbf{y}S_y + \mathbf{z}S_z = \frac{\hbar}{2}\boldsymbol{\sigma}\,, \tag{2.2}$$

where in the S_z basis the Cartesian components of σ are the Pauli matrices [66]

$$\sigma_x = \begin{pmatrix} 0 & 1 \\ 1 & 0 \end{pmatrix} \;;\; \sigma_y = \begin{pmatrix} 0 & -i \\ i & 0 \end{pmatrix} \;;\; \sigma_z = \begin{pmatrix} 1 & 0 \\ 0 & -1 \end{pmatrix} \tag{2.3}$$

In a homogeneous magnetic field the spin wavefunction evolves subject to the Hamiltonian

$$H = -\gamma\mathbf{S}\cdot\mathbf{B}\,, \tag{2.4}$$

where γ is the ^{3}He gyromagnetic ratio, $\gamma = 2\pi \times 32.43\,\mathrm{MHz/T}$ [61]. The polarizing hexapole magnet (Figure 2.2) is designed so that atoms emerge in an eigenstate of S_x, which in the S_z basis takes the form

$$|\Psi\rangle = \frac{1}{\sqrt{2}}\begin{pmatrix} 1 \\ 1 \end{pmatrix}. \tag{2.5}$$

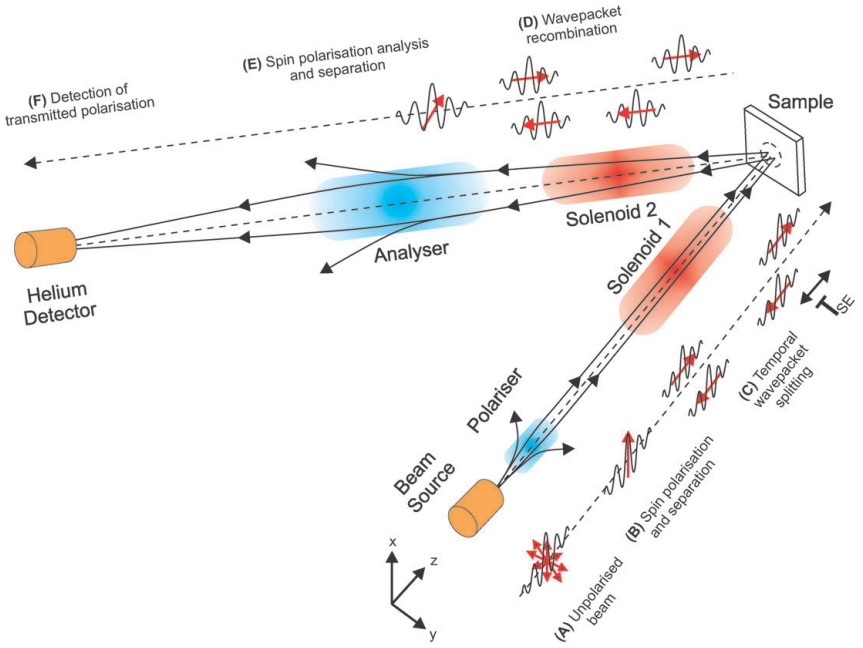

Figure 2.2: Illustration of the helium-3 surface spin echo principle and setup, showing the wavepacket-based physical interpretation of the spin echo time t_{SE}. Reproduced from reference [65] with permission of the PCCP Owner Societies. The beam is produced in the source (**A**), then its nuclear spin is polarized in the **x** direction by the polarizer at **B**. The polarized atoms travel into a solenoidal field (**C**) parallel to **z**. The solenoidal field is generated by a current I_{SE} in a long, cylindrical electromagnetic solenoid whose axis is the beam line. Each atom can be treated as a superposition of its two S_z eigenstates as described by Equation 2.5. The two components travel at different speeds through the field, and reach the sample with a relative time delay t_{SE} as given by Equation 2.6. The He atoms scatter from the sample surface, and those with the correct outgoing direction of travel pass down the outgoing beamline. In the outgoing precession solenoid **D**, the two S_z spin components are recombined by a magnetic field integral equal to the incoming field integral but in the opposite direction. If the surface changes during the time interval t_{SE}, the wavepacket recombination is imperfect which leads to a reduction in the interference effects which define the polarization as illustrated in Figure 2.5. The polarization is measured using the spin-analyser **E** and detector **F**, as described in Section 2.1.4.3.

The atom then passes through a finite region of magnetic field $\mathbf{B} = B\mathbf{z}$ along the central axis of the incoming precession solenoid, exchanges a small energy $\hbar\Delta\omega$ in a scattering process, and passes through an oppositely aligned magnetic field with the same field integral $\int B\,dl$. The magnetic field is produced by a current in the solenoids called the spin echo current, I_{SE}. The precession-scattering-precession sequence evolves the spin state to a new linear superposition of S_z eigenstates with a relative phase proportional to the spin echo time t_{SE}, defined as

$$t_{SE} = \frac{\hbar\gamma}{mv^3}\int B\,dl\,, \tag{2.6}$$

where v is the velocity of the atom. The spin echo time is represented physically in Figure 2.2 via the separation of spin-up and spin-down wavepackets by the incoming precession field. The spin state in terms of t_{SE} is

$$|\Psi\rangle = \frac{1}{\sqrt{2}}\begin{pmatrix} e^{-i\Delta\omega t_{SE}/2} \\ e^{+i\Delta\omega t_{SE}/2} \end{pmatrix}. \tag{2.7}$$

The expectation of σ_x for a given energy exchange $\Delta\omega$ is therefore:

$$\langle\Psi|\sigma_x|\Psi\rangle = \cos(\Delta\omega\, t_{SE})\,. \tag{2.8}$$

The experimental result is averaged over all detected atoms. Within a Born approximation for quasielastic scattering, the scattering probability is proportional to a adsorbate-dependent form factor squared $|F(\Delta\mathbf{K})|^2$, multiplied by the dynamical structure factor $S(\Delta\mathbf{K},\Delta\omega)$ which depends on the dynamics of the system [67, 68]. The form factor can be thought of as the scattering amplitude from a static adsorbate, and depends on the adsorbate-induced perturbation to the static helium-surface potential.

Assuming the form factor varies slowly with $\Delta\mathbf{K}$, the differential scattering probability at a fixed crystal orientation is proportional to $S(\Delta\mathbf{K},\Delta\omega)$ alone. By averaging 2.8 over all energy exchanges, the expectation of σ_x as measured in an experiment can be written in terms of the intermediate scattering function $I(\Delta\mathbf{K},t)$ defined as

$$I(\Delta\mathbf{K},t) = \frac{\int e^{i\Delta\omega t}S(\Delta\mathbf{K},\Delta\omega)\,d\Delta\omega}{\int S(\Delta\mathbf{K},\Delta\omega)\,d\Delta\omega}\,. \tag{2.9}$$

The expectation of σ_x is the real part,

$$\langle\Psi|\sigma_x|\Psi\rangle = \mathrm{Re}[I(\Delta\mathbf{K},t_{SE})]\,, \tag{2.10}$$

and similarly the expectation of σ_y is the imaginary part [61],

$$\langle\Psi|\sigma_y|\Psi\rangle = \mathrm{Im}[I(\Delta\mathbf{K}, t_{SE})]\,. \tag{2.11}$$

Before continuing with the description of the experiment, I signpost the significance of the functions introduced to describe adsorbate dynamics. Equation 2.9 defined $I(\Delta\mathbf{K}, t)$ as a Fourier transform of $S(\Delta\mathbf{K}, \Delta\omega)$ between the frequency and time domains. Applying a Fourier transform between the reciprocal and real space domains defines a third conceptually important function, the pair correlation function $G(\mathbf{R}, t)$. In the limit where the dynamics of the ensemble of scattering centres is classical, $G(\mathbf{R}, t)$ is probability of finding a particle at $\mathbf{R}' + \mathbf{R}$ at time t given that there was a particle at $\mathbf{R}$ at time t, averaged over $\mathbf{R}'$. The scattering function $S(\Delta\mathbf{K}, \Delta\omega)$ for one particle can be written in terms of the matrix elements of the operator $\exp(i\Delta\mathbf{K}\cdot\mathbf{x})$ between energy eigenstates of the unperturbed system [67, 68]. The corresponding $I(\Delta\mathbf{K}, t)$ is simply the autocorrelation of $\exp(i\Delta\mathbf{K}\cdot\mathbf{x})$, which often makes it the most convenient of the three functions to calculate, either analytically or numerically, as demonstrated in Chapters 3 and 4.

When the final polarization has an imaginary part, the spin direction has been systematically rotated away from the x direction by the precession-scattering-precession sequence as a result of imbalanced energy gain and loss probabilities. The imaginary part of the polarization is important to consider when applying Fourier filtering as in Section 2.2.4, due to the potentially large asymmetry between the energy gain and energy loss probabilities associated with inelastic features such as phonons. In measurements of jump diffusion (Chapters 5 and 6), the imaginary part is generally not relevant and will not be shown explicitly in polarization scans.

To describe inelastic (or very broad quasielastic) features of HeSE spectra quantitatively, the nonlinear relationship between wavelength changes and energy changes must be taken into account. The description in terms of $\Delta\omega$ (Equations 2.7 to 2.9) suffices for studies of relatively slow diffusion, in which the relevant energy transfers are orders of magnitude below the mean incident energy such that changes in energy and changes in wavelength are linearly proportional. However, the time an incoming or outgoing helium atom spends in the corresponding solenoidal field is proportional to its wavelength, not the energy. Therefore the spin echo lineshape is a Fourier transform of scattering probability in the wavelength domain $S(\lambda_1 \to \lambda_2)$ [69]. Defining a variable κ in terms of the spin echo time t_{SE} and mean incident wavelength λ as

$$\kappa = \frac{2\pi\hbar}{m\lambda^3} t_{SE}\,, \tag{2.12}$$

the polarization is given [69] by an integral over the incoming wavelength distribution

$p(\lambda_1)$

$$P(\kappa) = \int d\lambda_1 \, d\lambda_2 \, p(\lambda_1) S(\lambda_1 \to \lambda_2) e^{2\pi i \kappa(\lambda_1 - \lambda_2)} \, . \tag{2.13}$$

The more general form 2.13 is used to derive the frequency of a dispersive inelastic feature from Fourier transforms of polarization scans in Chapter 6. Strictly, the wavelength-dependent transmission probabilities between the first precession solenoid and the detector should be taken into account in any detailed quantitative analysis of $P(\kappa)$, but the position of an inelastic peak should not be significantly affected.

2.1.3 Sample preparation and manipulation

The experiments reported in the present Thesis were performed on single-crystal samples of Cu(111), Ru(0001) and Pd(111). The $\oslash$10 mm×1 mm single crystal samples (Surface Preparation Laboratories, Netherlands) were mounted on a six-axis manipulator and transferred into the magnetically shielded scattering chamber of the spin echo spectrometer [70]. Occasionally samples were transferred without breaking vacuum using the lock/load transfer tool [71]. More often, samples were transferred *ex situ* followed by bakeout. After a bakeout the base pressure of the scattering chamber was typically 2×10^{-11} mbar as determined by an extractor ion gauge. The sample temperature T_s was monitored with a type-K thermocouple spot-welded to the sample mount at the sample edge. Radiative heating up to about 900 K was provided by a coiled tungsten filament at the underside of the sample. To obtain higher temperatures, electron impact at around 1 kV on the underside of the sample (simultaneously, on the sample mount) provided additional heating power. Electron impact heating was necessary for annealing Ru(0001) and Pd(111), and for performing the very high temperature measurements of C/Ru(0001). The sample is held in continuous thermal contact with a liquid nitrogen-filled coldfinger via flexible copper strips which deliver an ultimate sample temperature of 97 K under ideal conditions [71].

All samples were cleaned, at least in part, with argon sputtering and annealing using a commercial ion source (PSP, model ISIS-3000). The surface was sputtered with 10 μA of Ar^+ at around 1 keV for 15 minutes and then annealed. The typical sputtering and annealing conditions used for each surface are summarised in Table 2.2. In the case of Ru(0001), argon cleaning was supplemented by cycles of oxygen cleaning. The sample was held at 700 K and exposed to around 300 L of molecular oxygen (1 L= 1.33×10^{-6} mbar·s). The surface oxygen was then removed by annealing repeatedly for c.1300 K, 2 minutes. Surface quality was monitored via helium diffraction patterns and the specular reflectivity R. R is defined in terms of three

Table 2.2: Cleaning parameters for the three surfaces measured in the present work, and typical reflectivity when the surface quality no longer improved with further cleaning. The quantities tabulated are the Ar^+ ion energy E, the surface temperature during sputtering T_{sp} and the annealing temperature T_{ann}.

Surface	**E(kV)**	$\mathbf{T_{sp}(K)}$	$\mathbf{T_{ann}(K)}$	**R**(%)
Cu(111)	0.8	300	800	50
Pd(111)	1.0	550	1100	45
Ru(0001)	1.0	300	1300	30

scattering chamber pressures: P_{on} on specular, P_{off} off specular (5° in practice) and P_{wob} without a beam, as

$$R = \frac{P_{\text{off}} - P_{\text{on}}}{P_{\text{off}} - P_{\text{wob}}}\,. \tag{2.14}$$

In the case of the oxygen-cleaned Ru(0001) surface, ^{3}He diffraction patterns were systematically checked in addition to R. Annealing was repeated until diffraction scans showed no structural features other than the specular peak and the principal diffraction peak of the Ru(001) surface. The typical reflectivity of each surface, after the surface quality stopped systematically improving with further cleaning cycles, is shown in Table 2.2.

Due to the fixed source and detector geometry, the desired azimuth and mean momentum transfer are accessed by rotation of the sample with respect to three angular degrees of freedom conventionally labelled α, β and γ. The angles are defined and understood in the following way:

- The axis of α rotation is the surface normal. Rotation in α changes the azimuth along which scattering takes place.

- The γ axis is perpendicular to the plane defined by source, sample and detector; $\gamma = 0$ when the sample faces the incoming beam, at which point the α axis points towards the beam source. Changing γ changes the mean momentum transfer. The γ axis is vertical in the lab frame.

- The β axis is perpendicular to the α and γ axes. Movement in β corresponds to a nodding motion of the crystal. Experiments at present are carried out at $\beta = 0$, which is achieved by frequently optimizing the received intensity with respect to β. When β is properly optimized, the α axis is horizontal in the lab frame.

2.1.4 Types of measurement

2.1.4.1 Uptake (deposition) curves

In an uptake measurement, scattered ^{3}He atom intensity is recorded as a function of time at a privileged $\Delta\mathbf{K}$ during exposure to an adsorbate. The most important privileged $\Delta\mathbf{K}$ is normally the specular condition. Under some conditions the specular intensity decays monotonically upon dosing, in which case the deviation from exponential decay can be used to infer information about interactions [72]. In other cases, the variation of specular with exposure has a complex structure involving minima and maxima, which often correspond to the formation of ideal ordered surface structures. Figure 2.3 shows two examples from the literature. A more complete picture is always provided by taking additional uptake curves at various diffraction conditions.

2.1.4.2 Diffraction scans

^{3}He diffraction scans are useful for keeping track of the quasi-static development of surface structure. In a diffraction scan the scattered helium intensity is recorded as a function of the crystal orientation, with no energy resolution. When the scattered intensity is dominated by elastic or quasielastic signal, the polar angle γ can be converted to a surface-parallel momentum transfer via

$$\Delta K = \bar{k}_i[\sin(\delta - \gamma) - \sin(\gamma)] \tag{2.15}$$

where $\bar{k}_i$ is the mean incident momentum of an atom in the beam, $\delta = 44.4°$ is the total scattering angle, and γ is the polar angle of the surface normal with respect to the incoming beam. The conversion to ΔK neglects the incident energy spread δE of the beam, which was typically 5 % of the mean beam energy, and frequently calibrated. δE leads to a broadening of structural features as a function of polar angle.

Above a clean close-packed metal surface, the lateral variation in the electron density at the classical turning point for helium scattering is very small. As a consequence, the associated helium diffraction peaks tend to be small [48]. Typically the ratio of the specular peak height and the first order diffraction peak height for clean Cu(111), Pd(111) or Ru(0001) as measured in the present work was around 10^5. The substrate atoms in the surface layer of fcc(111) and hcp(0001) surfaces form a hexagonal lattice, which has six-fold rotational symmetry. The surfaces themselves have three-fold symmetry due to the substrate layers below the surface. The situation is

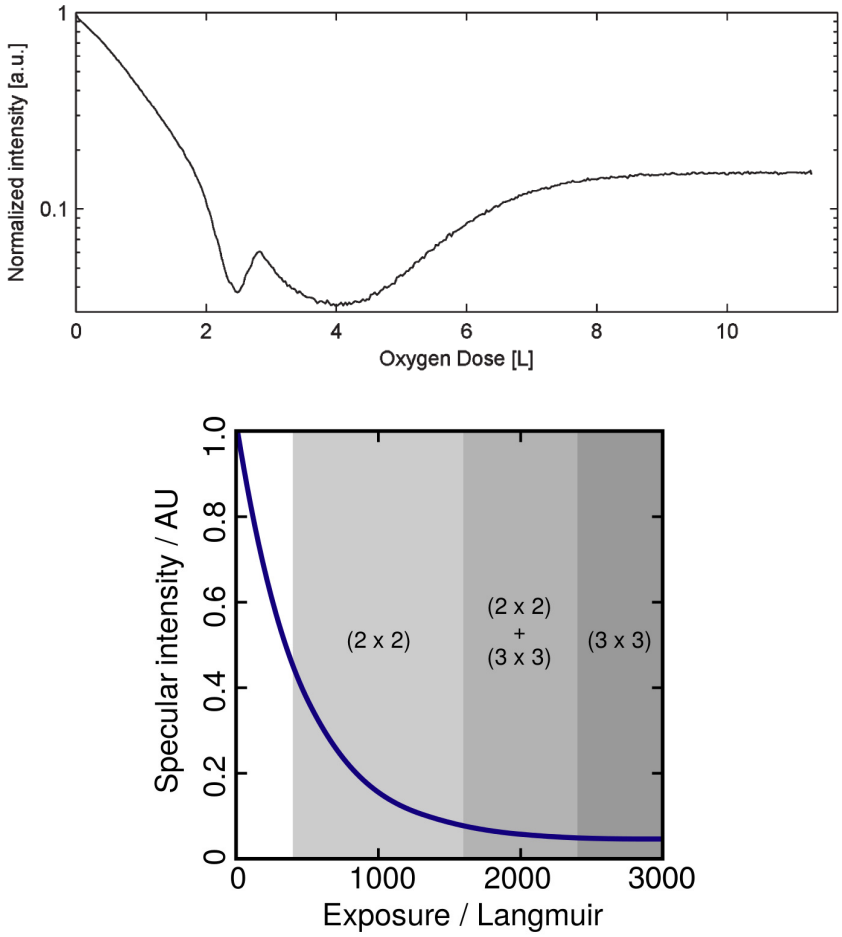

Figure 2.3: Uptake curves from helium scattering experiments. Upper plot: variation of specular intensity with exposure for O/Ru(0001) at 300 K [73]. Reprinted with permission from reference [73], Copyright (2011) American Chemical Society. The uptake curve is structured, implying that ordering takes place near certain ideal coverages, in particular $\theta = 0.25$ ML and 0.5 ML (saturation). Lower plot: specular uptake for H/Cu(111) at 130 K [74]. Reprinted from reference [74], Copyright (2003), with permission from Elsevier. Although ordered surface structures are known to form (indicated on the plot), the decay of specular is monotonic, which suggests that the surface order during deposition evolves in a smooth way with increasing coverage, which is consistent with the islanding behaviour seen in Chapter 6.

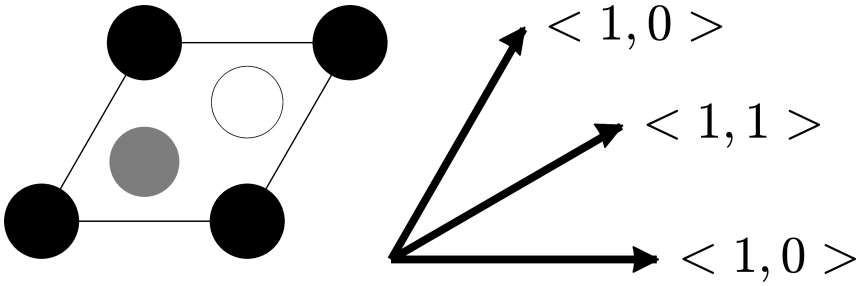

Figure 2.4: Definition of the high-symmetry surface directions on fcc(111) and hcp(0001). Black circles represent surface substrate atoms. The grey circle shows the position of the first subsurface layer, and the empty circle represents the second subsurface layer (fcc(111), with ABCABC stacking) or the "missing" layer (hcp(0001), with ABAB stacking). The "hcp" threefold hollow site is defined as being over the second atomic layer, and the "fcc" site is the other threefold site. The high symmetry directions $< 1, 0 >$ and $< 1, 1 >$ are labelled by their composition out of the two primitive lattice vectors defining the conventional parallelogram-shaped primitive unit cell. No distinction is made between $< 1, 0 >$ and $< 0, 1 >$ since they cannot be distinguished by HAS or HeSE.

illustrated in Figure 2.4. Because the position of the subsurface layers provides only a minor modification to the helium-surface potential, diffraction scans of fcc(111) clean surfaces have approximate sixfold symmetry. The approximate sixfold symmetry can be seen in LEED patterns (e.g. [75]), and HAS is less sensitive to the sub-surface structure so the deviation from sixfold symmetry is even less noticeable in HAS.

Simple approximations can be used to understand the qualitative features of diffraction patterns in the context of the experiments in Chapters 5 and 6. In Chapter 5 a graphene overlayer is grown on Ru(0001). The graphene structure is only weakly distorted by the underlying support, and becomes commensurate with the clean surface over a long repeat length, with 25×25 unit cells of the graphene layer matching 23×23 clean primitive cells. The structure is referred to as a moiré pattern. In principle, if the primitive unit cell of the structure is a 23×23 expansion of the primitive surface cell, diffraction peaks could be seen at $\Delta\mathbf{K}$ on the clean surface reciprocal lattice contracted by a factor of 23. However, not all those peaks are observed. Firstly, the odd-order peaks are not seen [76] because the unit cell can be divided into 2×2 almost identical sub-cells. Secondly, peaks which are far from the diffraction peaks of the pure graphene or pure Ru are strongly suppressed, and are more strongly suppressed as island sizes increase. The effect can be understood qualitatively within the eikonal hard-wall approximation [77], a semiclassical expression for the scattering amplitude $F(\Delta\mathbf{K})$ in terms of a

corrugation function $\xi(\mathbf{R})$ which describes the height of the surface:

$$F(\Delta\mathbf{K}) = \frac{-1}{S}\int_u d\mathbf{R}\, \exp\left[i\Delta\mathbf{K}\cdot\mathbf{R} - i\Delta k_z(\Delta\mathbf{K})\xi(\mathbf{R})\right]. \tag{2.16}$$

A moiré patterned surface can be modelled by a corrugation function which is the sum of a function $\xi_1(\mathbf{R})$ which has the periodicity of the substrate, and a function $\xi_2(\mathbf{R})$ with the periodicity of the adsorbate overlayer (graphene):

$$\xi(\mathbf{R}) = \xi_1(\mathbf{R}) + \xi_2(\mathbf{R})\,. \tag{2.17}$$

If the surface-perpendicular momentum transfer Δk_z does not vary strongly with $\Delta\mathbf{K}$, the expression 2.16 is a Fourier transform of a product, and is therefore the convolution of two diffraction patterns, say $F_1(\Delta\mathbf{K})$ for the clean surface,

$$F_1(\Delta\mathbf{K}) = \frac{-1}{S}\int_u d\mathbf{R}\, \exp\left[i\Delta\mathbf{K}\cdot\mathbf{R} - i[(k_{i,z} + k_{G,z})]\xi_1(\mathbf{R})\right], \tag{2.18}$$

and $F_2(\Delta\mathbf{K})$ for the graphene layer, where ξ_1 is replaced with ξ_2. Within the convolution picture, the comb of possible moiré peaks arises as additions and subtractions of the reciprocal lattice vectors of the substrate and graphene layers respectively [78]. As a corollary, the weaker the high-order diffraction patterns associated with ξ_1 and ξ_2, the more strongly suppressed are the moiré peaks which are not derived from ξ_1 or ξ_2 individually but depend on the convolution for their existence. The eikonal approximation is not expected to be quantitatively accurate for the scattering conditions in the HeSE spectrometer, and is used here only as a qualitative tool for understanding the form of the diffraction pattern. Given a well-defined monolayer, quantitative information on the interaction potential between He atoms and the moiré-patterned surface could be obtained by comparing experimental intensities to numerically accurate calculations using, for example, the well-established close-coupling method [79]. However, that direction is not pursued in the present Thesis.

For adsorbate overlayers at low coverage, the kinematic scattering approximation is a convenient way to understand the relationship between overlayer structure and the diffraction pattern. The kinematic approximation was already introduced in the context of HeSE dynamical measurements and quasielastic scattering 2.1.2, but there the variation of absolute scattered intensity with energy transfer $\hbar\Delta\omega$ at approximately-fixed $\Delta\mathbf{K}$ is of the most interest, whereas in diffraction scans the variation of intensity with $\Delta\mathbf{K}$ is measured. The kinematic scattering amplitude from adsorbates at positions $\mathbf{R}_n$ written in terms of a single-adsorbate scattering

form factor $F(\Delta\mathbf{K})$, reads

$$A(\Delta\mathbf{K}) \propto F(\Delta\mathbf{K}) \sum_n e^{i\Delta\mathbf{K}\cdot R_n} , \tag{2.19}$$

which implies a factorizing total intensity,

$$I(\Delta\mathbf{K}) \propto |F(\Delta\mathbf{K})|^2 S(\Delta\mathbf{K}) , \tag{2.20}$$

$S(\Delta\mathbf{K})$ is the structure factor

$$S(\Delta\mathbf{K}) = \sum_{m,n} \langle \exp(i\Delta\mathbf{K} \cdot [\mathbf{R}_m - \mathbf{R}_n]) \rangle , \tag{2.21}$$

akin to $S(\Delta\mathbf{K}, \Delta\omega)$ but with no energy resolution. The kinematic approximation can be justified within the first Born approximation [67] as described in Section 2.1.2 in relation to the dynamical signatures of the HeSE experiment.

The factorized form 2.20 shows that there are two possible sources of features in diffraction scans of adsorbate layers: the spatial arrangement of adsorbates, and the helium scattering form factor of a single adsorbate. The relationship between the structure factor and the overlayer structure is characterized by the following properties:

- the structure factor of a completely disordered system is a constant;
- the structure factor of a two-dimensional lattice is the reciprocal lattice;
- the structure factor of an isotropic system is isotropic in $\Delta\mathbf{K}$.

Qualitatively, if a low-coverage ordered structure (say, in a hexagonal arrangement) loses its perfect order (upon heating, for example) but maintains some radial order because of mutual interactions, then the diffraction peaks of the ordered structure will spread and merge, forming a ring with approximately circular symmetry. Therefore a broad peak in the diffracted intensity at roughly the same ΔK along two high-symmetry azimuths can be indicative of radial order. Previous diffraction scans of H/Ru(0001) at low coverage displayed the phenomenology just described, and the broad feature was reproduced by calculating $S(\Delta\mathbf{K})$ for a radially interacting system by lattice Monte Carlo simulations [35]. However, the adsorbate form factor, i.e. the $\Delta\mathbf{K}$-dependent scattering amplitude from a single adsorbate, can also possess non-monotonic structure, i.e. oscillations, which can be seen experimentally [80]. Therefore, a broad peak along two high symmetry azimuths is not guaranteed to be due to repulsive interactions but could be a form factor effect. The interpretation for H/Ru(0001) is explored further in Chapter 6.

2.1.4.3 Polarization scans

A polarization scan consists of a measurement of $P(t_{SE})$ under otherwise fixed conditions. The experiment was formulated above in terms of expectations σ_x and σ_y. In practice, the polarization is determined using an equivalent formulation in terms of intensities (the raw experimental observable). Specifically, an ideal spin analyser oriented to select the state $|x\rangle$ transmits an atom with a probability proportional to

$$|\langle x|\Psi\rangle|^2\,, \tag{2.22}$$

where the state $|x\rangle$ has the matrix representation

$$|x\rangle = \frac{1}{\sqrt{2}}\begin{pmatrix} 1 \\ 1 \end{pmatrix}. \tag{2.23}$$

Before the analyser stage, the spin state is of the form

$$|\Psi\rangle = \frac{1}{\sqrt{2}}\begin{pmatrix} e^{-i\theta/2} \\ e^{+i\theta/2} \end{pmatrix}. \tag{2.24}$$

The transmission probability through the analyser is then

$$|\langle x|\Psi\rangle|^2 = \cos^2\left(\frac{\theta}{2}\right) = \frac{1}{2}\Big(1+\cos\theta\Big)\,. \tag{2.25}$$

If the phase of the initial spin state is varied in some way, such that the spin state before entering the first precession solenoid is not $(1,1)$ but $(e^{-i\phi/2}, e^{+i\phi/2})$ then the transmission probability becomes

$$\cos^2(\theta-\phi) = \frac{1}{2}\Big(1+\cos\theta\cos\phi+\sin\theta\sin\phi\Big)\,. \tag{2.26}$$

Averaging over the beam then gives the variation of intensity with ϕ as

$$I(\theta) \propto \quad 1+\langle\cos\theta\rangle\cos\phi+\langle\sin\theta\rangle\sin\phi \tag{2.27}$$

$$= 1+\langle\sigma_x\rangle\cos\phi+\langle\sigma_y\rangle\sin\phi\,. \tag{2.28}$$

Experimentally, the phase angle ϕ is controlled by a phase coil before the incoming main precession coil, which adds to the magnetic field integral that precesses the spin of incoming atoms. The ratio r of the current I_p in the phase coil, and the current I_1 in the main precession solenoid that would generate the same spin precession is a calibrated constant $I_p/I_1 = 1323.0 \pm 2.1$ [28]. The alternative would be a spatial rotation of the spin polarizer (or analyser), which is impractical. Because

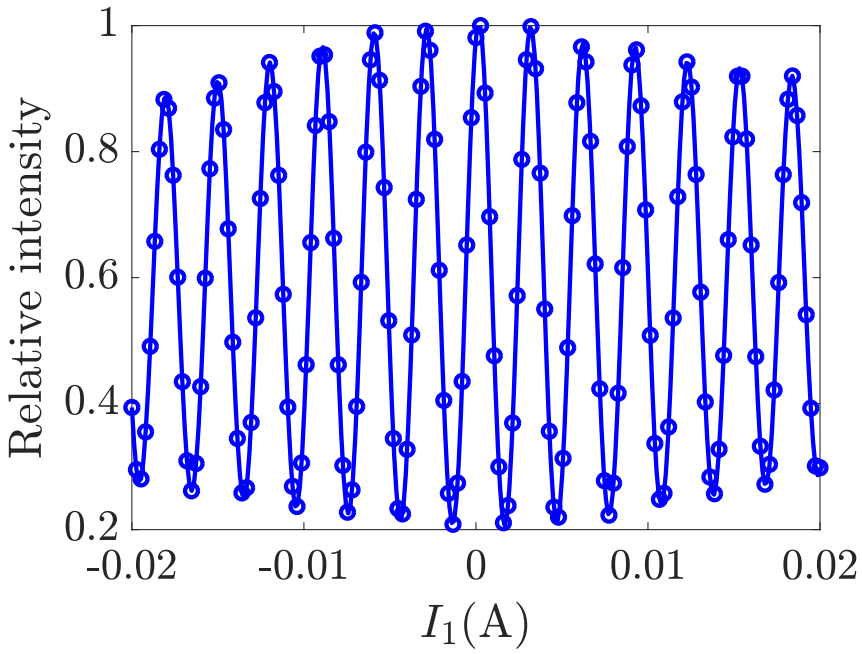

Figure 2.5: Variation of detected He atom intensity with the current I_1 in the incoming precession solenoid, while $I_2 = 0$ in the outgoing solenoid. The points are experimental data; the solid curve is a spline to guide the eye. The current in the incoming coil induces the rotational phase ϕ leading to intensity oscillations as described in Equation 2.27. The functional form of $I(\phi)$ is a cosine multiplied by an approximately Gaussian envelope, which are used to determine a mean energy and energy spread for the incoming beam. In dynamics measurements the intensity variation over the central region $0 \leq \phi < 2\pi$ is used to measure the polarization according to Equation 2.30, using the phase coil rather than the incoming precession solenoid to effect the phase shifts.

of the finite incident energy spread of the beam, the phase introduced by the phase coil is not strictly equal for all incoming atoms. However, the associated aberration is negligible as long as the incoming beam energy spread is a small fraction of the mean energy [69]. Figure 2.5 illustrates the variation in transmitted intensity as the current I_1 in the incoming precession solenoid is varied, with zero current in the outgoing solenoid. The intensity follows a cosine form, with a decaying envelope due to the finite incident energy spread. Since the phase coil and the incoming precession coil both contribute to the total precession of incoming atoms, the same behaviour is seen when the current in the phase coil is varied with $I_1 = 0$ and $I_2 = 0$. Due to hardware constraints, the incoming solenoid is used to calibrate the beam energy distribution since large phase shifts are required, while the phase coil is used to sample in the range $0 \leq \phi \leq 2\pi$ during dynamics experiments. Measurements of the type shown in Figure 2.5 were used to calibrate the mean beam energy before dynamics experiments, as is usual practice [69].

The polarization as a function of I_1 and I_2 is determined by four point mea-

surements. Specifically, the intensity is sampled at $\phi = \{0, 1, 2, 3\}\frac{\pi}{2}$ by varying the phase coil current with I_1 and I_2 fixed. For all polarization measurements reported in the present work, I_1 and I_2 were held equal and opposite, of magnitude I_{SE} as described in Section 2.1.2. The sampled intensities are fitted to

$$I(\phi) = G(\phi)\big[A\cos(\phi) + B\sin(\phi)\big] + C\,, \tag{2.29}$$

where $G(\phi)$ is a Gaussian envelope function derived from the pre-calibrated incident energy spread. By comparison with the result 2.27, the polarization is extracted as

$$p = \frac{A + iB}{C - \mathrm{b}}\,. \tag{2.30}$$

where the background count rate b (detector count rate in the absence of a beam) is measured to high precision before each loop. Four-point measurements will be revisited in the context of detector noise in Section 2.3.

2.2 Data processing

Here I describe the models and methods used to process experimental data in Chapters 5 and 6.

2.2.1 Discrete jump models

In a discrete jump model, particle position is restricted to take discrete values, and transition between them instantaneously, with a probability per unit time that depends on the initial and final sites. In the present Thesis all experimental studies were carried out on close-packed hexagonal surfaces whose unit cell is illustrated in Figure 2.4. The following convention is used throughout for surface directions. The vectors that form the conventional primitive unit cell are used as a basis. A direction parallel to the atomic rows on the close packed surface is therefore referred to as $< 1, 0 >$, and a direction rotated by 30° is referred to as $< 1, 1 >$. The same surface-labelling scheme is used for fcc(111) and hcp(0001) surfaces, to emphasise their similarity when it comes to surface diffusion.

No distinction is made between $< 1, 0 >$ and $< 0, 1 >$. The clean fcc(111) or hcp(0001) surface has threefold rotation symmetry, so $< 1, 0 >$ and $< 0, 1 >$ are not strictly equivalent, as described in Section 2.1.4.2. The inequivalent directions related by a 60° rotation cannot be distinguished via jump diffusion signatures under the assumption of kinematic scattering, because classically the ISF has the symmetry

$I(\Delta\mathbf{K}, t) = I(-\Delta\mathbf{K}, t)$. (The $\Delta\mathbf{K}$ inversion symmetry will be reiterated for the specific jump models in the present Section, and in the discussion of the microscopic definition of the classical ISF in Chapter 3). Nonetheless, the ISF is sensitive to the inequivalence of different adsorption sites within a unit cell, even if they are degenerate.

Two types of jump model are relevant to the present work,

1. Chudley-Elliott (CE) models [81], in which the available sites form a Bravais lattice (with hexagonal symmetry, in the case of fcc(111) or hcp(0001) surfaces);

2. "non-Bravais" models which are periodic with two adsorption sites per unit cell.

In the CE model, the ISF at fixed $\Delta\mathbf{K}$ decays exponentially in time. The derivation relies on the interpretation of the ISF as the spatial Fourier transform of a time-dependent probability, which will be considered in detail in Chapter 3. In short, the exponential nature of the ISF arises because the probability of a particle being located on a given lattice site n evolves in time according to

$$\frac{\partial}{\partial t} P(n;t) = \Gamma_{in} - \Gamma_{out}\,, \tag{2.31}$$

where Γ_{in} and Γ_{out} are the probability per unit time for the particle to jump into site n from other sites, or out of site n to other sites. Because Γ_{in} and Γ_{out} are proportional to probabilities on site n and neighbouring sites, the solution is an exponential in time. The final result is

$$I(\Delta\mathbf{K}, t) = \exp(-\alpha(\Delta\mathbf{K})|t|)\,, \tag{2.32}$$

in which $\alpha(\Delta\mathbf{K})$ is a Fourier series over the reciprocal lattice, with components related to discrete jumps of jump vector $\mathbf{j}$ with rate Γ_j by

$$\alpha(\Delta\mathbf{K}) = \sum_{\mathbf{j}} 2\Gamma_{\mathbf{j}} \sin^2\left(\frac{\Delta\mathbf{K}\cdot\mathbf{j}}{2}\right). \tag{2.33}$$

Allowed jump vectors are always linear combinations of the primitive lattice vectors, as intra-cell motion is neglected. The jump vectors necessarily come in symmetry-related pairs $(\mathbf{j}, -\mathbf{j})$. In the present Thesis I count all jump vectors individually, so that for example there are six types of nearest-neighbour jump on the hexagonal Bravais lattice. The Chudley-Elliott form is expected to be applicable for systems where the only stable adsorption site is unique within the unit cell, for example top

sites of an fcc(111) system. However, it can also apply to a very close approximation when there are two stable adsorption sites separated in energy by $\Delta E \gg k_B T$ such that the occupation of the metastable site is so rare that it can be treated as part of the diffusion barrier between the stable sites.

The ISF has been derived for jump systems with multiple adsorption sites per unit cell [82, 83], in other words multiple sublattices. The special case relevant to the present Thesis is the case where the two hollow sites in a hexagonal unit cell both function as adsorption sites of similar energy. In analysing carbon and hydrogen diffusion data (Chapters 5 and 6), the jump rates have been parametrized as exponentially distributed up to third-nearest-neighbour length, a reasonable assumption used previously [84] to reduce the number of free parameters in the jump model. Figure 2.6 illustrates double and triple jumps within the model. The ISF takes the form of a biexponential decay, i.e.

$$I(\Delta\mathbf{K}, t) = A_1(\Delta\mathbf{K}) e^{-\alpha_1(\Delta\mathbf{K})t} + A_2(\Delta\mathbf{K}) e^{-\alpha_2(\Delta\mathbf{K})t} , \tag{2.34}$$

where $\alpha_{1,2}$ and $A_{1,2}$ are derived by considering the evolution of probability density [84].

Here I summarize the core results of the multiple-sublattices calculation of [84]. Write the jump rates $1/\tau_{ijk}$ from sub-lattice i to j via jump vector via different jump vectors $\mathbf{l}_{ijk}$. Define a matrix $\mathbf{A}$ as

$$\mathbf{A} = \sum_k \frac{1}{\tau_{jik}} \exp(-i\Delta\mathbf{K} \cdot \mathbf{l}_{ijk}) - \delta_{ij} \sum_j \frac{1}{\tau_{ij}} , \tag{2.35}$$

where $1/\tau_{ij}$ is the total jump rate from sublattice i to j. Let c_i be the relative concentration of particles in sublattice i. Define a matrix $\mathbf{T}$ with elements

$$T_{ij} = \frac{1}{c_i} \delta_{ij} , \tag{2.36}$$

and construct the (Hermitian) matrix $\mathbf{B}$,

$$\mathbf{B} = \mathbf{T}\mathbf{A}\mathbf{T}^{-1} , \tag{2.37}$$

with eigenvalues M_p and the associated eigenvectors $\mathbf{b}^p$, whose elements will be called b_i^p. Defining the decay amplitudes as

$$w_p(\Delta\mathbf{K}) = \Big| \sum_i \sqrt{c_i} b_i^p \Big|^2 , \tag{2.38}$$

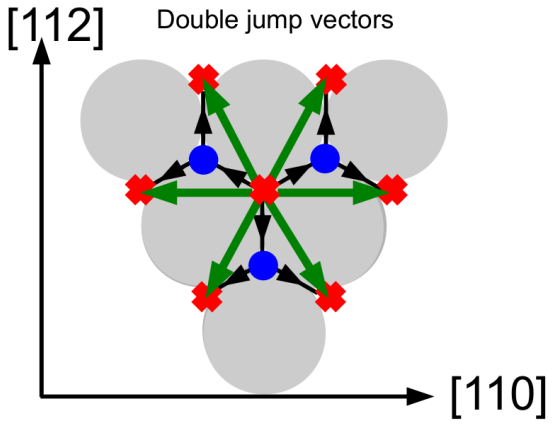

(a) Double jumps on fcc(111) or hcp(0001) surfaces.

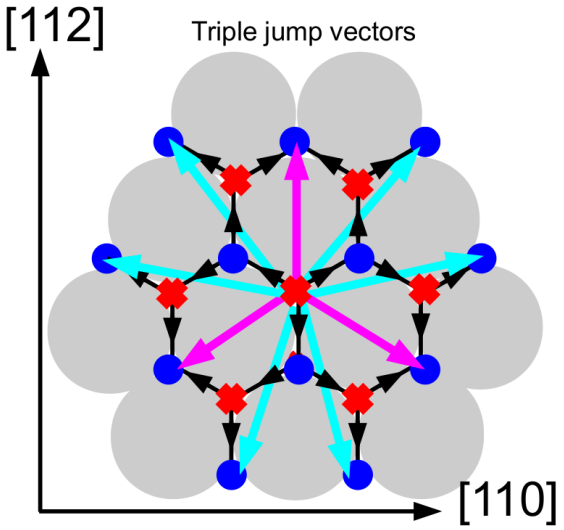

(b) Triple jumps on fcc(111) or hcp(0001) surfaces.

Figure 2.6: From [84]. Illustration of double jumps (2.6a) and triple jumps 2.6b on an fcc(111) or hcp(0001) surface. Single jumps are represented by black arrows in both Figures. The directions referred to as [110] and [112] in the diagrams correspond to $< 1, 0 >$ and $< 1, 1 >$ respectively. Double jumps (green) take the diffusing adsorbate from its initial site to another site on the same sublattice. The double jump vectors are evaluated in Table 2.4 and contribute diagonal terms to the matrix $\mathbf{A}$ of Equation 2.35. Single and triple jumps take the adsorbate to the opposite sublattice, and contribute off-diagonal terms. The two distinct types of triple jump are shown as blue and cyan vectors. The two distinct types of triple jump are assumed to occur with equal rates.

Table 2.3: Single jump vectors out of hollow sites of type $i = 1$ as defined in the main text.

Description	**Cartesian vector**
Vertical down	$a \begin{pmatrix} 0 \\ -\frac{1}{\sqrt{3}} \end{pmatrix}$
Diagonal (up, right)	$a \begin{pmatrix} \frac{1}{2} \\ \frac{1}{2\sqrt{3}} \end{pmatrix}$
Diagonal (up, left)	$a \begin{pmatrix} -\frac{1}{2} \\ \frac{1}{2\sqrt{3}} \end{pmatrix}$

the ISF is given by

$$I(\Delta\mathbf{K}, t) = \sum_p w_p(\Delta\mathbf{K}) \exp(M_p(\Delta\mathbf{K})t) \,. \tag{2.39}$$

Because $\mathbf{B}$ is Hermitian, its eigenvalues are real and therefore the ISF is real, and so $I(-\Delta\mathbf{K}, t) = I(\Delta\mathbf{K}, t)$. That is, the ISF is invariant under 180° rotations, and therefore 60° rotations of fcc(111) and hcp(0001) surfaces.

For hollow-hollow diffusion, $p = \{1, 2\}$. Define λ as the ratio of occupations of the two sublattices, i.e. $c_2 = \lambda c_1$ (λ no longer represents the wavelength as it did earlier in the present Chapter.) The total exit rates from sub-lattice 1 to 2 and the reverse are τ_{12} and $\tau_{21} = \lambda\tau_{12}$, which are related by detailed balance to maintain the equilibrium concentration ratio.

Expressions for $\mathbf{A}$ along the high symmetry directions $< 1, 1 >$ and $< 1, 0 >$ are tractable for simple enough jump models Here I will derive the result when single, double and triple jumps are allowed. The remainder of the derivation will use $Q \equiv |\Delta\mathbf{K}|$ for economy of notation and for consistency with the original presentation [84].

Single jumps (black arrows in Figure 2.6) connect inequivalent sites. For each site there are three possible single jumps. Define sites of type $i = 1$ as those where one of the outbound single jumps is vertically down the page. Table 2.3 gives the available single jump vectors from sites of type $i = 1$. The available jumps from sites of type 2 are their negatives.

For a model with single jumps only, evaluating $\mathbf{A}$ along $< 1, 1 >$ (the y direction) according to the definition 2.35 gives

$$\mathbf{A} = \begin{pmatrix} A_{11} & A_{12} \\ A_{21} & A_{22} \end{pmatrix}$$

Table 2.4: Double jump vectors, out of hollow sites of either type. Each jump vector **j** has a partner $-\mathbf{j}$ as in the Chudley-Elliott case. The description in the first column applies to one of each pair.

Description	**Cartesian vector**
Along row	$\pm a \begin{pmatrix} 1 \\ 0 \end{pmatrix}$
Diagonal (up, right)	$\pm a \begin{pmatrix} \frac{1}{2} \\ \frac{\sqrt{3}}{2} \end{pmatrix}$
Diagonal (up, left)	$\pm a \begin{pmatrix} \frac{1}{2} \\ -\frac{\sqrt{3}}{2} \end{pmatrix}$

$$= \begin{pmatrix} -\frac{1}{\tau_{12}} & \frac{1}{\tau_{21k}}(\exp(iQ\frac{a}{\sqrt{3}}) + 2\exp(iQ\frac{a}{2\sqrt{3}}) \\ \frac{1}{\tau_{12k}}(\exp(-iQ\frac{a}{\sqrt{3}}) + 2\exp(-iQ\frac{a}{2\sqrt{3}}) & -\frac{1}{\tau_{21}} \end{pmatrix}. \tag{2.40}$$

Each of the τ_{12k} are equal as they refer to three completely equivalent processes. Therefore, $\tau_{12k} = 3\tau_{12}$. Applying the detailed balance relations phrased in terms of λ, the matrix becomes as stated in [84],

$$\mathbf{A} = \frac{1}{\tau_{12}} \begin{pmatrix} -1 & \frac{1}{3\lambda}(\exp(iQ\frac{a}{\sqrt{3}}) + 2\exp(iQ\frac{a}{2\sqrt{3}}) \\ \frac{1}{3}(\exp(-iQ\frac{a}{\sqrt{3}}) + 2\exp(-iQ\frac{a}{2\sqrt{3}}) & -\frac{1}{\lambda} \end{pmatrix}. \tag{2.41}$$

The **A** matrices for the triple jumping case, using all the jump types indicated in Figure 2.6, are constructed by direct extension. Double jumps are between equivalent sites, and are indicated in green arrow in Figure 2.6. For sites of either hollow type, there are six available double jumps and the jump vector sets are identical for both types of site. Table 2.4 lists all the allowed double jumps in the Cartesian basis. Table 2.5 lists the triple jumps from $i = 1$ sites. There are two types of triple jump of different length, indicated by magenta and cyan arrows in Figure 2.6. Although they are of different length, they are both counted as triple jumps because the corresponding minimum-energy path in the continuous potential possesses three approximately straight barrier-crossing sections connected by wells (hollow sites) in which the particle must turn a corner to continue a long jump.

It is convenient to write the total jump rate out of sublattice $i = 1$ as τ^{-1}, which defines τ as a mean residence time. Then, divide the jumps up into single, double and triple jumps in the proportions p_1, p_2 and p_3 respectively, such that the total jump rate out of sublattice $i = 1$ due to single jumps is given by p_1/τ and so on. Then, the rates associated with the distinct types of single, double and triple jumps are found by dividing the total single/double/triple jump rate by the number of that

Table 2.5: Triple jump vectors, out of hollow sites of type $i = 1$, described with reference to Figure 2.6. It is easily checked that the magenta jump vectors have magnitude $2a/\sqrt{3}$ while the cyan vectors have magnitude $a\sqrt{7/3}$, as stated in [84]. The triple jump vectors from sites of type $i = 2$ are the negatives of the vectors in the table.

Description	**Cartesian vector**
Magenta, vertical up	$a\begin{pmatrix} 0 \\ \frac{2}{\sqrt{3}} \end{pmatrix}$
Magenta, diagonal down	$a\begin{pmatrix} \pm 1 \\ -\frac{1}{\sqrt{3}} \end{pmatrix}$
Cyan, approx horizontal	$a\begin{pmatrix} \pm\frac{3}{2} \\ \frac{1}{2\sqrt{3}} \end{pmatrix}$
Cyan, diagonal up	$a\begin{pmatrix} \pm 1 \\ \frac{2}{\sqrt{3}} \end{pmatrix}$
Cyan, approx vertical down	$a\begin{pmatrix} \pm\frac{1}{2} \\ -\frac{5}{2\sqrt{3}} \end{pmatrix}$

type of jump. For example, the rate of single jumps vertically down out of $i = 1$ sites is $p_1/(3\tau)$. The fact that two different routes are available to make a magenta jump can be accounted for by considering the two routes as distinct jumps but with the same jump vector. The number of distinct types of triple jump is therefore 12. The matrix elements of $\mathbf{A}$ along $< 1, 0 >$ (the x direction) are then,

$$A_{11} = \frac{p_2}{6\tau}\Big[2\cos(Qa) + 4\cos(\frac{Qa}{2})\Big]\,; A_{22} = A_{11}/\lambda\,; \tag{2.42}$$

$$\begin{aligned} A_{12} = & \quad \tfrac{p_1}{3\tau\lambda}\Big[1 + 2\cos(\tfrac{Qa}{2})\Big] && (2.43)\\ & + \tfrac{p_3}{6\tau\lambda}\Big[1 + 2\cos(Qa)\Big] && (2.44)\\ & + \tfrac{p_3}{12\tau\lambda}\Big[2\cos(\tfrac{3Qa}{2}) + 2\cos(Qa) + 2\cos(\tfrac{Qa}{2})\Big]\,; && (2.45) \end{aligned}$$

$$A_{21} = \lambda A_{12}^*\,. \tag{2.46}$$

Along $< 1, 1 >$ (the y direction),

$$A_{11} = \frac{p_2}{6\tau}\Big[2 + 4\cos(\frac{\sqrt{3}}{2}Qa)\Big]\,; A_{22} = A_{11}/\lambda\,; \tag{2.47}$$

$$A_{12} = \frac{p_1}{3\tau\lambda}\left[2\exp(\tfrac{-\sqrt{3}}{2}iQa)\right] \tag{2.48}$$

$$+\frac{p_3}{6\tau\lambda}\left[\exp(-\tfrac{2}{\sqrt{3}}iQa) + 2\exp(\tfrac{1}{\sqrt{3}}iQa)\right] \tag{2.49}$$

$$+\frac{p_3}{12\tau\lambda}\left[2\exp(-\tfrac{1}{2\sqrt{3}}iQa) + 2\exp(-\tfrac{2}{\sqrt{3}}iQa) + 2\exp(\tfrac{5}{2\sqrt{3}}iQa)\right]; \tag{2.50}$$

$$A_{21} = \lambda A_{12}^* \,. \tag{2.51}$$

The proportions $p_{1,2,3}$ can reasonably be constrained by applying a survival probability model, in which the rate of individual single, double and triple jumps are in a geometric ratio $1 : s : s^2$. The net rates of all single, all double and all triple jumps are then in the ratio $p_1 : p_2 : p_3 = 3 : 6s : 12s^2$, which is equivalent to the previous geometric ratio but for $s \leftrightarrow 2s$. The definition I am using for s is different from the one defined in the cited work [84] by that factor of 2. Here $s < 1$ for realistic surface dynamics. Finally, the absolute proportions p_1 are determined by the normalization $p_1 + p_2 + p_3 = 1$.

2.2.2 Basic fitting

In situations where it is appropriate to fit a polarization scan (or a portion thereof) to a model function, the fit has been performed using the MATLAB `fit` function, which implements a weighted nonlinear least squares method [85]. In other words, given a set of data $\{y_i\}$ and corresponding model values $\{f_i\}$ which depend on a set of parameters with independent Gaussian uncertainties σ_i, the quantity

$$Q = \sum_i \frac{(y_i - f_i)^2}{2\sigma_i^2} \tag{2.52}$$

is minimized. Q is the weighted mean square residual between the data and model values. The probability of obtaining the data given the model is

$$p(\{y_i\}|\{f_i\}) \propto \exp(-Q)\,, \tag{2.53}$$

and therefore minimizing Q is equivalent to maximizing the conditional probability. For scans repeated over multiple loops, the uncertainties were taken as the standard deviation across the loops. For single-loop scans, a uniform uncertainty of 0.01 was assumed, which is in line with the signal-to-noise on typical polarization measurements as determined in Section 2.3. When a uniform uncertainty is used, its exact value is not important since Q will be minimized for the same parameter set regardless of a constant scaling of the σ_n.

Basic fitting is often not useful for biexponential lineshapes because of the difficulty in resolving the two components [71]. Therefore, when basic fitting is the appropriate method, the functional form appropriate for jump diffusion studies is usually

$$P(t) = Ae^{-\alpha(t)} + C\,, \tag{2.54}$$

where A is the amplitude and C is a constant offset known as the static polarization. The physical origin of C lies in static defects, which could be:

- immobile coadsorbed species (present only in small concentrations after cleaning);
- step edges;
- islands of the main adsorbed species in equilibrium with a lattice gas whose diffusion is being measured;
- intensity diffracted elastically by the clean surface, if near a diffraction condition.

The amplitude A for jump diffusion is normally substantially less than 1, due to the following factors which all reduce it:

- the maximum transmitted polarization of the instrument in the absence of any surface dynamics, is less than 100% (65% is typical);
- a finite fraction of the beam is scattered elastically (leading to a finite C);
- a finite fraction of the beam is scattered inelastically or by fast processes which manifest as a rapid initial decay of the ISF before the long-time decaying tail (explored further in Section 3.1);
- a portion of the main decay might consist of a faster exponential component.

2.2.3 Fit-start-time optimization

For the basic fitting method described above to be viable, a defensible model function is required, and the model might not be applicable to an entire polarization scan but only a portion of it. The long-time limit of the ISF on a corrugated surface typically represents jump diffusion, for which the ISF is analytically known to be a single exponential decay (Chudley-Elliott model, Equation 2.33) or a multiple exponential decay (e.g. the non-Bravais jump model of the previous Section 2.2.1). Experimentally, the exact time at which the long time limit applies is not known in

advance. One method of dealing with an unknown best start time is to increase the start time until the results of fitting do not vary in any meaningful way. That method has been applied in cases where the desired outcome of fitting a set of polarization scans is an $\alpha(\Delta\mathbf{K})$ representing the slowest resolved decaying component, and a faster second exponential component cannot be systematically determined. Figure 2.7 shows a polarization scan taken from Chapter 5, which is described well by a single exponential fit.

Figure 2.8 shows another scan for the same system, at a different ΔK, when a single exponential fit is not a good description. The fitted decay rate varies systematically with the start time, but reaches an approximate plateau after 100 ps, after which the fitting parameter fluctuates. Extending the fit start time to 100 ps selects the slower exponential component.

2.2.4 Fourier filtering

In some situations (such as for H/Pd(111) data in Section 6.4) the main decay of a polarization scan, due to adsorbate diffusion, is masked at moderately short spin echo times by strong oscillations due to inelastic scattering of helium atoms from surface phonons. The oscillations in the time domain can be largely removed using the fact that they are well separated from the quasielastic peak in the frequency domain. I have used the method as applied to the analysis of Na/Cu(111) data previously [28] to reduce the influence of phonons in measurements where they are a significant feature of the raw data. I summarise the method here and illustrate its application to model data; the application to experimental data is described in context in Chapter 6. Suppose we have a continuous function $I(t)$ over a time domain running from 0 to T. The Fourier transform is defined (for discrete frequencies $\omega_k = 2\pi k/T$) as

$$S(\omega_k) = \int_0^T e^{-i\omega_k t} I(t)\, dt\,. \tag{2.55}$$

If $I(t)$ is uniformly sampled, which is the case for all data in the present Thesis, then the integral can be approximated as a Riemann sum,

$$S(\omega_k) = \Delta t \sum_{n=1}^{N} e^{-i\omega_k t_n} I(t_n)\,, \tag{2.56}$$

which is the discrete Fourier transform, proportional to the MATLAB function `fft` [86].

Oscillations in $I(t)$ generally lead to an inelastic peak in $S(\omega)$ which can be removed or reduced by interpolating the background intensity through the peak in

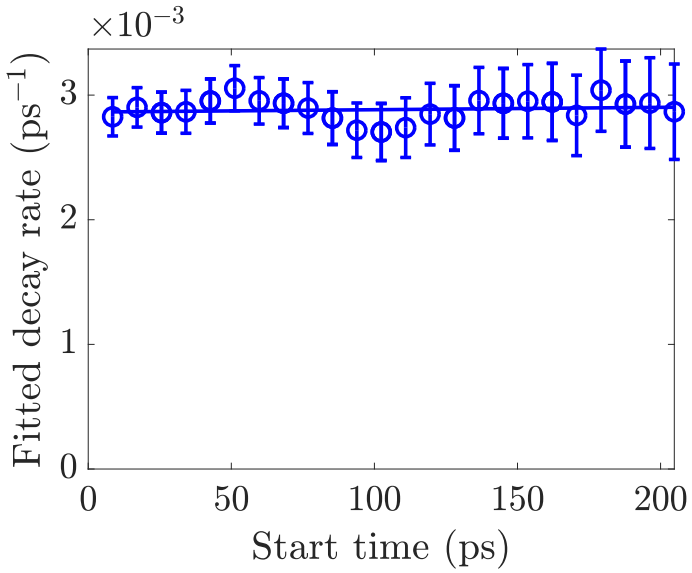

(a) Variation of single exponential decay rate with start time.

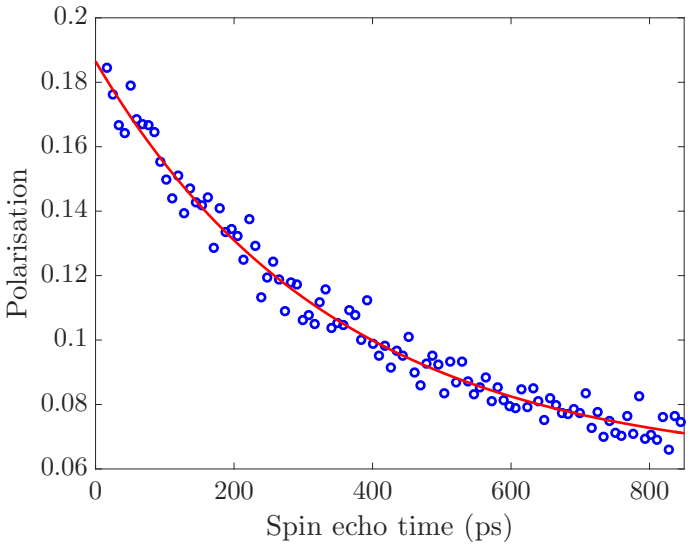

(b) Variation of single exponential decay rate with start time.

Figure 2.7: Analysis of a polarization scan for the system C/Ru(0001) at 700 K and $\Delta K = 0.6\,\text{Å}^{-1}$. In Figure 2.7a the fitted single exponential decay rate is shown as a function of the start time (earliest t_{SE}) used in the fit. The best fit parameter (decay rate) does not vary significantly or systematically with the choice start time, as illustrated by the solid trend line, which is essentially flat and lies within the statistical error bars (68% confidence interval) in all cases. Figure 2.7b shows the polarization scan (blue circles) and the best single exponential fit (red solid curve). The fit uses only data with $t_{SE} > 100\,\text{ps}$, but describes the entire scan well.

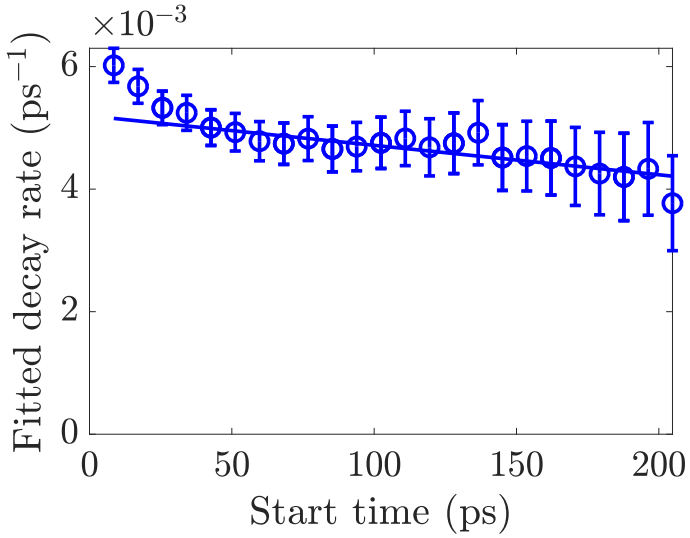

(a) Variation of single exponential decay rate with start time.

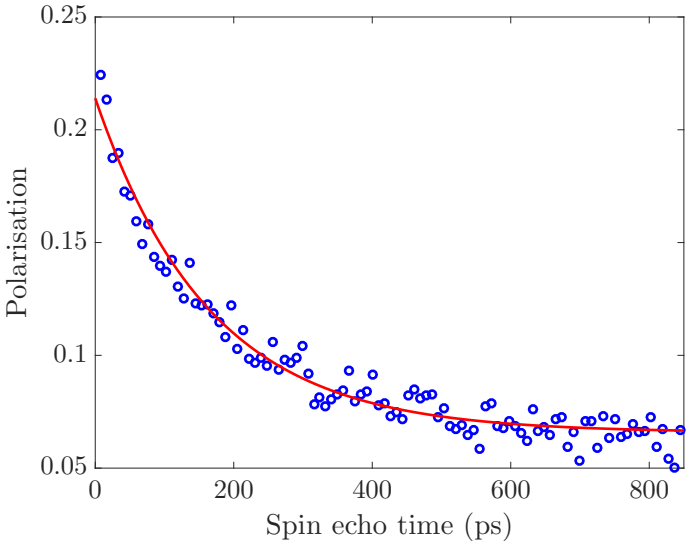

(b) Variation of single exponential decay rate with start time.

Figure 2.8: Analysis of a polarization scan for the system C/Ru(0001) at 700 K and $\Delta K = 1.9\,\text{Å}^{-1}$. Figure 2.8a shows the fitted single exponential decay rate as a function of the shortest t_{SE} included in the fit. In contrast to Figure 2.7, there is a systematic variation of the best fit parameter with start time, and the variation is particularly strong for start times below about 50 ps, as illustrated by the deviation from the solid trend line that has been fitted to the series for start times greater than 50 ps. As in Figure 2.7, the error bars on the fitted parameter (decay rate) are 68% confidence intervals. Figure 2.8b shows the polarization scan (blue circles) and the best single exponential fit for $t_{SE} > 100$ ps. Unlike in the case shown in Figure 2.7, there is a systematic deviation at short times.

the Fourier domain. Figure 2.9 illustrates the procedure for a model lineshape of the form

$$I(t) \propto A\exp(-\alpha|t|) + B\exp(i\Omega t)\exp(-\gamma|t|)\,, \tag{2.57}$$

which contains a decaying tail of decay rate α, and an inelastic feature of frequency Ω and width γ. A and B are real numbers of comparable size. The inelastic peak is greatly reduced by replacing most of the peak with a smooth interpolation of the background, which in the model case consists of the base of the peak itself. Fourier filtering is applied in Chapter 6 to Pd(111) data at high temperatures, where the appropriate values of Ω and the peak width are chosen on a scan-by-scan basis by inspection of the Fourier space lineshapes.

2.2.5 Fitting very slow decays

In the context of quantum diffusion (Chapter 6), it is desirable to distinguish between slow and very slow decays. Here I explore the extent to which very slow decays can be resolved, firstly by least squares fitting and then using a method based on integrating out the decay amplitude and static offset, leaving the probability distribution of the decay rate alone. The Bayesian approach to lineshape analysis has been explored previously for a range of decay amplitudes, time windows and noise levels, for statically offset mono- and bi-exponential lineshapes [71]. Here I specialize the discussion at an early stage to the conditions associated with the main intended application, namely measuring decay rates in polarization scans of H/Ru(0001) and D/Ru(0001) at low temperature.

The increased energy resolution of HeSE over HAS was cited earlier (Section 2.1.2) as one of the key motivating factors for using the method to study adsorbate diffusion. It has been noted in previous accounts of the Cambridge HeSE instrument [61] that there are at least three different measures of dynamical resolution associated with the HeSE experiment

- the energy resolution for $S(\Delta K, \Delta\omega)$ reconstruction, given no prior information about the spectrum;

- the slowest resolvable exponential decay rate α in the t_{SE} domain when the polarization can be assumed to follow $p(t_{SE}) = ae^{-\alpha|t_{SE}|} + c$ but the amplitude a and static offset c are unknown;

- the slowest resolvable exponential decay rate α in the t_{SE} domain when a or c can be assumed.

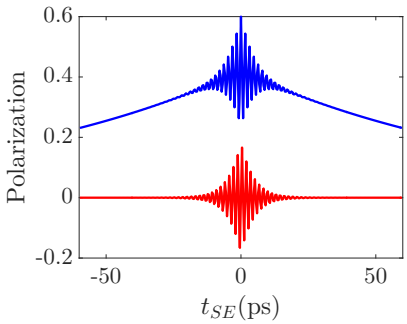

(a) Polarization scan in the time domain

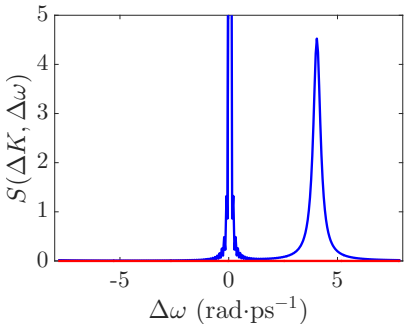

(b) Polarization scan in the Fourier domain

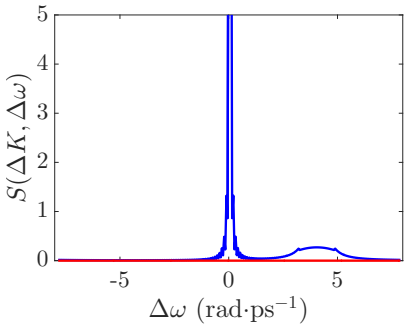

(c) Polarization in the Fourier domain after applying window

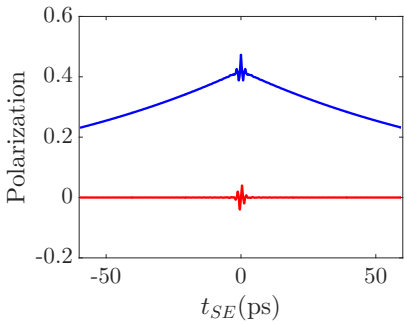

(d) Polarization scan transformed back to the time domain

Figure 2.9: Fourier filtering procedure for model data of the form $I(t) \propto A\exp(-\alpha|t|) + B\exp(i\Omega t)\exp(-\gamma|t|)$. The polarization scan is converted to the Fourier domain using a discrete Fourier transform, and the centre of the inelastic peak is cut out by smoothly interpolating the peak base. The model function was chosen to represent a broad single-sided inelastic peak, as seen in the experimental data.

The energy resolution for spectrum reconstruction is given by the energy spacing associated with a discrete Fourier transform of data in the t_{SE} domain where the t_{SE} range is made as large as possible. For a maximum t_{SE} of 850 ps, the associated energy spacing is

$$\Delta E \approx 2\,\mathrm{neV}\,, \tag{2.58}$$

which is associated with an exponential decay rate of $\alpha \approx 2 \times 10^{-3}\,\mathrm{ps}^{-1}$ if ΔE is interpreted as the width of the narrowest resolvable Lorentzian function in the energy exchange domain.

Given the mono-exponential plus static assumption for the lineshape

$$p(t_{SE}) = ae^{-\alpha|t_{SE}|} + c\,, \tag{2.59}$$

the slowest resolvable decay rate is significantly slower than the rate associated with the energy resolution for spectrum reconstruction ΔE. It has been asserted [61] that if the maximum t_{SE} is 700 ps then α can be resolved down to $0.75\,\mathrm{ns}^{-1}$ if a and c are free parameters, and if a and c can be strongly constrained then resolving down to $\alpha \approx 0.015\,\mathrm{ns}^{-1}$ is feasible. Anticipating the later application to scans of Ru(0001) with a maximum t_{SE} of 850 ps and a typical noise on the polarization of 1 %, I will now quantify the limits of the resolvable decay rate for those parameters, by simulating and fitting exponential decays and investigating the progression of fitted parameters with the underlying parameters.

Figure 2.10 shows simulated polarization scans over the range $0 < t_{SE} < 850\,\mathrm{ps}$, for $\alpha = 1 \times 10^{-3}$ and $\alpha = 10^{-5}$, with amplitude $a = 0.5$, static $c = 0.1$ and Gaussian noise with standard deviation 0.01. There is no difficulty fitting the decay parameters a, α and c for the faster-decaying scan using least-squares minimization.

The extent of the reliability of least-squares fitting for decay rates in the range $1 \times 10^{-5} \leq \alpha \leq 1 \times 10^{-3}$ can be established by plotting the fitted parameters as a function of the underlying parameters. Figure 2.11 shows the progression of the least-squares best fit values of a, α and c as a function of α, where all other conditions are held constant as in Figure 2.10 ($a = 0.5$, $c = 0.1$, Gaussian noise 0.01). Under those conditions, the correct decay parameters are reliably identified down to $\alpha \approx 5 \times 10^{-4}\mathrm{ps}^{-1}$, below which the slow decay is frequently mis-identified as a fast decay with a high static level.

Under the assumption of Gaussian uncertainties on individual polarization measurements, the relative probability that a parameter set $\{a, \alpha, c\}$ produces a polar-

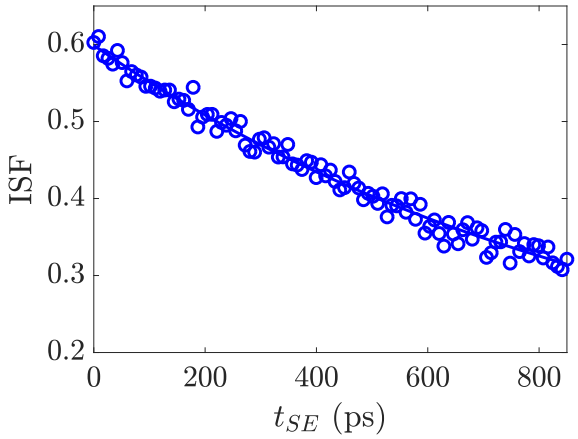

(a) A polarization scan with decay rate $\alpha = 1 \times 10^{-3}\,\mathrm{ps}^{-1}$.

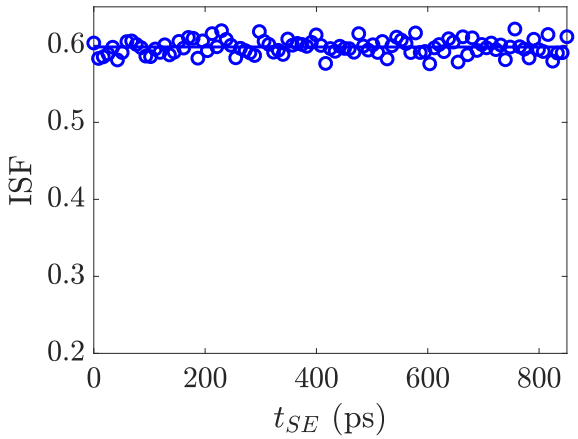

(b) A polarization scan with $\alpha = 1 \times 10^{-5}\,\mathrm{ps}^{-1}$.

Figure 2.10: Simulated polarization scans of the form $P(t_{SE}) = ae^{-\alpha t_{SE}} + c$, with $\alpha = 1 \times 10^{-3}\,\mathrm{ps}^{-1}$ (Figure 2.10a and $\alpha = 1 \times 10^{-5}\,\mathrm{ps}^{-1}$ (Figure 2.10b. An amplitude and static $a = 0.5$, $c = 0.1$ applies to both scans, and a Gaussian noise with standard deviation 0.01 is applied to each point. Best fits are overlaid as solid curves. The lineshape in Figure 2.10a has decayed by approximately one time constant, and extracting the correct values of a, c and α by standard least squares fitting presents no difficulty. The decay in Figure 2.10b is so slow that the lineshape appears linear over the t_{SE} window. The decay rate cannot be reliably determined by least squares fitting without strong constraints on a or c. Figure 2.10b bears a strong resemblance to experimental scans for D/Ru(0001) at low temperature (Figure 6.9).

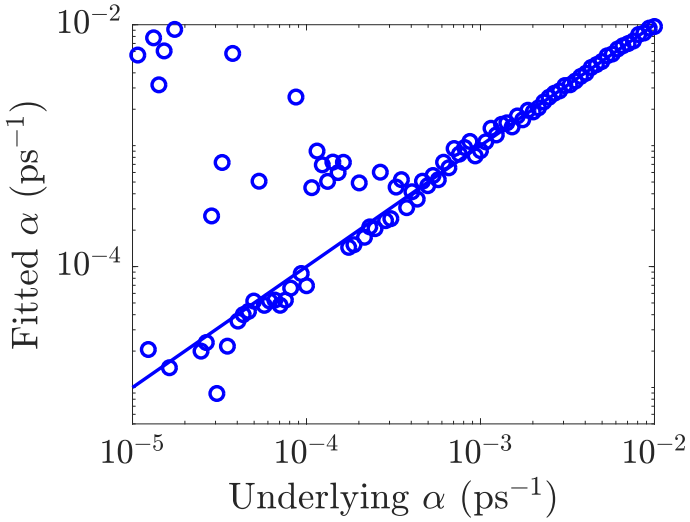

(a) Variation of the least-squares best fit value of α as the decay rate of the underlying polarization $p(t_{SE})$ is varied.

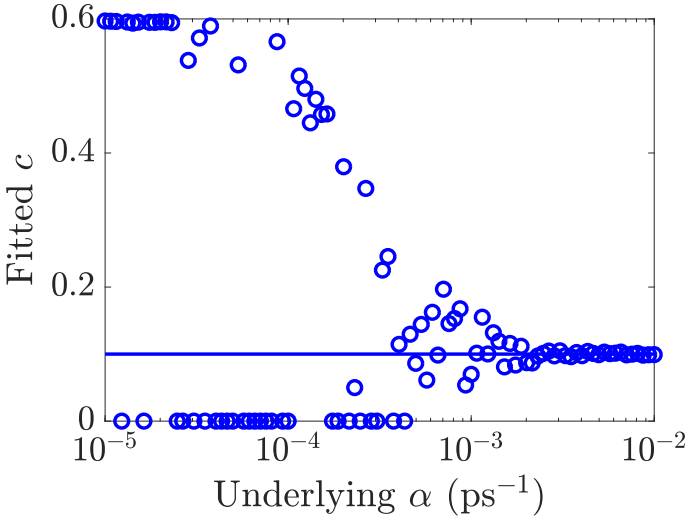

(b) Variation of fitted c with underlying α.

Figure 2.11: Variation of the fitted parameters α, a and c of an exponential decay, as a function of the underlying decay rate of the simulated lineshape $p(t_{SE}) = ae^{-\alpha t_{SE}} + c$, under the conditions described in Figure 2.10. Figure 2.11a shows the variation of fitted α with underlying α. To be more explicit: every point in Figure 2.11a is derived by performing a standard least-squares fit to an exponential lineshape with amplitude $a = 0.5$, static $c = 0.1$, Gaussian noise with $\sigma = 0.01$, and an decay rate given by the value indicated on the horizontal axis, referred to as the underlying α. The vertical axis shows the best-fit decay rate returned by the least-squares fitting routine, namely the MATLAB `fit` function with the adjustable options chosen to guard against systematic partial optimization or start-point dependent effects. Random start points, an unlimited number of allowed iterations, and a tolerance of 10^{-15} on the least-squares objective function were used. The fitted α correctly tracks the underlying α (i.e. lies on the solid "$y = x$" line shown) for underlying α greater than about $\alpha \approx 5 \times 10^{-4}\,\text{ps}^{-1}$. At slower underlying rates, the slow decay with large amplitude cannot be reliably distinguished from a fast decay with high static. The corresponding fitted values of the static, for the same simulated scans, are shown in Figure 2.11b where the solid line simply indicates the fixed underlying c. The value of α at which the fits become unreliable can be associated with the instrumental energy resolution for a known lineshape [61] quoted in the main text.

ization scan $p(t_{SE})$ is given by

$$\rho(a,\alpha,c) \propto \exp\Big(-\sum_i \frac{(y_i - f_i)^2}{2\sigma_i^2}\Big)\,, \tag{2.60}$$

where f_i are the values of the model function evaluated at the t_{SE} at which data y_i are available. In Section 2.2.2, the least squares method was justified by the fact that minimizing the exponent in Equation 2.60 maximizes the relative probability of a given parameter set. However, if we are interested in the most likely decay rate α, regardless of the values of a and c, then it is convenient to find the relative probability of α for any value of a and c. Assuming, in the absence of any data, equal *a priori* probabilities for all values of a, α and c within plausible ranges, then the relative probability density of α implied by a data set is given by the marginal distribution [87],

$$\rho(\alpha) = \int da \int dc\ \rho(a,\alpha,c)\,. \tag{2.61}$$

The argmax[1] of $\rho(\alpha)$ is then the most likely value of α. Analytical approximations that increase the speed of the marginalization operation have been described elsewhere [71] and have been implemented in the code used to analyse several scans simultaneously by the Bayesian approach as described in Section 2.2.6. The analytical approximations used there are appropriate for scans in which a and c can legitimately be integrated from $-\infty$ to ∞ due to $\rho(a,\alpha,c)$ being negligible for $a < 0$ and $c < 0$. However, a and c cannot be negative on physical grounds. Therefore in the present Section, and the applications in Sections 5.2.2.1 and 6.3.5 when attempts are made to fit very slowly decaying polarization scans, a and c have been integrated over positive values only. Performing the c integral in Equation 2.61 then gives [88]:

$$\rho(a,\alpha) \propto \exp\Big(-\textstyle\sum_i \frac{(y_i - a f_i)^2}{2\sigma_i^2}\Big) \int_0^\infty dc\, \exp\Big(-\tfrac{1}{2}Ac^2 + Bc\Big) \tag{2.62}$$

$$= \sqrt{\tfrac{\pi}{2A}}\exp\Big(\tfrac{B^2}{2A}\Big)\Big[1 + \mathrm{erf}\Big(\tfrac{B}{\sqrt{2A}}\Big)\Big]\,, \tag{2.63}$$

where

$$A = \sum_i \frac{1}{\sigma_i^2}\,; B = \sum_i \frac{y_i - a f_i}{\sigma_i^2}\,, \tag{2.64}$$

and f_i are the values of the normalized model function $\exp(-\alpha t_i)$ for spin echo times t_i. The integral over the amplitude a is then performed numerically, using 1000 points in the present work. The semi-analytical integration over $c > 0$, $a > 0$ is not limited to the exponential function but can be performed the same way for any other normalized model function.

Figure 2.12 shows $\rho(\alpha)$ derived from simulated polarization scans with $a = 0.5$,

[1] The value of the function input that maximizes the output.

$c = 0.1$ and three different underlying values of the exponential decay rate, namely $\alpha = 1 \times 10^{-3}\,\mathrm{ps}^{-1}$, $1 \times 10^{-4}\,\mathrm{ps}^{-1}$ and $\alpha = 1 \times 10^{-5}\,\mathrm{ps}^{-1}$. In the first case, the decay rate is straightforwardly resolved by standard least squares fitting, without bias, and $\rho(\alpha)$ has a clear maximum. In the second case where the underlying decay rate is $1 \times 10^{-4}\,\mathrm{ps}^{-1}$, $\rho(\alpha)$ has a clear and repeatable maximum at the correct value of α, albeit with a long tail at larger α. When $\alpha = 1 \times 10^{-5}\,\mathrm{ps}^{-1}$, the maximum in $\rho(\alpha)$ is generally a reasonable guide to the true decay rate but has a large spread.

To assess if the maximum of the distribution $\rho(\alpha)$ provides a reliable estimate of the true decay rate, the distribution of the argument maximum $\bar{\alpha}$ can be constructed from a large number of repeat simulations. Figure 2.13 shows histograms of $\bar{\alpha}$ derived from 1000 independent sample polarization scans of the type described in Figure 2.11a, for three different values of the underlying decay rate. The results suggest that $\rho(\alpha)$ is a sensible estimate of the true decay rate even when the rate is as slow as 1×10^{-5}, and in that case the estimate is only weakly biased if at all. On the other hand, the probability of the decay rate being inferred as precisely zero is not negligible, and for any given scan $\rho(\alpha)$ has a very long tail. The relatively high apparent resolution of the marginalized $\rho(\alpha)$ from the histograms in Figure 2.13 is therefore a consequence of simulating scans with a large underlying a and low c.

2.2.6 Bayesian analysis of multiple scans

A common situation arising in the analysis of HeSE data, and which is particularly relevant to diffusion of hydrogen on fcc(111) and hcp(0001) surfaces, is as follows:

- data are available at many $\Delta\mathbf{K}$;
- a highly plausible underlying model of the jump dynamics is known in advance (e.g. based on prior knowledge of the adsorption sites), and has a manageable number of parameters such as 2 or 3;
- the plausible underlying model contains multiple exponential decays at certain $\Delta\mathbf{K}$, possibly all $\Delta\mathbf{K}$;
- separate exponential decays not easily resolvable, within individual polarization scans;
- each polarization scan has a fit start time (Section 2.2.3), static offset C, and model amplitude A which are unknown *a priori*.

In order to make progress with datasets of the type detailed above, it is fruitful to explicitly maximize the probability of data given model, which by Bayes' theorem is

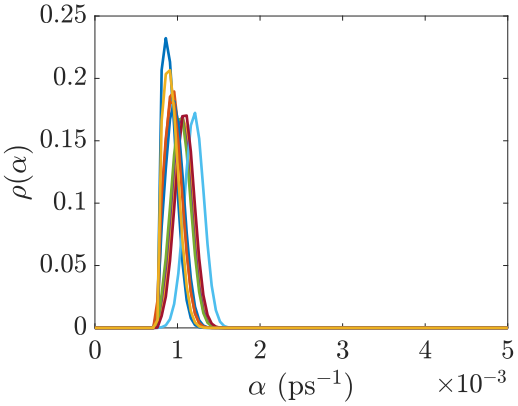

(a) The distribution $\rho(\alpha)$ derived from ten independent simulated exponential polarization scans with $\alpha = 1 \times 10^{-3}$.

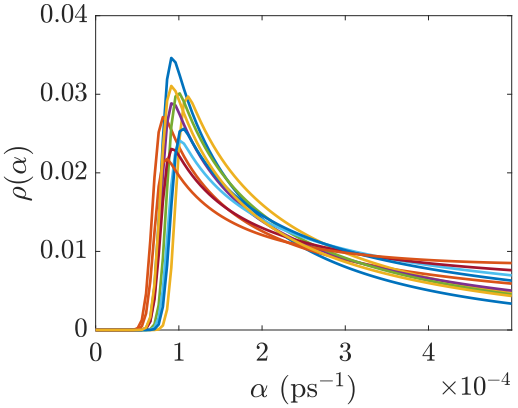

(b) As in 2.12a but for $\alpha = 1 \times 10^{-4}$.

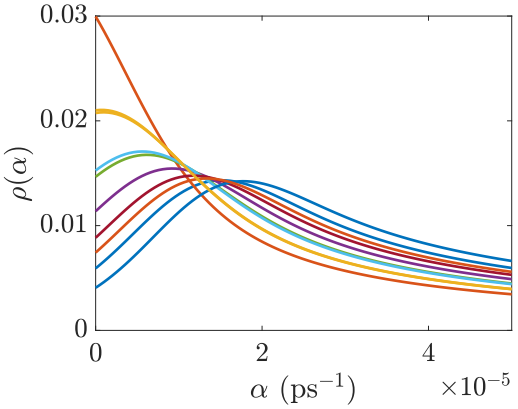

(c) As in 2.12a but for $\alpha = 1 \times 10^{-5}$.

Figure 2.12: Inferred distribution $\rho(\alpha)$ derived from exponential simulated lineshapes under the conditions given in Figure 2.11, where t_{SE} is sampled uniformly from 0 to 850 ps in 101 points. For each value of the underlying decay rate, ten scans are simulated and $\rho(\alpha)$ is constructed independently from each one. The distribution is calculated using the semi-analytical method described by Equation 2.62. In Figure 2.12a, the decay is relatively fast and can be fitted reliably using standard least squares minimization, in which the set $\{a, \alpha, c\}$ is found that maximizes $\rho(a, \alpha, c)$. The marginalized distribution $\rho(\alpha)$ is sharply defined around the correct value of α. When the true decay rate is 1×10^{-4} as in Figure 2.12b, the lineshape cannot be fitted reliably by unconstrained standard least squares as demonstrated in Figure 2.11a. The marginalized distribution $\rho(\alpha)$ has a clear and repeatable maximum at the correct value of α, albeit with a long tail. Finally, when $\alpha = 1 \times 10^{-5}$ the maximum of $\rho(\alpha)$ normally provides a reasonable estimate of the decay rate, but with a large spread.

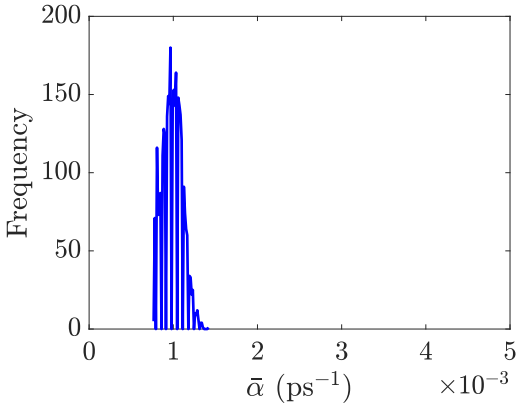

(a) The distribution of the values of α that maximizes $\rho(\alpha)$ when the underlying decay rate is $1 \times 10^{-3}\,\mathrm{ps}^{-1}$.

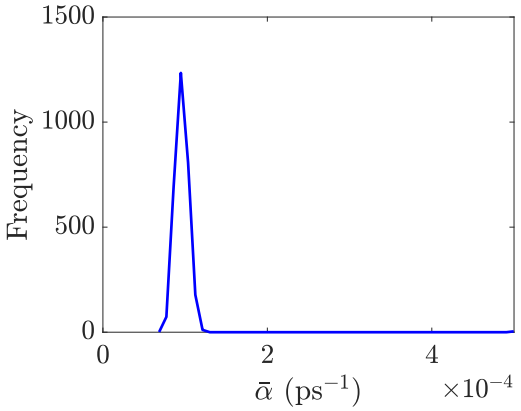

(b) As for Figure 2.13a but with an underlying decay rate of $1 \times 10^{-4}\,\mathrm{ps}^{-1}$.

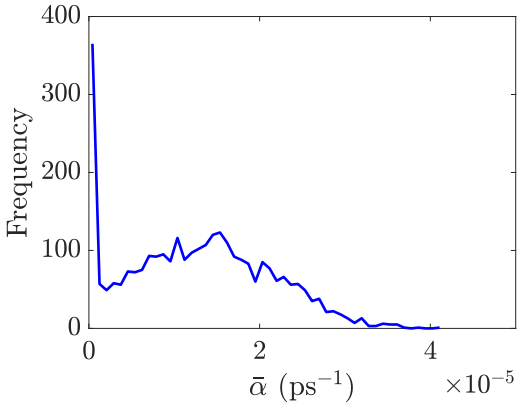

(c) As for Figure 2.13a but with an underlying decay rate of $1 \times 10^{-5}\,\mathrm{ps}^{-1}$.

Figure 2.13: Histograms showing the distribution of $\bar{\alpha}$, the value of α that maximizes the marginalized distribution $\rho(\alpha)$ (Figure 2.12). The decay parameters a and c are marginalized over a 100×100 grid using $0 \leq a \leq 0.7$ and $0 \leq c \leq 0.7$. The true underlying amplitude and static level are $a = 0.5$ and $c = 0.1$. Three different underlying decay rates are investigated. The histograms show that $\bar{\alpha}$ provides a good estimate of the true decay rate in all cases, with only a weak bias in the slowest decaying case.

proportional to the probability of the model given the data. Suppose the underlying model is described by a parameter set τ. In order to combine different scans and obtain a global probability of a model given an entire dataset, the probability is obtained for the k^{th} dataset individually using the same Gaussian expression as in Section 2.2.2,

$$p_k(\{y_i\}|\{f_i(\tau,a,c)\}) \propto \exp\Big(-\sum_i \frac{(y_i - f_i(\tau,a,c))^2}{2\sigma_i^2}\Big), \tag{2.65}$$

and integrating (marginalizing) over the unknown a and c as in Section 2.2.5 to obtain a function describing the probability of the k^{th} dataset, $p_k(\tau)$. The global probability $p(\tau)$ is the product of all the p_k.

The implementation can be separated into the construction of the p(data|model) function, and the maximization method. For all analyses in Chapters 5 and 6, the implementation of p(data|model) was largely carried over from previous studies using the Bayesian technique[1] (such as [89]). The only material modification is the use of the triple jumps model (Section 2.2.1) rather than a single jumps model. When a single jumps model is used, with two parameters such as τ and λ, a grid search to locate the maximum probability is efficient enough, and can be conveniently used to represent uncertainties on the fitted parameters via a plot of the probability distribution $p(\tau,\lambda)$ [35, 89]. The extra parameter in the triple jumps model makes a grid search unwieldy, and so the p(data|model) function was passed to the MATLAB routine `fminsearch` which is generally far more efficient at locating the maximum probability.

Unlike in single scan fitting, the absolute uncertainties on each individual polarization scan are important in the Bayesian procedure. For polarization scans recorded over multiple loops, the standard deviation between loops was used as the uncertainty. For polarization scans without multiple loops, the uncertainty was taken as a fixed value for each scan, given by the mean square residual of a free biexponential fit. As seen in Chapter 2, for a fixed mean signal the uncertainty on the polarization is generally only a weak function of the polarization itself. Therefore, using a single uncertainty across a scan is a very reasonable assumption. The output uncertainties on the fitted parameters have been quantified by evaluating the model functions from the best fit, adding Gaussian noise of the experimentally determined magnitude, and re-fitting the noisy simulated dataset from scratch with the Bayesian method. The standard deviation of the result after repeatedly fitting independent noisy simulated datasets has been used as the uncertainty in all cases.

For Bayesian analysis it is convenient to algorithmically select the minimum t_{SE}

[1] Function originally written by Dr John Ellis.

for each dataset on a scan-by-scan basis. One method for doing so is to optimize a goodness-of-fit parameter (GOF). Given data y_i $(i = 1, 2, \cdots, n)$ with mean $\bar{y}$ and corresponding values of the fit f_i, the adjusted R^2 is defined as:

$$R^2 = 1 - \frac{(n-1)\sum_{i=1}^{n}(y_i - f_i)^2}{(n-m)\sum_{i=1}^{n}(y_i - \bar{y})^2}\,, \tag{2.66}$$

where m is the number of fitting parameters. In applying the Bayesian method to experimental data, the minimum t_{SE} for each scan has been chosen to optimize the adjusted R^2 for a free biexponential fit. For scans where the sampling interval in t_{SE} is a few picoseconds, optimizing the minimum t_{SE} using R^2 is almost always equivalent in practice to using all points except $t_{SE} = 0$.

The adjusted-R^2 statistic has been used in the present work because it has previously been shown to produce physically sensible results when analysing multi-component HeSE lineshapes [28]. The statistic is not used here to distinguish between different models for the lineshape (e.g. to indicate whether a bi-exponential fit is to be preferred over a mono-exponential), nor to rigorously assess the absolute suitability of the fitting model. Nevertheless, replacing an appropriate fitting function with an inappropriate one will typically reduce the adjusted R^2 either by increasing the typical model-data deviation or by requiring a larger number of free parameters to achieve the same quality of fit. The motivation for maximizing R^2 with respect to the amount of data included at the start of a scan can be seen more easily if we note that in our case m in Equation 2.66 is fixed and satisfies $m << n$. E.g. for a bi-exponential fit $ae^{-\alpha_1 t} + be^{-\alpha_2 t} + c$ using the last 95 points of a polarization scan with 101 points, $m = 5$ (5 free parameters) and $n = 95$ (number of data included in fit). When the minimum t_{SE} included in the fit is varied, n varies at fixed m but the case $n \approx m$ never arises, as that would imply we are only using the last five or so data in the scan, which will never optimize R^2 under any reasonable conditions. Therefore, the fraction in Equation 2.66 is approximately

$$\frac{\sum_{i=1}^{n}(y_i - f_i)^2}{\sum_{i=1}^{n}(y_i - \bar{y})^2}\,, \tag{2.67}$$

which is the mean square residual of the best fit, divided by the mean square residual that would have arisen if we had used a flat fitting function $f(x) = \mathbf{const}$. By optimising R^2 we are trying to make the fraction 2.67 as close to zero as possible. In general the best fit to any data set using the correct model function will give the mean square residual on the scale of the experimental uncertainty, say σ^2, assuming roughly uniform uncertainties σ. However, increasing the range of included data at the short-time end of the scan will increase the total systematic variation in the data which will increase the denominator of the fraction we would like to minimise. As

long as the extra data included is still well described by the model function, R^2 will then increase. However, if we include a point that is not sufficiently well described by the model function, it will tend to increase the mean square residual and reduce R^2. The absolute value of the optimum R^2 for any given polarization scan is sensitive to the relative scale of the uncertainties and the end-to-end polarization decay captured in the available t_{SE} window. Most scans analysed in the Bayesian routine had an optimal R^2 of 0.95 or greater. For example, for the C/Ru(0001) scans illustrated in Figures 2.7 and 2.8, the optimized values of the adjusted R^2 are 0.98 and 0.97 respectively. According to the arguments given in the present paragraph, a low R^2 is generally associated with a slow decay or small amplitude of the model function in the complete lineshape, and/or a low signal-to-noise ratio.

I emphasise that the overall purpose of a GOF statistic here was not to select a preferred functional form of the fit, although a GOF statistic has previously been used for that purpose in essentially the present context [90]. Instead, the choice of the fitting function is motivated by a combination of physical grounds and the inability of simpler models to adequately represent the data, while the GOF is used to decide which data (below a certain cutoff spin echo time) are not encompassed by the model. A deeper statistical investigation of the best choice of the cutoff time would be valuable further work and could proceed by considering the variation with cutoff time of the fitting probability, integrated over all parameters, by analogy with an approach that has been described for distinguishing single and multiple Lorentzian fits [87].

2.3 Performance of the ionizing detector

A high sensitivity helium atom detector is a crucial part of HAS experiments. The detector in the HeSE experiment requires a high ionization efficiency, a large dynamic range and a low mass-selected background count rate at the mass-to-charge ratio $m/z = 3$. The requirements in terms of time response are rather relaxed compared to those in time-of-flight experiments [91], since the standard dwell time at each point during a four-point measurement (Section 2.1.4.3) is 500 ms. The initial measurements with a ^{3}He beam as proof of the helium spin echo principle [92] used a commercial mass spectrometer as the helium detector, but surface science experiments using the technique have been performed with in-house detectors from the beginning [93].

The first surface science measurements on the Cambridge HeSE instrument were published in 2004 [94]. The efficiency of the detector at that time [70] was deter-

mined as 2×10^{-5}, with a background count rate of 750 Hz. The integrated helium flux at the sample surface was $1.5 \times 10^{14}\,\mathrm{s}^{-1}$. Since then, the helium beam source has been upgraded to roughly double that intensity [95]. An improved detector was installed in 2011 and has been operating continuously ever since. The improved detector is the product of an extensive development programme involving experimental characterization, simulation and prototyping [96, 97, 98, 99]. Improvements in detector signal-to-noise ratio (SNR) allow improved spin echo experiments along various directions including:

- distinguishing between subtly different models of the surface dynamics, which is particularly relevant to models with multiple decays in the lineshape (Chapter 6 especially);
- measuring small changes in polarization, which is relevant to lineshapes with very small or slow decays;
- reducing the scan acquisition time, eliminating contamination effects, which is relevant in hydrogen-isotope experiments where contamination by H needs to be avoided when measuring D (Section 6.3).

Additional motivation for helium detector development comes from the detector requirements of helium atom microscopy [100, 101], for which improved signal-to-noise on $m/z = 4$ can greatly reduce image acquisition times. However, the present Section focuses solely on the performance of the spin echo detector. The results quantify the limiting factors in different signal regimes, and contribute to the understanding of where to focus future development efforts.

2.3.1 Helium detector: implementation

The helium detector can be considered as three subsystems: the solenoidal ionizer, ion optics including mass selection, and ion collection / current measurement. The layout of the ionizer is shown in Figure 2.14, reproduced from [99] where the design, operation and selection of parameters are discussed in great detail. The system is radially symmetric, and the beam enters from the left. Electrons are emitted from the cathode **B** and injected into the ionization region **E** with the help of the electron repeller **A**. The electrons are trapped radially by the magnetic field generated by the solenoid **F**, and longitudinally by the electrostatic potential. End effect coils **G** increase the efficiency of ion extraction. The tilting coils **H** are normally unused. The ion barrier ring **C** repels ions to ensure they exit at the correct end of the ionizer. Ions are extracted by the extraction tube **D**. External water cooling is provided via pipes **J**, while a water jacket **I** keeps the vacuum chamber walls cool.

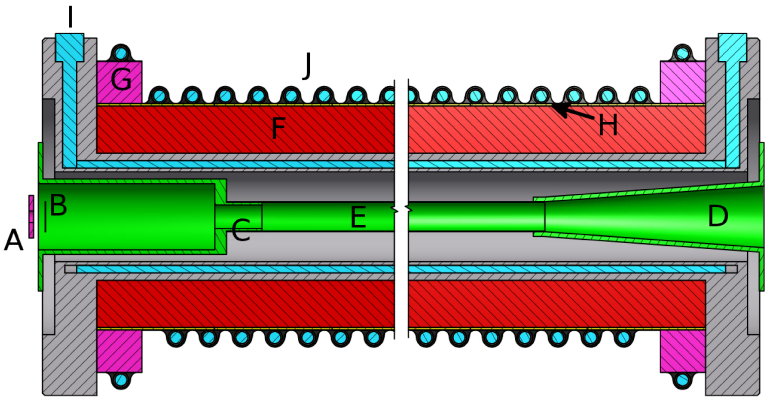

Figure 2.14: From [99]: diagram of the ionizer on the spin echo spectrometer. The solenoid (**H**) is 800 mm in length. The operation is described briefly in the main text, and extensively in [99]. The labelled components are: **A** electron repeller, **B** cathode, **C** ion barrier ring, **D** ion extraction tube, **E** ionization region **F** solenoid, **G** end effect coils, **H** tilting coils, **I,J** water cooling.

The outgoing ion beam passes through a set of ion optics including a mass-selecting d.c. electromagnet. A novel feature of the ion optics after the mass selection stage is the off-axis positioning of the multiplier assembly, as illustrated in Figure 2.15. The off-axis geometry has been found empirically to reduce the background count rate at $m/z = 3$ by eliminating high-energy neutral atoms created in the mass selector [99]. Ions are directed towards the dynode by electrostatic pusher plates, while neutral atoms do not reach the dynode as there is no line of sight from the mass selector.

After mass selection the ion current can either be received directly by the Faraday cup (Figure 2.15), or amplified by an electron multiplier (Channeltron), and the current is finally read by a picoammeter. To protect the Channeltron from sputtering and so greatly extend its lifetime, the Channeltron is preceded by a conversion dynode. The dynode/multiplier assembly is shown in Figure 2.16. The gain of the Channeltron is controlled by the potential difference between its front and back. The back potential V_{CB} is always set to 300 V in normal operation. The front potential V_{CF} then controls the gain. The potential V_D of the dynode can, in principle, be varied independently of V_{CF}. However, it has been shown empirically [99] that the gain of the entire assembly is maximised when $V_D = V_{CF}$, so in normal operation the two potentials are shorted together. Future planned improvements to the design include placing a grid in front of the Channeltron to improve the trajectories of electrons released in the first impact with the Channeltron. Empirically, installing a grid has improved the conversion efficiency on a sister detector being developed

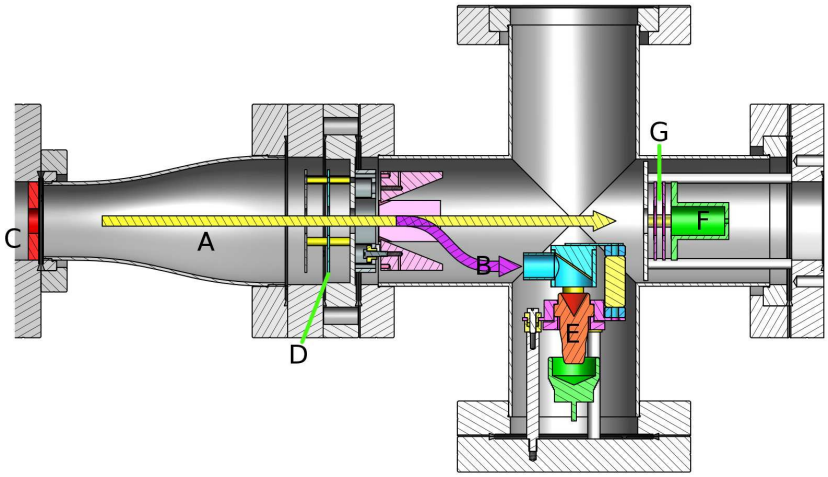

Figure 2.15: From [99]: the ion optics after the mass selection stage. The novel feature of the design, which greatly reduces the background count rate on mass 3, is the off-axis positioning of the multiplier assembly. The ion beam can be directed along trajectory **A** to the Faraday cup **F**, or be pushed onto trajectory **B** electrostatically so that it reaches the dynode and releases electrons to the front of the Channeltron **E**. The aperture **C** prevents line-of-sight between the mass selector and the off-axis ion collecting assembly.

as part of the helium microscopy project [102]. The optimal configuration is then expected to have $V_{CF} \neq V_D$, but for now the two potentials are always pinned together. A selection of standard detector settings is shown in Table 2.6.

The amplification stage introduces additional complexity into the analysis of signal and noise. For one thing, the ion-electron conversion efficiency of a gold surface could be dependent on the incident ion, even at constant m/z. In other words, a high-mass, high charge species such as C^{4+} might well release a different number of electrons on average, than a low-mass, low-charge species such as $^3He^+$. Also, in principle dark counts (spontaneous emission and amplification of electrons) could be a factor in the background signal, although they are insignificant compared to electrical interference under normal operating conditions [99]. The SNR is also affected by the statistics of one-to-many electron conversion in the Channeltron. At low signal, the output of the Channeltron consists of well-separated current pulses, each originating from one incident electron. However, the pulse size is not a single number but follows a distribution of finite width. As a corollary, the SNR on the final output at low signal levels is worse than the shot noise limit, by a factor related to the pulse height distribution [99]. The SNR on low-signal measurements shown in Section 2.3.2.2 cannot be rationalized quantitatively without the numerical factor originating in the pulse height distribution.

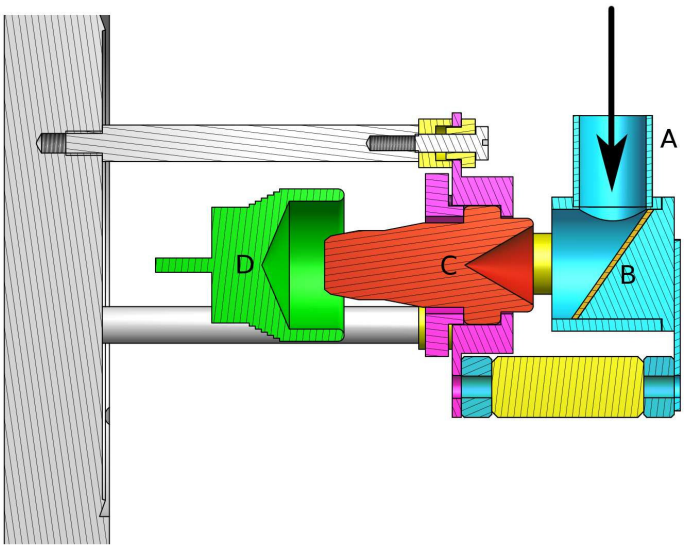

Figure 2.16: From [99]: diagram of the dynode/multiplier assembly. Incident ions strike the gold surface **B** of the dynode which releases $\mathcal{O}(1)$ electrons in response. The electron signal is multiplied by the Channeltron electron multiplier **C** and received by the Faraday cup **D**.

Table 2.6: Parameters and standard settings on the detector.

Parameter	**Value**
Solenoid length	800 mm
Cathode current	2 A
Emission current	1 mA
Cathode, liner, repeller potential	688 V, 980 V, 600 V
Chan B potential	300 V
Chan F potential	$1.6 \leq V_{CF} \leq 2.5$ kV
Dynode potential	$= V_{CF}$

Table 2.7: Values of the Chan F potential V_{CF} used for extensive measurement series in the present Section, and the associated gain for $^3He^+$ ions taken from the blue curve of Figure 2.18.

$\mathbf{V_{CF}}$ **(kV)**	**Gain**
1.6	113
2.0	2150
2.05	2870
2.25	8800
2.5	29380

2.3.2 Detector characteristics: measurement and analysis

2.3.2.1 Gain, efficiency, background

The *de facto* default setting of the Channeltron front potential is $V_{CF} = 1.6\,\mathrm{kV}$. In that condition, the gain of the dynode-multiplier assembly at the time of measurement to be determined directly by scanning the $m/z = 3$ peak in electron current, then immediately running down the multiplier and repeating the scan by measuring the ion current in Faraday cup mode. The mass scans are shown in Figure 2.17. The gain G of the multiplier assembly is simply the ratio of the peak heights, which was determined as:

$$G = 113 \ (V_{CF} = 1.6\,\mathrm{kV}) \tag{2.68}$$

The gain at a single V_{CF} is a calibration point that allows the gain to be found at all values of V_{CF}, by adjusting V_{CF} with a constant ion current. The results are shown as blue points on Figure 2.18, with a blue curve as a guide to the eye. The curve shows that an additional factor of 260× gain is available beyond the default value, with the current hardware. Since the gain is still increasing rapidly with signal at $V_{CF} = 2.5\,\mathrm{kV}$, additional gain could be accessed at even higher V_{CF}, which is limited by the power supply rather than any fundamental limit. Shown in red on the same plot is a series of gain measurements recorded at the time of the detector installation, approximately five years earlier. The absolute value of the red data was calibrated using pulse-counting measurements, using background gas with no helium beam. Assuming the relative conversion efficiency of He^{3+} and other ions is not too extreme, it is apparent that a significant bedding-in of the multiplying assembly has taken place: a much higher V_{CF} is required to achieve the same gain. A list of the values of V_{CF} used for extensive constant-gain measurements in the present Section, and the associated gains, is given in Table 2.7.

Once the gain is known, we can estimate the efficiency η of the ionizer, and compare it to the η estimate performed at the time of commission. η is defined as the number of ions produced per incident atom in the beam. The intensity of

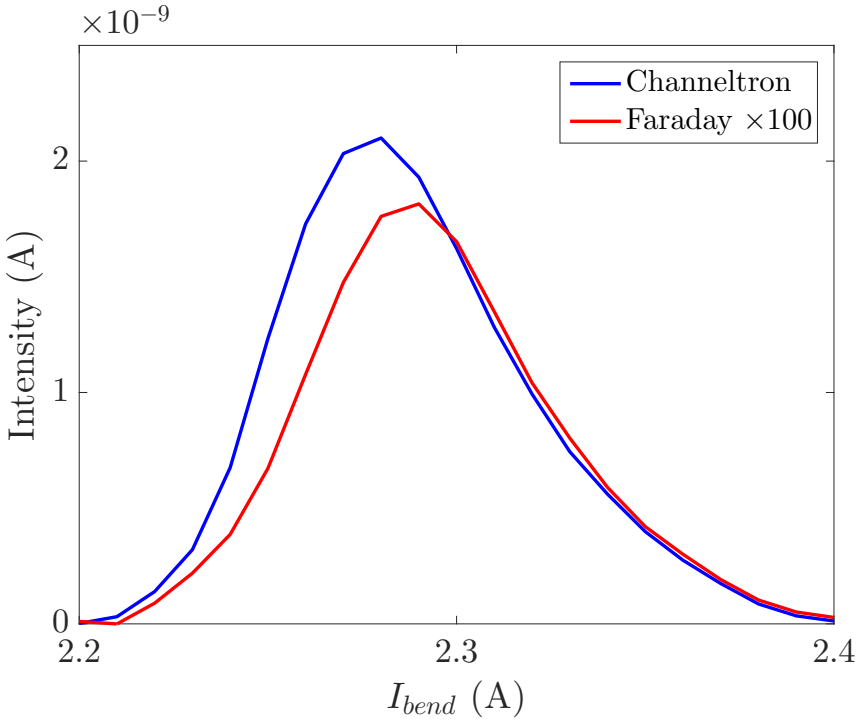

Figure 2.17: Measurements of detector output current in Channeltron mode (blue, electron current) and Faraday cup mode (red, ion current). The mass selecting magnet current I_{bend} is scanned over the mass-3 helium peak. The helium-3 is specularly reflected from a Ru(0001) crystal in the scattering chamber.

the incoming beam can be estimated using reflectivity measurements and a known pumping speed of the scattering chamber. The reflectivity was defined in Section 2.1.3. A simple estimate of the efficiency was derived [99] in terms of the extractor gauge pressure rise ΔP(mbar) in the scattering chamber due to the beam, gauge factor α, pumping speed S (mbar·l/s), specular reflectivity R, detector output ion current ΔI, electron charge e and the number of atoms Γ in 1 mbar·l of gas at room temperature:

$$\eta = \frac{\alpha \Delta I}{e \Gamma \Delta P S} \times \frac{1-R}{R} \,. \tag{2.69}$$

Soon after installation, the efficiency of the new detector to a helium-3 beam was estimated as 1.3×10^{-3}. During the experiments on Ru(0001) reported in Chapters 5 and 6, a typical concurrent set of values was $\{\Delta P = 5 \times 10^{-10}\,\text{mbar}, \Delta I = 5 \times 10^{-9} A, R = 35\%\}$. Applying Equation 2.69 gives

$$\eta = 2 \times 10^{-3} \,, \tag{2.70}$$

where the same estimate of the pumping speed $S = 400\,\text{l/s}$ has been applied as in the original calculation. The efficiency is in reasonable agreement with the estimate performed years earlier.

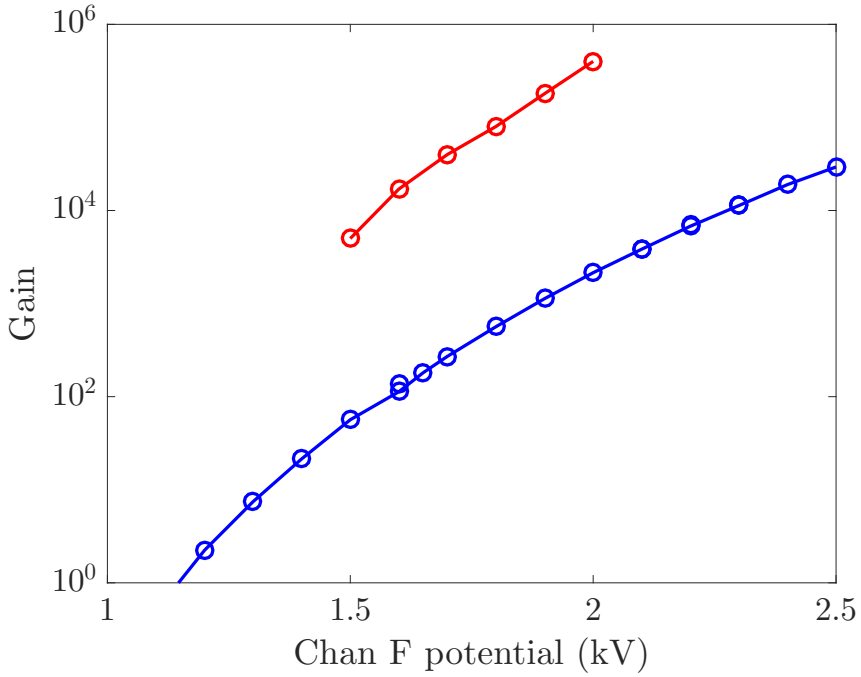

Figure 2.18: Variation of the gain of the dynode-multiplier assembly with the potential V_{CF} of the front of the multiplier. Red: measurements performed at the time of installation, calibrated using pulse counting techniques [99]. The red data were acquired without a beam, and therefore refer to the gain associated with a component of the background gas. Blue: measurements performed several years later, calibrated directly using a moderately intense helium beam. The blue data therefore refer to the gain associated with $^3He^+$ ions.

Three major measures have been taken to minimise the $m/z = 3$ background count rate with respect to the beam count rate. Firstly, the liner potential with respect to the cathode is held at 292 V, which is the best compromise in terms of reducing the background from multiply charged ions (e.g. C^{4+}), and maintaining sensitivity to ^{3}He. The potential of the liner with respect to the cathode affects the electron energy distribution. By not allowing too many high energy electrons to remain in the solenoidal trap, the amount of multiple ionization can be reduced. The second major anti-background measure is the off-axis post-mass selection geometry of the multiplier assembly, which reduces the contribution from high-energy neutral atoms which can release electrons from the dynode. Thirdly, great care was taken to reduce the $m/z = 3$ contribution from hydrogen deuteride (HD). After baking the detector, the $m/z = 3$ background current was reduced by a factor of 3 by an activation cycle of two commercial non-evaporative getter pumps, and a further factor of 6 by flashing (heat cycling) the detector liner which has been sputter-coated with Ti, Va and Zr. The detector is pumped by turbomolecular pumps in series, to avoid a compression-limited regime, and backed by a dry pump. After flashing the liner, the detector was operated under continuous turbomolecular pumping for about five years before the measurements reported here. During dynamics measurements of the Ru(0001) surface, the typical multiplied background count rate at $V_{CF} = 2.25\,\mathrm{kV}$ was 75 MHz. Figure 2.18 indicates a gain of 9×10^3. The associated background ion count rate is therefore:

$$(m/z = 3)\text{bkg ion counts} \approx 8500\,\mathrm{Hz}\,. \tag{2.71}$$

The same conclusion results at other values of the gain. Comparing to the figures for the previous detector [70], the background ion count rate has increased by a factor of 10 but the mass-selected efficiency has increased by a factor of 100, so effectively the background has been improved by a factor of 10.

2.3.2.2 SNR measurements via intensity time series

For spin echo measurements we are mostly interested in the noise characteristics at $\mathcal{O}(1)$ Hz, the dwell time of intensity measurements during a typical four-point measurement of polarization (2.1.4.3). The SNR under various conditions can be determined by measuring the output signal over the course of minutes, with an integration period of O(1) s. To be more specific, all measurements were conducted with an integration time of either 500 ms or 1000 ms. The results under a 500 ms count time are adjusted by a factor of $\sqrt{2}$. Assuming the noise is effectively white, we are then comparing like with like even though two different integration times were

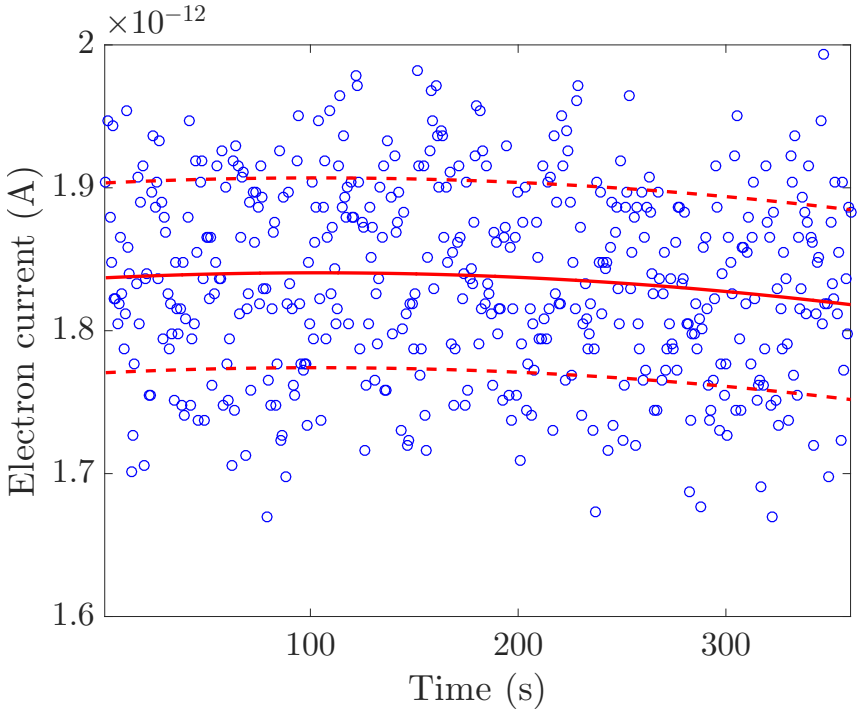

Figure 2.19: A typical intensity time series with the helium beam off. Each blue point is a reading of the electron current with a 500 ms integration time. The smooth polynomial fit, which here is essentially flat, is shown as a solid red curve. The dashed red curves indicate ± one standard deviation.

used. A typical intensity time series without the beam present, the slow polynomial fit, and the standard deviation of the data with respect to the fit, is shown in Figure 2.19. The time series is fitted to a fourth-order polynomial and the noise is defined as the standard deviation of the residuals. The SNR is then simply the mean signal divided by the noise. In all cases the variations in signal associated with the non-constant terms in the polynomial fit are negligible compared to the constant term, although not negligible compared to the noise which is why they must be fitted and subtracted. The slow polynomial fit can account for slow fluctuations in the instrument caused by slow feedback loops, e.g. in the lab temperature and beam nozzle temperature. The polynomial fit allows the effect of very slow components to be eliminated without measuring for long enough to rigorously eliminate them in the Fourier domain.

The present Chapter refers to measurements recorded with and without a helium beam. Measurements with the beam were taken from uptake curves and polarization scans recorded during HeSE investigations[1] whose main purpose was to study a particular surface system rather than characterize the detector. Measurements without the beam were recorded specifically for the investigation of detector noise.

[1] Almost all of which are reported in Chapters 5 and 6.

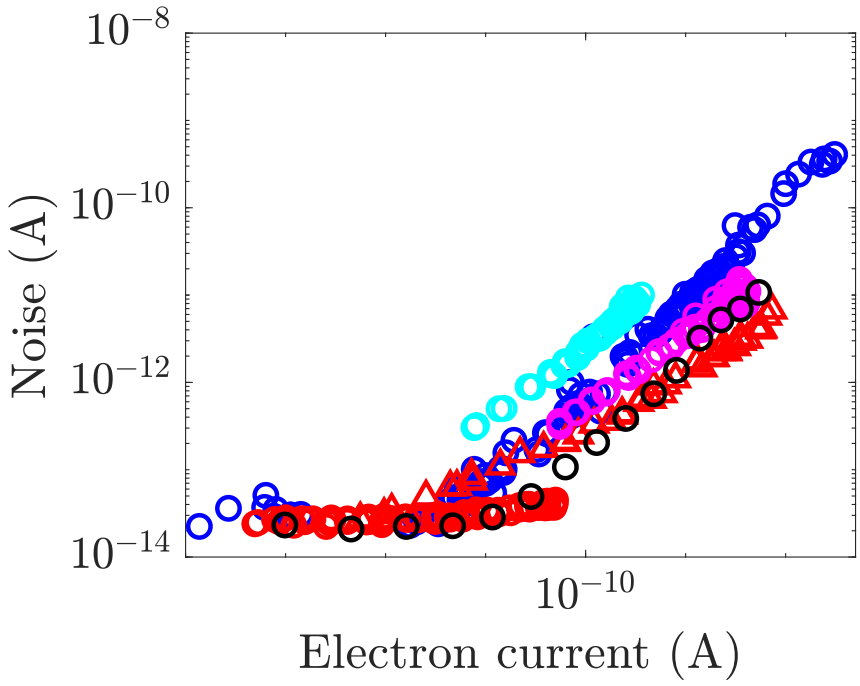

Figure 2.20: Noise as a function of electron current, under a range of conditions. The noise is defined as the standard deviation of intensity time series after subtracting a smooth polynomial background as illustrated in Figure 2.19. A key feature of the plot is that for low output currents, a baseline noise of 3×10^{-14}A applies universally. The baseline noise applies to the electron current, and is independent of the gain. I refer to the constant contribution to the noise as electrical noise due to its origin [99] as discussed in the main text.

There is a wide range of conditions and parameters that can be tuned and influence the signal and/or noise. Here I focus on the selected m/z, the intensity of the helium beam, and the gain of the dynode-multiplier assembly. In Figure 2.20 shows noise as a function of electron current, where the noise is defined as the standard deviation extracted from time series like the one shown in Figure 2.19. It is clear that there is a universal baseline noise on the output current, which holds under a range of circumstances. I will refer to the baseline noise as "electrical noise" E, with

$$E = 2.5 \times 10^{-14}\,\mathrm{A}. \tag{2.72}$$

It has been found empirically that most of the electrical noise remains even when the multiplier is turned off and there is no input ion current [99]. The noise mostly vanishes when the picoammeter output is recorded but the picoammeter is disconnected from the detector. Therefore we can conclude that the electrical noise is mostly made up of pickup associated with the detector/picoammeter connections.

There is a striking difference between the data for residual gas in the detector, and the data for the helium beam. Results expressed as signal-to-noise ratio (SNR) are shown in Figure 2.21. The gain is the same for both datasets. The data re-

ferring to the beam were taken during the course of surface science experiments, and so the variation in the atom intensity incident on the detector originates in the scattering chamber via crystal rotations and uptake of adsorbates. The background measurements were taken by varying m/z in the vicinity of $m/z = 2$, so the dominant contribution is H_2^+. The notable feature of Figure 2.21 is that the maximum observed SNR for background gas is approximately 1 in 1000, whereas the best achievable SNR when measuring the beam intensity saturates at a far lower value. Qualitatively the results are entirely consistent with observations made at install time [99]. I will refer to the saturation SNR in the presence of the beam as beam noise. It was previously found [99] that when the integration time is significantly less than 1000 ms the beam noise is substantially reduced by turning off the source cryocooler, which maintains the required low temperature of the nozzle in the helium-3 source [103] but as a side effect generates vibrations at a base frequency of 2 Hz. When measuring with an integration time of 500 ms or 1000 ms the effect of turning off the cryocooler might be statistically significant, but is not qualitatively visible in the same way as the improvement seen at smaller integration times. For the data shown in Figure 2.21 the beam noise factor f_b is

$$f_b \approx 1\% \,, \tag{2.73}$$

but it is possible that the beam noise could vary with the condition of the source, the scattering conditions (specular/off specular) or even the state of the detector, depending on the root cause which is still unknown.

The best observed SNR for measurements of the $m/z = 2$ background is an improvement on the value of 1/480 determined at install time. Defining the noise with respect to a 1000 ms integration time rather than 500 ms will be responsible for part of the difference. Under some circumstances, the cap on SNR in the absence of a beam is dominated by fluctuations of the emission current, caused by PID regulation of the cathode current. I will refer to the linearly scaling noise in the absence of a beam as emission stability noise. Figure 2.21 gives an upper bound on the emission stability factor f_e on $m/z = 2$ in the absence of the beam:

$$f_e \lesssim 0.07\% \,. \tag{2.74}$$

It is not too surprising that a slightly different figure for f_e is found when repeating the measurement after some years, as the pressure in the detector is significantly lower the second time around, and so the response of the detector to fluctuations in the cathode current is expected to be slightly different.

There is strong evidence for another factor that can limit the SNR of measure-

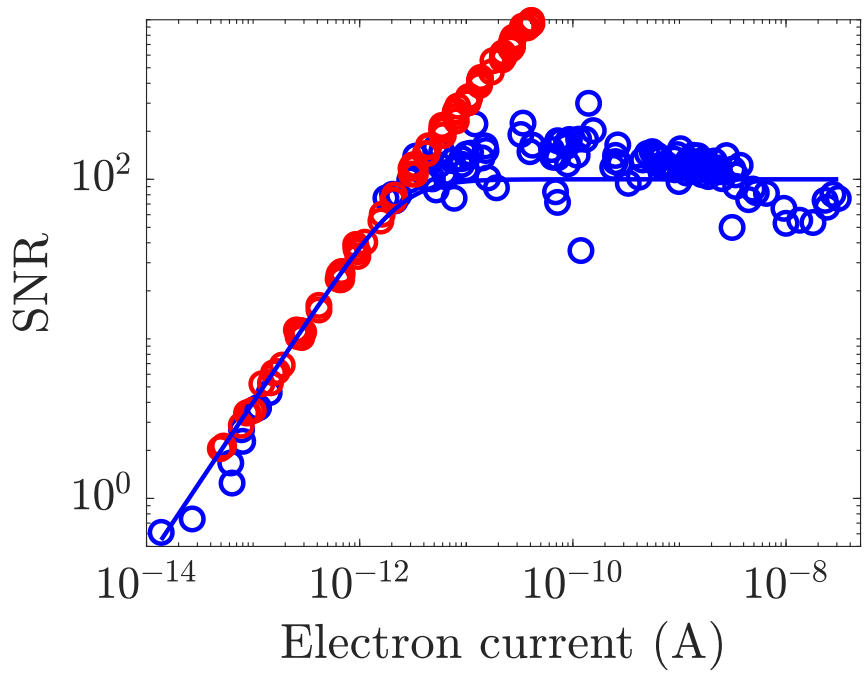

Figure 2.21: Comparison of the SNR when varying the intensity of a helium beam (blue circles), and varying the m/z selection in the absence of the beam (red circles). The key feature is that the maximum SNR is much greater in the absence of the beam. The blue curve is the quadrature addition of electrical noise and beam noise. No shot-like contribution is needed in order to interpret the data.

ments performed without the beam, coming from a more detailed comparison of different m/z background peaks. Table 2.8 lists the peak heights. The $m/z = 4$ peak is only 100× smaller than the $m/z = 2$ peak, which suggests that multiply ionised species are the dominant contributors to the $m/z = 4$ peak, since the isotopic abundance of D_2 is many orders of magnitude less than 1%. However, the contribution of multiple ions to the $m/z = 3$ background is much smaller, due to the choice of relative potential of the cathode and liner [99]. As well as recording peak heights, noise measurements were taken on the $m/z = 1, 2, 4$ peaks and are shown in Figure 2.22. The $m/z = 2$ data from the previous plot are reproduced as a reference point (red circles). The $m/z = 2$ data at a higher gain ($V_{CF} = 2.05\,\text{kV}$) are shown as red triangles. Unlike the $V_{CF} = 1.6\,\text{kV}$ data, the $V_{CF} = 2.05\,\text{kV}$ data show a clear shot noise regime: instead of an abrupt transition from the electrical noise regime to a constant-SNR regime (as seen, for example, in the with-beam data), there is a smooth crossover where shot noise dominates. The solid red curve drawn through the red triangles is a model of the noise $N(I)$ as a function of the electron current I in which electrical noise, emission stability noise and a term originating in shot noise are added in quadrature. However, the shot-like term is taken as twice the theoretical shot noise. Because the electron current is measured via analogue integration rather than pulse counting, the SNR of the electron current is lower

Table 2.8: Typical background signal on different mass peaks, expressed as electron current I_e when $V_{CF} = 1.6\,\mathrm{kV}$. The $m/z = 4$ background is much greater than the $m/z = 3$ background, which implies that the contribution at $m/z = 4$ from multiply ionised species such as C^{3+} is much larger than the contribution from D_2. The contribution of multiply-ionised species to the $m/z = 3$ peak is much smaller, and the ratio of the $m/z = 2$ and $m/z = 3$ peaks is roughly consistent with H_2 vs HD isotopic ratios.

m/z **peak**	I_e **(A) at** $V_{CF} = 1.6\,\mathbf{kV}$
1	3×10^{-10}
2	6×10^{-10}
3	2×10^{-13}
4	5×10^{-12}

than the SNR of the ion current, due to convolution of the incoming ion statistics with the pulse height distribution of the conversion dynode and then the multiplier. Measurements and simulations of the pulse height distribution at install time [99] showed that the multiplier and analogue counting arrangement reduce the SNR by a factor of 2. Therefore, the theoretical shot noise multiplied by a factor of 2 is used as an estimate of the contribution which arises from ion shot noise. Taking the shot noise correction into account, the solid red line is generated by the model

$$N^2 = E^2 + 4I/G + (f_e I)^2 \,. \tag{2.75}$$

where E is the constant electrical noise, the emission stability factor f_e is taken as its estimated upper limit of 0.7%, and $2\sqrt{I/G}$ is the corrected shot noise. The value of G taken from Table 2.7 leads to an overestimate of the shot noise. The gain is not expected to be in perfect agreement with the calibrated value for a different ion ($^3He^+$). Using $G = 2870/2$ produces the solid red curve in good agreement with the data, which implies that the gain of the multiplier assembly is roughly a factor of 2 lower for H_2^+. With regard to the other mass peaks: the range of the data is much more limited, but in both cases the data appear to be transitioning to a linearly scaling noise regime where the stability factor is much lower than for the $m/z = 2$ peak. An intrinsic instability in the solenoidal trap could be responsible. An instability in the ionization region could affect the noise on different ions in different ways, depending on the various timescales in the system which will depend on their mass and charge. However, the range of the $m/z = 1$ and $m/z = 4$ data is too small to fit a functional form with any confidence, and therefore more experimental characterization as well as simulation of possible mechanisms of instability would be required to identify the origin of the noise.

As an alternative perspective on the shot noise interpretation of Figure 2.22, I

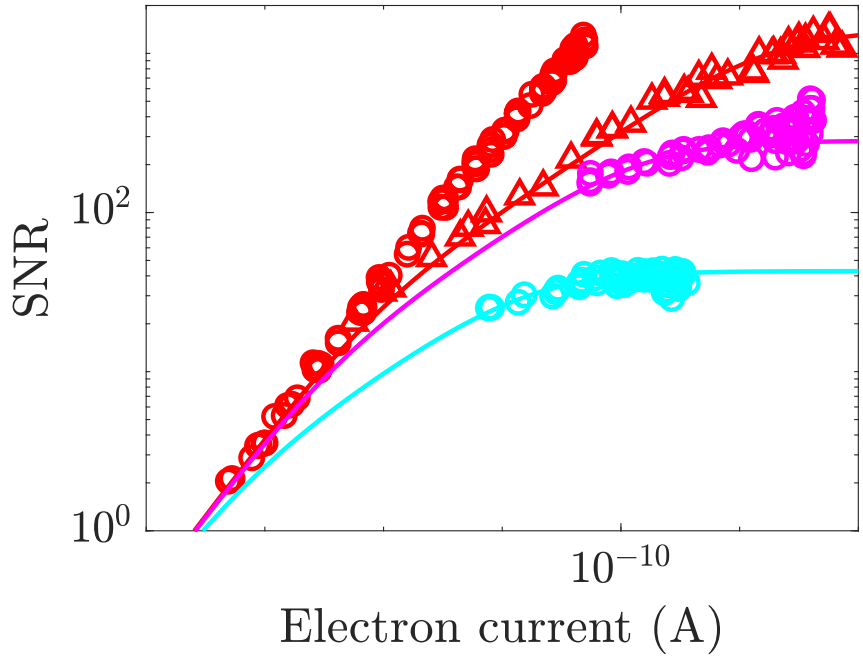

Figure 2.22: SNR of the background at the accessible mass peaks: $m/z = 2$ (red circles, $V_{CF} = 1.6\,\mathrm{kV}$; red triangles, $V_{CF} = 2.05\,\mathrm{kV}$); $m/z = 1$ (magenta circles, $V_{CF} = 2.05\,\mathrm{kV}$); $m/z = 4$ (cyan circles, $V_{CF} = 2.5\,\mathrm{kV}$). The interpretation is discussed in the main text.

consider the SNR at a constant ion current while varying the gain on the detuned $m/z = 2$ peak. The results are shown in Figure 2.23 as black circles. The results of keeping the gain constant and varying the m/z tuning are reproduced for comparison (red circles). At small electron currents the curves overlay each other exactly as the noise is dominated by the constant "electrical" term. The limiting SNR of the variable-gain data is lower than that of the variable-m/z data, which implies that the noise at the high gain end is dominated by a shot-like term. The solid black curve is simulated by adding the electrical noise and the corrected shot noise in quadrature. The stability noise is irrelevant. The solid black curve correctly predicts the levelling off of the SNR, using the gain calibrated from the red triangular data in Figure 2.22. The black curve is not a fit, as it uses only parameters that have been independently derived. As with the previous $m/z = 2$ data involving shot noise, the data are consistent with the $m/z = 2$ gain being very similar to the $m/z = 3$ gain, indicating that there is little difference between each case in terms of the ion/electron conversion statistics at the dynode.

The simple model 2.77 developed so far for the noise contains a constant electrical term, a linear "beam" or "stability" term, and a corrected shot contribution that agrees well with the gain curve calibrated at $m/z = 3$ using the helium beam. The model will now be applied to a meta-analysis of real surface science data recorded on the instrument, mostly associated with experiments reported in the present Thesis.

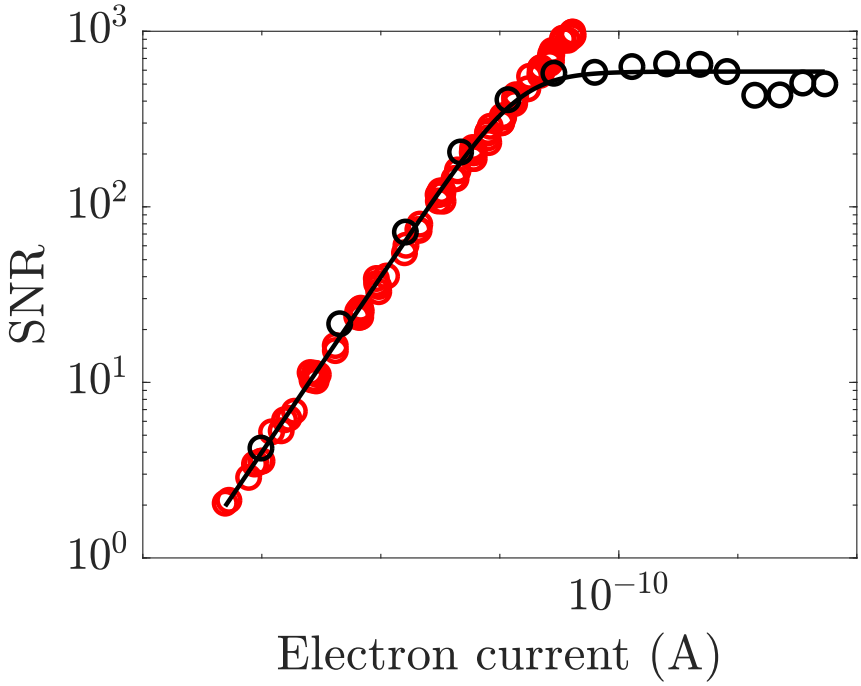

Figure 2.23: SNR as a function of electron current when varying the ion current (red circle) via tuning $m/z \approx 2$ across the background H_2 peak, and varying the multiplier gain at constant ion current (black circles) on the shoulder of the same peak. Saturation of the SNR with gain indicates that the result is shot noise limited.

2.3.3 Noise regimes and spin echo measurements

HeSE experiments are concerned with measuring the spin polarization of the ^{3}He beam after it has scattered from a surface. As explained in Section 2.1.4.3, the polarization is a complex quantity that can be determined by sampling the intensity as a spin rotation angle ϕ is varied (Equation 2.29). The standard sampling method is to measure the intensity at the four points $\phi = \{0, \pi/2, \pi, 3\pi/2\}$. Two simulated four-point measurements are shown in Figure 2.24. In each case, the underlying polarization is chosen to be real, because for the applications in later experimental Chapters 5-6 the imaginary part is generally insignificant.

In a typical HeSE investigation of adsorbate diffusion, the ^{3}He polarization is recorded as a function of the spin echo time t_{SE} (Section 2.1.2), for different states of the surface (e.g. orientation, temperature, adsorbate coverage). The functional form expected of $p(t_{SE})$ depends on the underlying surface dynamics, as illustrated in Section 2.2.1. $p(I_{SE})$ is typically sampled at $\mathcal{O}(100)$ points. At each value of t_{SE}, a four-point measurement is recorded. The standard integration time for each intensity reading in the four point measurement is 500 ms. In practice, 100 four-point measurements are performed in about 10 minutes. If the same set of t_{SE} are revisited repeatedly, each set of $p(t_{SE})$ data is referred to here as a loop. The background count rate b is measured at the start of every loop, to high accuracy using an integra-

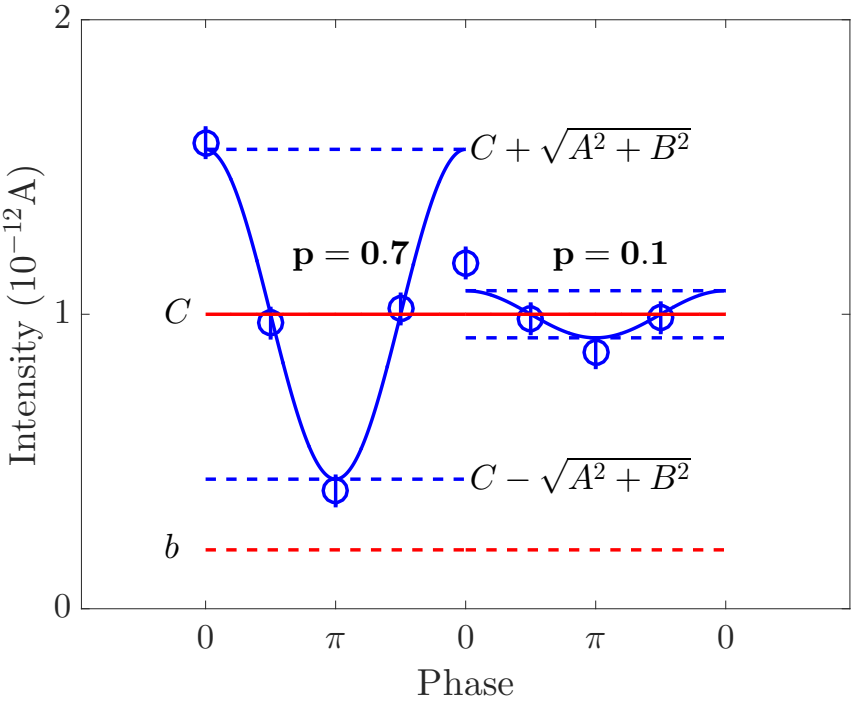

Figure 2.24: Simulated four point measurements for a large and smaller real-valued polarization p. The intensity is simulated using Equation 2.29. The simulated intensities can be converted back to a polarization using Equation 2.30 with best-fit values for A, B and C, which is how the polarization is measured in practice. The background count rate b is shown as 1/10 of the mean helium count rate C. For illustration, absolute Gaussian noise is applied to all intensity readings, which has more of a detrimental effect on the measured polarization when p is small. For clarity concerning polarization as a complex quantity: p is allowed to be complex, and even when intensities are simulated from a real value of p, the polarization determined by a best fit will generally have a small imaginary part when noise is introduced on the intensities, because the uncertainties in A and B can be recast as uncertainty in the phase and magnitude of p, not just the magnitude. However, the underlying value of p is chosen to be real here both for simplicity and because the vast majority of polarization measurements in the present Thesis are approximately real.

tion time of several seconds, and used for all calculations of p within that loop. As long as there is no evidence that p is changing with time due to, e.g. contamination of the surface, then it is appropriate to combine the separate loops to obtain the mean and uncertainty of $p(t_{SE})$ at the sampled points. Simulated polarization scans in Figure 2.25, and the corresponding marginalized posterior probability distributions $\rho(\alpha)$ (Section 2.2.5) illustrate the detrimental effect of noise on the analysis of HeSE lineshapes, in the special case of a mono-exponential lineshape.

In general the four points in a polarization measurement could fall into different regimes with respect to the limiting factor on SNR. For example if $p = 1$ then one of the four points measured will consist almost entirely of background signal. However, in practice p never exceeds about 0.7, and much of the time we are interested in measuring fairly small polarizations of 0.1 or less, in which case the four points of a four-point measurement will tend to fall in the same regime of SNR. Therefore it will not be at all surprising to find a measure of noise on the polarization that follows the same trends as the noise on the intensity. For data where multiple loops are available, I quantify the noise as the standard deviation of the complex polarised amplitude

$$P = A + iB \tag{2.76}$$

where the standard deviation of a complex variable is the r.m.s. distance in the complex plane from the mean value. I stress that in the present Chapter, two different complex quantities are used to describe the variation of detected helium intensity with the incoming spin rotation angle (Section 2.1.4.3):

- the polarization p a complex dimensionless quantity, defined by Equation 2.30 whose modulus is in the range $0 < |p| < 1$;
- the polarized amplitude P, a complex quantity with units of intensity (e.g. units of current, A), defined by Equation 2.76.

Figure 2.26 shows the noise on P as a function of the mean electron current, at various gains. The standard deviation was taken across multiple loops of polarization scans performed on stable systems. The noise on polarization measurements follows the same trend as the noise on repeated measurements of the intensity, in other words it is a constant at low values of the mean ion current, and transitions to a linear function of the intensity as the ion current increases.

Figure 2.26 shows polarization noise ΔP as a function of the ion current, for various values of the gain and for different 4-point count times. The noise is defined as the standard deviation of the complex polarised amplitude, while the ion current is estimated by C in the polarization measurements, divided by the gain determined

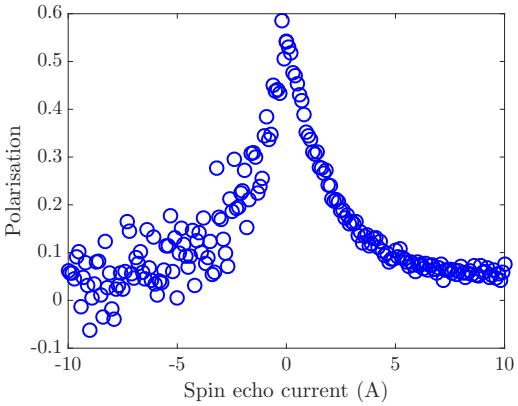

(a) Simulated polarization scans with a constant noise N on the polarization of $N = 0.01$ (right) and $N = 0.05$ (left).

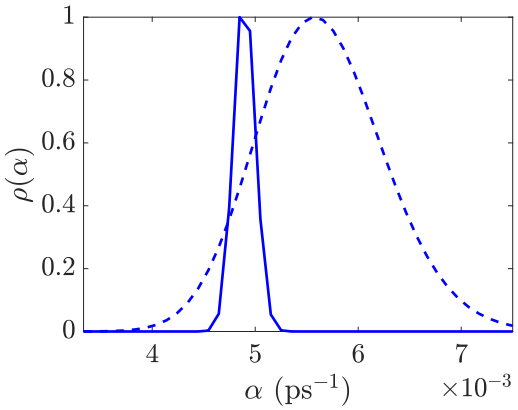

(b) The marginalized probability distribution for the decay rate α derived from the scan with $N = 0.01$ (solid blue curve) and $N = 0.05$ (dashed blue curve).

Figure 2.25: Illustration of the decrease in parameter resolution when the noise on polarization scans is increased. An underlying lineshape of the form $p(t_{SE}) = a\exp(-\alpha t_{SE}) + c$ was simulated with parameters $a = 0.5$, $c = 0.05$, $\alpha = 0.05$. The lineshape is shown in Figure 2.25a for a realistic experimental t_{SE} sampling, with an added Gaussian noise of magnitude $N = 0.01$ (right) and $N = 0.05$ (left). The marginalized posterior relative probability of α, produced by the methods described in Section 2.2.5, is shown in Figure 2.25b. The very broad $\rho(\alpha)$ for the $N = 0.05$ simulation, and the large uncertainty on α, illustrates the importance of low noise on the polarization. For clarity, I emphasise that the overall shift of the broader distribution away from the true value of α is not a systematic, repeatable feature of the illustration: it is a consequence of inferring the distribution from the simulated data subject to a particular realization of the random noise. Repeating with independent samples of the random noise in general leads to different inferred distributions which are sometimes biased above the underlying α and sometimes below, but are centred on the underlying α on average.

Table 2.9: List of the experimental systems represented on Figure 2.26.

System	Gain	Count time (ms)	Marker
H/Pd(111)	113	1000	Blue circle
CO/Pd(111)	113	500	Magenta circle
H/Cu(111)	2150	1000	Red circle
H/Ru(0001)	2150	500	Cyan circle
O/Cu(111)	2150	500	Cyan triangle
H/Ru(0001)	8800	500	Green circle

from Figure 2.18. The nature of each data series is given in Table 2.9. The solid curves are all derived from the same model applied at the appropriate gain and count time. We model the polarization noise across all datasets with the same simple model as used for the intensity time series, which combines the electrical noise E, corrected shot noise $2\sqrt{I/G}$, and beam noise $f_b I$:

$$\Delta P^2 = \frac{1}{2}\left[(E^2 + 4I/G + (fI)^2\right]. \tag{2.77}$$

The factor of 1/2 is semi-empirical, but makes sense as multiple readings of the intensity make up a single polarization measurement. The noise is adjusted by a factor of $\sqrt{2}$ when a count time of 500 ms is used. The minimal model assumes that the shot noise on the $m/z = 3$ background can be absorbed into the shot noise term by using the total measured current I for the shot noise calculation. That assumption requires the ion/electron conversion properties to be much the same for the $m/z = 3$ background ions as they are for ^{3}He ions, and therefore the model would need to be generalized further to be used in situations where the beam intensity is comparable to the background. The vast majority of the data presented here is well above background, so the distinction between shot noise on the beam and shot noise on the background is not critical for explaining the data. The shot noise on the background could be determined via gain and I_{bend}-dependent SNR measurements on the $m/z = 3$ peak.

2.3.4 Conclusions

I have characterized the performance of the helium detector on the Cambridge helium-3 spin echo spectrometer, by analysing a large set of real experimental data for their signal to noise properties, and performing measurements on the atom detector in isolation. The ionization efficiency of the new (2011) detector for a helium-3 beam is $\eta = 2 \times 10^{-3}$, an improvement of 100× over the previous design, facilitated by the large ionization volume. The background count rate has been improved over the previous design by a factor of 10. However, the signal-to-noise ratio is the most

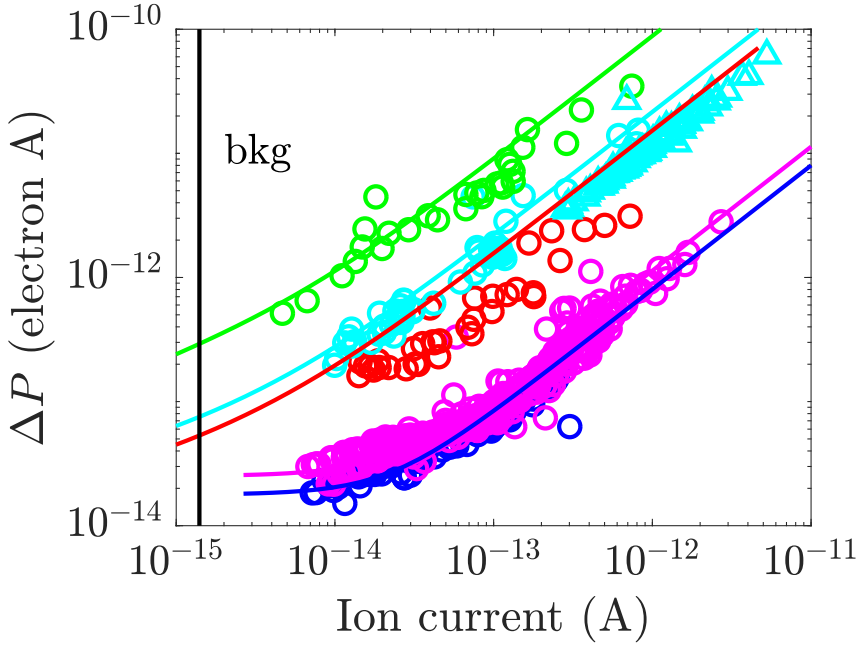

Figure 2.26: Noise as a function of mean ion current, where noise is defined as the standard deviation of the complex polarized amplitude (Equation 2.76) over multiple loops of polarization scans on stable systems. Points represent various datasets from HeSE experiments most of which are reported in full in Chapters 5 and 6. In most case, the polarization was measured over multiple loops, and the noise ΔP is quantified as the spread in repeated measurements of the same polarized amplitude. Different gains and different count times are represented in the plot. The data series are given in Table 2.9. A substantial proportion of the lower gain data was limited in SNR by the electrical noise limit, whereas essentially all of the higher-gain data appears to lie in the beam noise limited regime. However, the constant of proportionality does not appear to be truly constant between different data sets. Neither does it scale monotonically with the gain, since the SNR of H/Cu(111) points (red) is greater than for the O/Cu(111) points (black). It is possible that the scale of the beam noise drifts very slowly with time. The data that comes closest to a shot noise limited regime is the data with the lowest ion current, but a high gain, namely the green H/Ru(0001) data. In the case of the green data, the noise has been extracted from single-loop polarization scans. ΔP for a single-loop scan has been defined as the standard deviation of the residuals between the four point fits and the four point data. Because a different method was used to extract the green data, the absolute agreement with the model curve is accidental, but the trend is entirely consistent with all the other data. It is clear that by increasing the gain of the multiplier, the SNR of low-signal measurements on Ru(0001) and O/Cu(111) were improved by bringing the measurements into the beam noise limited regime. By contrast, the SNR of measurements on Pd(111) is very poor at low signals due to the electrical noise limit.

important performance metric, which motivated measurements of the detector noise under a range of conditions.

The noise N, on repeated measurements of the final output current of the detector (mean value I) can be realistically modelled via a constant term E of electrical origin, a term $\propto \sqrt{I/G}$ originating in shot noise where G is the detector gain, and a term $f_e I$ linearly proportional to mean current, where f_e is a constant:

$$N^2 = E^2 + 4I/G + (f_e I)^2 \,. \tag{2.78}$$

Noise in the measurement of intensity leads to noise in measured polarization. The noise on intensity and polarization follow the same trends as a function of signal. The majority of the polarization data recorded for the present Thesis was limited in quality by the term $f_e I$ where f_e is approximately 1% when measuring a helium-3 beam intensity. The apparent m/z-dependent stability factor of Section 2.3.2.2 demonstrates that the high value of f_e when measuring helium-3 is not necessarily due to beam source fluctuations but could be intrinsic to the detector. Some polarization measurements were limited in SNR by the constant electrical noise E, but in all the cases analysed the electrical noise limit could have been avoided by increasing the gain of the multiplier assembly, bringing the measurements back into the regime where f_e is the limiting factor. The high ionization efficiency of the new detector means that the shot noise regime is hardly ever relevant, but it would become more relevant if f_e was significantly reduced from 1 %.

2.4 Summary and outlook

The principles of helium-3 surface spin echo spectroscopy (HeSE) have been outlined, and the experiment has been placed in context as an atom-scattering technique. I have described different types of measurement that can be performed on the HeSE spectrometer, and the physical information those measurements are expected to reveal, which will be used in Chapters 5 and 6. The most important kind of measurements, unique to HeSE, are polarization scans which reveal information about the surface dynamics, and are largely interpreted in terms of the intermediate scattering function (ISF), a correlation function whose microscopic origins and evaluation are examined in detail in the following two Chapters.

I have described the statistical methods used to analyse individual polarization scans, and also collections of polarization scans where it is beneficial to perform a global analysis referred to as Bayesian analysis. Bayesian analysis is particularly helpful when analysing lineshapes containing more than one exponential component,

because of the difficulty of directly fitting two components given a single scan. The physical situation in Chapters 5 and 6 which leads to a biexponential model is that of adsorbates performing jump diffusion on fcc(111) and hcp(0001) surfaces where the adsorption sites are nearly-degenerate fcc and hcp hollow sites. If multiple jumps are allowed for, the model contains three adjustable parameters. Minor adjustments to previous implementations of the global Bayesian method are described which make fitting of a three-parameter jump model practical. The inclusion of multiple jumps in the model is important since all the systems studied with Bayesian analysis later on (C/Ru(0001), H/Ru(0001), H/Pd(111), H/Cu(111)) are best fit with a non-neglible multiple jump fraction.

The statistical analysis methods will cope with a modest amount of noise, but minimizing the experimental noise is very important when it comes to distinguishing subtly different models of dynamics. Therefore, the ionizing detector has been characterized with a focus on its signal-to-noise ratio (SNR). Under typical measurement conditions, the limiting factor in the instrument noise is a contribution that scales linearly with the signal, giving a constant SNR of around 1% with a 1 s integration time. The linear noise dominated the total noise for almost all measurements reported in Chapters 5 and 6, and is therefore a very important issue to address in the future. Previously the intrinsic detector SNR in the absence of a beam had been measured as around 1/500. The measurements in the present Chapter confirmed that result when the selected $m/z = 2$, but show evidence for an apparent mass-dependent stability, which is significantly worse at $m/z = 3$. Therefore, although factors external to the detector could contribute to the linear noise, it is also possible that the noise originates within the detector itself.

Chapter 3

Open classical systems

HELIUM-3 spin echo experiments are normally concerned with the statistical dynamics of adsorbates in thermal equilibrium. The natural way to describe statistical motion is via conditional probabilities, or equivalently by correlation functions. The intermediate scattering function (ISF) is one such correlation function and provides a unifying mathematical description of different types of equilibrium dynamics including ballistic, diffusive and vibrational motion. In general the equilibrium surface dynamics, as described by the ISF, cannot be qualitatively described in terms of a single process. However, complex motion can often be decomposed into different types of behaviour associated with widely separated timescales. For example an adsorbate in a corrugated potential energy landscape will undergo rapid driven damped vibrations, and site-to-site jumps at a much lower rate. Both processes will be reflected in the ISF, and in many cases the ISF can be described as having different components, each with their own amplitude. In Section 3.1 I introduce the classical ISF and its general properties, and present some simulated and analytical examples of components-with-amplitudes.

Previously it has been established by numerical simulation that the presence of memory effects in the heat bath can reduce the amplitude associated with the slowest decaying component in the ISF [28]. In Section 3.2 I derive the analytical ISF for an adsorbate on a flat surface subject to a Generalized Langevin Equation (GLE) in which the thermal environment has a finite memory time in its response to the adsorbate motion. The result provides an analytical perspective on the (experimental and simulated) amplitudes of lineshape components for diffusion on weakly corrugated surfaces. Opening up the range of exactly solvable systems could stimulate further experiments on weakly corrugated systems and facilitate a more rigorous analysis of data for which ballistic motion is important (e.g. Xe/Pt(111) [104, 28], Li/Cu(111) [28] and aromatic molecules on carbon surfaces [105].)

The GLE is a convenient computational tool and can explain aspects of experimental data which cannot be explained with a memory-free Langevin approach [28]. The model GLE considered in the analytical work is derived from a very simple model of a heat bath, but one that is superficially similar to a harmonic substrate. A many-body simulation of an adsorbate on a harmonic slab contains memory effects implicitly, but is not guaranteed to be describable via a simple memory kernel. In the final Section I describe some preliminary investigations on the microscopic connection between many-body adsorbate/slab simulations and the GLE. The frictional kernel derived from simulation is highly structured in the frequency domain and oscillatory in the time domain.

3.1 The intermediate scattering function (ISF)

The ISF is the central concept in most HeSE investigations of adsorbate dynamics. As well as being an approximation to experimentally measured lineshapes (Section 2.1), it provides a natural and efficient description of dynamics in its own right. Some examples of analytical ISFs were introduced in Section 2.2 without detailed proof. In the present Section, the ISF is introduced from a microscopic viewpoint. To set the context for the later analytical work, some standard results for the ISF in simple cases are reviewed. Additionally, I present some simple analytical approximations for the effect of the fast intra-cell dynamics on the long-time decay of the ISF, when the time scales of vibrations and jumps are well separated. The standard method for calculating ISFs from classical simulations is introduced and the results are compared to the analytical approximations.

3.1.1 Classical definition

A natural way of describing the equilibrium dynamics of a single particle is via van Hove's pair correlation function $G(\mathbf{R}, t)$. Using angle brackets to represent an average, the function is defined as

$$G(\mathbf{R}, t) = \left\langle \int d\mathbf{R}' \delta(\mathbf{R} + \mathbf{R}(0) - \mathbf{R}') \delta(\mathbf{R}' - \mathbf{R}(t)) \right\rangle . \tag{3.1}$$

$G(\mathbf{R}, t)$ is the $\mathbf{R}'$-averaged probability of finding the particle at position $\mathbf{R}' + \mathbf{R}$ at time t given it was at $\mathbf{R}'$ at time 0. If we define the ISF $I(\Delta\mathbf{K}, t)$ as a spatial Fourier

transform of $G(\mathbf{R}, t)$,

$$I(\Delta\mathbf{K}, t) = \int d\mathbf{R}\, e^{-i\Delta\mathbf{K}\cdot\mathbf{R}}\, G(\mathbf{R}, t)\,, \tag{3.2}$$

and perform the δ-function integrations, the result is

$$I(\Delta\mathbf{K}, t) = \langle e^{i\Delta\mathbf{K}\cdot\mathbf{R(t)}} e^{-i\Delta\mathbf{K}\cdot\mathbf{R(0)}} \rangle\,. \tag{3.3}$$

The ISF can therefore be described as the autocorrelation of an amplitude $e^{i\Delta\mathbf{K}\cdot\mathbf{R}(t)}$.

The meaning of the average $\langle \cdots \rangle$ in Equation 3.3 can be written generically in terms of conditional probabilities:

$$I(\Delta\mathbf{K}, t) = \int d\mathbf{R}\, d\mathbf{R}'\, p(\mathbf{R}) e^{i\Delta\mathbf{K}\cdot\mathbf{R}'} e^{-i\Delta\mathbf{K}\cdot\mathbf{R}} p(\mathbf{R}'|\mathbf{R})\,, \tag{3.4}$$

where $p(\mathbf{R})$ represents the equilibrium probability of the particle residing at $\mathbf{R}$, and $p(\mathbf{R}'|\mathbf{R})$ the conditional probability to move to $\mathbf{R}'$ in time t. The representation 3.4 makes no explicit reference to environmental degrees of freedom to which the particle is coupled. According to 3.4, the ISF provides a description of a stochastic process defined by $p(\mathbf{R})$ and $p(\mathbf{R}'|\mathbf{R})$.

An alternative approach to thermal equilibrium behaviour is to consider a gigantic closed system, with a total energy E Boltzman-distributed according to $p(E) \propto e^{-\beta E}$ which represents a temperature $T = (k_B\beta)^{-1}$. The global system evolves deterministically, but from initial conditions $\{\mathbf{R}_n\}$, $\{\mathbf{P}_n\}$ which follow the thermal distribution. If $H(\{\mathbf{R}_n\}, \{\mathbf{P}_n\})$ is the classical Hamiltonian (total energy) as a function of positions $\mathbf{R}_n$ and momenta $\mathbf{P}_n$,

$$H(\{\mathbf{R}_n\}, \{\mathbf{P}_n\}) = \sum_n \frac{\mathbf{P}_n^2}{2m_n} + V(\{\mathbf{R}_n\})\,, \tag{3.5}$$

then the generic probability-based definition for the ISF translates to:

$$I(\Delta\mathbf{K}, t) = \frac{\int d\{\mathbf{R}_n\} \int d\{\mathbf{P}_n\}\, e^{i\Delta\mathbf{K}\cdot\mathbf{R}(t)} e^{-i\Delta\mathbf{K}\cdot\mathbf{R}} e^{-\beta H}}{\int d\{\mathbf{R}_n\} \int d\{\mathbf{P}_n\}\, e^{-\beta H}}\,. \tag{3.6}$$

The Hamiltonian H controls both the definition of thermal equilibrium, and also the deterministic dynamics via Hamilton's equations of motion[1]

$$\dot{\mathbf{R}}_i = \frac{\partial H}{\partial \mathbf{P}_i}\,; \dot{\mathbf{P}}_i = -\frac{\partial H}{\partial \mathbf{R}_i}\,. \tag{3.7}$$

Features of the gigantic-closed-system approach include:

[1] No more or less than Newton's laws, for Hamiltonians of the form considered here.

- The dynamics of a single selected particle are stochastic as a result of the statistical initial conditions;

- In some model cases initial conditions can be integrated out analytically to derive exact forms for $I(\Delta\mathbf{K}, t)$ (see Section 3.2);

- A large, deterministically evolving system can be quantized, and therefore provides a starting point for the calculation of the ISF in the quantum mechanical case (Chapter 4).

The definition 3.3 immediately implies $I(-\Delta\mathbf{K}, t) = I^*(\Delta\mathbf{K}, t)$. However, classical evolution backwards in time is equivalent to forward evolution in time starting from reversed initial velocities. Since the distribution of initial conditions in Equation 3.6 is symmetric in the momenta, $I(\Delta\mathbf{K}, t)$ is symmetric in time. Additionally, because $I(\Delta\mathbf{K}, t)$ is an autocorrelation, the Wiener-Khinchin theorem [106] ensures that the Fourier transform of $I(\Delta\mathbf{K}, t)$ is real. For consistency, $I(\Delta\mathbf{K}, t)$ must be real and symmetric in time, and is therefore symmetric in $\Delta\mathbf{K}$ as well[1]. Symmetry in $\Delta\mathbf{K}$ and t can be verified for the analytical classical ISFs quoted or derived later in the present Chapter, and also applies to the jump model ISFs of Chapter 2. In the case of jump models, the origin of the time symmetry is more naturally explained by microscopic reversibility [107], the idea that in equilibrium not only should $p(x)$ be constant, but there should be no net flow of particles around a system: all forward and backward transition rates must balance. In the notation of the definition 3.4, microscopic irreversibility can be expressed as

$$p(\mathbf{R})p(\mathbf{R}'|\mathbf{R}) = p(\mathbf{R}')p(\mathbf{R}|\mathbf{R}')\,, \tag{3.8}$$

which when substituted into the definition 3.4 implies that $I(-\Delta\mathbf{K}, t) = I(\Delta\mathbf{K}, t)$.

3.1.2 Analytical results for the ISF

The ISF can potentially be calculated analytically from the definition 3.6 for any classical system that is exactly solvable in the traditional sense (i.e. the time evolution of co-ordinates can be determined analytically from arbitrary initial conditions). For the stochastic-process definition 3.4, the ISF can be calculated analytically if the conditional probability evolution is simple enough, for example in the jump diffusion models of Section 2.2.1.

[1] As seen in Section 2.2.1, one consequence of $\pm\Delta\mathbf{K}$ symmetry is that jump diffusion ISFs cannot be used to distinguish 60°-rotated inequivalent directions on fcc(111) or hcp(0001) surfaces.

3.1.2.1 Flat surfaces ($V(R) = 0$)

The simplest microscopic system is a free particle. Classically and quantum mechanically, the time evolution of particle co-ordinate x in one dimension is given in terms of the momentum p by $x(t) = x(0) + p(0)/m$. In the classical case, integrating $\exp(i\Delta K[x(t) - x(0)])$ over initial momenta governed by the canonical distribution $\propto \exp(-\frac{1}{2m}\beta p^2)$ at inverse temperature $\beta = (k_B T)^{-1}$, gives the well known result for ballistic motion [104, 61]),

$$I(\Delta K, t) = \exp\Big(- \frac{k_B T}{2m}(\Delta K t)^2 \Big) , \tag{3.9}$$

which is a Gaussian function whose decay frequency scale increases linearly with ΔK.

The derivation of the ballistic lineshape assumed an initial thermal equilibrium state which must result from the action of a heat bath (the substrate), but the evolution of the particle's position follows a free trajectory with no explicit coupling to the bath. The ballistic result is therefore plausible on timescales shorter than the thermalization period (γ^{-1}, for a Langevin particle). Including the thermalization mechanism in the dynamics changes the functional form of the lineshape. A key stepping stone to the analytic results derived in Section 3.2 is the ISF associated with the Langevin equation (LE) on a flat surface. The LE reads:

$$m\ddot{x} = -m\gamma\dot{x} + F(t)\,;\;\; \langle F(t)\rangle = 0\,;\;\; \langle F(t)F(0)\rangle = m\gamma k_B T\delta(t)\,. \tag{3.10}$$

$F(t)$ is a random force taken here as Gaussian-distributed, of zero mean, and uncorrelated as described by the Dirac delta function $\delta(t)$. In other words, if the force is regarded as supplying an impulse over short time intervals δt, then for each time interval separately the probability distribution of the impulse is a Gaussian whose width is determined by the correlation $\langle F(t)F(0)\rangle$, but also the impulses in successive time intervals are completely uncorrelated, no matter how short the intervals. γ is known as the friction and has dimensions of rate; in the case of a flat surface it is the relaxation rate of the velocity autocorrelation function (VACF) [26],

$$\langle v(t)v(0)\rangle = \langle v^2\rangle e^{-\gamma t}\,. \tag{3.11}$$

The connection between γ and $F(t)$ is a special case of a more general fluctuation-dissipation relation discussed in Section 3.2. For the time being, the important property of the forces $-\gamma m v(t)$ and $F(t)$ acting in tandem is that they thermalize the particle at the temperature T of equation 3.10.

The ISF of a particle obeying the classical Langevin equation is conveniently derived from the VACF, as discussed in detail in Section 3.2.2. The final result is [26],

$$I(\Delta K, t) = \exp\left(\Delta K^2 \frac{k_B T}{m\gamma^2}(1 - \gamma|t| - e^{-\gamma|t|})\right). \tag{3.12}$$

It is easily shown that in the short time limit the Langevin lineshape matches that of ballistic motion. At long times, the Langevin lineshape is proportional to $\exp(-D\Delta K^2|t|)$ where D is the standard Brownian diffusion coefficient,

$$D = \frac{k_B T}{m\gamma}. \tag{3.13}$$

3.1.2.2 Harmonic systems

The ISF for a classical particle obeying the Langevin equation in a harmonic potential

$$V(x) = \frac{1}{2} m\Omega^2 x^2 \tag{3.14}$$

takes the form [108]:

$$I(\Delta K, t) = \exp\Big(- \frac{k_B T}{m\Omega^2}\Big[1 - e^{-\gamma t/2}\{\cos(ft) + \frac{\gamma}{2f}\sin(ft)\}\Big]\Big), \tag{3.15}$$

where $f = \sqrt{\Omega^2 - \gamma^2/4}$. The ISF for globally harmonic systems, in which $V(x) = 0$ but the particle is immersed in a bath of harmonic oscillators, will be analysed in detail in Sections 3.2 and 4.2. For now it is relevant to study the long time limit (static level) $I(\Delta K, \infty)$ which is a thermodynamic quantity independent of the dissipation strength:

$$I(\Delta K, t \to \infty) = \exp\Big(- \frac{k_B T}{m\Omega^2}\Big). \tag{3.16}$$

The static level of the ISF is nonzero, as a result of the confined nature of the diffusion. The calculation of the static level can also be carried out by taking the form 3.4, which in one dimension reads

$$I(\Delta K, t) = \int dx\, dx'\, p(x) e^{i\Delta K x'} e^{-i\Delta K x} p(x'|x), \tag{3.17}$$

and setting $p(x'|x) = p(x')$, in other words the final position x' at long times follows the thermal distribution, completely independent of the initial position x. Then,

$$I(\Delta K, t) = \Big(\int dx\, p(x) e^{i\Delta K x}\Big)\Big(\int dx\, p(x) e^{-i\Delta K x}\Big) \tag{3.18}$$

$$= \frac{\int dx\, e^{-\beta m\Omega^2 x^2/2} e^{i\Delta K x}}{\int dx\, e^{-\beta m\Omega^2 x^2/2}} \frac{\int dx\, e^{-\beta m\Omega^2 x^2/2} e^{-i\Delta K x}}{\int dx\, e^{-\beta m\Omega^2 x^2/2}} \tag{3.19}$$

$$= \left| \frac{\int dx\, e^{-\beta m\Omega^2 x^2/2} e^{i\Delta K x}}{\int dx\, e^{-\beta m\Omega^2 x^2/2}} \right|^2 \tag{3.20}$$

$$= \exp\Big(-\frac{k_B T}{2m\Omega^2} \Big) \exp\Big(-\frac{k_B T}{2m\Omega^2} \Big) = \exp\Big(-\frac{k_B T}{m\Omega^2} \Big) . \tag{3.21}$$

The idea of a $p(x'|x)$ which is decorrelated at a long enough time can therefore be used to derive an exact result about the amplitude of an ISF component, namely the static level of the harmonic oscillator ISF. The same construction will shortly be used to derive an approximate result about amplitudes for a Langevin particle in a periodic potential.

3.1.3 Amplitudes, components, long-time limits

There is no generally applicable analytical result for the ISF in periodic potentials for all t, although in some regimes an approximate form can be constructed out of the 'building blocks' of analytic vibrational and hopping lineshapes [108]. However, stochastic simulations are routinely used to calculate the classical ISF efficiently (e.g. [109, 110, 25]). Including a potential of mean force $V(x)$ which represents the adiabatic interaction with a surface, the LE (3.10) generalizes to

$$m\ddot{x} = -V'(x) - m\gamma\dot{x} + F(t)\,; \langle F(t)F(0)\rangle = m\gamma k_B T \delta(t) . \tag{3.22}$$

in which $F(t)$ is the random force and $-m\gamma\dot{x}$ the frictional force. The long-time average distribution of the particle's position is the thermal equilibrium distribution[1],

$$p(x) = \frac{1}{Z} e^{-\beta V(x)} . \tag{3.23}$$

As long as the adsorption minima are well defined, the conditional distribution $p(x'|x)$ at long times depends only on the initial unit cell, not the initial intra-cell position. The ISF therefore factorizes at long times into a fully decayed confined-diffusion ISF, and a diffusive tail. In other words, the ISF at long times should become a product of the jump diffusion lineshape and the completely dephased, long-time limit of the ISF for intra-well motion. The long time limit of the dephased

[1] It is not obvious from the Langevin equation as introduced so far that thermal equilibrium of the form 3.23 is maintained, but it is easily checked by viewing the Langevin equation as a limit of the generalized Langevin equation which results from the Hamiltonian 3.29, and imposing global equilibrium on the system-plus-bath.

intra-well motion is therefore the amplitude of the subsequent, slow decay of the ISF due to jumps. In a sinusoidal potential

$$V(x) = V_0 \sin\left(\frac{2\pi x}{a}\right), \tag{3.24}$$

the analogy between intra-cell motion and motion in the confined harmonic potential leading to Equation 3.20 suggests an intra-cell factor of

$$\left| \frac{\int_{-a/2}^{a/2} dx\, e^{-\beta V_0 \sin(2\pi x/a)} e^{i\Delta K x}}{\int_{-a/2}^{a/2} dx\, e^{-\beta V_0 \sin(2\pi x/a)}} \right|^2 \tag{3.25}$$

associated with a spatial distribution $\propto \exp(-\beta V(x))$ in an individual unit cell. The static level in a harmonic well with the frustrated translation frequency constitutes a cruder estimate of the intra-cell factor, and will be a systematic underestimate for a sinusoidal potential in which the well is systematically shallower than its harmonic extrapolation.

The analytical estimates for the decay amplitude can be tested by numerical Langevin simulations. The Langevin simulations whose results are illustrated in Figure 3.1 were performed in a sinusoidal potential $V(x) = V_0 \sin(2\pi x/a))$ with $V_0 = 50\,\mathrm{meV}$, $a = 2.55\,\text{Å}$, at $T = 200\,\mathrm{K}$ and $\gamma = 3\,\mathrm{ps}^{-1}$ using a timestep of 5 fs and Verlet integration [111]. 300 independent simulation runs were performed. The ISF is calculated from each simulated trajectory $x(t)$ using the Wiener-Khinchin theorem, and the ISFs from the separate runs are combined to give a mean and standard deviation. Therefore, the average in expression 3.3 is partly performed by time averaging, and partly by ensemble averaging. The long time tail of the ISF is fitted by nonlinear least squares from a suitable start time as discussed in Section 2.2.3. The predictions of Equation 3.25 closely describe the numerical decay amplitudes as shown in Subfigure 3.1c. The theory of the decay amplitude based on the intra-well factor takes only the thermal equilibrium spatial distribution as input, and therefore does not require detailed knowledge of the thermalization mechanism (e.g. the value of γ).

If surface-perpendicular momentum transfer Δk_z is included in the calculation of the ISF via

$$I(\Delta\mathbf{k}, t) = \left\langle \exp(i[\Delta k_z \cdot z(t) + \Delta\mathbf{K}\cdot\mathbf{R}(t)]) \exp(-i[\Delta k_z \cdot z(0) + \Delta\mathbf{K}\cdot\mathbf{R}(0)]) \right\rangle, \tag{3.26}$$

then the decay amplitude is reduced further. If the three-dimensional potential energy surface $V_{3d}(\mathbf{R}, z)$ is separable into $V(\mathbf{R}) + V_z(z)$, then z-motion and surface-parallel motion are completely independent, and the ISF factorizes into a z part and

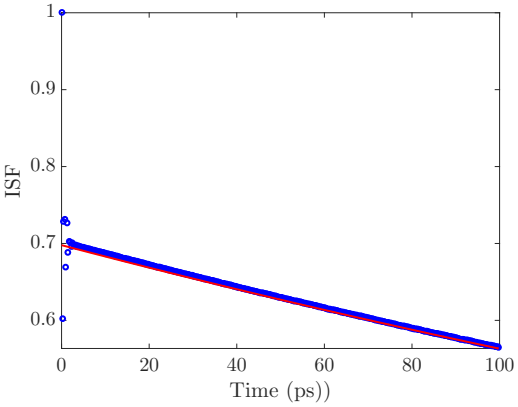

(a) ISF $I\Delta K, t)$ at $\Delta K = 2.2\,\text{Å}^{-1}$ from Langevin simulations.

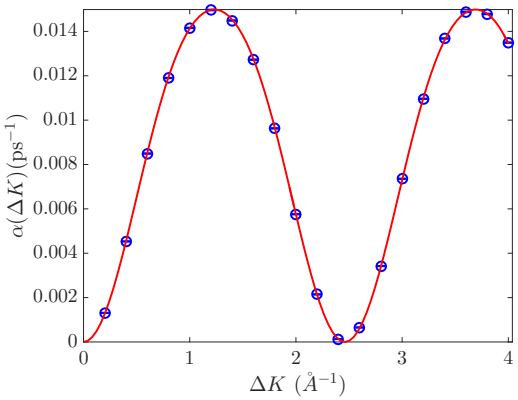

(b) The ΔK-dependent dephasing rate of the tail of the ISF.

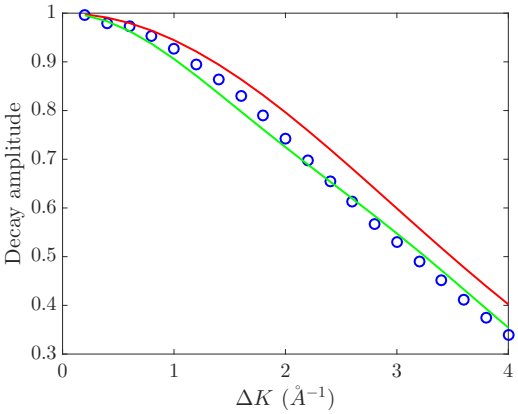

(c) The ΔK-dependent decay amplitude.

Figure 3.1: Numerical results of one-dimensional Langevin simulations performed in a sinusoidal potential $V(x) = V_0 \sin(2\pi x/a))$ with $V_0 = 50\,\text{meV}$, $a = 2.55\,\text{Å}$, at $T = 200\,\text{K}$ and $\gamma = 3\,\text{ps}^{-1}$ using a timestep of 5 fs and Verlet integration [111], for 300 independent runs. Blue points represent numerical simulation data throughout. Figure 3.1a shows the first 100 ps of the ISF at $\Delta K = 2.2\,\text{Å}$, which has a decay amplitude of 0.70. The red line indicates the start of an exponential fit to the long-time tail. There is no intercept, so the intercept of the fitted curve with the vertical axis is equal to the decay amplitude. Figure 3.1b shows the decay rate $\alpha(\Delta K)$ which is sinusoidal in ΔK, indicating jump motion; the solid curve is the best fit to the Chudley-Elliott model (Section 2.2.1) with 90 single jumps. Figure 3.1c shows the monotonically decreasing ΔK-dependent decay amplitudes. The green solid curve overlaid is not a fit to the simulation data; it is the prediction of Equation 3.25 numerically integrated over one unit cell of $V(x)$. The simple estimate based on the harmonic well frequency (Equation 3.16) is shown in red, and reproduces the trend but not the quantitative results.

an x, y part. If the z-motion is of the dephased-harmonic variety described by 3.15 then the decay amplitude associated with surface-parallel diffusion will be further reduced by the factor

$$\exp\Big(-\frac{k_B T}{m\Omega_z^2}\Delta k_z^2\Big), \tag{3.27}$$

where Ω_z is the surface-perpendicular vibrational frequency. If the perpendicular vibrational height and frequency do not depend too strongly on x, y then a separable potential is a reasonable approximation. For an 8 meV beam of ^{3}He in the $\delta = 44°$ geometry of the Cambridge spin echo spectrometer, $k_z \approx 6\text{Å}^{-1}$ at specular reflection, which is larger than the surface-parallel ΔK normally probed. Therefore, in a 3-dimensional molecular dynamics simulation, the amplitude of the decaying tail of the ISF is significantly reduced by surface-perpendicular motion as long as the vibrational frequency is not too high. In particular, the decay amplitude is significantly less than unity even when $\Delta K = 0$. In a pairwise-Morse molecular dynamics model of Na/Cu(001), the surface-perpendicular vibrational frequency was found as 28 rad·ps^{-1} [112], which Equation 3.27 predicts will result in a main decay amplitude of around 0.65 at $\Delta K = 0$, at a simulation temperature of 155 K. Figure 3.2 shows ISFs calculated from molecular dynamics simulations of that system when Δk_z is neglected (blue) and accounted for (red). The reduction in the amplitude of the long-time decay is consistent with the simple factorization approximation 3.27. The present claim, that the amplitude of the decaying tail of an ISF can be quantitatively estimated from the harmonic frequency, is a relatively modest but secure claim about the complete lineshape in the limit of well-defined adsorption sites and jumps. Attempts have been made to analyse and model the interplay of vibrational and jump motion in more detail [108] but are not considered further in the present Thesis.

When the diffusion barrier between adjacent sites is sufficiently low, a neat separation of timescales will no longer hold, and the amplitude associated with the fast and slow components depends on the details of the dynamics during barrier crossing as well as in the wells. In those cases, the amplitude of the tail is affected by the memory properties of the dynamical friction kernel. Numerical results in that category have been presented for simulations of Li/Cu(111) [28], and the situation will now be analysed analytically in the special case of diffusion on a flat surface.

3.2 Analytical Generalized Langevin lineshapes

In the previous Section results were presented from simulations of the Langevin Equation (LE). There are several motivating factors for studying instead the Gener-

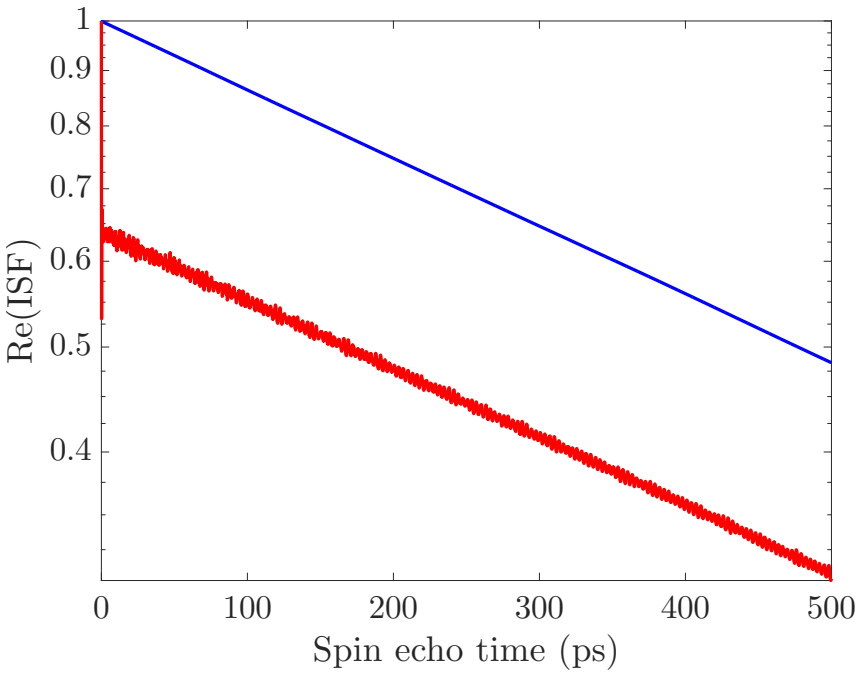

Figure 3.2: ISF at $\Delta K = 0.1\,\text{Å}^{-1}$ derived from an adsorbate-plus-slab simulation of Na/Cu(001) at a temperature of 155 K when momentum transfer is considered as a two-dimensional variable (blue) and three-dimensional variable (red). The long-time diffusive tails are straight lines on the logarithmic representation, with the same gradient governed by the $\alpha(\Delta K)$ associated with surface-parallel jump diffusion. The significant initial drop in the three-dimensional calculation is in agreement with the prediction of equation 3.27 based on a simple factorization argument. In the two-dimensional calculation there is a negligible initial drop because ΔK is small.

alized Langevin Equation (GLE) in which the frictional force depends on the recent history of the velocity while the independent random noise source has a non-uniform power spectrum. One factor is conceptual: the LE is not physically realistic, as any physical heat bath has a finite response time and cannot supply impulses which are uncorrelated at arbitrarily short times. Experimentally, the effect of a finite memory time in the bath has an effect on lineshapes at short times (during the ballistic/diffusive transition), and the relative amplitude of different components on the ISF. Additionally, because the time taken to cross a barrier or traverse a well region in a corrugated potential is small, memory effects have an influence on the friction-controlled corrections to the transition-state-theory jump rate as discussed further in Section 4.5.1. In the present Section, new analytical results for the ISF of a particle diffusing on a flat surface subject to the GLE are derived, which explain analytically the phenomenology derived from simulation [28].

3.2.1 Background

In real systems the random impulses exerted by the bath (substrate) cannot have a white noise power spectrum. Whether or not the Langevin equation provides a good approximation to the dynamics depends on the physical mechanism of dissipation. For dissipation governed by electron-hole pair creation and annihilation, the Langevin description is plausible because the energy scale of the excitations (width of conduction band) is generally large compared to the typical energy scales associated with adsorbate diffusion (e.g. vibrational frequencies in adsorption sites). The electronic γ can be estimated from first principles [113]. By comparing the first-principles estimate with the value of γ required to match experimental results, the importance of other dissipation channels can be determined [25], assuming the Langevin description is adequate when all dissipation channels are included. However, phononic dissipation cannot generally be described via white noise, as demonstrated by molecular dynamics simulations of an adsorbate on a harmonic solid ([114], also see Section 3.3). Whenever bath excitations above a certain energy are inaccessible, it is reasonable to expect the noise power density to possess a cutoff frequency ω_c, above which the power density is zero or falls rapidly to zero. An arbitrary noise spectrum defines a Generalized Langevin Equation (GLE), which in one dimension reads:

$$m\ddot{x}(t) = -V(x) - \int^t m\gamma(t-t')\dot{x}(t')dt' + F(t)\,, \tag{3.28}$$

where $V(x)$ is a static potential energy landscape, $\gamma(t)$ is a causal function known as the friction kernel, and $F(t)$ is a self-correlated random force. In equilibrium, noise

and dissipation are linked by a fluctuation-dissipation relation [115] which generalizes the correlation function $\langle F(t)F(0)\rangle$ shown in the white-noise case 3.10. The fluctuation-dissipation relation, and prescriptions for the lower limit of the friction integral, will be specified in Section 3.2.2. The details of the friction kernel and the statistics of the associated noise are highly dependent on the specific system studied. However, there are many reasons to consider the effect of a simple analytic noise spectrum. For one thing, representing the friction kernel compactly with a small number of parameters means that the parameter space can be feasibly explored. Also, specific choices of the friction kernel can lead to greatly simplified analytical and numerical methods. The choice of an exponential kernel $\gamma(t) = \gamma\omega_c e^{-\omega_c t}$ is often the simplest choice, because its Laplace transform has only a single, simple pole. The Langevin equation corresponds to the limiting case $\omega_c \to \infty$. The exponential kernel appears in several analytical results concerning the effect of a cutoff frequency in equilibrium dynamics. In activated diffusion, ω_c has an impact on the jump rates, both in the moderate-to-high friction regime [116] and the energy diffusion limited regime [117]. However, there is an interplay between γ and ω_c such that knowledge about jump distributions is not especially diagnostic of γ or ω_c individually since they can to some extent be traded off against each other. The short-time behaviour of correlation functions is more sensitive to the exact kernel.

The effects of a finite ω_c can be seen in experimental measurements that quantify surface diffusion on all timescales, from the timescale of inter-well jumps down to the timescale of ballistic motion and intra-well diffusion. The ballistic-to-Brownian transition has been studied experimentally for mesoscopic particles in a liquid environment [118, 119], via the VACF. HeSE provides access to the analogous information on the atomic scale. The frictional coupling γ can be quantified by optimising the simulation to reproduce inelastic [120] or quasi-elastic [105] features in the experimental lineshapes.

3.2.2 Analytical results

3.2.2.1 Ensemble average formulation

I consider the GLE arising from a well-known type of linear system-bath Hamiltonian,

$$H = \frac{p^2}{2m} + V(x) + \sum_\alpha \left[\frac{p_\alpha^2}{2m_\alpha} + \frac{1}{2}m_\alpha\omega_\alpha^2(x_\alpha - \frac{c_\alpha x}{m_\alpha\omega_\alpha^2})^2\right], \tag{3.29}$$

which describes a particle of mass m linearly coupled via coefficients c_α to a large set of harmonic bath modes indexed α, with masses m_α and frequencies ω_α. H is known in the literature as the Caldeira-Leggett Hamiltonian, owing to its use in a

study of quantum Brownian motion [121] as well as dissipative tunneling problems [122]. The linearity of the coupling in x_α the Hamiltonian 3.29 is plausible because when a particle interacts with a large number of environmental degrees of freedom (modes), it can perturb each environmental mode very weakly even when being perturbed very strongly itself by the accumulated interaction with a large number of modes [122]. The use of a coupling linear in x is a more subtle assumption, but is justifiable because for any value of x, minimizing the total potential energy in 3.29 with respect to the bath co-ordinates returns $V(x)$, so in one sense periodicity with respect to the system co-ordinate is maintained. However, the corresponding values of x_α at which the potential is minimized are not periodic functions of x, which would be expected if the model Hamiltonian was rigorously derivable from a more fundamental description of the system and environment. More flexible system/bath coupling models including a periodic coupling have been considered in the context of atom/surface scattering in the presence of phonons [123, 124]. The issue of nonlinear coupling is discussed further in Section 3.3.2, but until then I assume the linear coupling form 3.29.

It turns out that the Hamiltonian 3.29 leads directly to a GLE, and therefore using the Hamiltonian as a starting point is equally justifiable as working from the phenomenological GLE (3.28) itself. The GLE follows from Hamilton's equations of motion (3.7) applied to the model Hamiltonian 3.29. The derivation is a special case of the working leading to Equation 3.83 in Section 3.3.2, and found in textbooks on the subject [30], so is not reproduced here. The particle co-ordinate x obeys

$$m\ddot{x}(t) = -V'(x) - \int_0^t m\gamma(t-t')\dot{x}(t')dt' + F(t)\,, \tag{3.30}$$

where the friction kernel is given by

$$\gamma(t) = \sum_\alpha \frac{c_\alpha^2}{m_\alpha \omega_\alpha^2}\cos(\omega_\alpha t) \tag{3.31}$$

and the fluctuating force is given by

$$F(t) = m\sum_\alpha \left[c_\alpha\Big(x_\alpha(0) - \frac{c_\alpha x(0)}{m_\alpha\omega_\alpha^2}\Big)\cos(\omega_\alpha t) + \frac{p_\alpha(0)}{m_\alpha\omega_\alpha}\sin(\omega_\alpha t)\right] \tag{3.32}$$

which is random because the initial conditions $\{x_\alpha(0), p_\alpha(0)\}$ are drawn from an initial probability distribution. When the initial distribution represents that of thermal equilibrium, the random force is found to be Gaussian, and have the fluctuation-dissipation property

$$\langle F(t)F(0)\rangle = mk_BT\gamma(t)\,, \tag{3.33}$$

where the angle brackets represent the canonical average over all possible initial states of the bath. Correlation functions such as $\langle F(t)F(0)\rangle$ can be calculated by setting $t = 0$ as a reference time, and calculating averages based on forward evolution of the system from its initial thermal state. The results are independent of the choice of reference time. Assuming a constant density of bath modes in ω_α, the couplings c_α can be specified in a straightforward way to construct an exponential kernel, namely

$$c_\alpha^2 \propto \frac{\omega_\alpha^2}{\omega_\alpha^2 + \omega_c^2}\,, \tag{3.34}$$

as can be verified by writing 3.31 in integral form. In other words, the global Hamiltonian can be parameterized in terms of the cutoff frequency, lending a secondary interpretation to ω_c.

We can derive $I(\Delta K, t)$ for an adsorbate in a one dimensional harmonic well of frequency Ω, for which the GLE reads

$$m\ddot{x}(t) = -\Omega x(t) - \int_0^t m\gamma(t-t')\dot{x}(t')dt' + F(t). \tag{3.35}$$

Following [125] we write the ISF as a cumulant expansion to the lowest order. The cumulant expansion relies on the exact relationship between the mean square of a Gaussian-distributed variable y, and the expectation of its complex exponential:

$$\langle e^{i\Delta K y}\rangle = \exp(-\Delta K^2\langle y^2\rangle)\,. \tag{3.36}$$

The result can be applied to the ISF by writing

$$y(t) = x(t) - x(0)\,, \tag{3.37}$$

and noticing that

$$x(t) - x(0) = \int_0^t dt'\, v(t')\,, \tag{3.38}$$

which upon squaring and ensemble-averaging becomes

$$\langle [x(t) - x(0)]^2\rangle = \int_0^t dt' \int_0^t dt''\, \langle v(t')v(t'')\rangle\,. \tag{3.39}$$

Using the time-symmetry of the VACF $\Psi(t) = \langle v(t)v(0)\rangle$, the result simplifies to a single integral,

$$\langle [x(t) - x(0)]^2\rangle = \int_0^t (t-t')\Psi(t')dt'\rangle\,. \tag{3.40}$$

The cumulant expansion for the ISF to lowest order is therefore

$$I(\Delta K, t) = \exp\Big(- \Delta K^2 \int_0^t (t - t')\Psi(t')dt' \Big) . \tag{3.41}$$

The cumulant expansion is exact for flat and harmonic potentials because the probability density for the particle position $x(t)$ is Gaussian at all times, and therefore the conditional probability density is Gaussian. An alternative demonstration of the cumulant expansion is provided in Chapter 4 which makes use of the fact that $x(t)$ can be written as a linear combination of global normal modes.

Within the canonical system-plus-reservoir framework, it is straightforward to prove the absence of certain correlations:

$$\langle F(t)v(0)\rangle = \langle x(t)v(0)\rangle = 0. \tag{3.42}$$

Because such correlations vanish, Laplace-transforming 3.35 yields the simple result

$$\hat{\Psi}(s) = \frac{k_B T/m}{s + \hat{\gamma}(s) + \Omega^2/s}. \tag{3.43}$$

which can be inverted using the Bromwich integral [106], as long as we can find the roots of the denominator. Now we introduce the exponential friction kernel

$$\gamma(t) = \theta(t)\gamma\omega_c e^{-\omega_c t} \tag{3.44}$$

with Laplace transform

$$\hat{\gamma}(s) = \frac{\gamma\omega_c}{s + \omega_c} \tag{3.45}$$

such that the Laplace transform of the VACF becomes

$$\hat{\Psi}(s) = \frac{s(s + \omega_c)k_B T/m}{s^3 + \omega_c s^2 + (\gamma\omega_c + \Omega^2)s + \Omega^2\omega_c} . \tag{3.46}$$

The exact inversion of $\hat{\Psi}(s)$ as specified here would be a natural starting point for an analytical investigation of the dissipation-induced broadening of inelastic lineshape features, in the presence of memory friction. Here we focus entirely on quasielastic features on the flat surface $\Omega = 0$, in which case all the poles of the denominator have negative real part and the Bromwich integral [106] can be applied straightforwardly with an integration contour consisting of the imaginary axis $\mathcal{IA}$ and a semicircle to the left of $\mathcal{IA}$. The denominator has two roots s_k which are the solutions of

$$s^2 + \omega_c s + \gamma\omega_c = 0 . \tag{3.47}$$

The Bromwich formula yields

$$\Psi(t) = \frac{k_B T}{m}\Big[p_1 e^{-s_1 t} + p_2 e^{-s_2 t}\Big], \tag{3.48}$$

where

$$p_1 = \frac{(s_1 + \omega_c)}{s_1 - s_2} \;;\; p_2 = \frac{(s_2 + \omega_c)}{s_2 - s_1}\,. \tag{3.49}$$

The inversion could alternatively be carried out using the ansatz of a biexponential VACF and matching coefficients after the forward Laplace transform. Integrating 3.48 according to the prescription in the cumulant expansion method, we arrive at the ISF in a product form:

$$I(\Delta K, t) = \prod_{k=1}^{2} \exp\Big(- \Delta K^2 \frac{k_B T}{m} \frac{p_k}{s_k}\Big[e^{-s_k t} + s_k t - 1\Big]\Big)\,. \tag{3.50}$$

Each factor in the product has the same collapsing-exponential form as the Langevin flat surface result, which can be recovered by setting $\omega_c \to \infty$.

Inserting explicit expressions for the roots of 3.47 yields for the ISF the closed form $I(\Delta K, t) = \exp[-\Delta K^2 X(t)]$ with

$$X(t) = \frac{k_B T}{m\gamma^2}\Big(\frac{\gamma}{\omega_c} - 1 + \gamma t + \frac{e^{-\omega_c t/2}}{\omega_c}[C\cosh(\omega' t) + S\sinh(\omega' t)]\Big) \tag{3.51}$$

where the coefficients C and S are given by

$$C = \omega_c - \gamma; \tag{3.52}$$

$$S = \frac{\sqrt{\omega_c}(\omega_c - 3\gamma)}{\sqrt{\omega_c - 4\gamma}}\,, \tag{3.53}$$

and the frequency scale ω' mixes the two basic frequency scales of the problem ω_c and γ in the following way -

$$\omega' = \frac{1}{2}\sqrt{\omega_c^2 - 4\gamma\omega_c}\,. \tag{3.54}$$

ω' becomes complex unless the cutoff frequency ω_c is at least four times faster than the basic 'strength' of the friction γ. The classical ISF remains real at all times.

We now compare GLE lineshapes for increasing values of the memory time. The results are plotted in Figure 3.3. The most readily apparent feature is an enhanced initial decay relative to the long-time exponential form. The suppression of the long time tail in the presence of memory is due to the presence of a faster-decaying factor in the general product expression 3.50. However, the decay rate of the slowest-

decaying factor at long times is unchanged by the memory. To be more concrete about the suppression of the long time tail, we note that the long time limit of the Langevin result is

$$I(\Delta K, t \to \infty) = \exp\Big(- \Delta K^2 \frac{k_B T}{m\gamma^2}\Big) \exp(-\gamma t)\,, \tag{3.55}$$

but in the present case with the inclusion of memory friction, the expression is modified to

$$I(\Delta K, t \to \infty) = \exp\Big(- \Delta K^2 \Big[\frac{k_B T}{m\gamma^2} - \frac{k_B T}{m\gamma\omega_c}\Big]\Big) \exp(-\gamma t)\,. \tag{3.56}$$

From these two forms we conclude that the GLE ISF in the long time limit is smaller than the corresponding LE ISF by the constant factor

$$\exp\Big(- \Delta K^2 \frac{k_B T}{m\omega_c\gamma}\Big). \tag{3.57}$$

The effect is illustrated in Figure 3.3, which shows the GLE and LE results normalized to each other at long times, for a range of memory frequencies ω_c. A notable consequence of the equality of the long-time decay rate for different ω_c is that the diffusion coefficient is independent of ω_c too, which I now show in one dimension. The diffusion coefficient is defined via the time evolution of the root mean square distance travelled, which can be derived from the classical ISF 3.3 by differentiation in ΔK:

$$\Big[- \frac{\partial^2}{\partial \Delta K^2} I(\Delta K, t)\Big]_{\Delta K \to 0} = \langle [x(t) - x(0)]^2 \rangle. \tag{3.58}$$

When the ISF at long times is Gaussian in ΔK and exponential in t, $\langle [x(t) - x(0)]^2 \rangle$ is dominated at long times by a term linear in t, which defines the particle motion as being diffusive. Writing the long time limit of the ISF as

$$I(\Delta K, t) = \exp\Big(- \Delta K^2 \frac{k_B T}{m\omega_c\gamma}\Big) e^{-\alpha \Delta K^2 t}, \tag{3.59}$$

where α is independent of ω_c, it follows that the constant of proportionality in $\langle [x(t) - x(0)]^2 \rangle \propto t$ at long times is simply α. Since α is independent of ω_c, so is the diffusion coefficient. Therefore the well-known diffusion coefficient 3.13 for Brownian motion, which holds for the Langevin equation with friction γ, also applies for the GLE with friction γ and arbitrary cutoff frequency.

A feature of the cases where $\omega_c < 4\gamma$, which is less visually obvious in Figure 3.3 is the set of oscillations due to the complex ω', which occurs even though there is no confining potential $V(x)$. The oscillations are a known phenomenon from GLE simulations [126], and are a prominent feature of the VACF, as will be seen in

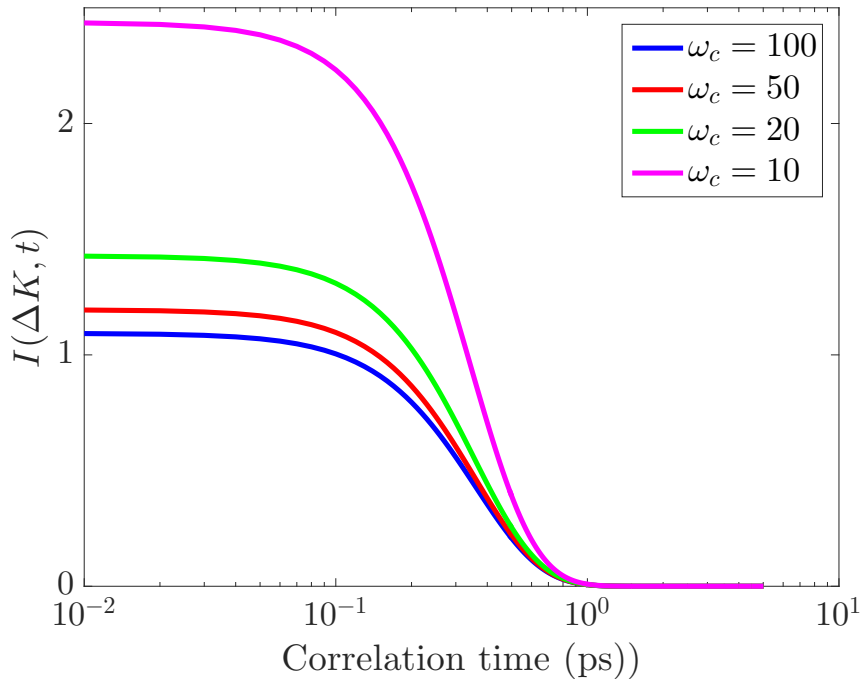

Figure 3.3: A series of analytic GLE lineshapes given by Equation 3.50, normalised to each other at long times, where they all lie on top of each other. At increasingly small values of ω_c, the relative amplitude of the remaining part of the lineshape increases in accordance with the factor 3.57. The memory time $\tau = \omega_c^{-1}$ was varied as shown in the Figure legend; the constant parameters were $m = 7\,\text{amu}$; $\Delta K = 1.0\,\text{Å}^{-1}$, $T = 150\,\text{K}$, $\gamma = 2\,\text{ps}^{-1}$.

Section 3.2.3. However, the effect is subtle in the ISF because the integration and exponentiation steps in the cumulant expansion both smooth out the oscillations.

3.2.2.2 Time average formulation

I now consider a GLE in which the memory properties, and the correlations of the fluctuating force, are expressed in the Fourier domain via a causal friction kernel and a fluctuation-dissipation theorem in terms of the power spectrum of the random force. Correlation functions can be expressed as time averages, and constructed via the Wiener-Khinchin theorem. I start from

$$m\ddot{x}(t) = -m\int_{-\infty}^{t} dt'\gamma(t-t')\dot{x}(t') + F(t) \tag{3.60}$$

where now the time integration extends to $-\infty$ and the random force has the power spectrum

$$\tilde{F}(\omega) = 2mk_BT\tilde{\gamma}'(\omega) \tag{3.61}$$

where $\tilde{\gamma}'(\omega)$ is the real part of the friction kernel, and the random force is Gaussian for consistency with the Hamiltonian model in 3.2.2.1. To find the velocity correla-

tion $\langle v(t)v(0)\rangle$ by time averaging, we construct $|\tilde{v}(\omega)|^2$ and make use of the power spectrum of the fluctuating force. Using the convention $\tilde{g}(\omega) = \int dt e^{i\omega t} g(t)$ for the forward Fourier transform, the power spectrum of the velocity becomes:

$$m^2|\tilde{v}(\omega)|^2 = \frac{2mk_BT\tilde{\gamma}'(\omega)}{|\tilde{\gamma}(\omega) - i\omega|^2}. \tag{3.62}$$

After introducing the exponential kernel, we arrive at

$$m^2|\tilde{v}(\omega)|^2 = \frac{2mk_BT\gamma\omega_c^2}{\omega^4 + \omega^2(\omega_c^2 - 2\gamma\omega_c) + \gamma^2\omega_c^2}. \tag{3.63}$$

There are four poles in the complex ω plane, of which two contribute residues in any specific Fourier inversion. We now perform the Fourier inversion assuming $t > 0$. Denoting the roots of

$$\omega^4 + \omega^2(\omega_c^2 - 2\gamma\omega_c) + \gamma^2\omega_c^2 = 0 \tag{3.64}$$

as ω_k and labelling them such that the first two roots (ω_1,ω_2) have negative imaginary part, the Fourier inversion

$$\langle v(t)v(0)\rangle = \frac{1}{2\pi}\int d\omega e^{-i\omega t}|v(\omega)|^2 \tag{3.65}$$

can be expressed in terms of those poles, via the residue theorem [106], as

$$\langle v(t)v(0)\rangle = -2i\frac{k_BT\gamma\omega_c}{m(\omega_1 - \omega_2)}\Big[\frac{e^{-i\omega_1 t}}{(\omega_1 - \omega_3)(\omega_1 - \omega_4)} - \frac{e^{-i\omega_2 t}}{(\omega_2 - \omega_3)(\omega_2 - \omega_4)}\Big]. \tag{3.66}$$

The solutions of 3.64 satisfy $\omega^2 = -s^2$ where s solves 3.47. Because the solutions s_k derived in the Laplace case have negative real part, the ω_k can be written as

$$\omega_1 = is_1;\ \omega_2 = is_2;\ \omega_3 = -is_1;\ \omega_4 = -is_2\,. \tag{3.67}$$

Substituting the roots ω_k into the Fourier inversion formula, one finds that the correlation function $\langle v(t)v(0)\rangle$ (and therefore $I(\Delta K, t)$) calculated by the time averaging formalism is identical to the one calculated by ensemble averaging. In other words, the device of extending the friction integral to the infinite past, combined with the fluctuation-dissipation relation as given in 3.61 represents exactly the same dynamical equilibrium properties as those represented by Hamiltonian evolution of a system-with-reservoir in a thermal state at a reference time. A recent careful mathematical analysis of the GLE in the form 3.30 has shown that the process is ergodic (never becomes metastably trapped) and converges to equilibrium (the Gibbs

distribution)[127], and therefore the existence of alternative statements of the GLE in terms of time averages and initial-condition averages is not surprising.

In the present section I have derived analytic lineshapes within two equivalent formulations of the GLE. The physical interpretation in each case is rather different, in particular the way in which initial conditions of the system particle are handled. In the next Section, numerical GLE trajectories are inspected to give further physical insight into the way the ISF is influenced by memory friction.

3.2.3 Numerical simulation

In the present Section numerical simulations are performed on a flat surface to give further insight into the analytical results, and demonstrate the self-consistency of the numerical and analytical methods. I use a method that is particularly convenient for exponential friction kernels. The extended phase space method of Ceriotti was introduced originally as a method to enhance canonical sampling efficiency in a context where the molecular dynamics are fictitious [128, 129], but nevertheless correctly simulates dynamical properties. I will give a succinct account in Section 3.2.3 of how the method incorporates memory friction. Simulations of exponential memory friction have been performed previously to examine the effect of memory on escape from a well [130]. In contrast the present simulations are concerned with the ISF at short correlation times, comparison between simulation and analytical theory, and the interpretation of the lineshape in terms of the realizations of the GLE generated by the simulation method.

Ceriotti's method [128, 129] was originally presented in a matrix formalism which allows for multi-exponential kernels; here I expand the relevant special case of an exponential kernel explicitly and show that it reproduces the GLE 3.60. Suppose our physical variable $x(t)$ is coupled to the motion of a fictitious velocity variable $p(t)$ which undergoes a Langevin process. To simplify the derivation, the potential $V(x)$ is neglected; it is simply 'carried through' when present, i.e. contributes $-V'(x)$ to the total force. The appropriate coupled equations for an exponential friction kernel are:

$$m\ddot{x}(t) = \sqrt{\gamma\omega_c}mp(t)\,; \tag{3.68}$$

$$m\dot{p}(t) = -\sqrt{\gamma\omega_c}m\dot{x}(t) - \omega_c mp(t) + \sqrt{2mk_BT\omega_c}R(t)\,, \tag{3.69}$$

where $R(t)$ is a normalised white noise source. To prove that the simulation prescription achieves the GLE 3.60, we transform the coupled equations to the Fourier

domain and eliminate the fictitious variable, and obtain:

$$m\dot{v}(t) = -m\int_{-\infty}^{t}\gamma(t-t')v(t')dt' + \omega_c\sqrt{2mk_BT\gamma}\,\mathcal{F}^{-1}\Big[\frac{\tilde{R}(\omega)}{\omega_c - i\omega}\Big] \tag{3.70}$$

where the power spectrum of the final term has the correct frequency dependence to satisfy the fluctuation-dissipation relation.

To benchmark the simulation, the ISF is simulated on a flat surface. A numerical method for simulating the GLE was developed previously in the language of digital filters [28]; the implementation used here uses a more traditional approach. The coupled equations 3.68 and 3.69 were solved using a velocity Verlet integrator. The remaining simulation parameters are $\gamma = 2.0\,\mathrm{ps}^{-1}$, $\omega_c = 1.0\,\mathrm{ps}$, $T = 150\,\mathrm{K}$, $m = 7\,\mathrm{amu}$. The resulting simulated lineshape at $\Delta K = 1.0\,\mathrm{\AA}^{-1}$ is shown in Figure 3.4, with the analytic result overlaid, showing good agreement. The ISF computed from the simulated trajectories was not constructed via the cumulant expansion, but directly from the definition 3.3. The simulations were performed for 100 particles with a timestep of 1 fs, for a total simulation time of 1 ns. The relatively long simulation time means we expect the boundary effects of the finite time domain to be negligible, but additionally a padding scheme was used to ensure we calculate the linear, not the cyclic correlation, when applying the discrete Wiener-Khinchin theorem. Similarly, the initial conditions were generated with a short 'pre-thermalization', but the simulation is much longer than the thermalization period, such that the exact nature of the pre-thermalization is not important.

The choice of simulation parameters is motivated by the promise of Li/Cu(111) as an experimental system whose lineshapes could display the enhanced ballistic phenomenology derived in the present work, due to the low diffusion barrier and the simple scattering form factor [28]. By simulating with $\omega_c < \gamma$ we are very far away from the Markovian limit, in other words the VACF displays significant oscillations. The analytic and simulated VACF are in good agreement and are plotted together in Figure 3.5.

The VACF provides some insight into the physical effects of memory friction. However, it would be desirable to directly explain the main features of the ISF in terms of the qualitative features of simulated trajectories. The key fact we would like to explain is that the amplitude of the long-time diffusive component in the ISF is reduced in the presence of memory, while the corresponding rate is unchanged. That result can be explained by direct comparison of simulated GLE trajectories that are equivalent in all respects other than the memory time. That is, two trajectories simulated in parallel using the same initial conditions and the same white noise, but differing in the way the extended phase space formulation filters the noise. A typical

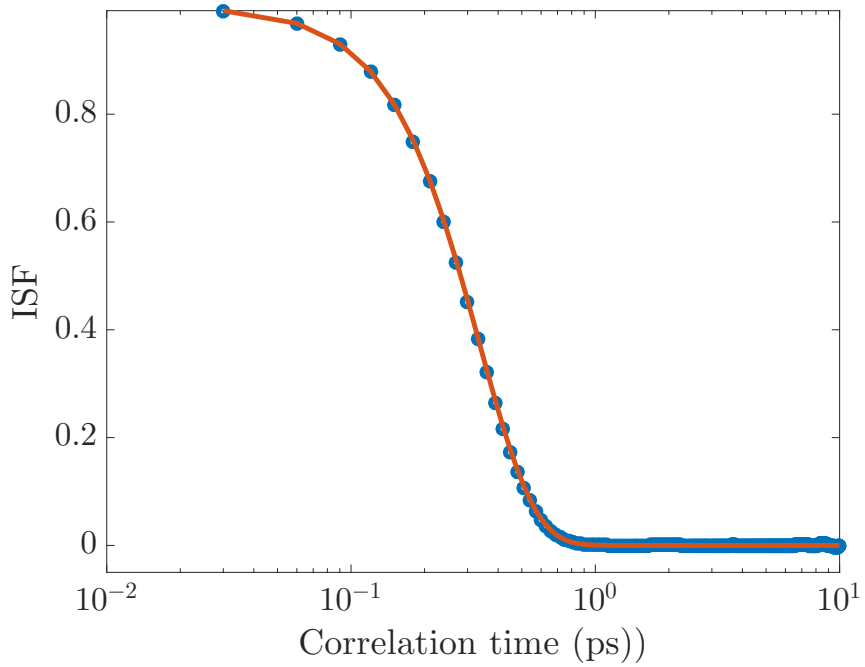

Figure 3.4: Simulated ISF (points) on the flat surface, at$\Delta K = 1.0\,\text{Å}^{-1}$. The key simulation parameters are $\gamma = 2.0\,\text{ps}^{-1}$, $\omega_c = 1.0\,\text{ps}^{-1}$, such that $\omega_c < \gamma$, namely we are well into the regime where memory is important. The analytic line is overlaid and shows good agreement with the simulation results. Additional simulation parameters are specified in the main text.

trajectory in a one-dimensional simulation is shown in Figure 3.6, over the course of a 20 ps time window, and compared with a 'Langevin' trajectory ($\omega_c = 500$). When memory is important, the effect of the GLE is to transform the Langevin trajectory with a low-pass filter. The GLE $\omega_c = 1.0\,\text{ps}^{-1}$ trajectory therefore tracks the Langevin trajectory over a long timescale, and the diffusion coefficient is unchanged by the introduction of memory. However, the lack of high-frequency components in $x(t)$ means that on short timescales, the GLE dynamics are closer to ideal ballistic motion, in comparison to the LE dynamics, an observation which is mathematically formalised by the reduced amplitude of the long-time diffusive component in an ISF normalised to unity. An x, y trajectory plot for a two-dimensional simulation provides an alternative visualization of the smoothing effect of memory friction [28].

3.2.4 Conclusions

Analytical ISFs have been derived for a classical adsorbate obeying a GLE on a flat surface with exponential memory friction. The expression is a product form, where each factor has the structure of the equivalent result for the Langevin equation (memory-free). Compared to the Langevin result, the diffusive tail in the long time limit is reduced, while its rate is unchanged. The relative amplitudes in the lineshape

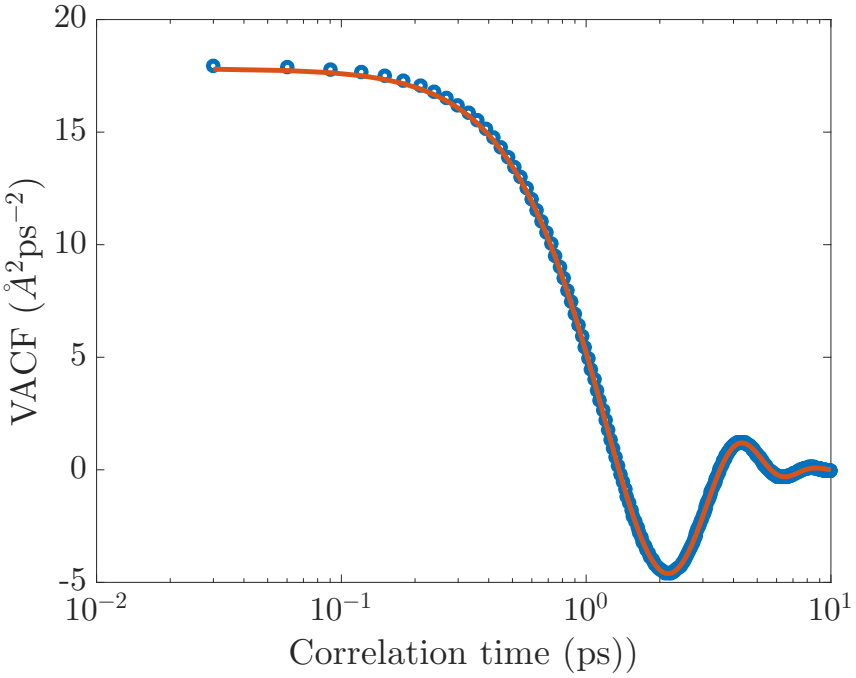

Figure 3.5: Simulated VACF (points) on the flat surface, with $\gamma = 2.0\,\mathrm{ps}^{-1}$, $\omega_c = 1.0\,\mathrm{ps}^{-1}$. There are obvious oscillations due to memory friction.

can be understood qualitatively on the basis of the suppression of high frequency components in $x(t)$ by the GLE with a finite memory time.

3.3 MD vs GLE

Adsorbate/surface dynamics are not often modelled by many-body adsorbate/slab simulations, due to the higher computational cost. However, many-body simulations can provide insight into the connection between conservative dynamics of large closed systems, and the dissipative dynamics of a selected particle (the adsorbate). Recently the connection was investigated via a coarse-grained approach [131], which showed that the simple Langevin model with a temperature dependent friction coefficient $\gamma(T)$ could faithfully reproduce the jump dynamics derived from slab simulations. Here I present a more microscopic approach to the comparison in which the non-Markovian nature of the friction kernel is accounted for. I briefly outline the directions along which a semi-analytical derivation of the friction kernel could proceed.

3.3.1 Many-body molecular dynamics simulations

Although the exponential friction kernel is a convenient model and achieves the purpose of representing a memory time, it is not guaranteed to be quantitatively

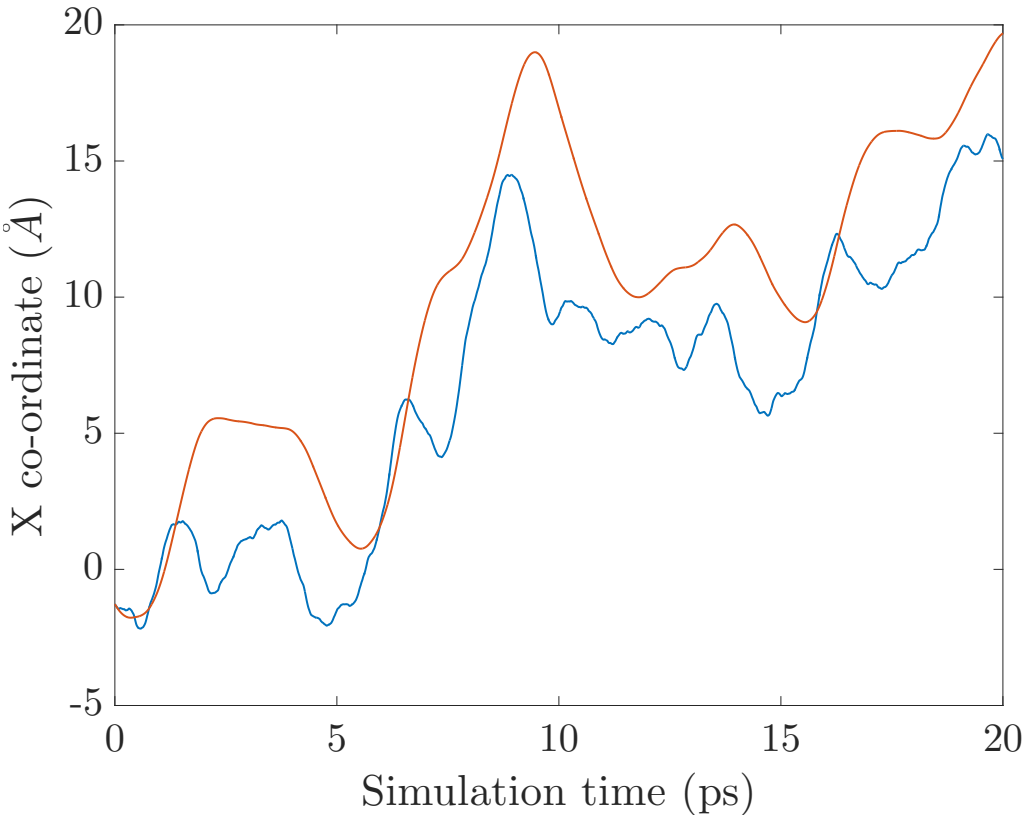

Figure 3.6: A 20 ps extract of two one-dimensional trajectories on a flat surface. The friction strength is $\gamma = 2\,\mathrm{ps}^{-1}$, with memory times of 1 ps (blue) and 0.02 ps (red). The case $\omega_c >> \gamma$ corresponds to the Markovian limit. As expected on the basis of the Fourier-space statement of the GLE, the trajectory simulated with a long memory time (low cutoff frequency) is a filtered (smoothed) version of the Langevin trajectory. An x, y trajectory plot for a two-dimensional simulation provides an alternative visualization of the smoothing effect of memory friction [28].

realistic when compared to many-body molecular dynamics (MD) simulations of surface diffusion in which susbtrate nuclear degrees of freedom are treated explicitly. In one study of the connection between many-body MD and the GLE, the friction kernel was extracted by fixing the adsorbate position at a barrier top and measuring the autocorrelation of the force on the adsorbate as the substrate evolves in time [114]. The resulting friction kernel is approximately time-local but has an oscillating tail, and its Fourier transform is peaked around a nonzero frequency. Oscillations in the friction kernel are not a surprise given the Bessel-function friction kernel that applies to the terminal particle in a finite harmonic chain [30]. In the analytic model, oscillations in time can be equated with a hard cutoff in ω induced by the finite maximum vibrational frequency in a harmonic chain.

In the present subsection I decompose the results of a many-body simulation into a systematic force $-\nabla V(\mathbf{R})$ and a residual ("non-adiabatic") force, and compare the power spectrum of the non-adiabatic force to a GLE simulation on the same potential of mean force $V(\mathbf{R})$. The model system Na/Cu(001) was chosen for the simulation because parameters have previously been found which reproduce the experimental atom/surface potential realistically using a simple pairwise Morse model for the adsorbate/substrate interaction, and pairwise harmonic interactions for the internal interactions in the substrate [112]. Explicitly, the potential energy of the many-body system can be written in terms of a substrate mass m_{Cu}, spring constant k_s and nearest neighbour equilibrium separation r_{NN}, an adsorbate mass m_{Na} and interaction parameters a, D_e and r_e defining the Morse interaction potential

$$V_M(r) = D_e(1 - e^{-a(r-r_e)})^2 \,. \tag{3.71}$$

The Morse interaction potential has an attractive well and a short-range repulsive region. D_e is the depth of the minimum in $V(r)$ at $r = r_e$. The parameter a controls the curvature of the potential minimum.

The numerical values of the substrate-substrate and adsorbate-substrate interaction parameters are given in Table 3.1. The global potential energy is then given in terms of the three-dimensional position vectors of the substrate $\{\mathbf{r}_i\}$ and of the adsorbate $\mathbf{r}_a$ by the sum

$$V(\{\mathbf{r_i}\}, \mathbf{r_a}) = \sum_{i>j}^{N.N.} \frac{1}{2} k_s (r_{i,j} - r_{NN})^2 + \sum_{i}^{r_{a,i}<r_c} V_M(r_{a,i}) \,, \tag{3.72}$$

where $r_{i,j}$ is the distance between substrate atoms i and j, and $r_{a,i}$ is the distance between substrate atom i and the adsorbate. The labels on the first summation indicate that each interacting pair is counted only once, and that substrate atoms

Table 3.1: Interaction parameters associated with the many-body molecular dynamics simulation analysed in the present Section. Values are quoted in common units as given in [112].

$\mathbf{m_{Cu}}$	$\mathbf{k_s}$	$\mathbf{r_{NN}}$	$\mathbf{m_{Na}}$	$\mathbf{D_e}$	$\mathbf{r_e}$	$\mathbf{a}$	$\mathbf{r_c}$
63 a.m.u	28 N/m	2.55 Å	22.9 a.m.u.	135 meV	3.30 Å	0.875 $Å^{-1}$	$4r_{NN}$

beyond nearest-neighbour separation do not interact directly. The labels on the second summation indicate that substrate atoms outside of the cutoff radius r_c away from the adsorbate are not counted.

The adsorption sites which emerge in the many-body interacting system are four-fold hollows, separated by the close-packing distance $a = 2.55\,\text{Å}$. The adsorption sites form a square lattice, which can be seen in Figure 3.7a which shows a sample trajectory (top) along with a `vmd` visualization of the three-dimensional system simulated. The simulation was run at $T = 155\,\text{K}$. The temperature is defined by the initial conditions: at the start of each simulation run each particle was given an initial velocity taken from the Maxwell-Boltzmann distribution at temperature T. Before time-evolving the system, the small random velocity of the centre of mass of the simulation was subtracted to prevent drift, and the angular momentum about the centre of mass of the system was subtracted. Slab dimensions of $24 \times 24 \times 18$ conventional fcc unit cells were used (with periodic boundary conditions), at which point the coarse-grained jump diffusion properties defined by $\alpha(\Delta\mathbf{K})$ do not change noticeably with system size in x, y or z. The simulation was performed using the HOOMD-blue code[1] code [134], running on the University of Cambridge Wilkes cluster [135].

I define $\mathbf{R}$ as the two-dimensional projection of the adsorbate position vector $\mathbf{r}_a$, and then define the adiabatic potential $V(\mathbf{R})$ via

$$p(\mathbf{R}) \propto e^{-\beta V(\mathbf{R})} \tag{3.73}$$

which is the thermal equilibrium condition that would be produced by the GLE, i.e. Equation 3.30 generalized to two spatial dimensions. It follows that

$$V(\mathbf{R}) = -k_B T \ln(p(\mathbf{R}))\,. \tag{3.74}$$

The distribution $p(\mathbf{R})$ is obtained by wrapping all particle positions into a single unit cell and making a two-dimensional histogram $p(x, y)$. The resulting $V(\mathbf{R})$ and a low-order Fourier fit are shown in Figure 3.8.

[1] A highly parallel, GPU-based code was chosen for reasons of speed, allowing the simulation of moderately large systems. The standard output format of the molecular dynamics program was converted to a more convenient form for analysis, using `ProDy` [132] and Scientific Python [133].

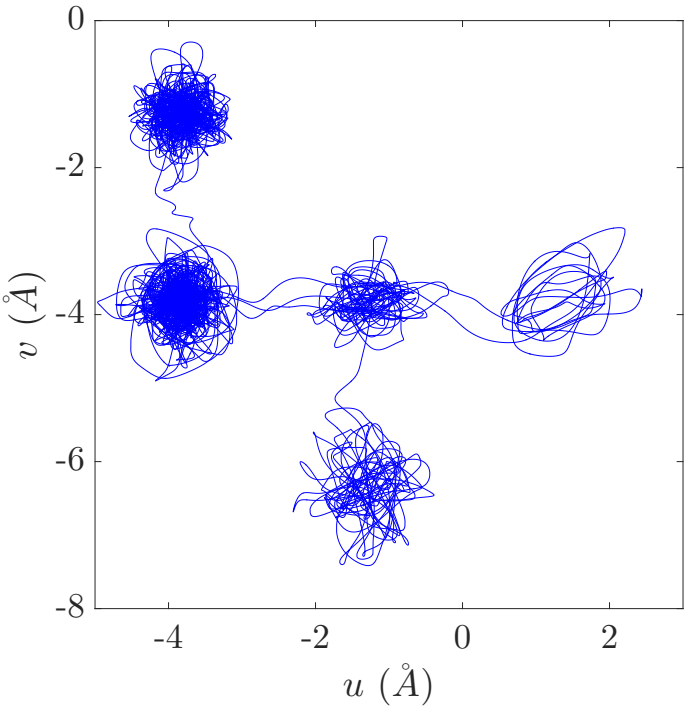

(a) Trajectory simulated by many-body (adsorbate/slab) MD.

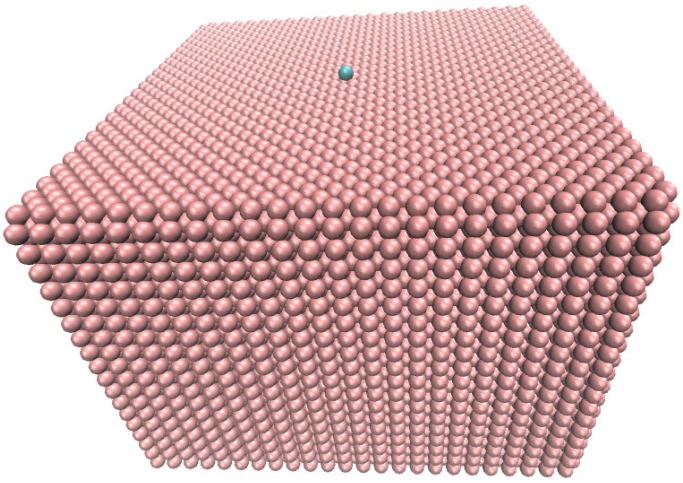

(b) Representation of the many-body system.

Figure 3.7: Figure 3.7a: a sample trajectory from adsorbate/slab conservative many-body MD, illustrating jump diffusion and the square symmetry of the surface. Figure 3.7b: visualization of the simulated system, produced using `vmd` [136].

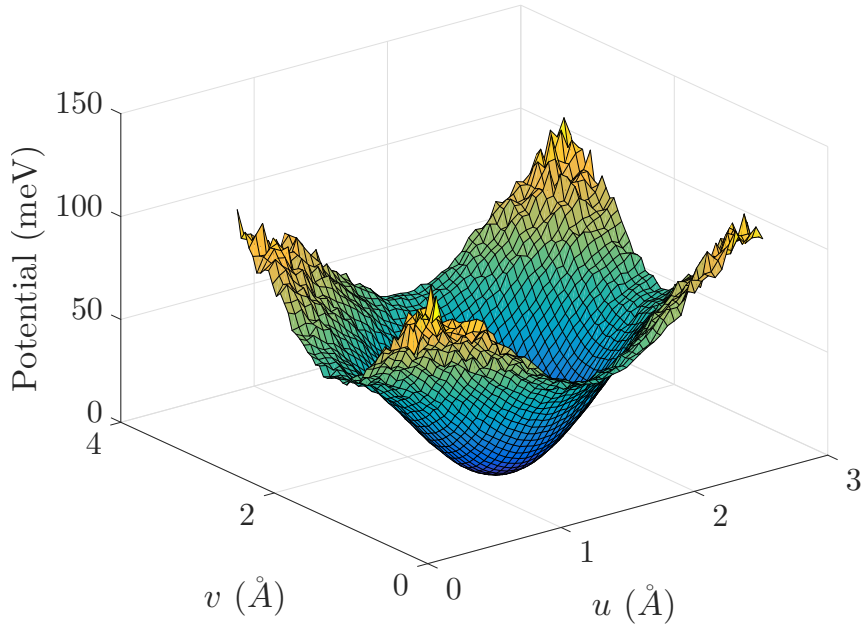

(a) Numerical adiabatic potential derived from adsorbate/slab simulation.

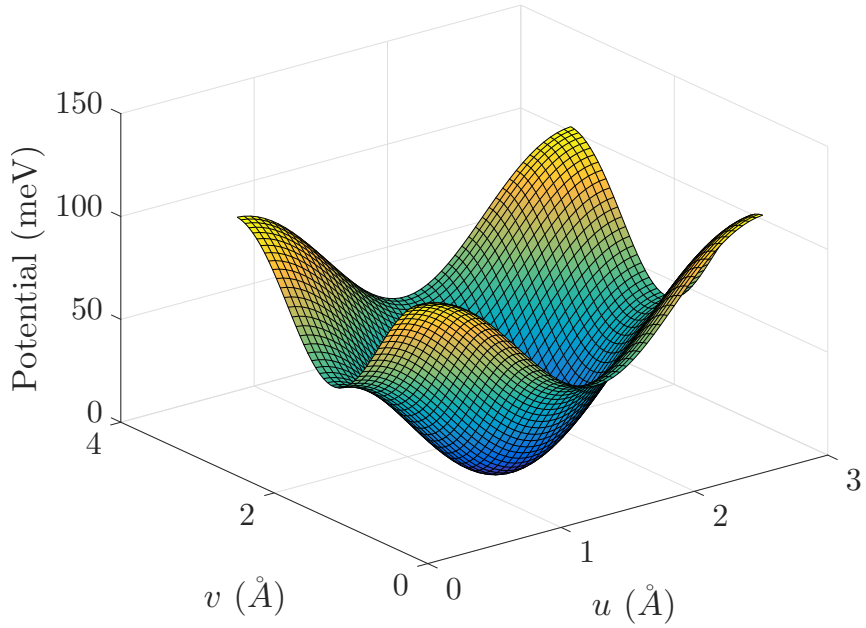

(b) Adiabatic potential fitted to a low-order Fourier series.

Figure 3.8: Upper figure: the adiabatic potential derived from a canonical molecular dynamics simulation by applying Equation 3.74 to the average spatial distribution $p(\mathbf{R})$. The spatial distribution is constructed out of co-ordinates wrapped into a single unit cell using a bivariate histogram. The lower plot shows a Fourier fit to the potential with components up to third order. The only significantly noisy region of the derived potential is around the top site.

Once a smooth adiabatic potential is constructed, it can be subtracted from the total force. Here I will call the result of the subtraction the non-adiabatic force. In the GLE the non-adiabatic force is the sum of a frictional force and a random force. Figure 3.9a shows a short sample of the nonadiabatic force in the u direction. A key feature of the nonadiabatic force derived from the many-body MD is that it is smooth on a timescale much longer than the simulation timestep. For comparison, the results of a GLE simulation over the derived potential energy surface, with a friction strength of $\gamma = 1.0\,\mathrm{ps}^{-1}$ and a relatively short memory time of $\tau = 0.1\,\mathrm{ps}$, are also shown. The x, y components of the random force were generated independently and with the same statistics, and the friction is taken as isotropic. The same timestep (5 fs) was used in the GLE simulation as for as the many-body simulation. The GLE simulation was performed using the method benchmarked for a flat surface in Section 3.2.3, except that here the systematic force $-\nabla V(\mathbf{R})$ is included. In other words, the equation simulated is

$$m\ddot{\mathbf{R}} = -\nabla V(\mathbf{R}) - \int_{-\infty}^{t} dt' \gamma(t-t')\dot{\mathbf{R}}(t') + \mathbf{F}(t)\,. \tag{3.75}$$

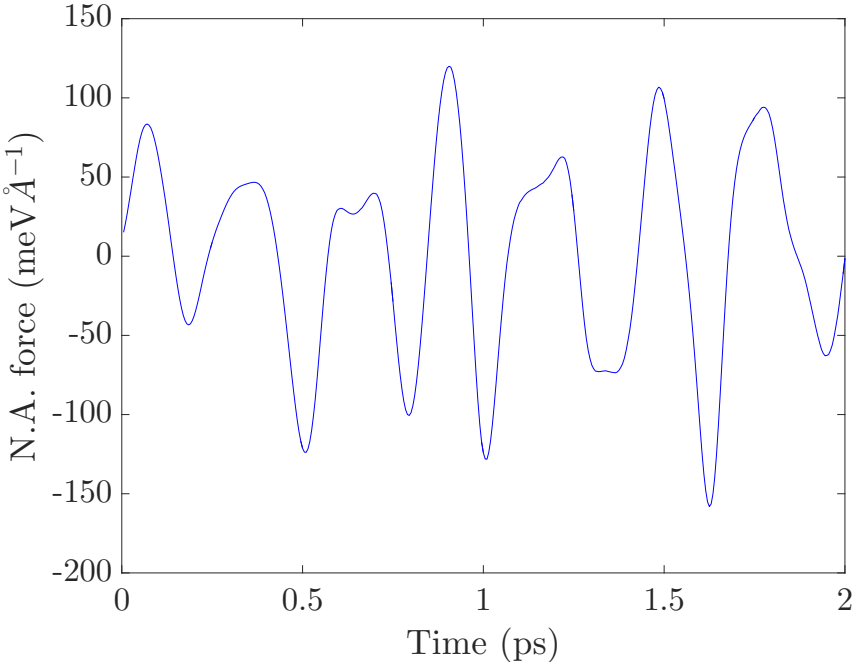

(a) Extract of nonadiabatic force from many-body MD simulation.

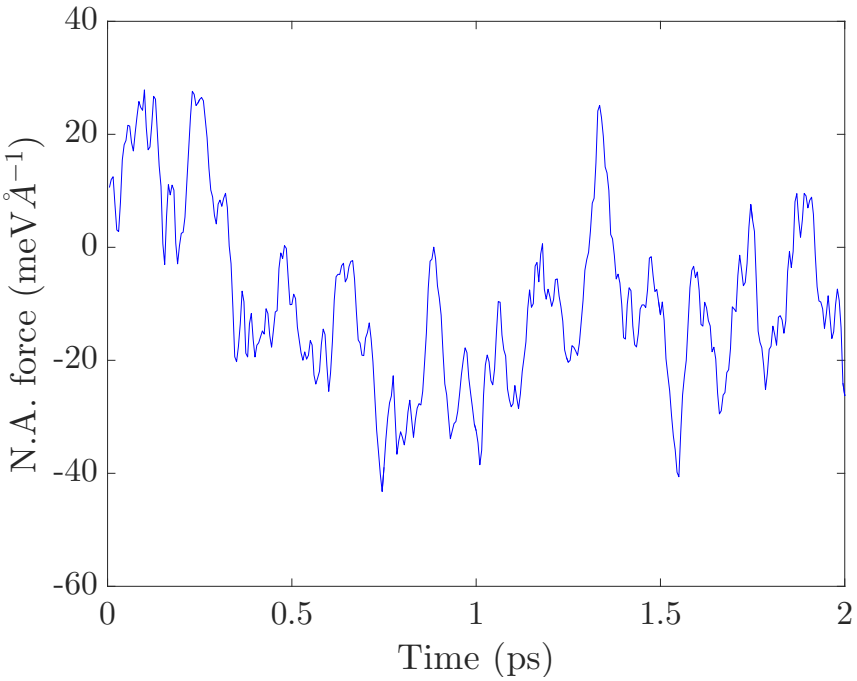

(b) Extract of nonadiabatic force from GLE simulation.

Figure 3.9: Short samples of the non-adiabatic force (frictional force plus random force) in the **x** direction. Figure 3.9a is from the many-body adsorbate/slab simulation. Figure 3.9b is derived from a GLE simulation on the adiabatic potential derived from the many-body MD simulation (Equation 3.74) at the same temperature (155 K) with a memory time $\tau = 0.1$ ps. The nonadiabatic force within the many-body MD simulation is smooth (self-correlated) on a timescale much longer than the timestep (5 fs).

To obtain the nonadiabatic force in Figure 3.9b, the GLE simulation data was analysed the same way as the many-body MD data, namely by subtracting the systematic force $-\nabla V(\mathbf{R})$. Qualitatively, the nonadiabatic force sample derived from the GLE simulation is smooth over many timesteps, but less smooth than the nonadiabatic force derived from the many-body MD. It is possible to be more quantitative by calculating the power spectra of the nonadiabatic force in each case.

Figure 3.10 shows the nonadiabatic force power spectrum in the frequency domain derived from the canonical MD simulation, in blue. The spectrum is the Fourier representation of $\langle F_x(t)F_x(0)\rangle$. Correlations of the form $\langle F_x(t)F_y(0)\rangle$ are negligible, and $\langle F_y(t)F_y(0)\rangle$ is equal to $\langle F_x(t)F_x(0)\rangle$ within noise. In order to understand the relationship between the power spectrum and an underlying effective GLE description, results are shown in red from the same GLE simulation represented in Figure 3.9. Both spectra show non-monotonic features, but the canonical MD is more structured and is more sharply cut off at high frequencies. The dashed red curve (scaled for clarity) is the analytical power density of the random force in the simulated GLE,

$$P(\omega) = mk_BT\gamma\frac{\omega_c^2}{\omega^2+\omega_c^2}\,. \tag{3.76}$$

The numerical power density derived from the GLE simulation (red points) contains a contribution from the random force and the friction. Interference between the two contributions causes a non-monotonic feature at low frequencies, but otherwise the power spectrum of the non-adiabatic force has the same smooth structure as the power density of the random force alone. Compared to the analytic and numerical GLE power spectra, the power density derived from the many-body simulation (blue points) is more structured (multiple broad features) and has a harder cutoff at high frequencies. The nonadiabatic force is not separated into a frictional and random component here, but the numerical comparison suggests that the frequency dependence of the friction kernel will have a similar structure to the power density of the nonadiabatic force. At least one contribution to the non-monotonic structure of the blue curve is likely to arise from the integration over z-motion, and therefore a logical step of further work would be to analyse the results of three-dimensional GLE simulations projected onto two-dimensions, just as has been done for the many-body simulation.

3.3.2 A more general microscopic model

As outlined in Section 3.2.2.1, a system/bath coupling linear in the system coordinate does not relate in any obvious way to coupling with lattice phonon modes,

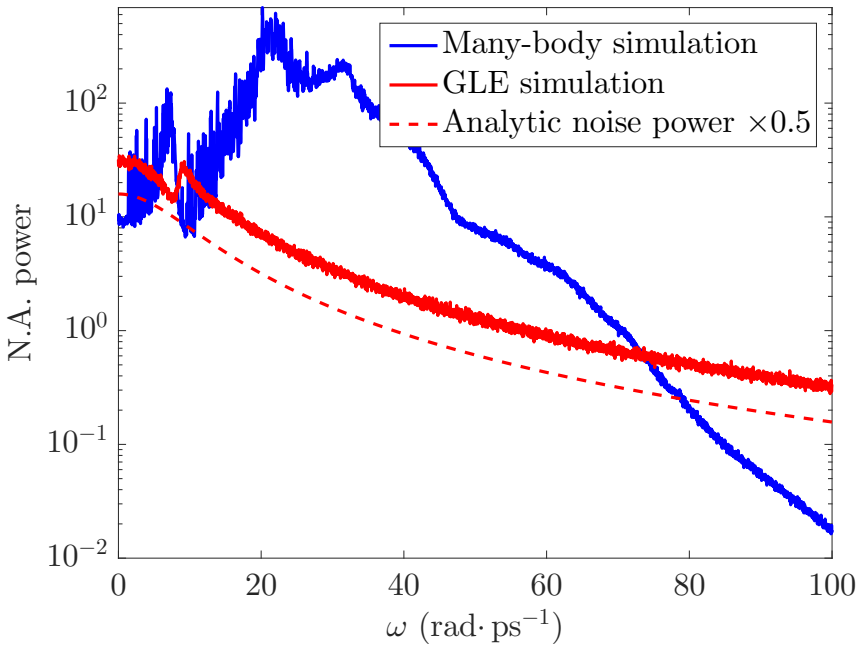

Figure 3.10: The nonadiabatic force power associated with a canonical MD simulation (blue points), and a GLE simulation (red points) over the equivalent adiabatic potential $V(\mathbf{R})$ (Equation 3.74). The nonadiabatic force is the sum of the frictional and random forces, which leads to a non-monotonic feature in the numerical GLE result, but otherwise the power spectrum derived from the GLE simulation follows the Lorentzian form of the analytical result 3.76. The analytical result is shown as a dashed red curve, scaled for clarity. Compared to the analytic and numerical GLE power spectra, the power density derived from the many-body simulation (blue points) is more structured (multiple broad features) and has a harder cutoff at high frequencies.

where the system/bath coupling, as well as the potential $V(x)$, might be expected to be periodic. As additional motivation, a deeper mathematical understanding of the relationship between the adsorbate/slab dynamics and the input parameters of the model is needed to progress the work of the previous section beyond the phenomenological stage. It is therefore worth considering to what extent the linear coupling model can be usefully generalized. Suppose a particle diffusing on a harmonic chain is represented by the Hamiltonian

$$H = \frac{p^2}{2m} + V(x) + \sum_k \frac{1}{2} m_k \omega_k^2 (x_k - \frac{c_k}{m_k \omega_k} F_k(x))^2 \,, \tag{3.77}$$

in which the coupling is nonlinear in the system co-ordinate. Caldeira and Leggett considered a Hamiltonian of the form 3.77 in their paradigm-setting work on dissipative tunneling, but specialised to the case of linear coupling for the purposes of detailed calculations. Periodic coupling functions have been considered (but not derived from an underlying global model) in the distinct physical context of atom/surface scattering [124, 123, 137] to model energy gain and loss distributions due to phonons. The present context of equilibrium surface dynamics is a little different to the problem of classical surface scattering, since the adsorbate and lattice cannot be assumed to be decoupled at some time in the past, or to only interact for a finite length of time.

Hamilton's equations of motion (as in 3.7) give the ordinary differential equations for x and x_k:

$$\ddot{x}_k = -\omega_k^2 x_k + \frac{c_k}{m_k} F_k(x) \,, \tag{3.78}$$

and

$$m\ddot{x} = -V'(x) + \sum_k F_k'(x) x_k - \sum_k \frac{c_k^2}{m_k \omega_k^2} F_k'(x) F_k(x) \,, \tag{3.79}$$

respectively. The solution of each individual bath mode evolution is

$$x_k(t) = x_k(0)\cos(\omega_k t) + \frac{p_k(0)}{m_k \omega_k}\sin(\omega_k t) + \frac{c_k}{m_k \omega_k}\int_0^t dt' \, \sin(\omega_k(t-t'))F_k[x(t')] \,. \tag{3.80}$$

Substituting the x_k solutions into the equation of motion for $x(t)$ gives a result that generalizes the Generalized Langevin equation 3.30. Defining

$$\gamma_k(t) = \frac{c_k^2}{m_k \omega_k^2}\cos(\omega_k t) \,; \tag{3.81}$$

$$\xi_k(t) = c_k[x_k(0)\cos(\omega_k t) + \frac{p_k(0)}{m_k \omega_k}\sin(\omega_k t)] \,, \tag{3.82}$$

the result is

$$\begin{aligned} m\ddot{x} = \; & -V'(x) - m\sum_k F_k'[x(t)] \int_0^t dt' \, \gamma_k(t-t') F_k'[x(t')]\dot{x}(t') \\ & + \sum_k F_k'[x(t)]\{\xi_k(t) - m\gamma_k(t) F_k[x(0)]\} \, . \end{aligned} \tag{3.83}$$

The first term on the right consists of the usual systematic force. The second term is the frictional force, which depends not only on the history of the velocity but on the history of a nonlinear function of position. The rest is the random force, which has a more complicated nonlinear form than in the standard GLE. The counter-term involving $x(0)$ is expected, as a comparable term appears in the linear case. Despite the new complexity, the random force must still be Gaussian when resolved onto any given position $x(t)$, because it can be written as

$$F(t) = \sum_k F_k'[x(t)]\{c_k[x_k(0) - \frac{c_k}{m_k\omega_k^2} F_k(x(0))] \cos(\omega_k t) + c_k \frac{p_k(0)}{m_k\omega_k} \sin(\omega_k t)\} \, , \tag{3.84}$$

which for fixed $x(t)$ is an expression linear in variables which are normally distributed at arbitrary initial time $t = 0$. However, when considered without position resolution, the x-dependence of the distribution will generally result in a non-Gaussian distribution of the noise. Another notable feature of the model 3.77 is the simultaneous linearity in bath co-ordinates and nonlinearity in particle co-ordinates, which breaks global translational invariance of the interaction. However, as shown in the following Section (3.3.3), the dynamics of the bath in the absence of the adsorbate involve long-range translations of individual particles in the bath, which suggests that the model makes more sense if long-range motion of the bath particles is disallowed (e.g. by including a local confining potential around lattice sites for each particle in the bath), which would break global translational invariance anyway.

3.3.3 Diffusion of tagged lattice particle

It has been shown [138] that any selected particle in a nearest-neighbour harmonic chain of equal mass particles undergoes a diffusive motion. Specifically, the VACF is given in terms of the mass m and the spring constant K by

$$\Psi(t) = \frac{k_B T}{m} J_0(2t\sqrt{\frac{K}{m}}) \, . \tag{3.85}$$

The diffusion coefficient is the time integral of $\Psi(t)$ [115],

$$D = \int_0^\infty \Psi(t) dt = \frac{k_B T}{m\omega_D} \, , \tag{3.86}$$

where ω_D has been defined as $2\sqrt{K/m}$. The diffusivity is that of a Brownian particle of mass m subject to a Langevin friction ω_D (i.e. replace γ with ω_D in Equation 3.13). If an adsorbate was attached to a fixed substrate atom, the implication is that it would be carried along in a diffusive motion even in the absence of hopping. The effect of tracer substrate atom diffusion on spin echo data has not been analysed. Diffusion of the adsorption sites could be a serious source of difficulty when trying to map a very large adsorbate-plus-slab simulation onto a GLE, because the assumption of an interaction which is linear in the bath co-ordinates is not self-consistent unless the bath motion is confined to small oscillations about lattice sites. Investigations of the system size-dependence of the fitted GLE description (potential and friction kernel) with simulation size would therefore be worthwhile, and the principles could be illustrated numerically for very long one-dimensional chains.

3.3.4 Conclusions

The output of a many-body adsorbate-plus-slab simulation has been analysed in terms of a systematic average force, and the fluctuating residual force which within the GLE framework is made up of friction and noise. The power spectrum of the residual force is highly structured in the frequency domain, compared to the power spectrum associated with a GLE simulation with an exponential friction kernel. Attention is drawn to a general microscopic model that could be used to model adsorbate-slab simulations and construct a semi-analytical connection with the GLE. However, the model cannot account for lattice-site diffusion, which should be investigated for larger simulation systems.

3.4 Summary and outlook

I have introduced the classical ISF from the open and closed systems perspective, and methods for its calculation and simulation. The key themes of the Chapter include memory effects, and the relative amplitudes of different components of the ISF, in situations where the separation into components is meaningful. For the case of a particle undergoing vibrations and jumps in a strongly corrugated potential, I have suggested a simple thermodynamic approximation for the effect of intra-cell motion and $z-$vibrations on the amplitude of the long-time decay of the ISF, and shown that the approximation is borne out by numerical simulation. Analytical results are derived which show that the finite memory time $\tau > 0$ of a Generalized Langevin heat bath reduces the relative amplitude of the slowest decaying component of the ISF, for diffusion on flat surfaces. The associated analytical result for the ISF is

readily generalizable to vibrational lineshapes in the presence of memory friction, and is a potentially valuable addition to the library of exact model ISFs. The result is generalized to the quantum mechanical case in the next Chapter.

A many-body simulation of an adsorbate on a harmonic-solid substrate has been analysed in terms of a systematic force arising from the average (adiabatic) potential $V(\mathbf{R})$ and the residual, nonadiabatic force which consists of friction and the random force. Compared to the smoothly decaying power spectrum associated with an exponential GLE kernel, the power spectrum of the nonadiabatic force in the many-body simulation is more sharply cut off at high frequencies. The many-body nonadiabatic power spectrum also contains non-monotonic structure at lower frequencies. Therefore, although the exponential kernel can conveniently and analytically account for some experimental phenomena, accurate microscopic modelling of phononic friction requires a more complex friction kernel.

Chapter 4

Quantum diffusion

Here I will derive the intermediate scattering function (ISF) within a microscopic quantum mechanical model for diffusion in equilibrium subject to memory friction. The model is the quantized version of the classical memory friction model considered in Chapter 3. The calculation demonstrates that an exact result for the quantum ISF of a dissipative system, with a continuum of bath modes, can be derived with standard operator methods and without resorting to specialized techniques. Because the result is valid for arbitrary memory friction it provides a flexible benchmark expression for future quantum mechanical simulations. Although the result does not find immediate application to experimental data in the present Thesis, as with the classical memory friction results, finding new exactly solvable models for the ISF is expected to stimulate further experimental work and rigorous analysis.

When the quantum subsystem is nonlinear, as in the case of a tunneling system, exact expressions for the ISF cannot be evaluated by comparable methods in the dissipative case. However, efficient numerical methods for correlation functions in dissipative tunneling systems in a truncated representation have been developed in the literature. In the second part of the Chapter I derive the analytical ISF of a quantum particle in a periodic tight-binding system in the absence of dissipation. The result provides an explicit expression for the expected form of a lineshape associated with coherent tunneling in a periodic potential. Including dissipation in the calculation is a serious task left as further work. Two promising methods for including dissipation [139, 140] will be discussed in Outlook (Chapter 7).

Under the assumption of diffusion by incoherent tunneling, the dissipative dynamics of a particle in a periodic potential can be described in terms of a jump rate. In Section 4.5 I describe the implementation of a dissipative quantum rate theory on first-principles potential energy surfaces. The results have a significant bearing

on the interpretation of spin echo measurements of hydrogen diffusion, including previous studies [43, 23, 36] and the experimental results presented in Chapter 6. Previously, a very high friction has been suggested in order to fit the jump rates in the semiclassical activated regime. However, the dissipative tunneling rate is enormously suppressed by such a strong friction, which would be completely inconsistent with the observation of fast deep tunneling of hydrogen on Ru(0001). Low friction provides a more consistent explanation of the relatively slow semiclassical rate and fast deep tunneling rate. The low friction interpretation is argued in more detail in Chapter 6 using a range of experimental evidence.

4.1 The quantum mechanical ISF

For a particle with position operator x in a quantum system governed by a time-independent Hamiltonian H, the appropriate generalization of Equation 3.6 replaces position and momentum integrals with traces over the matrix representations of operators:

$$I(\Delta\mathbf{K},t) = \frac{\mathrm{tr}\{e^{i\Delta\mathbf{K}\cdot R(t)}e^{-i\Delta\mathbf{K}\cdot R(0)}e^{-\beta H}\}}{\mathrm{tr}\{e^{-\beta H}\}}\,. \tag{4.1}$$

The following points are helpful to understand the origin and meaning of the formula.

- in a closed system, quantum mechanical operators evolve according to [66]

$$A(t) = \exp\left(\frac{iHt}{\hbar}\right)A(0)\exp\left(\frac{-iHt}{\hbar}\right); \tag{4.2}$$

- $e^{-\beta H}$ is the quantum mechanical statistical operator, which takes the form $\sum_n e^{-\beta E_n}|E_n\rangle\langle E_n|$ in the energy basis, which imposes a Boltzmann distribution of the total energy;

- the trace is independent of the basis chosen, but in the energy basis the denominator reads $\sum_n e^{-\beta E_n}$ and is therefore the partition function

- the normalization always ensures that $I(\Delta\mathbf{K},0) = 1$;

- $\mathbf{R}(0)$ is a Schrödinger operator, and $\mathbf{R}(t)$ is the corresponding Heisenberg operator;

- the Fourier transform of the quantum definition is the dynamical structure factor $S(\Delta\mathbf{K},\Delta\omega)$ [67, 68],
  $S(\Delta\mathbf{K},\omega) = \sum_n e^{-\beta\omega_n}\sum_m |\langle m|e^{i\Delta\mathbf{K}\cdot\mathbf{R}}|n\rangle|^2\delta(\omega,\omega_m-\omega_n)\,.$

The evaluation of the quantum ballistic ISF in one spatial dimension illustrates the main points involved in evaluating 4.1 for linear systems. The Hamiltonian of a free particle of mass m is

$$H = \frac{p^2}{2m} \tag{4.3}$$

and therefore it is convenient to evaluate 4.1 in the momentum basis. $x(t)$ is formally the same as in the classical case,

$$x(t) = x(0) + \frac{p(0)t}{m}\,. \tag{4.4}$$

The first exponential operator takes the form

$$\exp\Big(i\Delta K\, x(t)\Big) = \exp\Big(i\Delta K\Big[x(0) + \frac{p(0)t}{m}\Big]\Big)\,. \tag{4.5}$$

Using the defining commutation relation for position and momentum operators

$$[x, p] = i\hbar\,, \tag{4.6}$$

and the Baker-Hausdorff lemma for two operators X and Y whose commutator is a complex number,

$$e^{X+Y} = e^X e^Y \exp\Big(-\frac{1}{2}[X, Y]\Big)\,, \tag{4.7}$$

the exponential operator 4.5 becomes

$$e^{i\Delta K\, x(t)} = \exp\Big(\frac{iE_r t}{\hbar}\Big)\exp\Big(i\Delta K\frac{p(0)t}{m}\Big)\exp\Big(i\Delta K\, x(0)\Big)\,, \tag{4.8}$$

where E_r is known as the recoil energy [141] which follows the free particle dispersion

$$E_r(\Delta K) = \frac{\hbar^2\Delta K^2}{2m}\,. \tag{4.9}$$

The final exponential operator factor in 4.8 cancels in the ISF's numerator with the following operator $\exp(-i\Delta K x(0))$, so the ISF numerator is of the form

$$\exp\Big(\frac{iE_r t}{\hbar}\Big)\,\mathrm{tr}\left\{\exp\Big(\frac{ipt}{m}\Big)\exp\Big(-\beta\frac{p^2}{2m}\Big)\right\}, \tag{4.10}$$

where $p = p(0)$ is used to represent the Schrödinger operator. The expression for the trace in the momentum basis is identical to the corresponding classical momentum integral that gives the classical ballistic ISF 3.9. Therefore, the quantum ballistic ISF takes the form

$$I(\Delta K, t) = \exp\Big(\frac{iE_r t}{\hbar}\Big)\exp\Big(-\frac{k_B T}{2m}(\Delta K t)^2\Big)\,. \tag{4.11}$$

The complex exponential factor corresponds to a shift by $E_r/\hbar$ in the Fourier domain, introducing the asymmetry in $\Delta\omega$ which is a necessary feature of all quantum lineshapes according to detailed balance.

4.2 Quantum Brownian lineshapes

In the present Section I generalize the analytical results of Section 3.2 to a quantum mechanical system with the same Hamiltonian.

4.2.1 Background

A wide range of approximate methods have been developed to treat the dynamics of open quantum systems. A feature common to all practical methods involving dissipation by a bath with more than a few degrees of freedom is the use of a model Hamiltonian, which allows the bath to be incorporated into the problem without having to consider its evolution numerically. For quantum Brownian motion of particle of mass m in an external potential $V(x)$ a standard model for the bath, and the system-bath interaction, is provided by the Caldeira-Leggett Hamiltonian [121] (introduced in the context of the classical GLE in Section 3.2):

$$H_{CL} = \frac{p^2}{2m} + V(x) + \sum_\alpha \left[\frac{p_\alpha^2}{2m_\alpha} + \frac{1}{2} m_\alpha \omega_\alpha^2 (x_\alpha - \frac{c_\alpha x}{m_\alpha \omega_\alpha^2})^2 \right], \tag{4.12}$$

in which the system particle is linearly coupled in its position co-ordinate to a bath of harmonic oscillators of frequency ω_α and mass m_α via coupling constants c_α. The quadratic nature of the bath in H_{CL} can be justified to some extent by a cumulant expansion of the functional integral describing the response of a more general bath [142], as long as the coupling to each individual bath mode is not too strong[1] Starting from a given model Hamiltonian, there are many different approaches to eliminate the bath and calculate real-time properties of the reduced quantum system. Thermal correlation functions (such as the ISF) can be attacked directly by path integral methods where the heat bath is represented implicitly by a so-called influence functional [143]. The resulting path integral expressions can be tackled, for example, by propagation of a tensor expression [139] or by stochastic methods using correlated noise [140] which draw a striking connection between path integral averages and the classical Generalized Langevin Equation (GLE). Those path

[1] As stated in Section 3.2, weak coupling to each individual bath mode is plausible even if the particle itself is strongly perturbed by the bath, as long as the number of interacting bath modes is large [121].

integral methods are discussed briefly in Outlook 7 in the context of incoherent tunneling rate calculations, but in the present Section I will use a more straightforward connection to the classical GLE, namely its operator-valued equivalent.

When quantum Brownian motion is modelled with the Caldeira-Leggett Hamiltonian above, the particle co-ordinate obeys the operator-valued quantum Langevin equation (QLE) [30]

$$m\ddot{x}(t) = V'(x) - m\int_0^t dt'\gamma(t-t')\dot{x}(t') + F(t)\,, \tag{4.13}$$

$$F(t) = m\sum_\alpha \left[c_\alpha(x_\alpha - \frac{c_\alpha x}{m_\alpha\omega_\alpha^2})\cos(\omega_\alpha t) + \frac{p_\alpha}{m_\alpha\omega_\alpha}\sin(\omega_\alpha t)\right], \tag{4.14}$$

where now and for the rest of the Chapter $x(t)$ represents a Heisenberg operator (or in the classical context, the evolution of $x(0)$), and $x \equiv x(0)$. The QLE is identical in form to the corresponding classical generalized Langevin Equation (GLE) 3.30. The quantum mechanical nature of the random force, which is linear in the Schrodinger operators for the bath, means that $x(t>0)$ has nonzero matrix elements across the entire global Hilbert space. Therefore direct simulation of the QLE is completely intractable. However, in the case where $V(x)$ is harmonic or absent, the linearity of the QLE means its solution can be written as a linear combination of $x, p, \{x_\alpha\}$ and $\{p_\alpha\}$. Therefore, correlation functions can be expressed entirely in terms of the time-dependent linear coefficients of the evolution, which are entirely determined by the classical GLE. Therefore, for Brownian motion in the absence of an external potential, the solution of the QLE is an appropriate method for calculating quantum correlation functions.

Previous calculations of the ISF for quantum Brownian motion were motivated by the atom-surface scattering context [141, 144, 145]. The exponent of the quantum ISF was found to contain an imaginary part which, in the ballistic limit (no environmental coupling), leads to a simple shift in the energy domain, where the magnitude of the shift follows the dispersion relation $\hbar\Delta K^2/2m$ of the free particle. The shift is therefore referred to as quantum recoil. When friction is introduced, the imaginary contribution to the ISF exponent is damped, and tends to a constant value rather than increasing linearly for all t. In the following, I will present exact expressions for the real and imaginary parts of the quantum exponent for arbitrary memory friction. The results are the time domain representation of the dynamical structure factor for a harmonic system, for which general expressions are known [60, 146, 145]. However, the traditional treatment of such phonon lineshapes proceeds via a multiphonon expansion, whereas here the quantum ISF will be related to the classical ISF in an exact and compact way.

4.2.2 Analytical results

4.2.2.1 Classical limit

The classical limit derived in Section 3.2 can and will be found as a limit of the quantum mechanical result. However, to lay groundwork for the full quantum calculation it is helpful to rederive the classical result using a representation of the system-bath coupling based on the global normal modes. The use of normal modes in the present work is conceptually related to a calculation by Pollak [147] in the field of rate theory which related a dissipative rate theory and multidimensional transition state theory (see Section 4.5.1). The connection is that in both cases although solving the normal modes problem completely is intractable, we can derive enough information about the normal modes transformation to compute a key quantity of physical interest.

Instead of the standard Caldeira-Leggett form 4.12 as written in Section 4.2.1, when $V(x) = 0$ we could equally well work in the global normal mode co-ordinates with frequencies $\{\Omega_k\}$, with

$$H_{CL} = \sum_k \left(\frac{p_k^2}{2m} + \frac{1}{2} m \Omega_k^2 y_k^2 \right), \tag{4.15}$$

and define the coupling between the system co-ordinate x and bath modes x_α via an orthogonal transformation, the first row of which reads

$$x = \sum_k d_k y_k \tag{4.16}$$

where the coefficients d_k form the first row of an orthogonal matrix, and are therefore the components of an orthonormal vector. For clarity I emphasise that the set of frequencies $\{\Omega_k\}$ is related to the set $\{\omega_\alpha\}$ but they are not the same set, and that if the set $\{\omega_\alpha\}$ contains N frequencies then $\{\Omega_k\}$ contains $N + 1$ frequencies.

As described in Chapter 3, the Caldeira-Leggett system-reservoir model leads to a Generalized Langevin Equation (GLE) for the system co-ordinate, and the GLE leads straightforwardly to a Laplace-space expression for the velocity autocorrelation function $\psi(t)$. The Gaussian statistics of the underlying Hamiltonian lead to the cumulant expansion of the ISF [26] in terms of the normalized velocity autocorrelation function (VACF) $\psi(t)$:

$$I(\Delta K, t) = \exp\Big[- \Delta K^2 \frac{k_B T}{m} \int_0^t dt' (t - t') \psi(t') \Big] \tag{4.17}$$

For Langevin friction, exponential memory friction and any other friction kernels $\gamma(t)$ for which the inverse Laplace transform of Equation 3.43 is tractable, the ISF can therefore be written in an exact closed form. The coupling coefficients c_α in the global Hamiltonian define the friction kernel, which determines $\psi(t)$ and therefore $I(\Delta K, t)$. However, by deriving the classical ISF in a structurally identical form from the d_k representation 4.16 of the coupling, we can find a simple relation between the d_k and $\psi(t)$.

Since classically $x(t)$ and $x(0)$ commute, we can write

$$I(\Delta K, t) = \langle \exp(i\Delta K[x(t) - x(0)]) \rangle \tag{4.18}$$

and use the linear transformation to normal mode co-ordinates,

$$I(\Delta K, t) = \langle \exp(i\Delta K \sum_k d_k[y_k(t) - y_k(0)]) \rangle \tag{4.19}$$

By definition, the time evolution of the global normal modes from their initial conditions p_k, y_k takes the form

$$y_k(t) = y_k \cos(\Omega_k t) + \frac{p_k}{m_k \Omega_k} \sin(\Omega_k t)\,. \tag{4.20}$$

Writing the thermal average as a phase space average over initial conditions, we arrive at

$$I(\Delta K, t) = \frac{1}{Z} \int dp_k dy_k e^{i\Delta K \sum_k d_k [y_k(\cos(\Omega_k t) - 1) + \frac{p_k}{m_k \Omega_k} \sin(\Omega_k t)]} \tag{4.21}$$

The momentum and position integrals are independent, but combine neatly via the identity

$$(1 - \cos(\Omega t))^2 + \sin^2(\Omega t) = 2 - 2\cos(\Omega t) \tag{4.22}$$

so the ISF takes the form

$$I(\Delta K, t) = \exp(-\Delta K^2 \sum_k \frac{d_k^2}{m_k \Omega_k^2 \beta}[1 - \cos(\Omega_k t)])\,. \tag{4.23}$$

The result can be cast into the cumulant expansion form 4.17 since

$$\int_0^t dt'(t - t')\cos(\Omega t') = \frac{1}{\Omega^2}[1 - \cos(\Omega t)]\,. \tag{4.24}$$

Within the c_α representation, the mode masses can always be made equal to each other and to the particle mass m, by trading the masses off against the coupling constants, in a way that leaves $\gamma(t)$ and therefore $I(\Delta K, t)$ unchanged. The c_α

representation can therefore be transformed into a d_k representation where all the global mode masses satisfy $m_k = m$, which simplifies the result to:

$$I(\Delta K, t) = \exp\Big[-\Delta K^2 \frac{k_B T}{m} \int_0^t dt'(t-t') \sum_k d_k^2 \cos(\Omega_k t') \Big] . \tag{4.25}$$

Therefore, $\sum_k d_k^2 \cos(\Omega_k t)$ is the normalised VACF, for example $e^{-\gamma t}$ for Ohmic friction. It is a general feature of system/reservoir models that the result does not depend on the exact set of d_k, but rather the spectral properties of the coupling. To reproduce, for example, Ohmic friction, the necessary spectral density of the coupling can be written with the density of states factor $g(\Omega)$ as:

$$g(\Omega) d^2(\Omega) \propto \frac{\gamma^2}{\Omega^2 + \gamma^2} . \tag{4.26}$$

In the Caldeira-Leggett representation of the same physical Hamiltonian, the defining spectral property of the system for Ohmic friction is

$$g_{CL}(\omega) c^2(\omega) \propto \omega^2 , \tag{4.27}$$

where $g_{CL}(\omega)$ is the density of the bath modes rather than the global normal modes. It is evident that there is a connection between the $\{c_\alpha\}$,$\{\omega_\alpha\}$ and the $\{d_k\}$,$\{\Omega_k\}$. Either representation is equally useful when it comes to deriving the classical ISF. However, in the quantum mechanical case the derivation is much simpler in the d_k representation.

4.2.2.2 Quantum mechanical correlation function

The main ingredient that carries over from the classical calculation is the time evolution of the operators. However, since the commutator $[x(t), x]$ is no longer zero, the product of exponential operators $e^{i\Delta K \cdot x(t)} e^{-i\Delta K \cdot x}$ must be disentangled using the Baker-Hausdorff theorem. As clearly explained in previous works, the disentangling operation generates complex factors in the ISF [141, 145, 144]. Meanwhile, the quantised energies of the global Hamiltonian modify the real part of the ISF exponent, in a way that is simple to express in the Fourier domain.

We begin by using the same normal mode representation as in the classical case, but writing the thermal average as a trace in the position basis:

$$I(\Delta K, t) = \frac{1}{Z} \int dy_k \langle y_k | e^{i\Delta K x(t)} e^{-i\Delta K x} e^{-\beta H} | y_k \rangle \tag{4.28}$$

$$= \frac{1}{Z}\int dy_k \langle y_k| e^{i\Delta K \sum_k d_k [y_k \cos(\Omega_k t) + \frac{p_k}{m_k \Omega_k}\sin(\Omega_k t)]} e^{-i\Delta K \sum_k d_k y_k \cos(\Omega_k t)} e^{-\beta H} |y_k\rangle \,. \quad (4.29)$$

Applying the Baker-Hausdorff identity in the form $e^{X+Y} = e^X e^Y \exp(-\frac{1}{2}[X,Y])$ to the first exponential operator, we can pull out the first of a series of contributions to the phase factor. Writing the complex factor outside the integral as

$$e^{iQ_1} = e^{\frac{1}{2} i\hbar \Delta K^2 \sum_k \frac{d_k^2}{m_k \Omega_k} \cos(\Omega_k t)\sin(\Omega_k t)}, \quad (4.30)$$

the ISF becomes

$$\frac{1}{Z} e^{iQ_1} \int dy_k \langle y_k| e^{i\Delta K \sum_k d_k y_k \cos(\Omega_k t)} e^{i\Delta K \sum_k \frac{p_k}{m_k \Omega_k}\sin(\Omega_k t)} e^{-i\Delta K \sum_k d_k y_k \cos(\Omega_k t)} e^{-\beta H} |y_k\rangle \,. \quad (4.31)$$

By operating on $\langle y_k|$ from the right three times in succession, the expression becomes

$$\frac{1}{Z} e^{iQ_1} \int dy_k e^{i\Delta K \sum_k d_k y_k \cos(\Omega_k t)} \langle y_k| e^{i\Delta K \sum_k \frac{p_k}{m_k \Omega_k}\sin(\Omega_k t)} e^{-i\Delta K \sum_k d_k y_k \cos(\Omega_k t)} e^{-\beta H} |y_k\rangle \quad (4.32)$$

$$= \frac{1}{Z} e^{iQ_1} \int dy_k e^{i\Delta K \sum_k d_k y_k \cos(\Omega_k t)} \langle y_k + \frac{\hbar \Delta K}{m_k \Omega_k}\sin(\Omega_k t)| e^{-i\Delta K \sum_k d_k y_k \cos(\Omega_k t)} e^{-\beta H} |y_k\rangle \quad (4.33)$$

$$= \frac{1}{Z} e^{iQ_2} \int dy_k e^{i\Delta K \sum_k d_k y_k (\cos(\Omega_k t) - 1)} \langle y_k + \frac{\hbar \Delta K}{m_k \Omega_k}\sin(\Omega_k t)| e^{-\beta H} |y_k\rangle \,, \quad (4.34)$$

where the new phase factor e^{iQ_2} is

$$\exp(iQ_2) = \exp\left(\frac{1}{2} i\hbar \Delta K^2 \sum_k \frac{d_k^2}{m_k \Omega_k}[\cos(\Omega_k t) - 1]\sin(\Omega_k t)\right). \quad (4.35)$$

Now we evaluate the matrix element in the remaining integral factor. The k^{th} matrix element belongs to the thermal density matrix of a harmonic oscillator of frequency Ω_k, and is therefore a standard result. The matrix element can be expressed in terms of the mean uncertainties in p_k and y_k[30]. Applied to the present case, the result is:

$$\begin{aligned} \langle y_k + a_k| e^{-\beta H_k} |y_k\rangle &\propto \exp(-\frac{1}{4} m_k \Omega_k \frac{(2y_k + a_k)^2}{\hbar \coth(\frac{1}{2}\beta\hbar\Omega_k)}) \\ &\times \exp(-\frac{1}{4} m_k \Omega_k a_k^2 \coth(\frac{1}{2}\beta\hbar\Omega_k)) \end{aligned} \quad (4.36)$$

where $a_k = \frac{\hbar \Delta K}{m_k \Omega_k} \sin(\Omega_k t)$. The second exponential factor can be taken outside the integral. Writing that factor as e^{R_1}, the ISF takes the form of a complex function multiplied by a Gaussian integral:

$$I(\Delta K, t) \propto e^{iQ_2} e^{R_2} \int dy_k \qquad \Big[\exp(i\Delta K \sum_k d_k y_k (\cos(\Omega_k t) - 1))) \\ \times \quad \exp(-\frac{1}{4} m_k \Omega_k \frac{(2y_k + a)^2}{\hbar \coth(\frac{1}{2}\beta\hbar\Omega_k)}) \Big] . \tag{4.37}$$

Performing the independent Gaussian integrals for all k, the result becomes

$$\begin{aligned} I(\Delta K, t) \quad &\propto \quad e^{iQ_2} e^{R_1} \\ &\times \quad \exp(\frac{1}{2} i\hbar \Delta K^2 \sum_k \frac{d_k^2}{m_k \Omega_k} (\cos(\Omega_k t) - 1) \sin(\Omega_k t)) \\ &\times \quad \exp(\Big(\frac{1}{4} \sum_k d_k^2 \frac{\hbar \Delta K^2}{m_k \Omega_k} [\cos(\Omega_k t) - 1]^2 \coth(\frac{1}{2}\beta\hbar\Omega_k) \Big) . \end{aligned} \tag{4.38}$$

Combining the remaining explicit exponents with the iQ_2 and R_1 from outside the final integral, we arrive at

$$I(\Delta K, t) = \exp(iQ(t)) \exp(R(t)) \tag{4.39}$$

where the phase factor is

$$\exp(iQ(t)) = \exp\Big(\frac{1}{2} i\hbar \Delta K^2 \sum_k \frac{d_k^2}{m_k \Omega_k} \sin(\Omega_k t) \Big) \tag{4.40}$$

$$= \exp\Big(\frac{1}{2} i\hbar \Delta K^2 \int_0^t dt' \frac{\Psi(t')}{k_B T} \Big) \tag{4.41}$$

and the "modified classical factor" is

$$\exp(R(t)) = \exp\Big(-\frac{1}{2} \Delta K^2 \sum_k \frac{d_k^2}{m_k \Omega_k} [1 - \cos(\Omega_k t)] \hbar \coth(\frac{1}{2}\beta\hbar\Omega_k) \Big). \tag{4.42}$$

The phase factor becomes unity in the limit $\hbar \to 0$. Assuming again that all the mode masses are equal, we can write $e^{R(t)}$ in a form that makes the connection to the classical result 4.25 much clearer:

$$\exp(R(t)) = \exp\Big(-\Delta K^2 \frac{k_B T}{m} \int_0^t dt' (t - t') \sum_k \psi_k(t') \frac{1}{2} \beta\hbar\Omega_k \coth(\frac{1}{2}\beta\hbar\Omega_k) \Big) , \tag{4.43}$$

where $\psi_k(t) = d_k^2 \cos(\Omega_k t)$. In the limit $\hbar \to 0$, we recover the classical result, Equation 4.25, as required.

Figure 4.1 illustrates the undamped (ballistic) quantum ISF, and the Brownian result for two different cutoff frequencies ω_c. The quantum Brownian results were constructed from the normal mode representations 4.40 and 4.43 using the double-Lorentzian form of $d(\Omega_k)$ which reproduces the classical velocity autocorrelation function 3.48. In principle, $d(\Omega)$ could be constructed instead by a numerical Fourier transform of a classical velocity autocorrelation which does not have such a simple analytical form.

4.2.3 Discussion

The compact quantum mechanical expressions 3.43-4.43 show that there is a simple relationship between the classical exponent of the ISF and the quantum exponent, for diffusion on a flat surface controlled by a linear interaction with a harmonic bath. The key quantity that links the two exponents is the spectral density of the coupling in the global normal modes representation, $g(\Omega)d^2(\Omega)$, which can be determined from the classical exponent. The quantum exponent can then be expressed in terms of integrals over the spectral density, modified to include functions of $\hbar\Omega$. It is straightforward to show that the form of $g(\Omega)d^2(\Omega)$ given earlier for Langevin friction reproduces the damped phase factor $\propto 1 - e^{-\gamma t}$ derived in previous works [141, 145, 144]. However, $g(\Omega)d^2(\Omega)$ can take simple forms beyond the Langevin limit. For example, in the case of an unconfined particle subject to exponential memory friction where the VACF is a biexponential, $g(\Omega)d^2(\Omega)$ simply becomes the sum of two Lorentzian functions. The results are equally valid in the presence of a confining harmonic $V(x)$.

Although the results 3.43-4.43 can be related to experimental lineshapes, they are also potentially valuable for benchmarking numerical methods. Quantum Brownian motion can be contrasted with another classic benchmark system, namely the dissipative two-state system (TSS) or spin-boson model [148]. The utility of the spin-boson model as a benchmark is independent of whether it realistically describes any given physical system, and the same is true of the quantum Brownian case, which strongly complements the spin-boson regime in that:

- the particle is free rather than tightly bound;
- the size of the Hilbert space of the particle remains infinite rather than being truncated to two states.

Issues that are relevant for both the TSS and quantum Brownian motion, and can be efficiently addressed for the latter through the analytical results 3.43-4.43, include

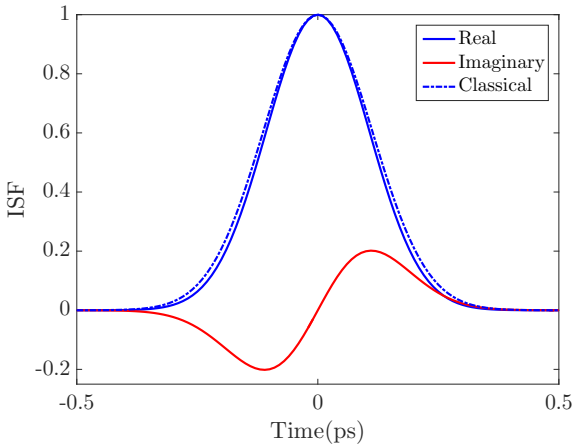

(a) Undamped quantum ISF.

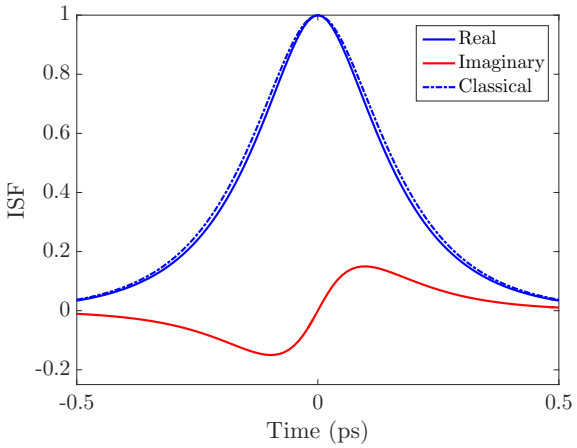

(b) Damped quantum ISF.

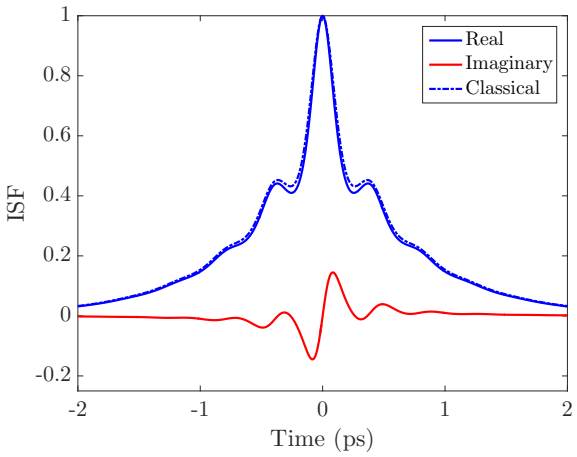

(c) Quantum ISF: strongly damped with long memory.

Figure 4.1: The quantum Brownian ISF illustrated at $\Delta K = 1.0\,\text{Å}^{-1}$ in the undamped (ballistic) case and in the damped case for two different cutoff frequencies in the friction kernel. The parameters common to each simulated lineshape are $m = 1\,\text{a.m.u.}$; $T = 100\,\text{K}$. Figure 4.1a shows the ballistic results, i.e. $\gamma = 0$. Figure 4.1b is plotted with $\gamma = 10\,\text{ps}^{-1}$ and $\omega_c = 50\,\text{ps}^{-1}$. Figure 4.1c is plotted with $\gamma = 50\,\text{ps}^{-1}$ and $\omega_c = 5\,\text{ps}^{-1}$ ($\tau = 0.2\,\text{ps}$), and shows oscillatory features due to the relatively long memory time.

the relative timescales of intrinsic susbsytem dynamics and the bath dynamics; the frequency dependence of the friction kernel, and the effect of different types of high-frequency cutoff in the bath response. Because the analytic results are universally valid for a globally harmonic system, they provide access to numerically difficult regimes. As seen in the lower plot of Figure 4.1, the qualitative behaviour of the ISF is strongly dependent on the relative timescales of the undamped motion, the friction γ and the memory time $\tau = 1/\omega_c$.

4.2.4 Conclusions

I have presented compact exact analytic forms for the intermediate scattering function describing the diffusion of a quantum particle in a flat or harmonic potential landscape, linearly interacting with a harmonic bath. The results relate to the main analytic result in Chapter 3 by providing a simple exact relationship between the classical and quantum mechanical result, for arbitrary memory friction as illustrated in Figure 4.1. The results could be useful for benchmarking numerical methods for calculating quantum correlation functions. Similar results have been derived in the literature, but the valuable features of the result as formulated above include:

- derivation via well-known operator methods;
- compact expression that concisely relates the classical and quantum mechanical results.

4.3 Coherent tunneling

Quantum tunneling is important in an enormous range of physical processes, including nuclear fission [149] and fusion [150], intermolecular hydrogen transfer [151], bimolecular chemical reactions [152], the dynamics of superconducting junctions [153], and surface diffusion [41, 154, 23]. The concept of tunneling is illustrated by a symmetric double well potential, in which the energy eigenstates are delocalised with equal amplitude in each well. The energy separation between the ground and first excited state defines a tunnel splitting Δ, analogous to the bandwidth in a multi-well extended system.

In the present Section I calculate the exact ISF for coherent tunneling in an extended tight binding system with one accessible energy band. In the tight-binding model, a restricted basis set of one localized state per unit cell is used, and the tunneling matrix element is a parameter that controls the mobility of the particle.

Tight binding is sometimes presented as a model for electronic bandstructure [155] but can equally well be used as a model for atomic tunneling in an extended system. The dynamical structure factor is already known for a coherent two-state system [156], but here I consider the opposite limit where the system is large enough for the energy eigenstates to form a continuous band. The model system can be considered as a tunneling analogue of ballistic motion on flat ($V(x) = 0$) surfaces. The results are not expected to be immediately applicable to experimental HeSE lineshapes, but indicate quantitatively how quantum coherence in an extended tunneling system could manifest itself in a HeSE experiment. At low temperatures and not-too-low dissipation strength, the dynamics of the tunneling particle can be described in terms of an incoherent hopping rate [157] rather than by coherent propagation. The transition between the two regimes is not investigated here, instead the completely dissipation-free case is worked out in detail.

The tight binding system in one spatial dimension is represented by the Hamiltonian

$$H = \delta(\phi + \chi) \tag{4.44}$$

where δ is a real number, and ϕ and χ are positive and negative translation operators

$$\phi = \sum_n |n+1\rangle\langle n| \;\; ; \;\; \chi = \sum_n |n-1\rangle\langle n| \,. \tag{4.45}$$

The states $|n\rangle$ are localized states assumed to be orthogonal. The eigenstates of H are the Bloch states

$$|k\rangle = \frac{1}{\sqrt{N}} \sum_n e^{ikn} |n\rangle \quad (-\pi < k \leq \pi) \,, \tag{4.46}$$

with dispersion relation

$$\epsilon(k) = -2\delta \cos(k) \,. \tag{4.47}$$

I will assume $\delta < 0$ so that $\epsilon(k)$ has a minimum at $k = 0$.

By analogy with the treatment of the two-state system briefly reviewed above [156], I define the ISF for the tight binding system by replacing x (continuous system position operator) with na where a is the lattice parameter and n is the discrete position operator,

$$n = \sum_{n'} n' |n'\rangle\langle n'| \,. \tag{4.48}$$

In other words, we are going to calculate

$$I(\Delta K, t) = \mathrm{tr}\Big\{ e^{i\Delta K a n(t)} e^{-i\Delta K a n(0)} e^{-\beta H} \Big\} \,. \tag{4.49}$$

The time evolution of $n(t)$ follows straightforwardly from the operator equation of motion $\dot{n} = i[H, n]/\hbar$. From the commutation relations

$$[\chi, \phi] = 0 \ ; \ [\chi, n] = \chi \ ; \ [\phi, n] = -\phi \,, \tag{4.50}$$

the closed-form evolution of $n(t)$ is given in terms of the Schrödinger operator $n \equiv n(0)$ by

$$n(t) = n + \frac{i\delta}{\hbar}(\chi - \phi)t \,. \tag{4.51}$$

After substituting $n(t)$ into the definition of $I(\Delta K, t)$, the derivation proceeds very much like the free-particle ballistic case, namely by using a disentangling theorem. We use a special case [158] of the well known Baker-Campbell-Hausdorff formula. The special case applies when the commutator of two operators X and Y is a linear combination of X, Y and the identity operator I:

$$[X, Y] = uX + vY + cI \,, \tag{4.52}$$

under which conditions the product of the exponentiated operators is:

$$e^X e^Y = \exp\Big(X + Y + f(u, v)[X, Y]\Big) \,, \tag{4.53}$$

with $f(u, v)$ given by

$$f(u, v) = \frac{(u - v)e^{u+v} - (ue^u - ve^v)}{uv(e^u - e^v)} \tag{4.54}$$

When the commutation relation can be specialized further to the case

$$[X, Y] = uX \,, \tag{4.55}$$

the result can be simplified further by taking the limit $v \to 0$, giving

$$e^X e^Y = \exp(X + Y + uf(u)X] \,, \tag{4.56}$$

where the scalar function $f(u) = f(u, v \to 0)$ is given by

$$f(u) = \frac{1 + e^u(u - 1)}{u(e^u - 1)} \,. \tag{4.57}$$

It is easy to verify that the relation in the opposite direction, which can be used to factorize the exponential of a sum of operators, is

$$\exp(X + Y) = \exp(\frac{X}{1 + uf(u)}) \exp(Y) \,. \tag{4.58}$$

Equation 4.58 can reduce the operator appearing inside the trace of Equation 4.49 to a form involving only ϕ and χ, independent of n, which allows easy evaluation of $I(\Delta K, t)$ in the Bloch basis. Firstly, we write out the time-evolved exponential operator

$$\exp(i\Delta Kan(t)) = \exp(i\Delta Kan - \Delta Ka\frac{\delta t}{\hbar}\chi + \Delta Ka\frac{\delta t}{\hbar}\phi) \tag{4.59}$$

and make the substitutions $X = \Delta Ka\frac{\delta t}{\hbar}\phi$, $Y = i\Delta Kan - \Delta Ka\frac{\delta t}{\hbar}\chi$. Applying the disentangling result 4.58 produces

$$\exp(\frac{\Delta Ka\delta t\phi/\hbar}{1 - i\Delta Kaf(-i\Delta Ka)})\exp(i\Delta Kan - \Delta Ka\frac{\delta t}{\hbar}\chi)\,. \tag{4.60}$$

Repeating with $X = -\Delta Ka\frac{\delta t}{\hbar}\chi$, $Y = i\Delta Kan$ gives the fully factorized version of $\exp(i\Delta Kan(t))$. Introducing the function $g(u) = (1 + uf(u))^{-1}$,

$$\exp(i\Delta Kan(t)) = \exp(\Delta K\frac{\delta t}{\hbar}a[g(-i\Delta Ka)\phi - g(i\Delta Ka)\chi])e^{i\Delta Kan}\,. \tag{4.61}$$

The third exponential factor, a function of the Schrödinger operator n, cancels within the ISF, leaving us with

$$I(\Delta K, t) = \mathrm{tr}\Big\{\exp(\Delta K\frac{\delta t}{\hbar}a[g(-i\Delta Ka)\phi - g(i\Delta Ka)\chi])e^{-\beta H}\Big\}\,. \tag{4.62}$$

Since $\phi|k\rangle = e^{-ik}|k\rangle$ and $\chi|k\rangle = e^{ik}|k\rangle$, the trace is conveniently evaluated in the $|k\rangle$ basis. Assuming a large number of sites N giving a continuum of k states, the ISF numerator is given by

$$\frac{1}{2\pi}\int_0^{2\pi} dk\exp(-2\beta\delta\cos(k))\exp(-\frac{t\delta}{\hbar}a\Delta K[g(i\Delta K)e^{ik} - g(-i\Delta K)e^{-ik}])\,. \tag{4.63}$$

Since $g(i\Delta K)$ and $g(-i\Delta K)$ are complex conjugates, by writing $g = g' + ig''$ with real and imaginary parts g' and g'' respectively, the integral can be recast as

$$\frac{1}{2\pi}\int_0^{2\pi} dk\exp(A\cos(k) + B\sin(k))\,, \tag{4.64}$$

where $A = -2\beta\delta - 2i\frac{t\delta}{\hbar}\Delta Kg''$ and $B = -2i\frac{t\delta}{\hbar}\Delta Kg'$. The integral has a standard special-function representation in terms of the zeroth-order modified Bessel function of the first kind $I_0(x)$. The correctly normalized ISF is given by

$$I(\Delta K, t) = \frac{I_0(\sqrt{A^2 + B^2})}{I_0(-2\beta\delta)}\,. \tag{4.65}$$

Figure 4.2 illustrates the analytical result 4.65 at times up to 1 ns. The blue solid

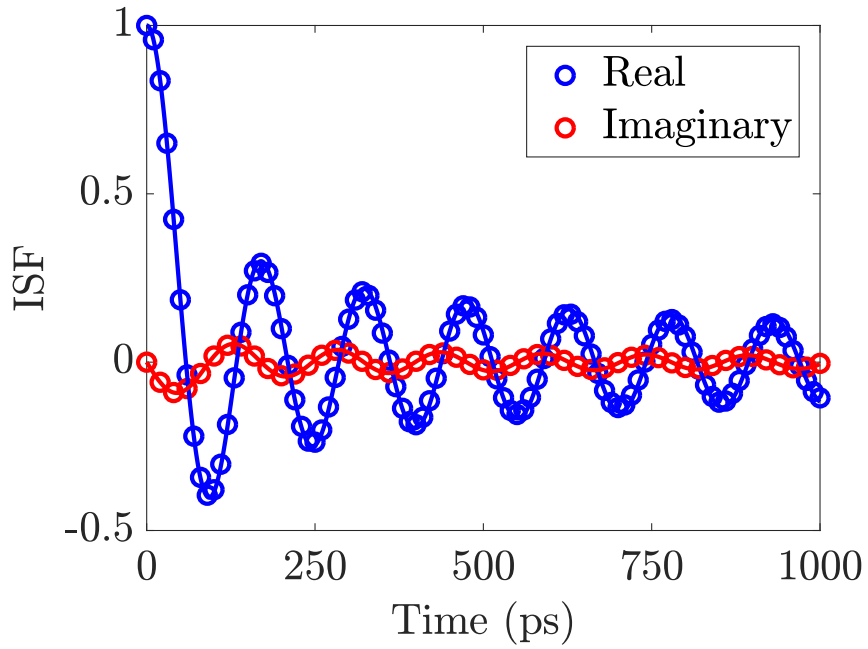

Figure 4.2: Illustration of the coherent tight binding ISF, at $\delta = 0.01\,\text{meV}$, $\Delta K = 1.0\,\text{Å}^{-1}$, $a = 1.5\text{Å}$, $T = 1\,\text{K}$. The real part of $I(\Delta K, t)$ is shown in blue; the imaginary part in red. The real part is symmetric in t, and the imaginary part is antisymmetric. The numerical results of evaluating the expression 4.49 are shown as open circles. The analytical expression 4.65 is shown as solid lines, and is in agreement with the direct numerical evaluation. The imaginary part is insignificant at, say, room temperature when $k_B T \gg \delta$ (thermal energy much greater than the bandwidth).

curve is the real part of the ISF at $\delta = 0.01\,\text{meV}$, $\Delta K = 1.0\,\text{Å}$, $a = 1.5\text{Å}$, $T = 1\,\text{K}$. The solid red curve is the imaginary part. An especially low temperature (and a rather large δ) are chosen in order to make the imaginary part visible. Numerical results obtained by direct matrix evaluation of Equation 4.49 in a finite basis with $N = 250$ are shown as open circles. Notable aspects of the ISF for coherent tunneling in a periodic, one-band system include its oscillatory nature, which is to be expected on the basis of the coherent oscillations of a two state tunneling system, and the rather slow decay of the envelope, whose tail is much longer than exponential.

4.4 Background: path integral calculation of quantum partition functions

The following Section (4.5) involves the calculation of rates via a thermodynamic method which formally consists of evaluating two quantum mechanical partition functions. The standard formulation of the method in the literature is based on path integrals [159, 30, 31]. Therefore I give a brief outline of the derivation and evaluation of path integral expressions for the partition function, which largely follows the

presentation in [160]. The path integral approach to quantum thermodynamics and dynamics is a substantial topic in its own right, and the presentation here is necessarily compact. Enough detail is given to explain the ingredients of the quantum rate formula within the bounce method, especially the bounce action and the fluctuation operator.

It is convenient to first give the path integral expression for a matrix element of the time evolution operator, which will eventually be turned into a partition function by a trace operation. The time evolution operator $U(t)$ associated with the Hamiltonian

$$H = \frac{p^2}{2m} + V(q) \equiv T + V \tag{4.66}$$

is

$$U(t) = \exp(-iH\frac{t}{\hbar}) \,, \tag{4.67}$$

with matrix elements in the co-ordinate basis

$$\langle q_f | e^{-iHt/\hbar} | q_i \rangle \,, \tag{4.68}$$

which are going to be written formally as a sum over paths in space at initial position q_i and final position q_f. First, the exponential is split up into the product of N short-time exponentials which represent evolution for a time $\Delta t = t/N$:

$$e^{-iHt/\hbar} = [e^{-iH\Delta t/\hbar}]^N \,. \tag{4.69}$$

As long as Δt is short enough, each short-time exponential can be approximately factorized:

$$e^{-iH\hbar\Delta t/\hbar} = e^{-iT\Delta t/\hbar} e^{-iV\Delta t/\hbar} + \mathcal{O}(\Delta t^2) \,. \tag{4.70}$$

Expanding the exponential within the matrix element 4.68 in that way, the matrix element becomes

$$\langle q_f | e^{-iHt/\hbar} | q_i \rangle = \langle q_f \wedge e^{-iT\Delta t/\hbar} e^{-iV\Delta t/\hbar} \wedge \cdots \wedge e^{-iT\Delta t/\hbar} e^{-iV\Delta t/\hbar} | q_i \rangle \,, \tag{4.71}$$

in which resolutions of the identity operator $\infty = \int dq \int dp_n |q_n\rangle\langle q_n|p_n\rangle\langle p_n|$ are about to be inserted at the wedge positions $\wedge$, where $n = 1, \cdots, N$. Because the $\langle q_n|p_n\rangle$ are plane waves, the matrix element becomes

$$\langle q_f | e^{-iHt/\hbar} | q_i \rangle = \int \prod_{n=1}^{N=1} dq_n \prod_{n=1}^{N} \frac{dp_n}{2\pi\hbar} \exp\left(-i\frac{\Delta t}{\hbar} \sum_{n=0}^{N-1} (V(q_n) + T(p_{n+1}) - p_{n+1}\frac{q_{n+1} - q_n}{\Delta t})\right) . \tag{4.72}$$

The momentum variables can be eliminated by using a standard multidimensional

Gaussian integral,

$$\int d\mathbf{v} \exp\Big(-\frac{1}{2}\mathbf{v}^T\mathbf{A}\mathbf{v} + \mathbf{j}^T\mathbf{A}^{-1}\mathbf{j}\Big)\,, \tag{4.73}$$

which gives the matrix element in terms of a multidimensional integral over q co-ordinates only,

$$\langle q_f|e^{-iHt/\hbar}|q_i\rangle \approx \int \prod_{n=1}^{N-1} dq_n \exp\Big[\frac{i}{h}\int_0^t dt' \Big(\frac{1}{2}m\dot{q}(t')^2 - V(q(t'))\Big)\Big]\,, \tag{4.74}$$

where the time integral is to be interpreted as a sum over the short time intervals $\Delta t = t/N$.

To obtain the quantum mechanical path integral

$$Z(\beta) = \mathrm{tr}e^{-\beta H} = \int dq\, \langle q|e^{-\beta H}|q\rangle\,, \tag{4.75}$$

the expression developed so far needs to be evaluated at a time $t = -i\hbar\beta$ and the co-ordinates q_i and q_f set equal and then integrated over. The result can be written as

$$Z(\beta) = \int \prod_{n=1}^{N-1} dq_n \exp\Big[-\frac{1}{h}\int_0^{\hbar\beta} d\tau \Big(\frac{1}{2}m\dot{q}^2 + V(q)\Big)\Big]\,, \tag{4.76}$$

where now $\dot{q}$ represents its derivative with respect to the variable τ, subject to periodic boundary conditions $q_N = q_0 (= q_i = q_f)$.

By keeping N finite in the above discussion, the results are kept conceptually quite straightforward: in general terms a vector-matrix-vector multiplication has been transformed approximately into a high-dimensional integral. There is no need to take the $N \to \infty$ limit in the course of applying the thermodynamic method in the next Section; instead, N becomes a numerical convergence parameter. The path integral can be approximated by expanding the action quadratically about the path $q_B(\tau)$ where the action is minimized, which is the multidimensional equivalent of approximating $\int dx \exp(-f(x))$ by expanding $f(x)$ about its minimum value and performing a Gaussian integral. An important result both conceptually and operationally for the path integral method is that the action is minimized for paths $q(\tau)$ that solve the classical equation of motion in the inverted potential $-V(q)$. In the present context there is a solution localized around the barrier top (a well in the inverted potential) known as the bounce path $q_B(\tau)$, with action labelled S_B. The numerical solution for the bounce path for a flexibly-parametrized barrier top is explored in the course of evaluating the quantum rate, in Section 4.5.4.

As well as being quadratic in the path variable, the expansion of the action is quadratic in $\hbar$, and therefore constitutes a semiclassical approximation. Assuming

there is only one classical solution with the necessary periodicity of $\hbar\beta$, standard Gaussian integrals give the semiclassical partition function as [30]

$$Z = \left| \det(-\frac{\partial^2}{\partial\tau^2} + V''[q_B(\tau)]) \right|^{-1/2} e^{-S_B/\hbar}, \tag{4.77}$$

where the differential operator whose determinant is taken has a finite matrix representation when the path is sampled at discrete points τ_n. In general, if there are multiple allowed classical paths, the Gaussian expansions around different paths can simply be added together.

The path integral method allows dissipation to be incorporated efficiently into the partition function, and by extension on quantum rates within the $\mathrm{Im}(F)$ framework. A harmonic bath linearly coupled to the co-ordinate q can be eliminated from the partition function exactly, leaving an expression which is formally identical to the non-dissipative partition function but where the action $S[q(\tau)]$ is replaced by an effective action which includes a damping kernel. The effective action is quoted as needed in the following Section.

4.5 Surface diffusion by incoherent tunneling

The ISF of a quantum particle subject to dissipation in a nonlinear potential is a very difficult quantity to calculate. However, some progress can be made after assuming the dynamics of the particle consists of incoherent jumps between neighbouring adsorption sites, and therefore the dynamics can be parametrized in terms of a jump rate[1]. By attempting to calculate a rate rather than the complete, exact dynamics via the ISF, the problem is enormously simplified. Methods that give rates without requiring the solution of the exact dynamics of a system form the subject of rate theory.

Previous rate-theoretical analyses of HeSE measurements of hydrogen diffusion have made use of either:

- semiclassical rate theories (Wolynes formula) [43];
- a transition state theory using the numerically exact hydrogen bandstructure calculated from the three-dimensional atom/surface potential [36];

[1]Except at very short correlation times. The validity of the jump description for longer correlation times could be unambiguously verified or refuted, in principle, by a fully quantum mechanical calculation of the ISF, which is not performed here. However, the real-time results in Section 4.5.6 for a biased two-state system strongly suggests that a jump description of dynamics is an appropriate for the real system.

- instanton-based rates in the dissipation-free limit [23].

In the present Section I carry out detailed rate calculations using the bounce or "Im(F)" method, which generalizes the Wolynes formula to the deep tunneling regime, and generalizes the instanton calculations to include dissipation. A critical discussion of the method is presented after the main calculations.

4.5.1 Background: classical rate theory

Figure 4.3a [161] illustrates a model potential energy curve for a system in which a rate description of the dynamics could be appropriate. Two wells A (oscillation frequency ω_0) and C are separated by a one-dimensional barrier B of energy V_b with respect to well A, and imaginary frequency ω_b. As long as the barrier is large compared to the thermal energy ($V_b \gg k_B T$), a particle will spend a very small fraction of its time in equilibrium near the barrier top. Assuming that dissipative coupling to the environment is not so strong that the particle's motion is overdamped, then qualitatively the motion will consist of oscillations whose amplitude fluctuates over time, occasionally growing large enough for the particle to cross the barrier (a fast event) and settle in the opposite well.

The simplest classical theory of the escape rate from well A is classical transition state theory (TST). In TST, the escape rate is given by the expectation of the outbound flux at the barrier top, divided by the population of the well region. Both quantities can be calculated analytically by expanding the potential quadratically at the well and barrier region. The well known result is [161]:

$$\Gamma_{TST} = \frac{\omega_0}{2\pi} e^{-\beta V_b} \,. \tag{4.78}$$

The exponential factor represents the relative probability of the particle reaching the barrier top, and the prefactor represents an attempt frequency. The attempt frequency is given by the oscillation frequency in the well region, which implies that the energy of the particle is randomized with each cycle through the well. The TST prefactor is always an over-estimate compared to any realistic dissipative model, because when the dissipation is strong enough to randomize the energy on each cycle in the well, it is also strong enough to induce recrossing at the barrier top.

Dissipation can be modelled using a phenomenological equation of motion, for example a GLE-like stochastic representation, or Fokker-Planck (Klein-Kramers) equation describing the evolution of probability density in phase space. The Klein-Kramers representation was used to derive the effect of not-too-weak dissipation on the escape rate [162] by finding a solution with a steady-state flux out of the

well region. Later the Generalized Langevin Equation representation was used to extend the result to frequency-dependent damping [116], by solving the dynamics over the barrier top. Figure 4.3b illustrates the calculation. The no-recrossing assumption of TST is generalized to an assumption of no direct crossing from the left of S_R (reactant state) and no recrossing from the right of S_P (product state). The rate is given in terms of the thermal probability $\psi(S_R)$ of a particle being at S_R, the associated distribution of velocities $\phi(v_0)$, and the conditional probability ρ to arrive some time later at S_P with a new velocity v, by the expression

$$\Gamma = \psi(S_R) \int_0^\infty dt \int dv_0 \, \phi(v_0) \int dv \, v_0 \, v \, \rho(S_P, v, t | S_R, v_0) \, . \tag{4.79}$$

Because GLE dynamics in a harmonic system can be solved exactly (Section 3.2), Γ can be evaluated exactly under the assumption of a harmonic barrier. The result in terms of the Laplace transform of the friction kernel $\hat{\gamma}$ is:

$$\Gamma = \frac{\lambda_r}{\omega_b} \Gamma_{TST} \; ; \; \lambda_r = \frac{\omega_b^2}{\lambda_r + \hat{\gamma}(\lambda_r)} \, . \tag{4.80}$$

Significantly, the same result can be derived by applying transition state theory assumptions to the linear coupling Hamiltonian representation of the same system (cf. Section 3.2) [147], treating the single unstable mode at the barrier top as the escape co-ordinate. In other words, a dissipative escape rate for a low-dimensional system can be formulated as a TST for a high-dimensional system. The multidimensional theory correctly models suppression of the jump rate at high friction by recrossing, but does not account for the suppression of the rate at low friction [163].

The stable states picture, or multidimensional TST, does not allow for the reduction in effective attempt frequency at low friction, where the frequency of independent attempts to cross the barrier is proportional to γ within the Langevin framework. As γ increases from zero, the jump rate smoothly increases, reaches a maximum below the TST limit, and decreases due to suppression by barrier-recrossing events [161]. The resulting form of $\Gamma(\gamma)$ is illustrated in Figure 4.4. The strong- and weak-friction limits have been known for a long time [162], while a quantitative analytical understanding of the intermediate region, known as the Kramers turnover problem, was developed more recently [165, 166].

Two assumptions in the moderate-to-high classical rate picture used above, which will be carried over to the quantum rate calculations, are:

1. A double-well system is assumed to be an adequate representation of a periodic, multi-well system;

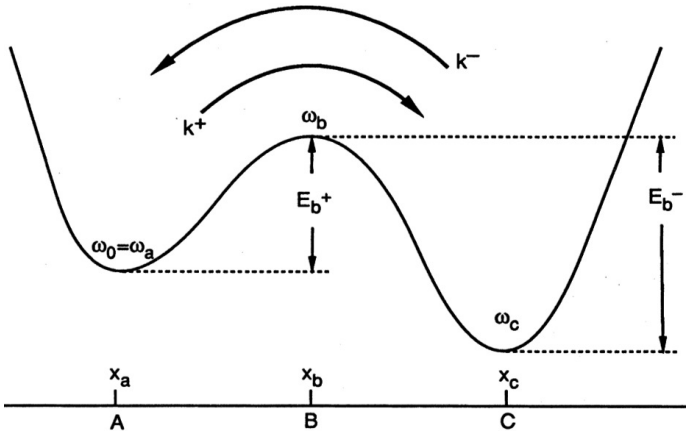

(a) A potential energy curve describing a metastable escape problem [161].

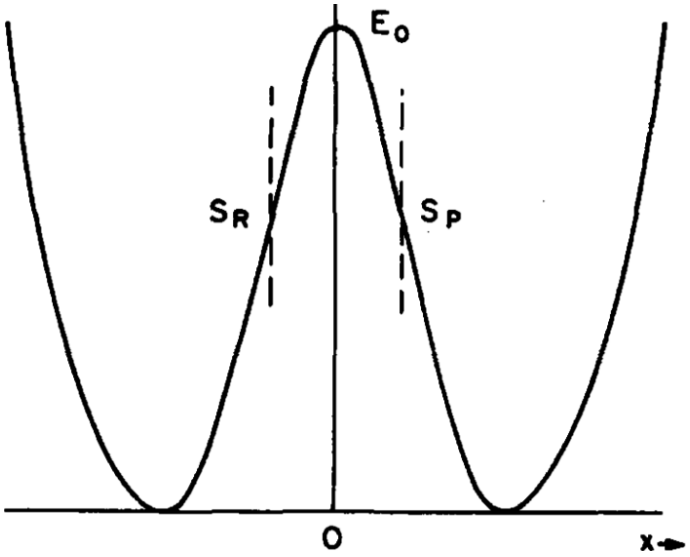

(b) Illustration of the stable states reaction rate theory [164].

Figure 4.3: Figure 4.3a (reprinted with permission from reference [161], Copyright (1990) by the American Physical Society) represents a standard form of potential energy curve used to model reaction rates, which can include jump rates in surface diffusion. Two wells A (oscillation frequency ω_0) and C are separated by a one-dimensional barrier B of energy V_b with respect to well A, and imaginary frequency ω_b. Figure 4.3b (reprinted from reference [164], with the permission of AIP Publishing) illustrates the same type of system but with an emphasis on the two positions S_R and S_P which are central to the stable-states rate theory 4.80. S_P is a point of no return for a particle crossing the barrier, and trajectories that begin to the left of S_R are assumed not to cross the barrier without first re-thermalizing in the left well.

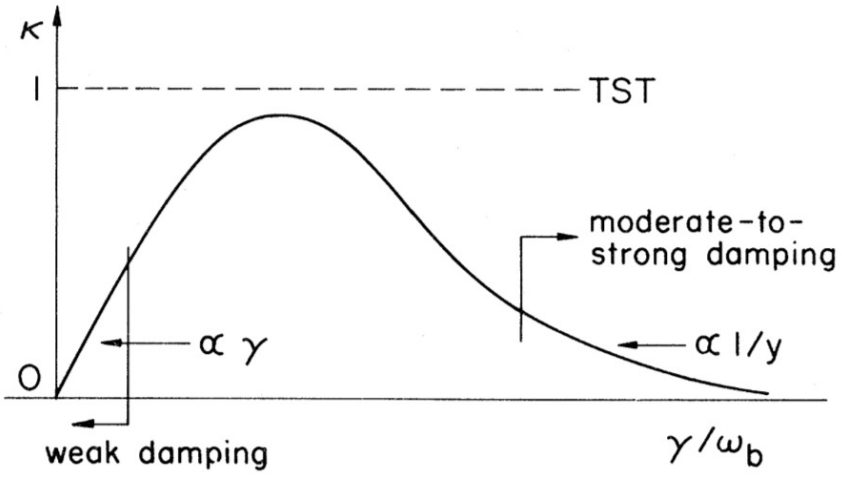

Figure 4.4: Schematic plot of the jump rate in activated diffusion, as a function of Langevin friction strength γ. Reprinted with permission from reference [161], Copyright (1990) by the American Physical Society. At small γ, the frequency of independent attempts at barrier crossing is proportional to γ, while at large γ the rate is suppressed by an increasing proportion of trajectories that cross the barrier top and recross into the reactant region.

2. The exact relative energy of well B is unimportant when calculating the escape rate from well A.

The first assumption is reasonable as long as the friction is high enough that most jumps in the multi-well system are single jumps. The second assumption is not unconnected: within the stable states picture the requirement is that S_P lies sufficiently far to the left of the second well that the exact dynamics once the particle passes S_P are irrelevant as long as they correspond to relaxation into the well. Because the particle is accelerated into the far well by the potential of mean force, it will on average lose energy via friction, and therefore as long as the dissipation is not too weak, relaxation into the far well is rather likely. However, at very low dissipation rates, the particle will often pass once through the well and back over the barrier, with a probability that depends on the exact nature of the target well. In the multi-well system, the particle would perform a multiple jump instead of being reflected.

4.5.2 Approaches to quantum rate theory

In the previous subsection it was argued that classical rate theory at finite friction, at least in the moderate-to-strong friction regime, is equivalent to transition state theory in a multidimensional system governed by non-dissipative (Hamiltonian) dynamics. Generalizing that idea to the quantum mechanical case provides a basis for

quantum mechanical rate theory, as the Hamiltonian can be quantized in a standard way[1]. Because quantum mechanical particles are not point objects, the concept of a flux evaluated at the barrier top is more slippery in quantum mechanics than in classical mechanics. Instead it is convenient to imagine the total flux out of a site as a non-local quantity, represented by a decrease in site occupation probability over time. The potential barrier is still a central object in the theory because it represents a bottleneck for probability flow. A somewhat formal, but very convenient scheme for calculating the outbound flux is given by the $\mathrm{Im}(F)$ or bounce method[2].

The bounce method for the quantum rate has the following attractive features which motivated its use in the present work:

- applies across the whole temperature regime relevant to HeSE experiments;
- takes a continuous potential as input, rather than an effective, truncated description as a two- or few-state system (see Section 4.5.6);
- computationally efficient, allowing a range of dissipation strengths to be easily explored;
- can be applied to arbitrary smooth barrier shapes, as will be demonstrated in Section 4.5.4.

The rate calculated within the bounce framework represents the escape rate from metastable sites to neighbouring stable sites, for example hcp to fcc sites for H/Ru(0001). The rate of transitions back to the metastable sites is assumed to be governed by detailed balance. The role of the site energy difference will be discussed further in Section 4.5.6 in the context of theoretical approaches distinct from the bounce method, namely real-time dynamics in the dissipative two-state system [148], and the bandstructure (ASTST) method [36].

4.5.3 The bounce method

Loss of occupation probability from a metastable system can be rephrased in terms of a complex free energy F. Assuming for the moment that a complex F can be meaningfully defined, the connection between $\mathrm{Im}(F)$ and the quantum rate is

[1] The same argument was used in Section 4.2 to derive the quantum ISF associated with the GLE

[2] "$\mathrm{Im}(F)$" refers to a calculation in which the free energy of a metastable system is formally complex. The term is used interchangeably with "bounce method" in the present Thesis, due to the way F is evaluated.

straightforward to demonstrate [30]. A complex free energy would arise in a system with complex eigenenergies

$$z_n = E_n - i\hbar\frac{\gamma_n}{2}\,. \tag{4.81}$$

Real energy eigenstates evolve with a phase factor of $\exp(-iE_nt/\hbar)$, and by analogy the total probability $|\Psi(t)|^2$ of a complex energy state decays exponentially in time, via

$$P(t) = e^{-\gamma_n t}\,. \tag{4.82}$$

Therefore γ_n corresponds to a rate of escape out of the n^{th} metastable state. If $\hbar\gamma_n << E_n$, the partition function is

$$Z = \sum_n e^{-\beta E_n} + i\frac{\hbar\beta}{2}\sum_n \gamma_n e^{\beta E_n}\,, \tag{4.83}$$

and the imaginary part of the free energy (after expanding $\ln(1+ix)$ as ix) is given by

$$\mathrm{Im}(F) = -k_BT\ln(Z) = -\frac{\hbar}{2}\frac{\sum_n \gamma_n e^{-\beta E_n}}{\sum_m e^{-\beta E_m}}\,, \tag{4.84}$$

which implies the thermally averaged escape rate

$$\Gamma = -2\,\mathrm{Im}(F)/\hbar\,. \tag{4.85}$$

A natural definition of the complex energies for a metastable system produces results for the rate that can be confirmed by other methods. The partition function of the metastable system can first be written, formally, in the general path integral form 4.76, and in particular as the semiclassical expansion 4.77. The path integral is over a large number of stable co-ordinates, and a single unstable co-ordinate [30]. The complex partition function is formally defined by distorting the integration path over the unstable mode to imaginary values of the integration co-ordinate, a procedure motivated by considering an unstable potential to be an analytic continuation of a stable potential [167, 168].

The subsequent dominant contribution to $\mathrm{Im}(F)$ comes from a path $q_B(\tau)$ known as the bounce path, which consists of an oscillation of period $\hbar\beta$ in the inverted barrier potential. For the non-dissipative system, the resulting imaginary free energy is expressed [169, 30] in terms of $q_B(\tau)$ with action S_B whose kinetic part is W_B:

$$\mathrm{Im}(F) = -k_BT\frac{\hbar\beta}{2}\sqrt{\frac{W_B}{2\pi\hbar}}\left|\frac{\det(-\partial^2/\partial\tau^2+\omega_0^2)}{\det'(-\partial^2/\partial\tau^2+V''[q_B(\tau)])}\right|^{1/2}e^{-S_B/\hbar}\,. \tag{4.86}$$

In the discretized path integral 4.76, $q(\tau)$ is sampled at discrete τ_n, which makes $q(\tau)$ analogous to a vector. Differentiation with respect to τ, and multiplication

by constant functions of τ, act as matrices on the $q(\tau)$ vectors. det indicates the determinants of those matrices, and det$'$ indicates the product of all nonzero eigenvalues. The result 4.86 applies when q_B is a non-constant bounce path, which exists only below a certain minimum temperature known as the crossover temperature T_0. The postulated relation 4.85 between $\mathrm{Im}(F)$ and the rate has been demonstrated explicitly via semiclassical transition state theory (SCTST) with a semiclassical propagator [170, 30]. The extension to dissipative systems has been carried out by considering the dissipative system as a high-dimensional conservative system [122, 159, 171]. The standard model which which some traction has been found is once again the linear-coupling Hamiltonian,

$$H_{CL} = \frac{p^2}{2m} + V(x) + \sum_{\alpha} \left[\frac{p_\alpha^2}{2m_\alpha} + \frac{1}{2} m_\alpha \omega_\alpha^2 (x_\alpha - \frac{c_\alpha q}{m_\alpha \omega_\alpha^2})^2 \right], \tag{4.87}$$

where $V(q)$ is now a metastable potential rather than the flat surface limit considered earlier in Section 4.2. The rate is found by:

- *either* calculating $\mathrm{Im}(F)$ using the global Hamiltonian [122, 159]
- *or* applying SCTST directly to the multidimensional system [171].

The two approaches give identical results. SCTST will be briefly reviewed in the supporting discussion in Section 4.5.6. If the postulated rate formula in terms of the free energy is extended to

$$\Gamma = -2\sigma \mathrm{Im}(F)/\hbar\,, \tag{4.88}$$

where $\sigma = 1$ for $T < T_0$, and $\sigma = T/T_0$ for $T > T_0$, then the two approaches agree in all temperature regimes [169, 147, 171, 30]. Expressions for the crossover temperature T_0 in terms of the barrier frequency ω_b and the friction γ are given in Section 4.5.3.1.

4.5.3.1 Phenomenology following from the bounce method

The phenomenology of dissipative quantum escape has been modelled extensively in the literature [159] using a cubic metastable escape potential, with linear dissipation. The cubic potential is conventionally [30] written as

$$V(q) = \frac{1}{2} m \omega_0^2 q^2 \left(1 - \frac{q}{q_0}\right). \tag{4.89}$$

The well region is located around $q = 0$. The potential is bounded on the left ($q < 0$) and unbounded on the right. q_0 is known as the tunneling length. $V(q) < 0$ for all

$q > q_0$. The barrier height is constrained in terms of ω_0 and q_0.

I now summarise the key results derived for the dissipative cubic escape problem, and leave a detailed discussion of the methods to Section 4.5.4. A set of rate curves illustrating the phenomenology is shown in Figure 4.5b, reproduced from [159]. Within the $\mathrm{Im}(F)$ description there is a special temperature known as the crossover temperature, which delineates three regimes known as the activated region, crossover region and tunneling region. The crossover temperature depends on the curvature of $V(q)$ at the barrier top, and on the friction kernel in the frequency domain. For Langevin friction the crossover temperature is given by

$$T_0 = \frac{\hbar}{2\pi k_B}\left(\sqrt{\omega_b^2 - \frac{\gamma^2}{4}} - \frac{\gamma}{2}\right). \tag{4.90}$$

In the activated region the rate is given by the infinite product [42]

$$\Gamma = \frac{\omega_R}{2\pi}\frac{\omega_0}{\omega_b}\left(\prod_{n=1}^{\infty}\frac{\nu_n^2 + \gamma\nu_n + \omega_0^2}{\nu_n^2 + \gamma\nu_n - \omega_b^2}\right)e^{-\beta V_b}\,, \tag{4.91}$$

which diverges at the crossover temperature. The result 4.91 was derived independently of the $\mathrm{Im}(F)$ theory, and can be derived without using path integral methods [172].

The divergence of Equation 4.91 at the crossover temperature can be traced back to the assumption of a globally parabolic barrier. Essentially, a Gaussian integral is performed over an unstable co-ordinate. Therefore, as T approaches T_0 from above, the infinite product formula becomes increasingly inaccurate unless the barrier is expanded to the next order in $q - q_b$. The rate near the crossover temperature can still be derived in a closed form, because integrals such as $\int \exp(-x^4)$ are tractable. As long as the barrier spreads out to become wider than parabolic at order $(q - q_b)^4$, then the integrals using the potential to that order all converge. It can be shown that a smooth formula connects the rate slightly above and slightly below the crossover temperature, and therefore smoothly connects the activated and the tunneling regime [159]. The crossover formula can be derived independently of the $\mathrm{Im}(F)$ method. The effect of dissipation on the crossover regime, at least in the case of Langevin friction, is to reduce the crossover temperature and increase the width of the crossover.

A key feature of the escape rate in the quantum tunneling region is an approximately exponential dependence on the dissipation strength. The strong dependence arises because coupling to the bath effectively increases the width of the barrier [30], and tunneling matrix elements are exponentially sensitive to the barrier width (a

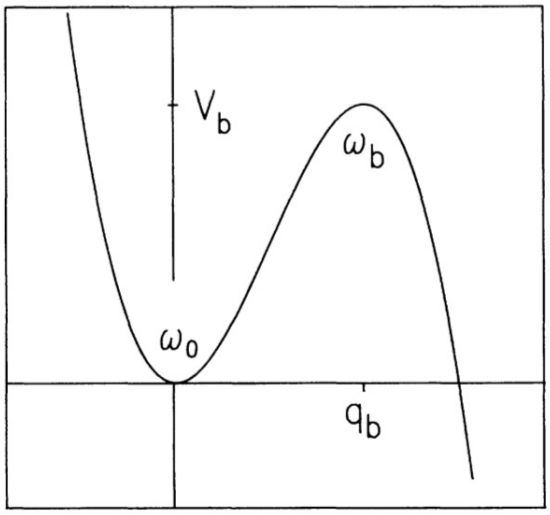

(a) The cubic escape potential, from [159].

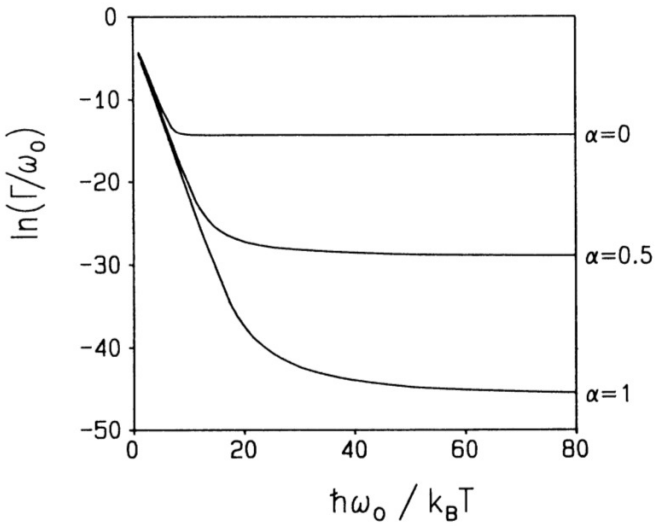

(b) Escape rates [159] from the cubic metastable potential above.

Figure 4.5: Illustration of the metastable cubic potential, and the temperature dependence of the dissipative thermal quantum escape rate [159]. Both figures reprinted with permission from reference [159], Copyright (1987) by the American Physical Society. Rates are plotted in the standard Arrhenius form for three values of the friction coefficient. The curves make clear the exponential suppression of the rate by dissipation, and also the reduction in the crossover temperature. Both the rates and the friction are given in a dimensionless format, with $2\alpha \equiv \gamma/\omega_0$. A key feature of the numerical results is that the deep tunneling rate (the rate in the regime where Γ is approximately independent of temperature) is exponentially sensitive to the friction, being very strongly suppressed by high friction.

well-known result for rectangular barriers, e.g. [173]). The exponential suppression of tunneling by coupling to the bath can alternatively be interpreted in terms of the overlap integrals of bath modes that respond adiabatically to the motion of the tunneling particle (see Section 4.5.6.1). Another effect of high friction which is extremely relevant to the interpretation of HeSE experiments in the deep tunneling regime, is that isotope effects are reduced. In the limit of very high friction $\gamma \gg \omega_0$, the rate below T_0 takes the form [30]:

$$\Gamma = 8\sqrt{6}\alpha^3\omega_0\sqrt{\alpha\frac{V_b}{\hbar\omega_0}}\exp\Big[-6\pi\frac{\alpha V_b}{\hbar\omega_0}\Big(1-\frac{T^2}{3T_0^2}\Big)\Big]\,. \tag{4.92}$$

Along with the isotopic conversion factors $\omega_{0,b} \to \omega_{0,b}/\sqrt{2}$ and $\gamma \to \gamma/2$ the analytic result predicts a factor of 4 for the isotope effect at low temperature, i.e. $\Gamma_H = 4\Gamma_D$. However, such a high friction is incompatible with the absolute rates determined experimentally.

Before progressing with details of the rate calculations, I briefly draw attention back to the experimental context and the possibility of hydrogen diffusion governed by a very high friction. To date, two hydrogen/metal HeSE datasets have been published, namely H/Pt(111) [43] and H/Ru(0001) [23]. The H/Pt(111) rate data showed a gentle curvature indicative of a quantum activated regime. No transition to deep tunneling was observed down to a temperature of around 80 K. The rate data was fitted using the Wolynes rate model (Equation 4.91) for the quantum activated rate [42] in which dissipation is characterised by the Langevin friction γ. The results were parametrized in terms of a renormalized barrier frequency x_b,

$$2x_b\omega_b = -\gamma + \sqrt{4\omega_b^2+\gamma^2}\,. \tag{4.93}$$

Rearranging for γ gives

$$\gamma = \frac{\omega_b^2(1-x_b^2)}{x_b\omega_b}\,, \tag{4.94}$$

and substituting the best fit parameters for protium (H) of $x_b = 0.21$, $\hbar\omega_0 = 31\,\mathrm{meV}$, $\omega_b = 5.4\omega_0$ gives the remarkably large friction coefficient

$$\gamma = 1200\,\mathrm{ps}^{-1}\,. \tag{4.95}$$

A relatively high friction might be expected on the basis of the low mass of hydrogen and the trend seen in the friction as a function of mass for the chemically similar alkali metal atoms Li-Cs on transition metal surfaces [174, 109, 175, 176, 28]. However the extreme contrast between, for example a friction of $\mathcal{O}(1000)\,\mathrm{ps}^{-1}$ for H and $\mathcal{O}(1)\mathrm{ps}^{-1}$ for Li [176, 28] seems implausible on the basis of a 7-fold difference in

mass. Instead, the consistency of a much lower friction interpretation of hydrogen dynamics is highlighted at various points in the present Chapter as well as Chapter 6.

The same data (H/Pt(111)) have also been independently analysed using an incoherent tunneling rate formula whose background is outlined in the supporting discussion in Section 4.5.6. The resulting friction parameter was more realistic with $\gamma_H = 13.6\,\mathrm{ps}^{-1}$. However, the assumptions behind the applied rate formula include a truncation approximation ("we have disregarded thermal excitations in either well" [177]), which would need to be justified in the regime of the experiment to demonstrate that the extracted friction is meaningful. By contrast: in the Wolynes model, the bounce method in general as applied in the present Chapter, and more obviously in the bandstructure (ASTST) method [36], excited states in the well are the leading source of temperature dependence in the quantum activated regime. The breakdown of a truncated incoherent tunneling model at high temperatures has been shown explicitly in a theoretical study of H/Cu(001) dynamics, [178] where STM provided the experimental results [41]. A key feature of the H/Cu(001) theoretical study, distinguishing it from the H/Pt(111) study, was that the tunnel matrix element Δ was estimated from first principles rather than fitted from the experimental rate data.

4.5.4 Application to arbitrary polynomial barrier

The cubic potential is limited as a description of real quantum escape problems, as the shape of the barrier cannot be tuned, and in particular the constraint $\omega_b = \omega_0$ always applies. Here the $\mathrm{Im}(F)$ method is adapted for a general polynomial potential. The fact that the potential is polynomial is important numerically but not conceptually. A polynomial is chosen because it enables a simple and convenient extension of the numerical methods applied to the cubic escape rate, and also because it can flexibly represent any reasonable local potential.

It is convenient to write the paths $q(\tau)$, appearing in the path integral expression of the partition function, as a Fourier expansion

$$q(\tau) = \sum_n Q_n e^{i\nu_n \tau} \tag{4.96}$$

where the ν_n required for the correct periodicity are the Matsubara frequencies [160]

$$\nu_n = \frac{2\pi n}{\hbar\beta}\,. \tag{4.97}$$

The partition function can then be written as a path integral which can be imagined as a high dimensional integral over paths sampled on a finely spaced grid of τ's.

$$Z(\beta) = \int \mathcal{D}q(\cdot) \exp(-S[q(\cdot)]/\hbar) \tag{4.98}$$

where the action $S[q(\tau)]$ is given by

$$S[q(\cdot)] = \int_0^{\hbar\beta} d\tau \left[\frac{1}{2} m\dot{q}^2 + V(q(\tau)) + \frac{1}{2} q(\tau) \int_0^{\hbar\beta} d\tau'\, k(\tau - \tau') q(\tau') \right]. \tag{4.99}$$

The damping function $k(\tau)$ is of the form

$$k(\tau) = \sum_n K_n e^{i\nu_n \tau} \tag{4.100}$$

where the Fourier coefficients K_n are related to the Laplace transform $\hat{\gamma}$ of the classical friction kernel by

$$K_n = \hat{\gamma}(\nu_n)|\nu_n|\,. \tag{4.101}$$

The elimination of the heat bath variables to produce an effective action of the form given in Equation 4.99 is a standard result in the thermodynamics of open quantum systems [30].

The semiclassical approximation consists of locating the stationary points of $S[q(\cdot)]$, expanding the action quadratically for nearby paths, and evaluating the resulting high-dimensional Gaussian integral. The paths $q(\tau)$ for which S is stationary are those that obey the classical equation of motion in the inverted potential, with the effect of the heat bath included rigorously and implicitly via a damping term. The equation of motion reads

$$m\ddot{q}(\tau) - \frac{\partial V(q)}{d\tau} - \int_0^{\hbar\beta} d\tau' k(\tau - \tau') q(\tau')\,. \tag{4.102}$$

which is the classical equation of motion in the inverted potential $-V(q)$ with an additional damping term. Owing to the standard terminology for the solutions, Equation 4.102 will be called the bounce equation. The bounce equation has solutions based in the well region and the barrier region. The inverted well is a barrier, and therefore the only periodic solutions are static ones with the particle precariously balanced at the barrier top. That observation, in combination with the semiclassical expansion of the path integral, reproduces the standard result for the partition function of a damped quantum harmonic oscillator which is readily derivable by other methods. In contrast, the inverted barrier is a well, and therefore there are nontrivial periodic solutions. Most realistic barriers are broader than parabolic to order

$(q - q_b)^4$, and so the time period of undamped oscillations in the inverted barrier increases with amplitude, and there is a minimum time period ($2\pi/\omega_0$) below which the periodic solution collapses onto a static trajectory where the particle rests stably at the minimum q_b of the inverted barrier. The temperature $(k_B\beta)^{-1}$ at which the collapse occurs is the crossover temperature T_0.

For the cubic potential the bounce equation of motion 4.102 in the Fourier domain is given by [30]

$$Q_n = \frac{\omega_0^2 \sum_m Q_{n+m} Q_n}{q_b(\nu_n^2 + \gamma|\nu_n| + \omega_0^2)} \tag{4.103}$$

which is evaluated by iteration. The iteration formula as written is unstable, but can be brought into an equivalent stable form by the transformation

$$Q_n = \frac{R_n}{R_0^2}\,, \tag{4.104}$$

which implies the iteration formula

$$R_n = \frac{\omega_0^2 \sum_m R_{n+m} R_n}{R_0^2 q_b(\nu_n^2 + \gamma|\nu_n| + \omega_0^2)} \tag{4.105}$$

The auxiliary path $r(\tau)$ with Matsubara components R_n is iterated to convergence, and then $q(\tau)$ is given by $q(\tau) = r(\tau)/R_0^2$ [159].

Going beyond the cubic potential, suppose the nonlinear part of the force, $F_{NL}(q)$, contains powers of q up to q^d (where $d \approx 20$ in practice for the numerical potential considered shortly). Choosing a transformation

$$Q_n = \frac{R_n}{R_0^a}\,, \tag{4.106}$$

the transformed iteration formula becomes

$$R_n = \frac{[F_{NL}(r/R_0^a)]_n}{R_0^{a(d-1)}(\nu_n^2 + \gamma|\nu_n| + \omega_0^2)}\,, \tag{4.107}$$

where the numerator is the n^{th} Matsubara component of $F(r(\tau)/R_0^a)$. A reasonable hypothesis would be that in order for the transformed iteration to converge, the power $a(d-1)$ in the denominator should be the same as the highest power of r in $F_{NL}(r)$. I therefore choose

$$a = \frac{d}{d-1}\,. \tag{4.108}$$

Empirically, the resulting iteration scheme always converges, and therefore provides a fast and robust way to find the bounce path $q(\tau)$ for an arbitrary polynomial barrier. Figure 4.6 shows the bounce path at a temperature slightly below the

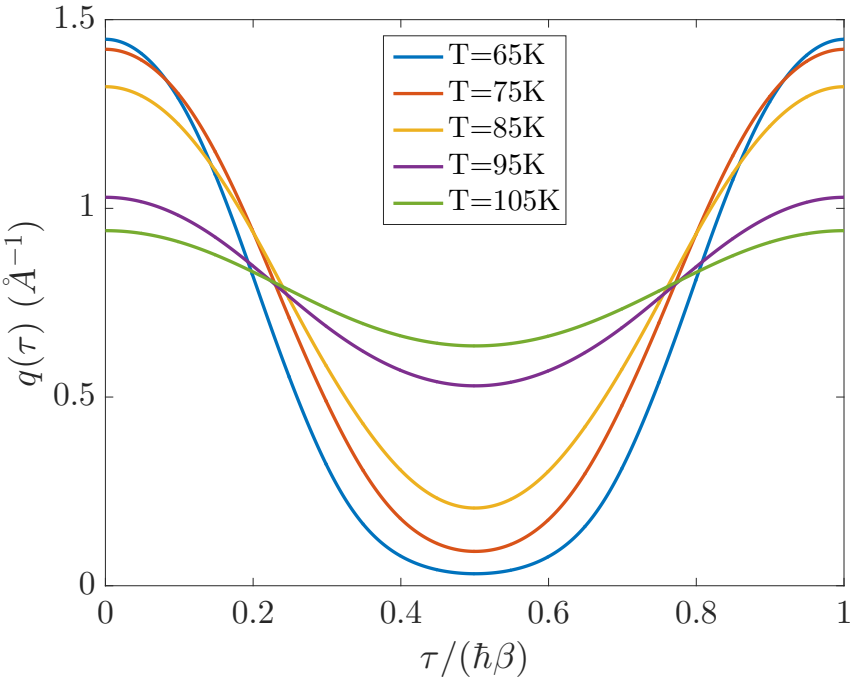

Figure 4.6: Illustration of the collapse of the bounce path $q(\tau)$ onto the barrier position as the temperature approaches the crossover temperature, which is. The escape potential has its barrier top at $q_b = 0.80\,\text{Å}^{-1}$ as shown in Figure 4.7. At temperatures below the crossover, the bounce path consists of a wide oscillation about the barrier top. The flattish region of $q(\tau)$ at the lowest temperature shown is a period spent near the bottom of the well. As T approaches T_0 from below, the amplitude of the bounce path goes to zero. The simulation is carried out with a friction of $1.0\,\text{ps}^{-1}$, and the crossover temperature is 114 K.

crossover temperature, and far below the crossover temperature, for the polynomial barrier used later to calculate escape rates for H/Ru(0001).

The bounce action S_B is found by evaluating the time integral 4.99 for $q_B(\tau)$. The integrand contains the bounce path, the time derivative of the bounce path, and the influence kernel. However, using the bounce equation 4.102 the influence kernel can be conveniently eliminated. In the case of the cubic potential the resulting expression is [30]

$$S_B = \frac{\omega_0^2}{6q_b}\hbar\beta \sum_{n,m} Q_n Q_m Q_{n+m}\,. \tag{4.109}$$

It is straightforward to show that in general the bounce action expressed as a τ integral over $q(\tau)$ is

$$S_B = \int_0^{\hbar\beta} d\tau\,[V(q) - \frac{1}{2}qF(q)]\,. \tag{4.110}$$

The harmonic part of $V(q)$ will always cancel in the integrand. In general there is no benefit of expressing the result in the Fourier domain. The τ integral is evaluated as a Riemann sum.

The bounce action defines the exponent in the quantum rate formula. The prefactor depends on the eigenvalues of the fluctuation operator Λ given by

$$\Lambda f(\tau) = -\frac{\partial^2}{\partial \tau} + [V''[q_B(\tau)]f(\tau)\,, \tag{4.111}$$

where the second term is simply a multiplication in the τ domain. To obtain the prefactor we need to represent the quantum fluctuation operator Λ in a suitable basis [1]. The standard choice is the Fourier basis. Writing the matrix representation of Λ as $\mathbf{C}$, the matrix elements are given for the cubic potential by [30].

$$C_{l,m} = [\nu_l^2 + \gamma|\nu_l| + \omega_0^2] - \frac{2\omega_0^2}{q_b} Q_{l-m}\,, \tag{4.112}$$

where the $l-m$ subscript arises from a convolution in the Fourier domain, derived from the term in the fluctuation operator that is diagonal in the τ domain (i.e. a straight multiplication by a function of τ). The appropriate generalization to higher degree polynomial barriers is

$$C_{l,m} = [\nu_l^2 + \gamma|\nu_l| + \omega_0^2] + [V''_{NL}(q_B(\tau))]_{l-m}\,. \tag{4.113}$$

The final term is evaluated by discrete Fourier transform to $q(\tau)$, then applying the second derivative of the nonlinear potential, then transforming back to the frequency domain. The harmonic part of $V(q)$, which contributes ω_0^2 to the diagonal of $\mathbf{C}$, could be absorbed into the Fourier transform method with the use of $V''(q)$ rather than $V''_{NL}(q)$; it is separated out only because the pattern $\nu_n^2 + \gamma|\nu_n| + \omega_0^2$ occurs so often that it is convenient to show it explicitly where possible. The eigenvalues of $\mathbf{C}$ include one negative value c_{-1}, one zero, and the rest, c_n, positive. Diagonalization of a moderately large $N \times N$ finite truncated version of $\mathbf{C}$ gives accurate results at $N \approx 1000$ for the range of γ considered here, when compared against the reference data in [159].

The rate prefactor below the crossover temperature T_0 contains the kinetic factor

$$W_B = m \int_0^{\hbar\beta} d\tau\, \dot{q}_B(\tau)\,, \tag{4.114}$$

which arises because of the τ-translation invariance of the equation of motion. Above T_0, the kinetic factor does not enter into the problem, because the bounce path has collapsed onto a constant $q(\tau) = q_b$, and a time translation has no effect on a constant path. Below T_0, the quantum rate is given in terms S_B, W_B and the eigenvalues of

[1] Recall from Section 4.4 that when paths $q(\tau)$ are represented over a τ grid of finite spacing, then $q(\tau)$ is analogous with a vector. The action of differential operators such as the fluctuation operator can then be represented in terms of matrices.

C, in the following way:

$$\Gamma = \sqrt{\frac{W_B}{2\pi\hbar}} \frac{\omega_0}{|c_{-1}|} \left(\prod_n \sqrt{\frac{\nu_n^2 + \gamma|\nu_n| + \omega_0^2}{c_n}} \right) e^{-S_B/\hbar}, \tag{4.115}$$

where the product over n is over all eigenvalues except c_{-1} and the zero, and over all the $\nu_n^2 + \gamma|\nu_n| + \omega_0^2$ factors except $n = 0$.

Around and above the crossover temperature, no significant modifications to the cubic-potential methodology are necessary, because the rate theory requires only a small number of parameters of the potential. In particular, far above T_0 we require only V_b, ω_0, ω_b and γ as input. Near T_0 we need the additional parameters c_3 and c_4 [30] which are coefficients in the expansion of the potential around the barrier to 4^{th} order. Evaluation of the rate for $T \gtrsim T_0$ is numerically trivial compared to the quantum rate calculations, as no matrix diagonalizations are required.

4.5.5 H/Ru(0001) escape potential and rates

The potential energy term $V(q)$ appearing in the Caldeira-Leggett Hamiltonian 4.12 is the minimum of the classical global potential energy with respect to the bath co-ordinates. For an adsorbate on a metal surface, and within the Born-Oppenheimer approximation [179] it is therefore reasonable to associate the potential energy term with the global system energy when the substrate is relaxed and the electrons are in their ground state with respect to the nuclear positions. Fluctuations of the lattice about the relaxed configuration, and excitations in the electron gas, should then appear as bath co-ordinates and contribute to the friction. The total energy of the electron gas has to be minimized to high relative precision, and that task falls to modern first-principles electronic structure methods such as density functional theory (DFT) [21].

The present Section makes use of a three-dimensional potential energy surface $V(x, y, z)$ calculated with DFT for a previous theoretical treatment of H/Ru(0001) diffusion [180]. As noted in the previous study, there is a substantial difficulty arising from the experimental comparison with DFT, namely that the fcc/hcp site energy difference calculated within DFT is not consistent with the experimentally derived value [23]. In fact there is about a 30 meV discrepancy between the two values. There is therefore some justification for applying a site-levelling transformation to the potential, which brings the calculated site energy difference into line with the experimental value of 22 meV. The site-levelling procedure is:

- reflect $V(x, y)$ about a line passing through top sites (which exchanges the

two types of hollow sites with each other, but maps top sites to top sites, and bridge sites to bridge sites);

- add linear combinations of the original and reflected potentials.

$V(x, y, z)$ is available at 31 x, y locations within the surface unit cell, at 31 values of the surface perpendicular co-ordinate z. After applying symmetry operations, the 31 points in x, y map onto 144 points representing a 12-fold contraction of the unit cell. The sampled x, y form a square lattice in the co-ordinate system

$$u = x - \frac{y}{\sqrt{3}} \; ; \; v = \frac{2y}{\sqrt{3}} \, , \tag{4.116}$$

in which the standard primitive surface unit cell is also square.

To extract the one-dimensional escape potential, $V(x, y, z)$ is first minimized in the z direction to produce a two-dimensional potential $V(x, y)$. $V(x, y)$ is interpolated onto a fine Cartesian grid, using MATLAB's `csape` function with periodic boundary conditions. The function $V(x, y)$ is shown in Figure 4.7. The x direction is the $< 1, 0 >$ direction as defined in Section 2.2.1, i.e. $\hat{\mathbf{x}}$ points between top sites. A transition path can be chosen whose properties are all parametrized in terms of x. Because we know the approximate shape of the transition path *a priori*, there is no need for sophisticated methods to find the exact path, which is found by minimising $V(x, y)$ in y. The transition path visits fcc and hcp sites alternately, and is illustrated in Figure 4.7. I define the reaction co-ordinate q as the distance travelled along the transition path. If g and h are the gradients dy/dx and dz/dx evaluated along the transition path, then the reaction co-ordinate can be written as

$$dq^2 = (1 + g^2 + h^2)dx^2 \, . \tag{4.117}$$

The present work uses only the one-dimensional potential energy because of the relative simplicity of finding the bounce path in one dimension. A one-dimensional approximation is justifiable because adsorption sites in the three-dimensional H/Ru(0001) potential are connected by narrow, approximately straight channels. It would be desirable to include all the degrees of freedom of $V(x, y, z)$ explicitly in the calculation in future work. Algorithms to locate the bounce path in a multidimensional potential are known (for example as stated in [185]). As long as transverse frequencies $\Omega_i(q)$ along the escape path do not vary too rapidly along the transition path the $\mathrm{Im}(F)$ rate is given by performing the one-dimensional calculation on a corrected potential $V(q) \to V(q) + \hbar \sum_i \Omega_i(q)/2$ [186] which could be described as a local zero-point energy shift. The simple correction does not hold when the transverse modes are strongly coupled to the environment, and therefore the effective

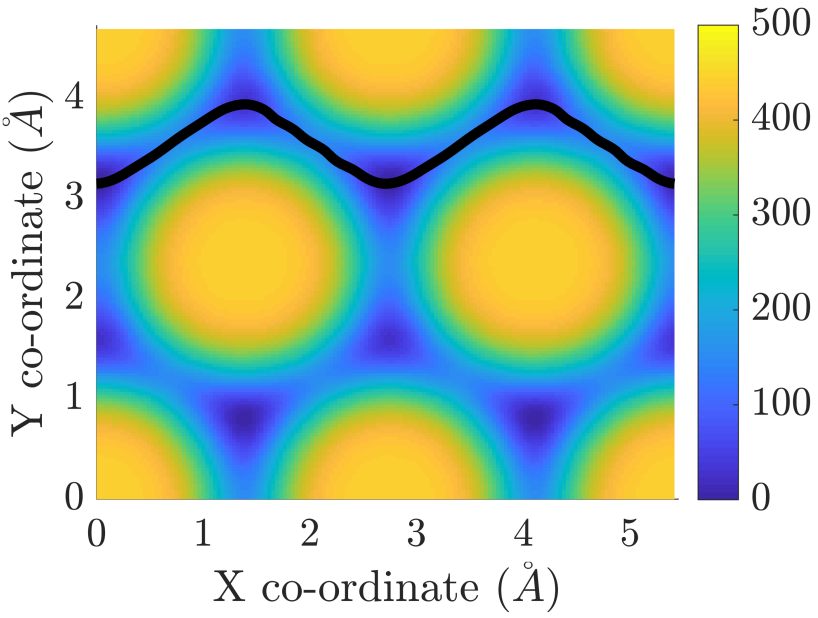

Figure 4.7: The smooth interpolated two-dimensional H/Ru(0001) potential $V(x, y)$ in units of meV, with a (non-unique) transition path shown as a solid black curve, used to model the quantum escape rate. The potential along the transition path is shown in Figure 4.8. The (pre-interpolated) potential was computed with DFT over a $31 \times 31 \times 18$ grid which, after applying symmetry operations, is a 12-fold contraction of the primitive surface unit cell. The DFT calculations were carried out by K. Thor Wikfeldt as part of the theoretical collaboration associated with the cited HeSE H/Ru(0001) experimental work [23, 180]. For each configuration of hydrogen on the surface, the PBE functional [181, 182] was used, with plane-augmented-wave pseudopotentials [183] as implemented by the VASP code [184] to evaluate the total energy which defines the potential energy surface. A 3×3 Ru(0001) supercell with four layers was used, and the substrate was allowed to relax.

one-dimensional potential could shift slightly with increasing friction. However, the adiabatic correction calculated from the transverse curvature at the well (hcp) and barrier (bridge) location is small. Vibrational frequencies at the well and barrier are collected for Ru, Pd and Cu in Table 6.1. The adiabatic correction is predicted to increase the barrier by approximately 10 meV for H, so the effective potential is not expected to change significantly with moderate friction. Because even the most well-converged DFT calculation is not systematically accurate down to the 10 meV level, for the calculations in the present Chapter the final one-dimensional model potential is rescaled for consistency with the activation energy measured in the quantum activated regime, which was 95 meV for hopping out of fcc sites, and by detailed balance is therefore 73 meV for hopping out of hcp sites, after subtracting the measured site energy difference of 22 meV.

The final effective one-dimensional escape potential used for the rate calculations is shown in Figure 4.8, in a high-order polynomial fitted representation. Although the potential is not completely characterized by a small number of parameters, there are still some key parameters that have a qualitative bearing on the escape rate. Numerical values of important parameters are given in Table 4.1. The well frequency ω_0 is important as it defines the maximum possible attempt frequency in the classical limit. Both the classical rate and the quantum tunneling rate are expected to have an approximately exponential dependence on V_b the barrier height. The barrier frequency ω_b is important as it sets the maximum possible crossover temperature. The (bare) tunneling length is defined as the first solution to $V(q) = 0$ for $q > 0$, and is significant because rate of quantum tunneling is exponentially sensitive to the barrier width as well as the height. Finally, the location of the barrier top is important for the escape rate methodology as it can be used to give a robust starting point for iteration to the bounce path. Here q_b is a little more than halfway to q_0; for the cubic potential the two distances are related by $q_b = 2q_0/3$.

Figure 4.9 shows the numerical $\mathrm{Im}(F)$ escape rate at four different values of the friction γ from the zero-friction limit up to $\gamma = 200\,\mathrm{ps}^{-1}$. Experimental data from Chapter 6 is overlaid; the experiment will be discussed in detail in the later Chapter. The experimental measure of the rate is the inverse residence time of a hydrogen atom in the metastable (hcp) site. There are three equivalent escape paths from each metastable site, which has been accounted for in the quantum rate calculation by multiplying the one-dimensional result by 3. Within the $\mathrm{Im}(F)$ framework the multiplication by 3 emerges automatically as we are required to sum over the three saddle points that contribute to the imaginary part of the partition function. As expected, the theory at low friction systematically overestimates the rate in the quantum activated regime, a fact which has previously been interpreted as implying

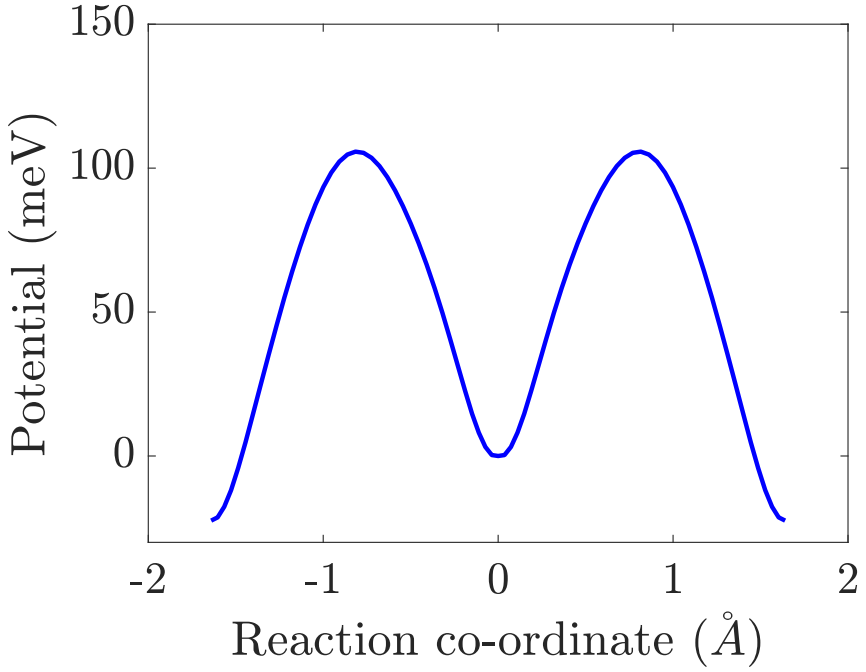

Figure 4.8: The escape potential $V(q)$ along the transition path. The well region is a metastable hcp site. The site-levelling operation described in the main text has been applied to enforce a fcc/hcp site energy difference equal to the experimental value of 22 meV. Additionally, the one-dimensional potential has been scaled to reproduce the apparent activation energy in the quantum activated regime of the rate curve. The deep tunneling rate derived from the rescaled potential agrees well with the experimental rate, suggesting that the rescaling is a sensible step by which to interpret and understand the experimental data, regardless of whether or not it can be justified from the *ab initio* potential in terms of adiabatic corrections from transverse vibrations.

Table 4.1: Key parameters of the effective escape potential shown in Figure 4.8. The potential describes metastable escape of hydrogen atoms from hcp threefold sites on Ru(0001). As described in the main text, the potential is given approximately by the first-principles DFT potential described in Figure 4.7, evaluated along the transition path between the hcp site and a nearest neighbour fcc site. However, the potential has been adjusted for consistency with experiment, in particular to match the activation energy for fcc to hcp hopping in the quantum activated regime. The value of the DFT calculation is to provide a realistic barrier shape, even though the absolute scale of the barrier has been tuned.

Parameter	**Value**
Well frequency ω_0	$113\,\mathrm{rad{\cdot}ps^{-1}}$
Barrier height V_b	106 meV
Barrier frequency ω_b	$82\,\mathrm{rad{\cdot}ps^{-1}}$
Crossover temperature T_0	100 K
Tunneling length q_0	1.45 Å
Barrier location q_b	0.8 Å

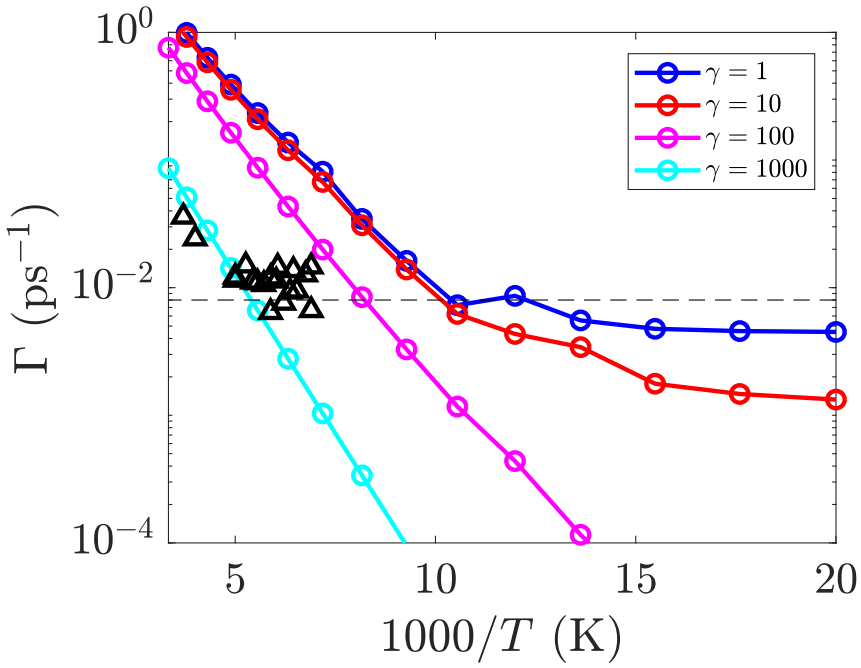

Figure 4.9: Temperature dependence of escape rate of $\Gamma = 1/\tau$ of H from the adjusted potential whose parameters are given in Table 4.1. τ is defined as the mean residence time in a threefold hcp site. The rate is given at $\gamma = \{1, 10, 100, 1000\}$ ps^{-1} (blue, red, magenta and cyan respectively). $\gamma = 0$ corresponds to the transition state theory limit. Black wedges represent experimental data discussed in detail in Chapter 6. The fact that the experimental rate is largely overestimated in the quantum activated regime is repeatedly returned to in Chapter 6 in the context of new experimental data, and assigned to low friction. The best description of the experimental deep tunneling rate, as estimated by the dashed black line, is achieved at low friction.

a high friction [43, 35]. However, an interpretation in which the friction is too low for the Wolynes rate to apply is more consistent with evidence from various directions including other HeSE experimental data as discussed further in Chapter 6. A low friction interpretation could also explain why the crossover temperature observed in present (Chapter 6) and past [23] H/Ru(0001) HeSE data, and H/Ni(111) data [36] is anomalously high. A low friction can limit the rate in the quantum activated regime as the assumption of initial equilibrium in the well assumes that transitions between the ground and excited well states are sufficiently fast. For tunneling out of the ground state, no such restriction applies, and so the approximately temperature-independent deep tunneling rate could be reached at a higher temperature than given by Equation 4.90 which is valid only for moderate to strong friction.

At low friction as suggested by the preceding discussion, the predicted isotope effect in the tunneling regime is very large. Figure 4.10 shows the H and D escape rates from the adjusted potential when $\gamma << \omega_0$. Experimental results from Section 6.3 are overlaid. The experimental data referring to D in Figure 4.10 can be

explained the same way as the H results: in the quantum activated regime, the experimental rate tracks the theoretical quantum activated rate except for a prefactor related to low friction. The rate is expected to stop falling when it reaches the deep tunneling regime where the rate of excitation between the ground and excited well states is no longer relevant. For weak friction, the theoretical escape rate in the deep tunneling regime is approximately 1000× slower for D than H. If the relatively low experimental rate in the quantum activated regime is indeed caused by low friction, then Figure 4.10 implies that a significantly faster D jump rate could have been observed at low temperatures in the HeSE experiments, if only the friction was higher. However, a faster rate would then also be expected for H hopping. There is no evidence in the theoretical framework of the present Section to suggest that very fast deep tunneling should be observed experimentally for D/Ru(0001).

4.5.6 Quantum rate theory: supporting discussion

The bounce method for the dissipative quantum escape rate is extremely convenient, but as presented so far relies on a rather formal hypothesis about complex energies. Additionally, the role of the target site, and the site energy difference, is not included explicitly in the calculation. In other words the escape rate from the metastable well to the neighbouring site is assumed to be the same as a fictitious escape rate in the absence of a second minimum in the potential. Neglecting the details of relaxation to the second site was justified heuristically for moderate to large friction in the classical case (Section 4.5.1), in other words the rate "from A to B" can be recast as a rate "from A to anywhere". It is plausible, but not completely obvious, that the same trick is allowed in the quantum rate problem.

In the present Subsection I outline supporting arguments and alternative perspectives on the quantum rate problem. However, the results obtained via the bounce method remain the central results of the Section.

4.5.6.1 Incoherent tunneling in the two-state system

Consider the two lowest energy eigenstates associated with a double-well potential such as that represented in Figure 4.3a. If the double well potential is symmetric then the eigenstates are delocalized across both wells (like Bloch states would be in the extended, periodic potential). The lowest energy eigenstate will be spatially symmetric, and the first excited state antisymmetric. The energy separation (tunnel splitting) can be written as $\hbar\Delta/2$ which is analogous to the bandwidth in a periodic potential. At low temperatures when only the lowest two energy eigenstates are

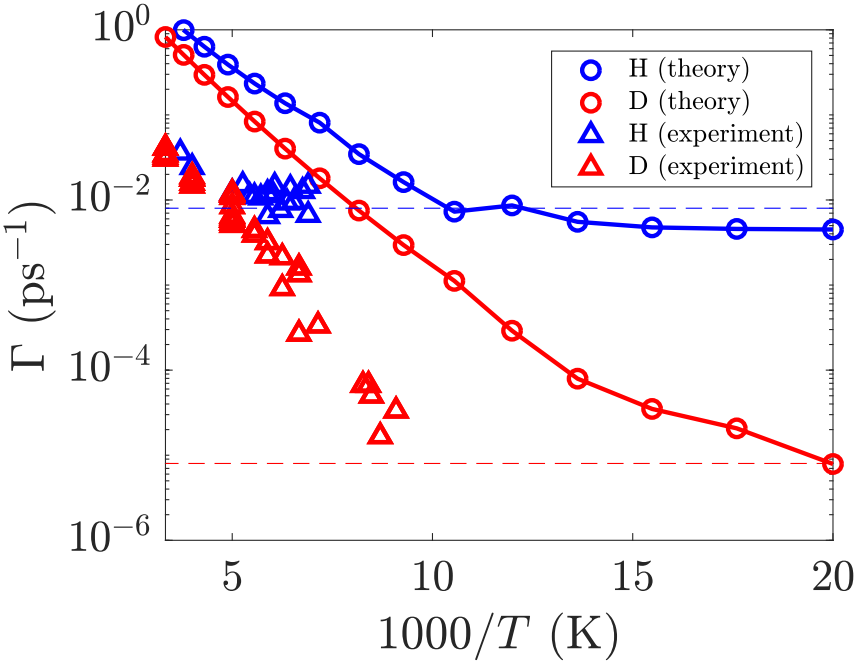

Figure 4.10: Temperature dependence of the escape rate $\Gamma = 1/\tau$ for H and D from the effective one-dimensional metastable potential shown in Figure 4.8, at a friction of $\gamma_H = 1\,\mathrm{ps}^{-1}$, $\gamma_D = 0.5\,\mathrm{ps}^{-1}$. τ is defined as the mean residence time in a threefold hcp site. Open circles represent theoretical results, and triangles of the same colour the corresponding HeSE experimental results. Dashed lines represent nominal deep tunneling rates. The experimental background and data analysis methods leading to the experimental rate curves are described in detail in Chaspters 2 and 6. The escape rate for H is as shown in Figure 4.9. The relationship between the theoretical and experimental rates can be rationalized in the same way for both isotopes, as discussed at length in the main text. In the quantum activated regime the theoretical rate curve gives a good description of the energetics (activation energy, gradient of the rate curve) but the absolute experimental rates are significantly slower, which could be caused by low friction and is consistent with multiple jumps being observed in the experimental data within the fcc/hcp triple jumps model of Section 2.2.1). However, the rate is effectively bounded from below by the deep tunneling rate which can be realized at significantly lower friction since there is no requirement for large energy transfers to reach the barrier top (classically) or the first excited well state.

Table 4.2: Order-of-magnitude energy scales that apply when H/surface diffusion potentials are truncated as described in the present section. The tunnel splitting between equivalent sites is taken as the bandwidth of the lowest band (fcc) for H/Ni(111) [36]. The tunnel splitting between inequivalent sites is taken as the bandwidth when the potential was completely symmetrized with respect to the site energy difference (see Figure 4.30 in [36].) The bias energy ϵ is typically much larger than either tunnel splitting. The well frequency $\hbar\omega_0$ is larger still, implying that a truncation scheme neglecting higher excited states at low temperatures is plausible. The thermal energy associated with HeSE experiments is shown for the nominal temperature range $70\,\mathrm{K} \leq T_s \leq 300\,\mathrm{K}$.

Parameter	**Value, H (meV)**	**Value, D (meV)**
Tunnel splitting $\hbar\Delta_0$, equivalent sites	5×10^{-4}	5×10^{-7}
Tunnel splitting $\hbar\Delta_0$, inequivalent sites	0.05	1.5×10^{-4}
Bias energy $\hbar\epsilon$	$\gtrsim 10$	$\gtrsim 10$
Well frequency $\hbar\omega_0$	100	70
Thermal energy $k_B T$	$6 - 25$	$6 - 25$

relevant, the Hamiltonian of the double well potential can be reconstructed from the low energy states as[1]

$$H = \frac{\hbar\Delta}{2}\sigma_x \equiv \frac{\hbar}{2}\begin{pmatrix} 0 & \Delta \\ \Delta & 0 \end{pmatrix}, \tag{4.118}$$

where σ_x is the Pauli matrix[2]. The basis states are equal mixtures of the delocalized energy eigenstates, analogous to Wannier states in the periodic potential. If instead the double well is asymmetric with a bias $\hbar\epsilon$ between the sites then the truncated Hamiltonian can be represented in a basis of localized states as

$$H = \frac{1}{2}\hbar\Delta\sigma_x + \frac{1}{2}\hbar\epsilon\sigma_z \equiv \frac{\hbar}{2}\begin{pmatrix} \epsilon & \Delta \\ \Delta & -\epsilon \end{pmatrix}. \tag{4.119}$$

The minimum energy of higher excited states with respect to the lowest two states is roughly the harmonic ladder energy $\hbar\omega_0$ where ω_0 is the well frequency. The typical energy scales for hydrogen diffusion in HeSE experiments are given in Table 4.2. The numerical tunnel matrix elements Δ_0 are inferred from a bare potential, neglecting coupling to the environment.

The advantage of constructing a truncated system is that it allows the $\mathrm{Im}(F)$ method to be verified by the direct calculation of a real-time conditional probability. I suggested earlier in the present Chapter that a calculation of the ISF would verify or refute any questionable assumptions underpinning a rate theory. In the case of the

[1] In Section 4.3, Δ was defined as an energy, but based on the more common convention in the two-state system literature, Δ and ϵ are defined here as frequencies

[2] The Pauli matrices were introduced in Section 2.1.2.

two-state system, results have been established for a quantity $P(t)$ which contains very similar information to the ISF. $P(t)$ is the probability of finding the particle in state $(1,0)$ of the TSS given that it was in the state $(1,0)$ at time $t = 0$ with the bath initially thermalized with respect to the definite initial state of the particle. Exponential relaxation of $P(t)$ to its equilibrium value strongly implies that the ISF at long times will be consistent with incoherent jump motion, since then $P(t)$ solves a master equation

$$\dot{P}(t) = \Gamma_2 - (\Gamma_1 + \Gamma_2)P(t)\,, \tag{4.120}$$

with forward jump rate Γ_1 and reverse jump rate Γ_2[1].

It was noted in Figure 4.6 that at low temperatures the bounce path $q_B(\tau)$ starts to develop a plateau where the particle rests in the reactant region for some time. When the system is only weakly biased, $q_B(\tau)$ develops two plateaus, one for the reactant region and one for the product region. Assuming Langevin friction still, [1] the escape rate $k^+(T,\epsilon)$ from the higher-energy site under such conditions can be derived within $\mathrm{Im}(F)$ as [187, 30]

$$k^+(T,\epsilon) = \frac{1}{4}\frac{\Delta^2}{\omega_c}\Big(\frac{\hbar\omega_c}{2\pi k_B T}\Big)^{1-2K}\frac{|\Gamma(K + i\hbar\epsilon/2\pi k_{BT})|^2}{\Gamma(2K)}e^{\hbar\epsilon/2k_BT}\,, \tag{4.121}$$

where ω_c is a frequency chosen somewhere between the energy scale of the bare TSS and the excited states of the full potential, beyond which bath modes are assumed to respond adiabatically. K is a dimensionless measure of the strength of friction, given in terms of the Langevin friction γ and the site separation q_0 by

$$K = \frac{m\gamma q_0^2}{2\pi\hbar}\,, \tag{4.122}$$

and Δ is a renormalized tunnel matrix element that depends on the bare tunnel matrix element Δ_0 and the coupling to the bath: roughly speaking it arises from the overlap integrals between high-frequency ($\omega > \omega_c$) bath oscillator states as they follow the tunneling particle adiabatically, however the precise form of Δ depends on

[1] In analogy with the Chudley-Elliott model, Section 2.2.1) but for just two sites such that the probability of occupying the second site is $1 - P(t)$.

[1] In the dissipative two-state literature, reference is often made to Ohmic dissipation, which is distinguished from Langevin friction here for clarity. The defining property of Ohmic dissipation is that the friction kernel in frequency space is non-zero at the origin. The low-frequency behaviour of the bath is particularly important for studies of the dissipative two-state system with low intrinsic energy scales. In contrast, a Langevin friction kernel remains constant up to arbitrarily high frequencies. Therefore, Langevin friction implies Ohmic dissipation but the converse is not true. As explored in detail earlier in the present Thesis for flat-surface dynamics, a realistic friction kernel has a physical cutoff frequency. In the present Section ω_c is a fictitious cutoff frequency used in the construction of an effective dissipative two-state Hamiltonian. The consequences of a physical cutoff frequency comparable to other frequency scales in the problem (ϵ, say) are not explored here, hence dissipation is described as Langevin friction.

the exact underlying continuous potential [188]. If the renormalized tunnel matrix element is used to construct the dissipative two-state system (spin-boson) Hamiltonian

$$H = \frac{1}{2}\hbar\Delta\sigma_x + \frac{1}{2}\hbar\epsilon\sigma_z + \frac{1}{2}q_0\sigma_z\sum_\alpha c_\alpha x_\alpha + \sum_\alpha \frac{1}{2}m_\alpha\omega_\alpha^2 x_\alpha^2\,, \tag{4.123}$$

with harmonic bath modes x_α then it can be shown that the real-time quantity $P(t)$ relaxes exponentially with a rate that agrees with the $\mathrm{Im}(F)$ calculations[189, 177, 148, 30], except at simultaneously weak dissipation, very low bias and very low temperature $k_BT \lesssim \hbar\Delta$, a regime that does not concern HeSE experiments at present. For completeness I note here that when treating the tunneling dynamics of the two-state system, progress can be made with mapping physical baths onto the harmonic bath, for example the renormalized tunnel matrix element has been derived when the bath is modelled as free fermions [190], and the combined action of electronic and phononic baths has been modelled as a harmonic bath with whose coupling spectral density is the sum of an Ohmic ($\propto \omega$) and super-Ohmic ($\propto \omega^3$) term [191]. Any further comparison of different families of heat bath and their inter-relationships is not part of the present work.

The application of the bounce method to a strongly biased system, where the details of the final state are assumed to be irrelevant and only the product and barrier region are considered explicitly, is therefore an extension of a case where the $\mathrm{Im}(F)$ rate can be verified by real time dynamical calculations. Proof of an exact or approximate correspondence between real time dynamics and the $\mathrm{Im}(F)$ rate for a strongly biased two-state system is beyond the scope of the present plausibility argument, but could be a valuable piece of further work. The bounce method as applied in the present work does not make use of a truncation approximation, and therefore automatically accounts for excited well states, hence the occurrence of a crossover to the quantum activated regime.

4.5.6.2 Bounce method and semiclassical transition state theory

Semiclassical transition state theory (SCTST) can be introduced along similar lines to the classical case. Under the general TST assumptions of thermalization and no recrossing, as discussed classically in Section 4.5.1, the rate is the thermal flux at the barrier top divided by the well population. In classical mechanics the unidirectional probability flux is given by the one-sided velocity weighted by the phase space probability density,

$$j = \frac{1}{Z}\int dq\,dv\,p(q,v)\,v\,\theta(v)\,, \tag{4.124}$$

where $\theta(v)$ is the Heaviside step function. In quantum mechanics the probability current in one dimension is defined as a spatially varying current $j(q)$ which allows the time-dependent Schrödinger equation to be written as a continuity equation. The wave mechanical expression for the flux associated with a wavefunction $\Psi(x)$ is given by a well-known expression [66],

$$j(q) = \frac{\hbar}{2mi}[\Psi^*(q)\frac{\partial\Psi}{\partial q} - \Psi(q)\frac{\partial\Psi^*}{\partial q}]\,. \tag{4.125}$$

Given the wave mechanical definition of the momentum operator $p = -i\hbar\partial x$, it is easy to verify that the flux associated with a plane wave state $\Psi(x) = \exp(ikx)$ is $\hbar k/m$, which is the classical velocity associated with momentum $p = \hbar k$. Both terms in the expression 4.125 contribute equally to the final answer.

The co-ordinate-based, wave mechanical definition of the flux can be recast in terms of a flux operator. The expectation of the operator $\delta(q-q_b)p/(2m)$ reproduces one term of the previous expression 4.125 for the flux at a given location q_b:

$$\langle\Psi|\delta(q-q_b)p|\Psi\rangle = \frac{\hbar}{2mi}\Psi^*(q)\frac{\partial\Psi}{\partial q}\,, \tag{4.126}$$

which can be demonstrated by inserting the identity $\mathbf{1} = \int dq|q\rangle\langle q|$ between the operators $\delta(q-q_b)$ and p. As in the classical case, we are actually interested in the one-directional or outbound flux, which can be defined by retaining only positive momenta. However, the expectation of the unidirectional flux operator in an arbitrary state, $\langle\Psi|\delta(q-q_b)p\theta(p)|\Psi\rangle$, is liable to be negative, leading to a rate that can change sign as the temperature changes. Therefore, the unidirectional flux as described here does not lead to a sensible rate theory.

Via a scheme known as a classical path approximation [170], the problematic $\langle\delta(q-q_b)\theta(p)p\rangle$ theory can be converted into a sensible rate theory in which the rate is always positive. The quantum propagator is taken as the Van Vleck semiclassical propagator [192] which consists of an expansion about classical paths, just as the partition function was expanded about classical paths in Equation 4.77 for example. The classical paths appearing in SCTST are strongly related to the bounce path in the $\mathrm{Im}(F)$ method. The rate is ensured positive if the flux is interpreted in terms of classical path velocities at the barrier, rather than momenta. Generalization to a dissipative system is achieved in a similar way to the classical case, by considering a dividing surface in the multidimensional co-ordinate space where most of the co-ordinates are bath modes. In doing so, results equivalent to the $\mathrm{Im}(F)$ theory have been derived at least down to the crossover temperature and slightly below [171].

As just presented, SCTST appears to rely on an arbitrary sleight of hand, when

momenta are replaced with velocities associated with a semiclassical expansion of the quantum propagator. However, the sleight of hand can be justified in some detail by considering the short-time limit of a well-defined time correlation function whose long-time limit represents the formally exact quantum rate [193]. Just as with classical TST, the loss of accuracy due to taking the short-time limit rather than the long-time limit of flux correlations can be viewed in terms of a recrossing probability [194]. As indicated in the context of the truncated two-state system (Section 4.5.6.1), rate calculations making use of correlation functions or time-dependent conditional probabilities are clearly preferable to thermodynamic theories using subtle approximations that are difficult to justify. Techniques that provide access to real-time quantities in dissipative systems are therefore a potentially rich source of further work on the subject. One such technique, the NIBA, has been described tangentially in Section 4.5.6.1. Two more feasible numerical techniques are described in Chapter 7.

4.5.6.3 Comparison with ASTST (bandstructure method)

In the classical transition state theory reviewed in Section 4.5.1, the rate is given as the flux at a barrier top divided by the population of a neighbouring well. The rate could alternatively be written as an integral over only states that propagate, since those are the states with a finite flux at the barrier top:

$$\Gamma \propto \int_{V_b}^{\infty} dE\, p(E) j(E)\,, \tag{4.127}$$

where $p(E)$ is the probability of the particle having energy E, and $j(E)$ is the flux at the barrier top. Particles in states with $E < V_b$ do not contribute to the rate.

In the quantized system, the energy eigenstates can be chosen as Bloch states $|k, n\rangle$ with wavevector k and band index n. All Bloch states propagate, and perturbation theory in k gives the mean propagation velocity v_g of a state $|k, n\rangle$ in terms of the dispersion relation $E(k)$ (at fixed n) as

$$v_g = \frac{1}{\hbar}\frac{\partial E_n}{\partial k}\,, \tag{4.128}$$

without requiring explicit knowledge of the eigenfunctions $\Psi_{k,n}(x)$ themselves [146]. In Actual States Transition State Theory (ASTST) [36], the rate is proposed as the mean unidirectional velocity, divided by the distance l between neighbouring sites.

The resulting rate expression is then (in one spatial dimension for simplicity)

$$\Gamma = \frac{1}{lZ} \sum_n \int dk\, v_g(k) e^{-\beta E(k)}, \tag{4.129}$$

where Z is the partition function $\sum_n \int dk \exp(-\beta E(k))$. The method gives very good agreement with experimental results in the quantum activated regime when the full three-dimensional potential is used to calculate the bandstructure [35, 36]. Inelastic tunneling between inequivalent sites is neglected in ASTST. Therefore the low-temperature ASTST rate tends to underestimate the experimentally observed low-temperature jump rate unless the site energy difference is artificially reduced to allow elastic tunneling between nearest neighbour adsorption sites. Curiously, ASTST exhibits a flat contradiction with theories of the incoherent tunneling rate, which suggests that the excellent agreement with experiment at higher temperatures could be accidental, or at least that further work is needed to clarify the physical significance of ASTST. To illustrate the problem, the ASTST rate can be evaluated in exact form for the simple one-dimensional tight-binding model of Section 4.3, where the dispersion relation is given by (Equation 4.47, where Δ has units of energy rather than frequency)

$$\epsilon(k) = -2\Delta \cos(k)\,. \tag{4.130}$$

At temperatures $T \gg \Delta/k_B$, occupation of all k-states is equally likely, in other words we can replace $e^{-\beta E(k)}$ with 1. Δ for elastic tunneling (e.g. fcc to fcc) is so small numerically that $T \gg \Delta/k_B$ is automatically satisfied in HeSE experiments to date and for the foreseeable future. The integral 4.129 is then easily evaluated as

$$\Gamma = \frac{\Delta}{\pi\hbar}\,. \tag{4.131}$$

The notable feature of Equation 4.131 is that the rate is linear in Δ, whereas the incoherent tunneling rate discussed in 4.5.6.1 is quadratic in Δ. Inspection of the rate curves for H and D in Figure 4.28 of [36] and comparison with Table 4.3 of the same reference where the lowest-band bandwidths for H and D are $0.5\,\mu$eV and 0.5 neV respectively, shows that the low temperature rates are consistent with the simple analytical prediction of 4.129 and indeed that the isotope effect Γ_H/Γ_D scales with Δ rather than Δ^2. The isotope effect predicted within the bounce method is of a similar order by accident, because it is associated with tunneling through one barrier rather than two, but the rate scales as Δ^2. The scaling of the rate with Δ^2 is a feature of so-called non-adiabatic transitions, where the tunnel splitting is much smaller than the response time of the bath [195]. When higher excited bands with a

relatively large bandwidth make a large contribution to the rate, as in the quantum activated regime, deviation from Δ^2 behaviour does not automatically make the theory unrealistic. Clarification of the conditions under which a diffusion rate or jump rate linear in Δ could really occur, and how those conditions relate to the validity of the bandstructure method as applied to HeSE experiments, is left as further work.

4.5.7 Conclusions

The bounce method has been used to calculate the thermal dissipative escape rate of hydrogen atoms out of the metastable hollow sites on Ru(0001). The escape rate can be plausibly identified with the jump rate. The escape potential is taken as the H/Ru(0001) potential calculated with DFT, evaluated along the transition path out of a metastable site. Dissipation is assumed to be linear, position-independent and frequency-independent, and is therefore parametrized by a Caldeira-Leggett model whose classical limit reproduces the Langevin equation with friction γ.

The rate as a function of temperature consists of an activated regime, a crossover regime and a tunneling regime of approximately constant rate. The rate in the activated regime is much higher than the rates observed with HeSE. If γ is adjusted to reproduce the experimentally observed activated rates, then the predicted rate in the tunneling regime is orders of magnitude slower than seen in experiment. If the rate in the activated regime is suppressed by a low friction rather than a high friction, then the absolute rates in the two regimes can be qualitatively reconciled. A low friction in the activated regime would imply multiple jumps, which have been observed previously in hydrogen diffusion and are seen also in Chapter 6.

At the low friction consistent with the H deep tunneling rates, the D tunneling rate is predicted to be $\mathcal{O}(1000)$ times smaller. The isotope effect is reduced at high friction, but the experimental data is inconsistent with a high friction regime.

4.6 Summary and outlook

In Section 4.2, analytically exact ISFs have been calculated for a particle obeying the quantum Langevin equation (QLE) on a flat surface, with arbitrary memory friction, in terms of the corresponding classical result. Related results were available beforehand, for surface diffusion subject to the QLE with a Markovian friction kernel, and for phonon lineshapes. Here the derivation of the QLE ISF has been presented starting from the definition of the quantum ISF, and a simple prescription

is given for converting the ISF of the classical system into the ISF of the quantum system. In the process of deriving the quantum result, an alternative perspective on the classical derivation was presented. As with the analytical GLE results of Chapter 3, there is no direct and immediate application for the results, but since the interpretation of spin echo data frequently makes use of analytical results from a standard library of dynamical signatures, there is a clear motivation to add results to the library, which can be used to analyse future experiments.

In the same vein, the exact ISF for a particle coherently tunneling in a periodic tight-binding system has been derived in Section 4.3. Previously the dynamical structure factor has been written down for the coherent two-state system, but the result is extended here to cover the case of a large periodic system where the Bloch energy eigenstates can be approximated as a continuous band. The result is verified against numerically exact evaluation of the ISF from its fundamental definition. In one sense, the coherent tunneling ISF is an analogue of quantum ballistic motion. The lineshape displays oscillations on a long timescale which in principle could be experimentally observable for very low temperature tunneling between degenerate sites with very low friction.

The thermal quantum dissipative escape rate of H (D) atoms from the metastable adsorption sites on Ru(0001) has been calculated, using the bounce method adapted to an arbitrary polynomial representation of the well region and diffusion barrier. The results show that the fast rate of tunneling at low temperature is not consistent with the high friction that has previously been proposed [43, 35] to explain the low prefactor for quantum activated diffusion at higher temperatures. The previous tentative anomalously small experimental isotope effect between H and D on Ru(0001) [35] cannot originate in strong friction, as the absolute jump rate becomes far too low. Although the present work provides evidence against strong friction at low temperature, the effect of very low friction is not included quantitatively and is an important direction for future study, along with the incorporation memory and spatially varying friction that could represent the influence of phononic dissipation more realistically. In general, improved first-principles inputs to the method is a rich area for further work, both in terms of more reliable potentials (cf. comments on fermionic DMC in Outlook, Section 7.1.5) and parameters describing dissipation.

Chapter 5

Surface diffusion of carbon and oxygen

The first HeSE measurements of carbon diffusion and oxygen diffusion are presented. The measurements in the present Chapter were not performed in the expectation of seeing the theoretical effects predicted in previous Chapters. Their common ground is relevance to technologically crucial processes, and the interplay between atomic-scale and mesoscopic processes.

5.1 Diffusion of graphene precursors on Ru(0001)

5.1.1 Background

Graphene (G) is a well known two-dimensional material with remarkable electronic properties [6]. Growth at transition metal surfaces such as Ru(0001) is a promising method for preparing high quality G for devices, for example via chemical vapour deposition [37]. It is well known that epitaxial G/Ru(0001) can also be formed by precipitation of dissolved carbon (C), which was observed as early as 1970 by LEED, where a moiré diffraction pattern develops at high temperature [196]. More recent real-space observations (e.g. [197]) show that precipitated G can have very long range order. Because G islands can grow coherently over substrate step edges by 'carpeting' [198] or 'etching' [199] epitaxial G can be ordered on a lengthscale much larger than the original terraces of the clean surface. Although one motivation for growing high quality G on metals is subsequent transfer to produce large-scale isolated G sheets, G/Ru(0001) can also be directly useful. For example, G/Ru(0001) is a suitable template for self-assembly of metal nanoclusters [200] or arrays of

nanoclusters [201]. Another potential application is in stable high-reflectivity mirros for He atoms: high-quality G/Ru(0001) has been observed to have around 23% reflectivity to thermal energy ^{4}He [202, 203], so has the potential to be made into a reflecting focussing component in helium atom microscopy [204].

Owing to lattice mismatch and the balance of C-C and C-Ru interactions, G on Ru(0001) forms a moiré structure (introduced in Section 2.1.4.2). A $(25 \times 25)/(23 \times 23)$ registry has been determined by surface x-ray diffraction [58], consistent with first principles calculations showing that the $(25 \times 25)/(23 \times 23)$ is preferred over $(12 \times 12)/(11 \times 11)$ [205]. The moiré structure of a high quality G layer is seen clearly in He atom diffraction [76, 206]. Prominent peaks appear at even orders along the direction $< 1, 1 >$ (as defined in Section 2.2.1). Throughout the present work the moiré peak at $\Delta K \approx 0.24\,\text{Å}^{-1}$ is used as a proxy for the presence of G. Diffraction scans recorded in the present work are compared with a He diffraction scan from the literature in Figure 5.1.

The cohesive and diffusive energetics of carbon clusters on metals are key background to the HeSE results to be presented shortly. The growth of G islands from surface C on Ru(0001) is a non-trivial process involving an interplay of diffusion, formation of C clusters, and attachment at island edges. It has been proposed that island growth is attachment-limited and proceeds through the formation of rare $N \approx 5$ clusters near island edges, an interpretation motivated by low-energy electron microscopy (LEEM) observations [207].

The properties of C clusters on Ru(0001) and other metal surfaces have been investigated extensively in theory and experiment. A summary is presented in Table 5.1. The natural starting point for the discussion of clusters is the C monomer. On Ru(0001) the monomer adsorbs at hcp hollow sites, with a calculated barrier of 870 meV to exit over bridge sites [208]. Lower diffusion barriers, but nonetheless of the same order, have been calculated for Ni(111) and Co(001) [3]. A diffusion barrier of 870 meV and a nominal but realistic rate prefactor of $1\,\text{ps}^{-1}$ implies a mean residence time at 1000 K of around 20 ns for a C atom at an adsorption site, which would be unlikely to limit the rate of G growth, but is slow on the timescale of the HeSE experiment. However, there is theoretical evidence that certain small carbon clusters could be more mobile, which motivates a brief review of dimers and trimers. It is relevant to mention calculations on other surfaces as well as Ru(0001) where the equivalent calculations are not available on Ru(0001), as an illustration of what could be possible on Ru(0001). In particular, on Ni(111) illustrates explicitly the assertion that a small stable cluster can be more mobile than the monomer.

On Ru(0001) there is a large energy barrier to dimer formation on a terrace and the dimer is unstable with respect to two monomers [208]. On Ni(111), the dimer

Table 5.1: Properties of carbon atoms and clusters on metal surfaces, chosen for relevance to surface diffusion of carbon on Ru(0001). The relevance of calculations on other surfaces is that exhaustive calculations of cluster stability and mobility on Ru(0001) have not been performed, while calculations on other surfaces suggest what could be plausible on Ru(0001). The stability is expressed in terms of the energy of a cluster compared to separate monomers; a positive energy indicates instability. The mobility is quantified either by the theoretical diffusion barrier, or by experimental observations of the species. '-' indicates fields where the result is not available. The key line which indicates the plausibility of a stable and highly mobile small cluster is highlighted in bold.

Surface	**Species**	**Stability** (meV)	**Mobility**	**Method**
Ru(0001)	Monomer	0	$E_A = 870\,\text{meV}$	DFT [208]
	Dimer	≈ 1000	-	DFT [208]
	'Magic' $N \approx 20$	< 0	Static, 900 K	STM [2]
Ni(111)	Monomer	0	$E_A = 400\,\text{meV}$	DFT [3]
	Dimer	-560	$E_A = 950\,\text{meV}$	DFT [209]
	Linear trimer	$\mathbf{-850}$	$\mathbf{E_A = 210\,meV}$	**DFT** [209]
Ir(111)	Monomer	0	$E_A = 750\,\text{meV}$	DFT [208]
	Dimer	$\approx +1000$	-	DFT [210]
	Linear trimer	$\approx +1000$	-	DFT [210]

has been calculated to be 0.21 eV more stable than separated monomers [209]. The diffusion barrier for the dimer on Ni(111) is higher than that for the monomer. The trimer is the smallest cluster in which there is in principle a choice between a linear structure (a chain), and a nonlinear or ring-like structure. On Ni(111) the linear trimer is predicted to be stable over monomers, and has a considerably lower surface diffusion barrier than either the monomer or the dimer [209]. Systematic calculations have also been performed for Ir(111) [210] which indicate that there are no stable small clusters or chains. The same type of systematic calculation has not been performed for Ru(0001). Chains on Ru(0001) have been observed experimentally by freezing the process of G growth after ethlylene deposition [211], but the presence of hydrogen limits the relevance of that observation to the current situation. In studies of Ru(0001), there has been more theoretical focus on large, stable and relatively immobile clusters. In agreement with calculated trends for other surfaces [210, 212, 213, 214], large $N \gtrsim 10$ clusters on Ru(0001) tend to be ring-like (rather than chain-like) and are described as sp^2-bonded, in other words their structural and electronic properties are reminiscent of G. There is experimental evidence for particularly stable ('magic') clusters within the cluster landscape, namely that during deposition-driven G growth the same types of cluster tend to form even when the deposited feedstock is varied [2]. The 'magic cluster' idea is well-supported theoretically [215, 216]. However, magic clusters are slow-moving, as evidenced by their direct observation in STM at high temperature (900 K) [2].

Although the dynamics of G growth are of wide interest, relatively little attention has been given to the rapid microscopic diffusion dynamics of precursor species. Experiments on growth dynamics have been limited to longer timescales. LEEM has been used to study G/Ru(0001) island growth dynamics on the scale of seconds and μm [217], and the diffusion of 'holes' in the C layer during ordering has been observed with STM [218] on the scale of minutes and tens of nanometres. It is possible the diffusion process measured in the present work could be observed in STM at lower temperatures, as long as the mobile species remains thermodynamically feasible. In the present work, HeSE reveals a nanosecond-scale jump diffusion process during G formation in the elevated temperature regime $550\,K \leq T \leq 1300K$. HeSE measurements are not typically performed at such high temperatures, and one reason is the increasing fraction of intensity scattered in multiphonon events. On Ru(0001) attenuation of the desired signal (decay amplitude) by the multiphonon background is not too severe, making very high temperature diffusion measurements feasible. The contribution of our experiments to the picture is to reveal strong evidence on Ru(0001) for a chain or cluster that is stable enough to be the predominant diffusing species under suitable conditions, yet significantly more mobile than C monomers, and orders of magnitude more mobile than the 'magic' clusters observed in STM.

5.1.2 Experimental methods and results

5.1.2.1 Sample preparation

The Ru(0001) single crystal sample was prepared according to the methods given in Section 2.1.3, giving a clean surface reflectivity of 30%. Carbon was precipitated from the bulk by annealing the sample. The annealing time and temperature required to precipitate a significant amount of surface carbon depended on how recently the surface had been cleaned. Directly after oxygen cleaning, holding the sample at 1000 K for around 1 hour was sufficient to produce a bright, sharp moiré feature at $\Delta K = 0.24\,\text{Å}^{-1}$ as illustrated in Figure 5.1. However, a similar end result was also seen after leaving the sample at an intermediate temperature (550 K) for several hours followed by a flash anneal to high temperature (1300 K), suggesting that at the intermediate temperature bulk diffusion allows carbon to concentrate in the near-surface region, and the flash anneal facilitates rapid diffusion to the surface and G island formation.

5.1.2.2 Structure of precipitated graphene

Figure 5.1 defines the high-symmetry surface directions $< 1,1 >$ and $< 1,0 >$, and shows two ^{3}He diffraction patterns along $< 1,1 >$. The scans were separated by a flash anneal and several hours of dynamics measurements at and around $T_s = 700\,\mathrm{K}$. As expected, extensive annealing leads to precipitation and ordering of surface carbon. A schematic representation of data from [206] is included in the Figure to highlight the general consistency between our results and data recorded for highly reflective G grown by ethylene deposition. The distinctive change between our two scans is the appearance of extra peaks characteristic of G/Ru(0001). The stronger decrease of the diffuse background signal with ΔK in the later scan is consistent with a reduction in the amount of disordered surface carbon. The fact that fewer peaks are visible in our data than the cited (pink) data can be attributed to the partial, rather than complete, coverage of the surface with G, which reduces the intensity of weak peaks to an undetectable level.

5.1.2.3 Nature of the dynamics

Most of the G/Ru(0001) polarization scans were measured at uniformly spaced spin echo times $0 \leq t_{SE} \lesssim 850\mathrm{ps}$; at higher temperatures a shorter time base was used owing to the faster dynamics. The central $t_{SE} = 0$ point of every scan was discarded. A typical experimental polarization scan is shown in Figure 5.2. The complete lineshape, with the exception of $t_{SE} = 0$, is well described by the functional form

$$I(\Delta\mathbf{K}, t_{SE}) = A_1(\Delta\mathbf{K})e^{-\alpha_1(\Delta\mathbf{K})t_{SE}} + A_2(\Delta\mathbf{K})e^{-\alpha_2(\Delta\mathbf{K})t_{SE}} + C(\Delta\mathbf{K}), \qquad (5.1)$$

The biexponential part is consistent with non-Bravais hopping as detailed in Section 2.2.1. The origin of the static level was discussed in 2.2.2.

Polarization scans were recorded at $T_s = 700\,\mathrm{K}$ along the $< 1,1 >$ and $< 1,0 >$ azimuths (as defined in Section 2.2.1 and illustrated in Figure 5.2), using a randomized order of polar angles γ. The entire dataset will be analysed with the hollow-hollow triple jumps model to extract quantitative jump model parameters. However, it is convenient to represent the data visually via the slower exponential decay rate (the slower of α_1 and α_2 in Equation 5.1), $\alpha(\Delta\mathbf{K})$.

The slowest non-static exponential component of each polarization scan, $\alpha(\Delta\mathbf{K})$, was extracted by increasing the start time of the fit until $\alpha(\Delta\mathbf{K})$ shows no material change (Section 2.2). $\alpha(\Delta\mathbf{K})$ is shown in Figure 5.3, for $T_s = 700\,\mathrm{K}$. The blue points along $< 1,1 >$ correspond to the first run, and the red points are the repeats; the two sets of results are plotted together and broadly agree. The measurements

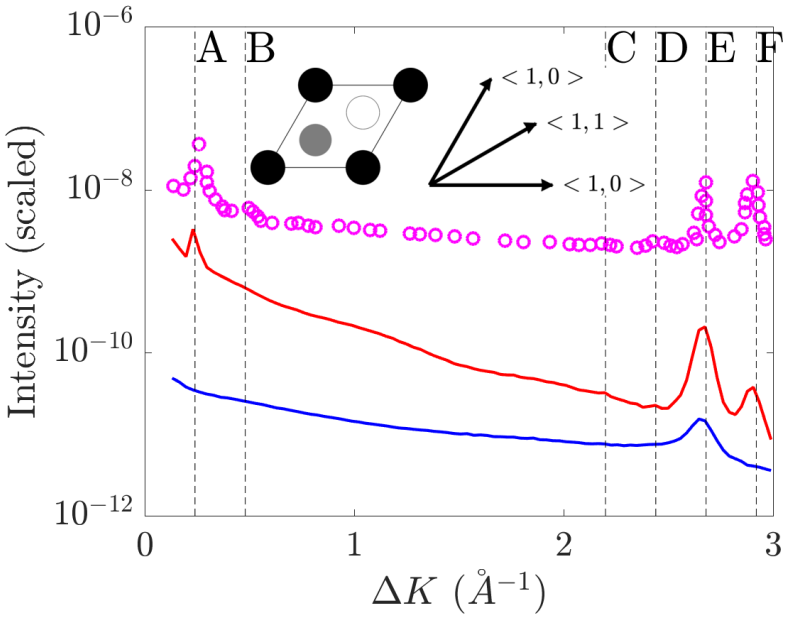

Figure 5.1: Definition of the high-symmetry surface directions (inset) and diffraction scans along the $< 1, 1 >$ azimuth. The three diffraction scans correspond to data taken before the extensive set of dynamics measurements (blue) as described in the main text, after those measurements (red) and for comparison a schematic representation of the data in [206] (magenta). In the drawing of the primitive surface unit cell, the black circles represent surface Ru atoms. The grey circle shows the position of the first subsurface layer, and the empty circle represents the "missing" layer that would be present for an fcc close packed surface, but is absent for the hcp(001) Ru surface. The high symmetry directions $< 1, 0 >$ and $< 1, 1 >$ are labelled by their composition out of the two primitive lattice vectors. Our measured data are given an arbitrary relative scaling for visual clarity. The data from [206] is given a logarithmic rescaling to highlight small features. The dashed lines indicate visible features. The scan of the 'clean' surface shows only the first order diffraction peak (**E**) of the Ru(0001) lattice. The scan taken at the end of the dynamics measurements shows two additional strongly defined features **A** and **F**. **F** corresponds to a very high order diffraction peak of the moiré pattern, with its intensity enhanced by the internal structure of the moiré unit cell; **A** is the second-order moiré peak. The odd-order moiré peaks have vanishingly small intensity due to the quasi-2×2 corrugation of the moiré unit cell [58]. The helium diffraction data from [206] shows further, smaller features **B,C,D**. **C** and **D** are weakly visible in our red scan, whereas there is no evidence for feature **B**. One approach to qualitatively understanding the diffraction pattern based on convolutions was outlined in Section 2.1.4.2; as noted in the same section, quantitative modelling of the diffracted intensity in order to elucidate the He/G/Ru(0001) interaction potential could be carried out in future using close-coupling scattering calculations [79].

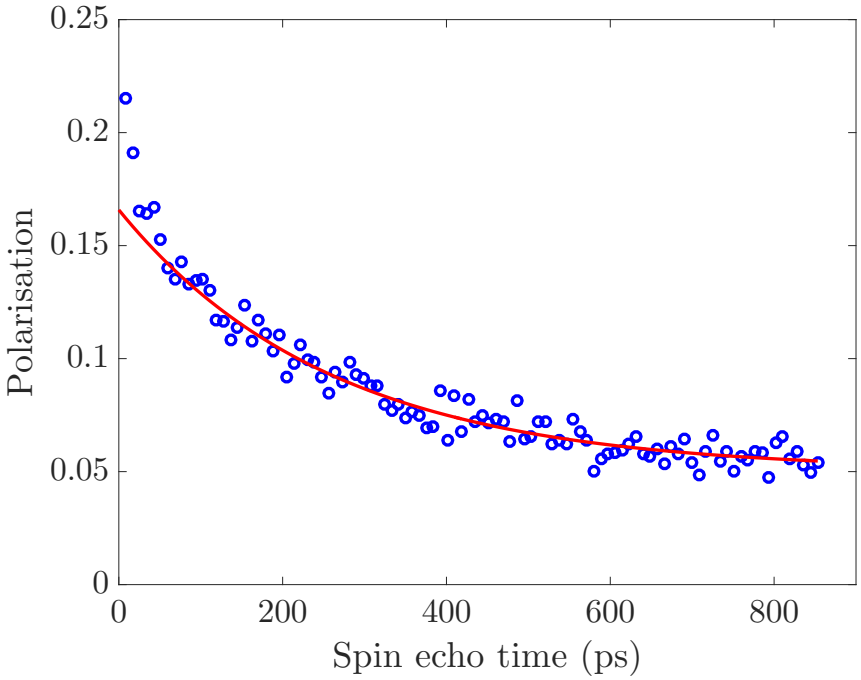

Figure 5.2: Experimental polarization scan $P(t_{SE})$ at $\Delta K = 1.7\,\text{Å}^{-1}$ along $< 1, 1 >$. The polarization is the raw data from the instrument, i.e. has not been re-scaled. The point $t_{SE} = 0$ has been removed for clarity. The solid line is the slower component of a biexponential fit. The first few points in the scan show a deviation from single-exponential behaviour. The decay rate of the faster component turns out to be independent of temperature, which essentially eliminates it as a signature related to the jump diffusion process. The presence of a component which is faster than the main decay, but on the timescale of a few tens of picoseconds rather than sub-ps, suggests that a non-Bravais hopping model (Section 2.2.1) is appropriate.

Table 5.2: Parameters of the non-Bravais, inequivalent-hollows triple jumps model (Section 2.2.1) applied to C/Ru(0001) polarization scans at 700 K, the same data which is represented in Figure 5.3 via its slowest decaying exponential component. τ is the mean residence time of the diffusing species in the metastable hollow. λ is the relative concentration in the more stable hollow. Detailed balance gives the site energy difference between the hollows as $\Delta E = k_B T \ln(\lambda)$. The survival parameter s describes the ratio of multiple jumps to single jumps, and is significant, demonstrating that the dynamical friction cannot be too large.

$\mathbf{T_s(K)}$	τ**(ps)**	λ	**s**	**ΔE (meV)**
700	51 ± 4	4.3 ± 0.3	0.33 ± 0.02	90

represented in Figure 5.3 span a time window of about 30 hours without surface cleaning[1], indicating that the diffusion process can run for a very long time without all the surface carbon being sequestered in G islands. The form of $\alpha(\Delta\mathbf{K})$ indicates diffusion by jumps. At small ΔK, $\alpha(\Delta\mathbf{K})$ rises quadratically from the origin. If the quadratic behaviour holds for ΔK down to zero, it indicates long-range diffusion. $\alpha(\Delta K)$ is measured reliably down to $\Delta K = 0.1\,\text{Å}^{-1}$ along $< 1, 0 >$, so the diffusion is unconfined on a lengthscale of at least $\frac{\pi}{0.1} \approx 30\,\text{Å}$. Meanwhile the high reflectivity and lack of static disorder on the clean surface suggests a low density of step edges, so it is reasonable to conclude that the Bravais lattice seen in the jump signature is associated with motion on terraces. After the initial rise, $\alpha(\Delta\mathbf{K})$ reaches a maximum halfway to the diffraction condition along the $< 1, 1 >$ azimuth, falling approximately symmetrically towards zero as the diffraction condition is approached, which is consistent with either the hexagonal Chudley-Elliott (CE) jump model or a non-Bravais generalization, as described in Section 2.2.1). The solid curves overlaid are fits of the experimental $\alpha(\Delta K)$ to the hexagonal CE model but are given as guides to the eye; because of the presence of a second exponential component the Bayesian method (Section 2.2) will be used for the quantitative analysis of the jump dynamics. The effective Chudley-Elliott jump rates are given in the Figure caption for completeness.

The systematic appearance of a faster component in the lineshapes motivates comparing the data with a non-Bravais hopping model. In Chapter 6 the fcc/hcp hollow non-Bravais hopping model of Section 2.2.1 is applied based on prior knowledge of the nature of the diffusing species and the associated first-principles potential energy surface. Here the same level of prior knowledge is not available; nevertheless the model can still be applied. The fit is carried out using the Bayesian method detailed in Section 2.2.6 are shown in Table 5.2. The detailed interpretation of the fitted will be discussed after the temperature-dependent data has been presented.

[1] A portion of the temperature-dependent data presented later in the Chapter was interleaved.

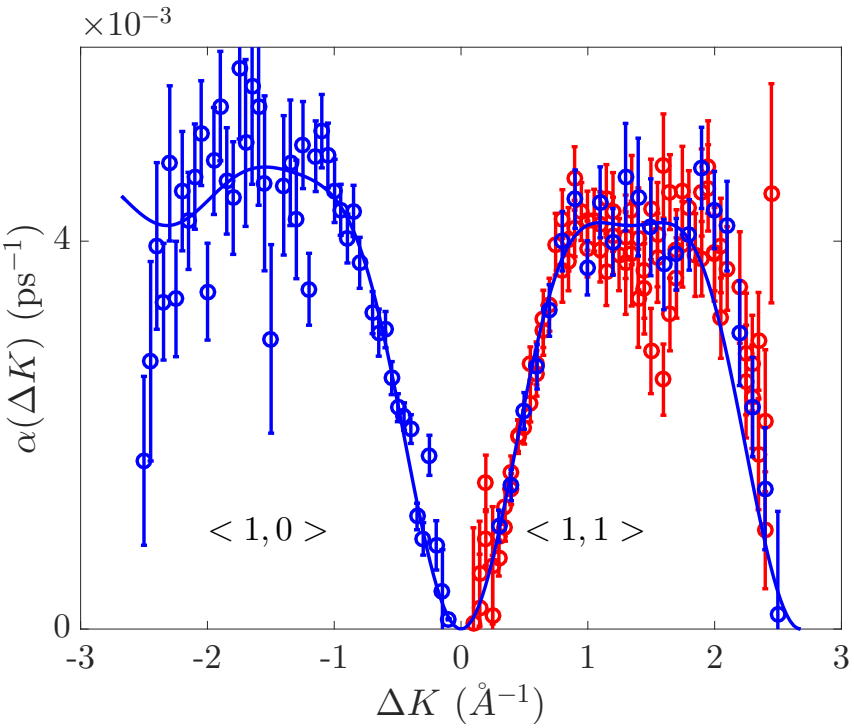

Figure 5.3: The function $\alpha(\Delta\mathbf{K})$ at $T_s = 700\,\mathrm{K}$ along the $< 1, 1 >$ azimuth (right) and $< 1, 0 >$ azimuth (left). $\alpha(\Delta\mathbf{K})$ is the decay rate of the slowest non-static exponential in the polarization scan at $\Delta\mathbf{K}$. The smooth curve is a fit to the Chudley-Elliott model as described in the main text. Defining the nearest, second and third nearest neighbour jump rates as $\Gamma_{1,2,3}$, the fitted rates are $\Gamma_1 = 0.85 \pm 0.05\,\mathrm{ns}^{-1}$, $\Gamma_2 = 0.20 \pm 0.05\,\mathrm{ns}^{-1}$ and $\Gamma_3 = 0.21 \pm 0.05\,\mathrm{ns}^{-1}$. The fact that a hollow-hollow non-Bravais jump model fits the data very well implies the Chudley-Elliott description is probably redundant in favour of the non-Bravais model which is fitted using the Bayesian method of Section 2.2.

5.1.2.4 Temperature dependence of dynamics

The temperature-dependent results are summarized in Figure 5.4. Interleaved with the $\alpha(\Delta K)$ measurements, polarization scans were recorded at fixed $\Delta K = 1.0\,\text{Å}^{-1}$, and for $550\,\text{K} \leq T_s \leq 850\,\text{K}$, for which $\alpha(T)$ is shown in blue in Figure 5.4. On a separate occasion, after annealing the clean surface for 1 hour at 1200 K until the characteristic moiré diffraction peak reappeared, polarization scans were recorded to extend the Arrhenius curve to very high temperatures, shown as blue triangles on Figure 5.4a. At the very high temperatures the Arrhenius data were taken at $\Delta K \approx 0.5\,\text{Å}^{-1}$, reduced compared to the lower temperature measurements in order to maintain a good signal/noise ratio. A consistent activation energy holds the entire temperature range, indicating they correspond to the same process. Figure 5.4b shows the temperature dependent τ^{-1} found by assuming that the survival probability s is constant with temperature, and that the concentration ratio λ scales as

$$\lambda = \exp\left(\frac{\Delta E}{k_B T}\right). \tag{5.2}$$

The agreement with the classical rate law is excellent when the measure $\Gamma(T) = \tau^{-1}(T)$, rather than $\alpha(T)$, is used for the rate.

The fact that a single diffusion process is observed up to $T_s = 1300\,\text{K}$ rules out all plausible gas phase contaminants except oxygen, which sticks strongly enough to Ru(0001) that it is worth explicit consideration. Oxygen is expected to desorb rapidly above 1100 K [219], in agreement with our own observations of the recovery of specular intensity during annealing; however, oxygen diffusion can also be ruled out directly. The red point in Figure 5.4a represents a low-coverage oxygen diffusion measurement, recorded after dosing 2×10^{-7} mbar·s molecular oxygen over the freshly cleaned surface at 700 K, leading to a specular attenuation $I = I_0/3$. The associated rate α lies an order of magnitude below the main (blue) curve. The size of the oxygen dose was chosen to ensure that oxygen dominated the scattered intensity in the subsequent polarization scan, while staying well clear of the ordered c(2 × 2)O/Ru(0001) superstructure (Section 5.2). O/Ru(0001) at low and high coverage is presented in detail in Section 5.2.

The solid line in Figure 5.4b is the best fit to the Arrhenius law

$$\Gamma(T) = \Gamma^{(0)} \exp(-\frac{E_A}{k_B T}). \tag{5.3}$$

with activation energy $E_A = 292 \pm 7\,\text{meV}$ and prefactor $2.45 \pm 0.25\,\text{ps}^{-1}$. Dividing by 3 gives the prefactor associated with escape over any one of the three escape paths from a higher-energy site, $\Gamma^{(0)} = 0.8 \pm 0.1$. The measured barrier is in flat con-

tradiction with the 870 meV first-principles barrier for C atom diffusion on terraces [208], so C monomer diffusion is ruled out immediately. Another revealing feature of the experimental rate curve is the jump rate prefactor Γ_0, since in conjunction with the survival ratio s it can be used to place constraints on the rate of energy exchange γ with the surface. If the Langevin equation is an adequate description of the activated motion, then γ can be identified with the Langevin friction.

At 700 K, the experimental survival ratio is 0.33, which provides a handle on the friction since s depends on γ. The probability of the adsorbate making it over a second barrier, given that it crossed the first, decays with the time spent in the well region due to the systematic braking force applied by the friction. For Langevin dynamics in a one-dimensional potential and not-too-strong friction, the jump distribution has been derived in terms of the mean energy loss parameter δ, which describes the conditional distribution ([165, 166] of the particle's energy ($\epsilon \to \epsilon'$) as it traverses from one barrier to the next:

$$P(\epsilon'|\epsilon) = \frac{1}{\sqrt{4\pi\delta}} \exp\Big[- \frac{(\epsilon' - \epsilon + \delta)^2}{4\delta} \Big], \tag{5.4}$$

leading to a distribution in the jump length j [117] of

$$p_{j+1} = \frac{j^{-3/2}}{\sqrt{\pi\delta}} e^{-j\delta/4} \ (j \geq 1). \tag{5.5}$$

Therefore the jump distribution is expected to be a strongly decaying function of the jump length j. For weak Langevin friction, δ is proportional to γ [220]. However, the full details of the potential energy surface, such as how effectively the adsorbate is steered along its non-straight transition path, will affect the exact relationship between γ and s, which motivates molecular dynamics simulations on a model two-dimensional potential representing the hexagonal surface.

A model two-dimensional potential for carbon diffusion can be created by rescaling the H/Ru(0001) first-principles potential. The barrier is adjusted by a global scaling, and the site energy difference is adjusted using the fcc/hcp transformation and averaging as described in Section 4.5. Figure 5.5 shows the results of point-particle Langevin simulations on the scaled potential energy surface, which indicate that a friction in the region of $0.2 - 0.4\,\mathrm{ps}^{-1}$ approximately reproduces the survival probability and absolute hopping rate. The inferred friction is considerably lower than the values typically found for the diffusion of aromatic molecules [105, 221, 24], in which there is a substantial contribution from the additional molecular degrees of freedom to the effective friction acting on the centre of mass co-ordinate [110]. The low friction is therefore consistent with the evidence from other directions that the

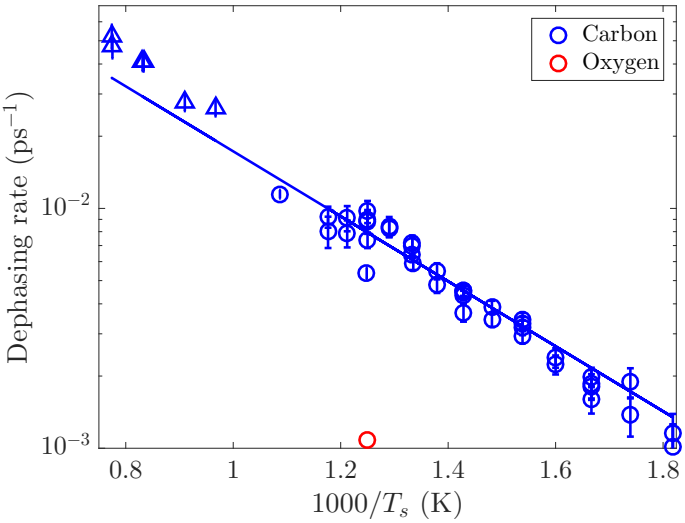

(a) Temperature dependence of C/Ru(0001) jump rate expressed as $\alpha(T)$.

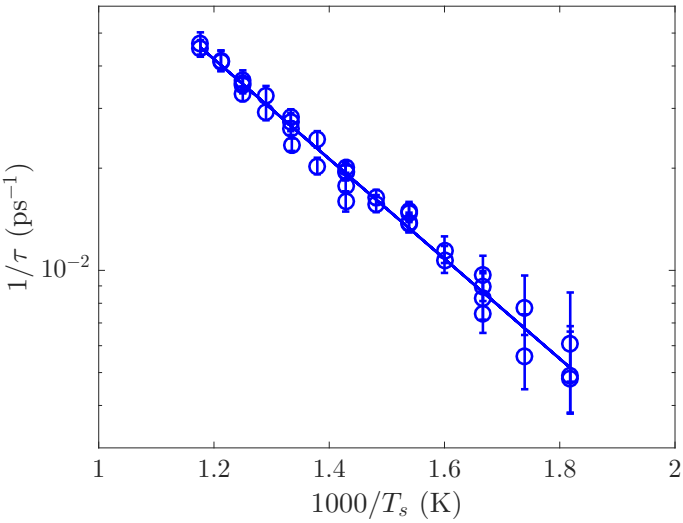

(b) Temperature dependence of C/Ru(0001) jump rate expressed as $\tau^{-1}(T)$.

Figure 5.4: Temperature dependence of the C/Ru(0001) dynamics expressed in two different ways. In Figure 5.4a the rate is expressed as $\alpha(T)$, the temperature-dependent dephasing rate. Blue points represent measurements at $\Delta K = 1.0\,\text{Å}^{-1}$ along the $< 1, 1 >$ azimuth. Blue triangles represent measurements at $\Delta K = 0.5\,\text{Å}^{-1}$ along the same azimuth. A consistent activation energy applies across the whole temperature range, suggesting that the same species and process dominates the diffusion from 550 K to 1300 K The red point represents a measurement of the oxygen diffusion rate at low coverage, and shows conclusively that the species responsible for the blue data is not residual oxygen. In Figure 5.4b the rate data is represented as the temperature-dependent escape rate τ^{-1} from the metastable hollow site, when the data is analysed within the framework of the non-Bravais, fcc/hcp model of Section 2.2.1. The extraction of a temperature-dependent τ^{-1} relies on the parameters fitted at 700 K with the Bayesian method (Section 2.2.6) and shown in Table 5.2. The survival parameter s is assumed to be temperature-independent, and the concentration ratio between the two sub-lattices in the model is assumed to vary as $\lambda = \exp(\Delta E/k_B T)$.

diffusing cluster consists of two or three atoms.

5.1.3 Further discussion on the nature of the diffusing species

The main pieces of evidence presented so far which support a small carbon cluster being responsible for the observed diffusion signature are:

- signature present up to $T_s = 1300\,\mathrm{K}$ (Figure 5.4);
- signature strongest when moiré pattern is well developed;
- much faster than oxygen diffusion (about $10\times$ faster at 700 K);
- activation energy $3\times$ too low for C atom diffusion ([208]; see Table 5.1);
- magic clusters of $N \gtrsim 20$ observed static in STM at high temperature [2].

As well as continuing up to 1300 K, the diffusion process illustrated by Figure 5.4a is observed down to 550 K, which is around 1/5 of the bulk melting point. Therefore, Ru/Ru adatom diffusion is inherently unlikely: any Ru atoms released by the growth of G islands should bind strongly to any available Ru step edge, rather than diffusing freely. As for whether we could be observing diffusion of Ru adatoms on G islands, it is relevant that in experiments where Ru nanoclusters were grown on G/Ru(0001) the Ru adatoms were always deposited by evaporation: Ru structures have not been observed to form spontaneously on G/Ru(0001) islands, implying the process is thermodynamically and/or kinetically suppressed. Additionally, evaporated Pb has been observed to intercalate under G islands when kinetics allow it [222], suggesting that the presence of metal atoms on G/Ru(0001) is unfavourable in general.

The diffusion process assigned to carbon cluster diffusion can be seen at small ΔK before the development of well-defined G islands. Figure 5.6 compares the $\alpha(\Delta K)$ of the main 700 K measurements with the $\alpha(\Delta K)$ measured when there is no evidence for graphene islands but the surface is not freshly cleaned. The two curves agree at small ΔK. The form factor of a carbon cluster is expected to fall off more strongly with increasing ΔK than the form factor of atomic species such as O, which is more slowly diffusing, leading to an apparent reduction in $\alpha(\Delta K)$ at higher ΔK. The $\alpha(\Delta K)$ recorded in the absence of the moiré peak is consistent with:

- a larger-than-atomic species being responsible for the faster diffusion signature;
- diffusion on patches of clean Ru(0001) rather than on the graphene islands themselves.

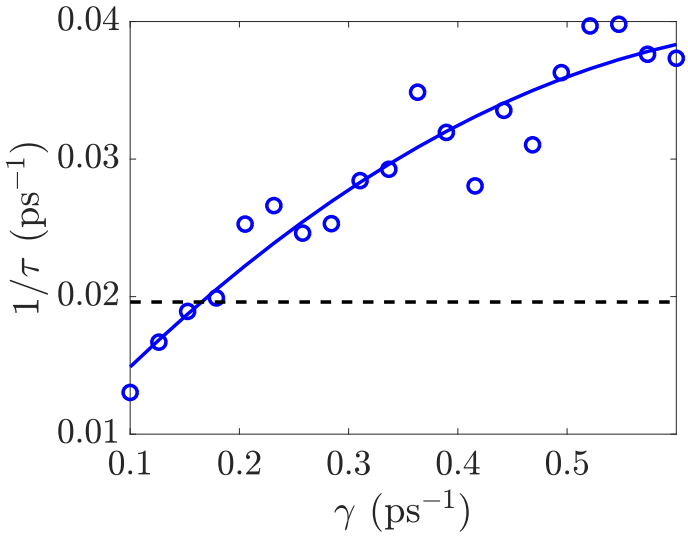

(a) γ-dependence of the inverse residence time τ^{-1} in point-particle Langevin simulations on the model two-dimensional C/Ru(0001) potential.

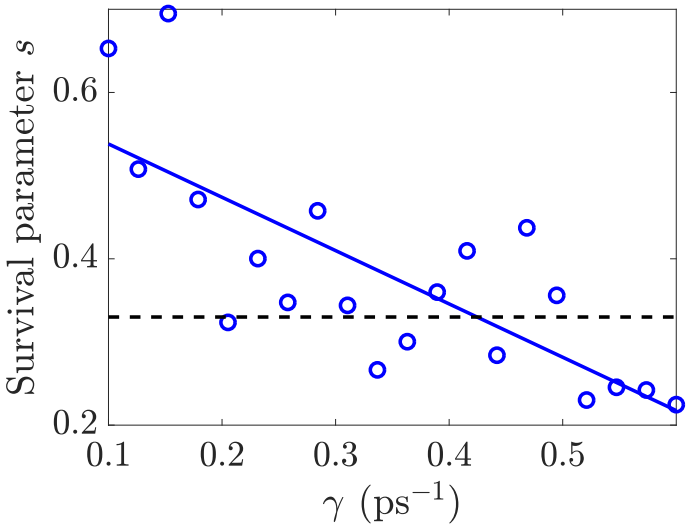

(b) γ-dependence of the survival parameter s in point-particle Langevin simulations on the model potential.

Figure 5.5: Dependence of the inverse residence time of a point particle of mass $m = 36$ amu, from Langevin simulations at $T_s = 700$ K with a timestep of 1 fs for 10 independent runs of length 10^4 ps. The two-dimensional model potential represents a hcp(0001) surface with a fcc/hcp site energy difference of 90 meV and a barrier from the higher-energy hollow of 292 meV. Solid blue lines indicate the trends in the simulation results. The model potential was constructed by scaling the H/Ru(0001) potential to give the correct barrier and site energy difference. τ and s were fitted using the same Bayesian method that was applied to the experimental data, with λ constrained as $\exp(\Delta E/(k_B T))$. The experimental values of τ and s are overlaid as dashed lines. The experimental τ and s are not quite reproduced at the same time, but $0.2 \lesssim \gamma \gtrsim 0.4\,\mathrm{ps}^{-1}$ approximately reproduces the experimental values, subject to the considerable uncertainty in the detailed form of the potential including the effect of neglected degrees of freedom.

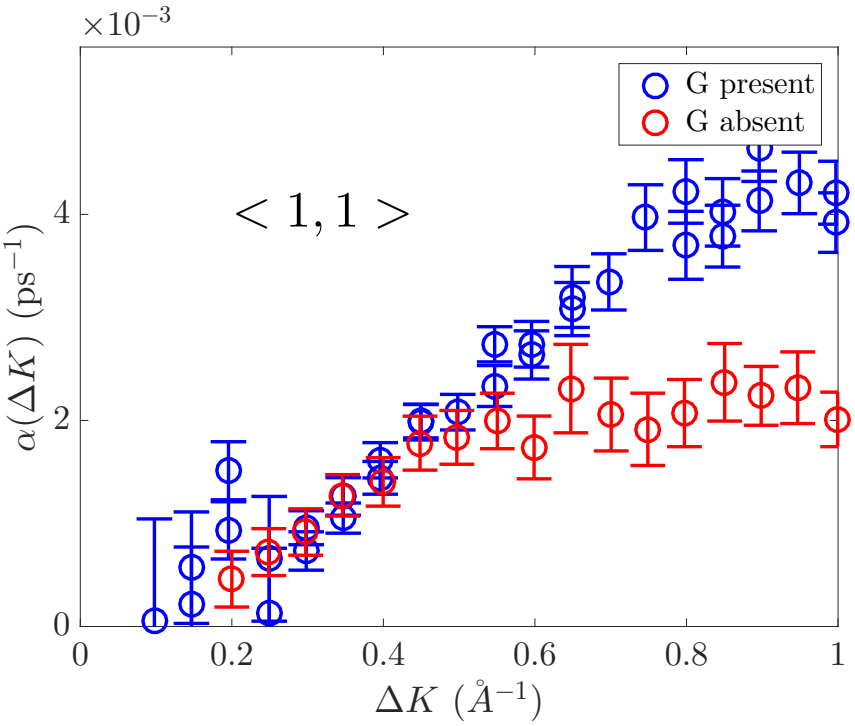

Figure 5.6: Figure 5.6 shows (red points) the $\alpha(\Delta K)$ along $< 1, 1 >$ derived from measurements performed when the surface was 28% reflective with no detectable moiré peak, after performing oxygen diffusion measurements and flashing off the oxygen. For comparison, the $\alpha(\Delta K)$ from the main 700 K experiments is reproduced (blue points). The rates agree at small ΔK, which suggests they represent the same process. The curves split apart at larger ΔK, suggesting that the lineshape receives intensity from a slower diffusion process, such as diffusion of atomic oxygen.

A summary of the evidence which points to carbon cluster diffusion, either by directly supporting the hypothesis or by disproving alternatives, is shown in Table 5.3

Table 5.3: A summary of the evidence which points to carbon cluster diffusion, either by directly supporting the hypothesis or by disproving alternatives.

Species/process	**Evidence**
C monomer	Theoretical diffusion barrier 870 meV [208]; experimentally 292 meV.
Small C cluster ($N \approx 3$)	Diffusion barrier potentially lower, if Ni(111) surface is a good guide [209]. Small clusters known to be important intermediates in G island growth [207].
Residual O	Direct measurement of low coverage O diffusion (Figure 5.4; Section 5.2).
C magic clusters ($N \gtrsim 20$)	Observed static in STM [2].
Ru/G	Thermodynamically unlikely (e.g. as evidenced by intercalation of other metal atoms [222]); kinetically unlikely because Ru atoms would need to hop up onto epitaxial G sheet
Ru/Ru	Diffusion process not observed on clean surface, and seen as cold as 550 K= $T_{melt}/5$
Diffusion on G	Diffusion process visible even when no well-defined moiré diffraction peaks

5.1.4 Conclusions

The diffusive surface dynamics of graphene precursors on Ru(0001) have been measured with HeSE. Surface diffusion is not visible immediately after sample cleaning. Extended annealing results in a partially graphene-covered surface exhibiting the diffusion process. A highly mobile species diffuses in the temperature range $550 \leq T_s \leq 1300$ K. The HeSE lineshapes are consistent with hopping between fcc and hcp hollow sites, with an activation energy of 292 ± 7 meV to escape the higher energy site, and a prefactor of $2.45 \pm 0.25\,\mathrm{ps}^{-1}$. Literature DFT calculations of diffusion barriers (Table 5.1) eliminate atomic C as the diffusing species, but suggest a $N \approx 3$ carbon cluster is likely.

5.2 Diffusion of O/Ru(0001) and O/Cu(111)

The first HeSE measurements of the surface diffusion of oxygen are presented. The jump dynamics of oxygen atoms on Ru(0001) are measured at $T_s = \{700, 800\}$ K

at low coverage, and at 800 K for a coverage approaching 0.25 ML. At the higher coverage, strongly correlated adsorbate motion is observed. The activation energy obtained by comparing the low coverage results to STM data is 650 ± 10 meV with a pre-exponential factor of $(5 \pm 3) \times 10^{12}\,\mathrm{s}^{-1}$. The diffusion rate is higher at high coverage, and is associated with a reduction in the diffusion barrier. When a low coverage of oxygen is adsorbed on Cu(111), mobile species are produced whose diffusive dynamics fall into the nanosecond time window.

5.2.1 Background

Elementary processes involving oxygen at surfaces are of cross-disciplinary interest. Transition metal oxides are a challenging arena for first-principles theory as they are electronically strongly correlated. A reliable first-principles description of such systems, even if restricted to the electronic ground state, requires a method able to account for strong electronic correlations in a more [223] or less [224] *ab initio* way. Meanwhile, many experimental investigations have reflected the need to understand oxidation on the mesoscale after large oxygen exposures giving rise to complex changes in surface morphology [225, 226, 227, 228]. However, experiments that contribute to a bottom-up understanding by quantifying the interaction of individual atoms with the clean surface are equally important, and HeSE experiments fall into the latter category.

The oxygen-covered Ru(0001) surface is interesting in a number of ways. The fully oxidized surface catalyses the oxidation of CO via a non-trivial mechanism in which O atoms are taken from the oxide and replaced later by oxygen from the gas phase [39]. Another topic of ongoing interest is the interaction of water with the oxygen-covered surface compared to the clean surface, in which clustering [229] and proton ordering [73] are enhanced on the oxygen-covered surface. Despite the complex behaviours that can occur when other species are present, O/Ru(0001) at submonolayer coverage admits a relatively straightforward description as a traditional chemisorption system. At room temperature, molecular O_2 adsorbs dissociatively with an initial sticking probability not significantly less than unity [230], and adsorbed O atoms are mobile enough to form long-range ordered structures. The migration of oxygen into the subsurface and bulk is negligible until the coverage of the adsorbed layer approaches 1 ML [231]. The hcp threefold site is predicted to be the preferred adsorption site associated with all the known ordered structures [232]. Direct observation of the room temperature jump dynamics became possible with the development of a sufficiently fast scanning tunneling microscope (STM) [233, 234]. Applying a plausible range of rate prefactors placed the diffusion barrier

in the range $550-700\,\mathrm{meV}$, which is consistent with theoretical estimates [235, 236]. As well as obtaining the absolute jump rate, the STM measurements highlighted the importance of O-O interactions, including an attractive interaction at separations corresponding to the formation of a 2×2 structure. In parallel, mutual interactions have been characterized via the phase diagram as explored through low-energy electron diffraction (LEED) [230, 237, 238]. In the temperature regime of relevance, there is a single phase boundary, an order-disorder line, which traces out a smooth curve $\theta(T)$, the coverage θ at which disordering occurs as a function of temperature. $\theta(T)$ has a maximum at $\theta\approx 0.25\,\mathrm{ML}$, reflecting the stability of the 2×2 structure. In general, mutual interactions also reveal themselves through the lengthscale dependence of structural dynamics [239], an effect seen in the present work (Section 5.2.2.1).

However challenging the first-principles description, in some ways O/Ru(0001) is a simple system, for example its phase diagram at moderate coverages can be modelled effectively with straightforward lattice gas descriptions [238]. The qualitative O/Cu(111) is more complicated [240]. More than 80 years ago it was known that the presence of oxygen at copper surfaces causes them to etch when heated in a vacuum [241]. A further hint that the presence of oxygen enhances the mobility of Cu surfaces was suggested by the thermal faceting of Cu spheres, which is facilitated by oxygen [242]. The passage from such broad-brush observations to a partial microscopic understanding of the processes occurring during the initial oxidation of Cu(111) has been far from trivial. Evidence from a range of techniques indicated that oxygen atoms do not adsorb above the clean surface like a normal chemisorbed species, but incorporate themselves approximately in the plane of the top copper layer [243, 244, 245], causing a significant local distortion [246]. Scanning tunneling microscopy (STM) facilitated a major step in understanding via the real-space observation of two types of oxygen-induced reconstruction known as the '29' and the '44' structures [247]. A comprehensive study of the atomic structure, the corresponding LEED patterns, and the associated surface morphology during oxide growth was carried out ten years later [248]. The study clarified the relationship between the oxidation conditions, especially the surface temperature, and the formation of the different reconstructions. During the initial stages of oxidation, streaky images were obtained indicating a rapid diffusion process beyond the accessible STM timescale. The present Section will extend that qualitative observation by demonstrating that a diffusive process, on disordered O/Cu(111) at low coverage, occurs on the nanosecond timescale.

5.2.2 Experimental methods and results

The single crystal Ru(0001) and Cu(111) surfaces were prepared according to the methods described in Section 2.1.3, with ultimate clean-surface reflectivities of 30% (Ru) and 50% (Cu). Surface structure and dynamics were investigated with diffraction and polarization scans. For the analysis of the O/Ru(0001) data it is necessary to introduce the coherent ISF for a system of interacting scatters:

$$I(\Delta\mathbf{K},t) = \left\langle \sum_{a,b} \exp\Big(i\Delta\mathbf{K}\cdot[\mathbf{x}_a(t)-\mathbf{x}_b(0)]\Big)\right\rangle, \tag{5.6}$$

which generalises the formulation for one particle (or independent particles) explored in Section 3. The corresponding pair correlation function in real space $G(\mathbf{R},t)$ is the van Hove function for a correlated many-particle system, [67] which describes collective diffusion via the probability of finding a particle at $\mathbf{R}'+\mathbf{R},t$ given that there was a particle (the same, or different) at $\mathbf{R}',0$ integrated over all $\mathbf{R}'$:

$$G(\mathbf{R},t) \propto \left\langle \sum_{a,b} \int d\mathbf{R}'\delta(\mathbf{R}+\mathbf{R}_a(0)-\mathbf{R}')\delta(\mathbf{R}'-\mathbf{R}_b(t))\right\rangle. \tag{5.7}$$

Various analytical forms for the $I(\Delta\mathbf{K},t)$ of non-interacting adsorbates have been given in Chapters 2,3,4. When inter-adsorbate interactions are included, then as long as the long-time tail of $I(\Delta\mathbf{K},t)$ continues to be well described by an exponential decay, the effect of the interactions on the dynamics can be described in terms of the modification to the $\alpha(\Delta\mathbf{K})$. In HAS, separate adsorbates contribute coherently to the scattering amplitude [61], and therefore the effect of correlated adsorbate motion is experimentally observable and encoded by Equation 5.6. Depending on the nature of the mutual interactions, the modification to $\alpha(\Delta\mathbf{K})$ can be fairly straightforward to interpret, for example the 'de Gennes narrowing' seen in the system Na/Cu(111) which can be explained in terms of pairwise dipole-dipole repulsion [25]. However, in some systems the mutual interactions change the effective (mean-field) single-particle potential without any direct evidence of correlated motion [249].

5.2.2.1 Structure and dynamics of O/Ru(0001)

A submonolayer coverage of O/Ru(0001) was prepared by leaking clean molecular oxygen into the scattering chamber with the surface held at 700 K. The dose was monitored via the helium specular reflected intensity I as a function of exposure x. The maximum coverage considered in the present study was obtained at the first minimum of $I(x)$. In a previous investigation on the same instrument [73], when

dosing at 400 K the first minimum is followed very shortly by a local maximum which we would expect to correspond to the ideal coverage of $\theta = 0.25$ ML. The minimum occurs at an exposure of approximately 90 % of the exposure required to reach the maximum, which suggests $\theta \approx 0.22$ ML at the minimum. The exposure conditions to reach the final coverage were 2.0×10^{-8} mbar for 50 s, or about 0.75 L where $1\,\mathrm{L} = 1 \times 10^{-6}\,\mathrm{Torr} \cdot \mathrm{s}$.

Figure 5.7 defines the high-symmetry surface directions $< 1,1 >$ and $< 1,0 >$ with respect to the clean surface structure, and shows the progression of the diffraction pattern along the $< 1,1 >$ azimuth with increasing oxygen exposure. The key feature of the final scan is the strong and fairly sharp half-order feature. The half order peak is attributed to the (2×2)O/Ru(0001) superstructure. Scans performed along $< 1,0 >$ after the same conditions show the corresponding peak in the correct place for interpretation as the 2×2 structure. The strong half-order peak along $< 1,1 >$ has a full width at half maximum of $0.08\,\mathrm{\AA}^{-1}$, or 5 %, which is broader than the resolution limit governed by the incident beam energy spread. The structural broadening is not surprising given that the coverage is slightly below ideal 2×2 coverage. Upon heating to 800 K the diffraction pattern broadened immediately, which is expected since the intensity of the corresponding LEED peak for the $\theta = 0.25$ ML structure decreases substantially between 700 K and 800 K [237].

The dose to minimum specular intensity was carried out on three separate occasions, after which different sets of polarization scans were carried out: at 700 K along $< 1,1 >$, and at 800 K along $< 1,1 >$ and $< 1,0 >$ over uniformly spaced spin echo times $0 \leq t_{SE} \lesssim 600$ps. A typical polarization scan at 800 K is shown in Figure 5.8 at $\Delta K = 0.95\,\mathrm{\AA}^{-1}$ along $< 1,1 >$. The red curve overlaid is a single exponential fit,

$$P(t_{SE}) = Ae^{-\alpha t_{SE}} + C\,. \tag{5.8}$$

Repeating the fit for scans at different $\Delta\mathbf{K}$ produces an $\alpha(\Delta\mathbf{K})$ and $C(\Delta\mathbf{K})$ that describe the whole dataset via

$$P(\Delta\mathbf{K}, t_{SE}) = A(\Delta\mathbf{K})e^{-\alpha(\Delta\mathbf{K})t_{SE}} + C(\Delta\mathbf{K})\,. \tag{5.9}$$

At 800 K there was evidence for slow, partial desorption during the measurements. Upon returning the system to 700 K, the diffraction pattern was less sharp than at the beginning of the dynamics measurements. However, the total diffracted intensities at 800 K associated with the measurements show the expected structural peaks, indicating that partial order was present throughout the 800 K measurements. The different $\Delta\mathbf{K}$ were visited in a random order, and therefore the presence of structural (2×2) features indicates that the (2×2) dynamical structure was

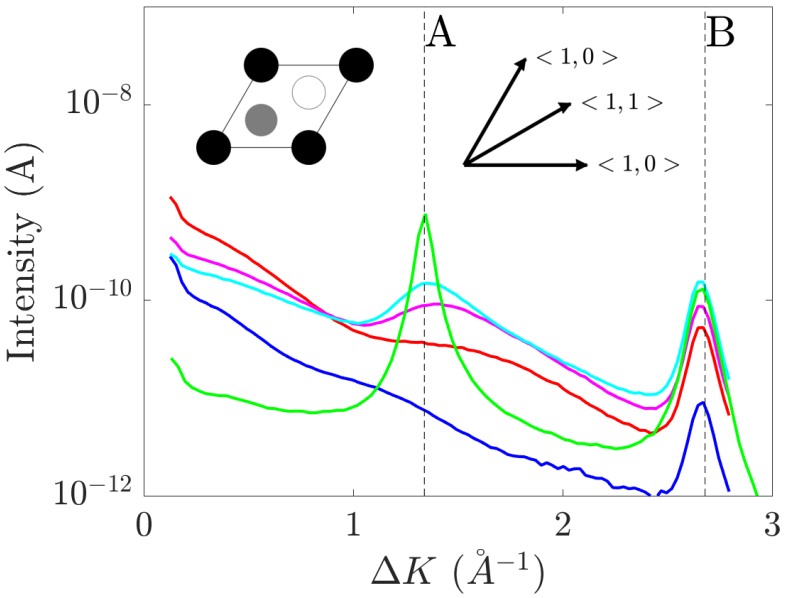

Figure 5.7: Diffraction scans of the clean and progressively more oxygen-covered Ru(0001) surface, along the $< 1, 1 >$ azimuth which is defined with respect to the real space lattice in the inset. **A** denotes the position of the half-order feature indicative of the 2×2 overlayer. **B** indicates the ideal position of the first-order peak which is present on the clean surface (blue) and enhanced by the ordered overlayer. As the oxygen coverage is increased (through red, magenta, cyan curves), the diffuse background intensity increases and acquires broad features that could be induced by the adsorbate form factor. At the highest coverage of slightly less than 0.25 ML (green curve), a reasonably sharp feature is present at the half-order condition.

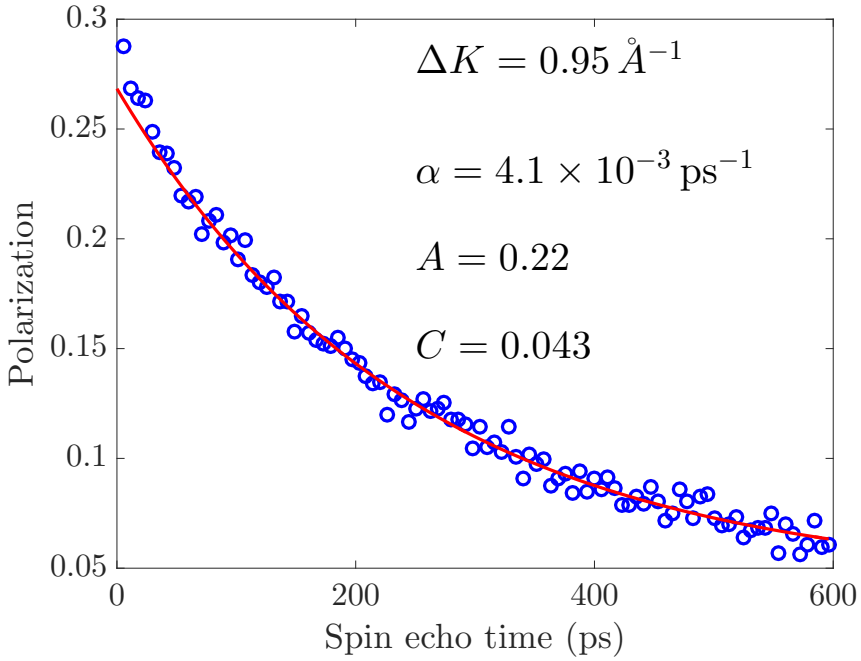

Figure 5.8: Polarization scan of Ru(0001) at $T_s = 800\,\mathrm{K}$, $\Delta K = 0.95\,\mathrm{\AA}^{-1}$ along the $< 1, 1 >$ azimuth, after dosing oxygen to the minimum in the specular reflected intensity, estimated as $\theta = 0.22\,\mathrm{ML}$. The best single exponential fit to the data at $t_{SE} > 100\,\mathrm{ps}$ is overlaid as a solid red curve. The point at $t_{SE} = 0$ is not included in the fitting procedure. Most of the lineshape is well described by a single exponential fit. The parameters α (slow decay), A (the associated amplitude) and C (static polarization) of the best fit are shown on the plot.

qualitatively maintained throughout the entire measurement set. It is possible that the reduced order after time spent at 800 K was not caused by desorption, but by contamination, for example carbon atoms segregating from the bulk.

The $\alpha(\Delta\mathbf{K})$ at 800 K and high coverage is shown in Figure 5.9, blue points. The $\Delta\mathbf{K}$ along each azimuth were visited in a random order, and the polarization scans were single-loop. The 800 K data suggest that $\alpha(\mathbf{K} = \mathbf{0})$ is either nonzero at the origin, or rises very steeply from the origin, which could be a consequence of the mutual interactions. There is a strong dip in the $\alpha(\Delta\mathbf{K})$ along $< 1, 1 >$ at the half-order diffraction condition. The dip implies that when the system is in a configuration close to an ideal 2×2 structure, that configuration decays more slowly than configurations that bear less resemblance to the ideal structure. On two separate occasions, measurements at 800 K were carried out at low oxygen dose of 0.15 L, approximately 1/5 of the dose used for the main measurement series. Scaling the coverage down linearly with exposure gives the estimate $\theta = 4 - 5\,\%$. In other words, the mean linear spacing between O atoms is more than 4 clean surface unit cells. The low coverage data are shown as two cyan points on Figure 5.9. The increase in coverage enhances $\alpha(\Delta K)$ very significantly, by about a factor of 4 (cyan to blue) at the two points where the comparison is available.

The description just given of the interacting structure, and its relationship to the dynamics, explains the shape of the $\alpha(\Delta\mathbf{K})$ but not its absolute magnitude, in particular the increase in α with coverage at the two $\Delta\mathbf{K}$ points where the comparison is available. Previous quasi-elastic scattering experiments have shown that inter-adsorbate interactions can affect activated surface diffusion in a variety of ways. In some systems the adsorbate dynamics are well described by motion in a potential energy landscape subject to pairwise interactions [25]. In others, the effect of finite coverage can be to change the average one-adsorbate potential energy landscape on the surface, with [249] or without [250] an accompanying increase in the activation energy. Additionally, interactions can contribute to the friction. For adsorbates diffusing in a very flat potential energy landscape and colliding with each other, the collisions lead to a strong coverage-dependence of the friction as shown experimentally for benzene diffusing on graphite [251]. The contribution of collisions to energy exchange can be modelled by adding a coverage-dependent contribution to the Langevin friction, an approximation known as the two-bath or interacting single adsorbate (ISA) model [252] which neglects statistical correlations between the coordinates of the distinct adsorbates but correctly captures the fact that increasing the coverage decreases the mean free path of any individual adsorbate. When the one-atom interaction potential with the surface is highly corrugated, a collisional description of inter-adsorbate interactions will be less appropriate, and in particu-

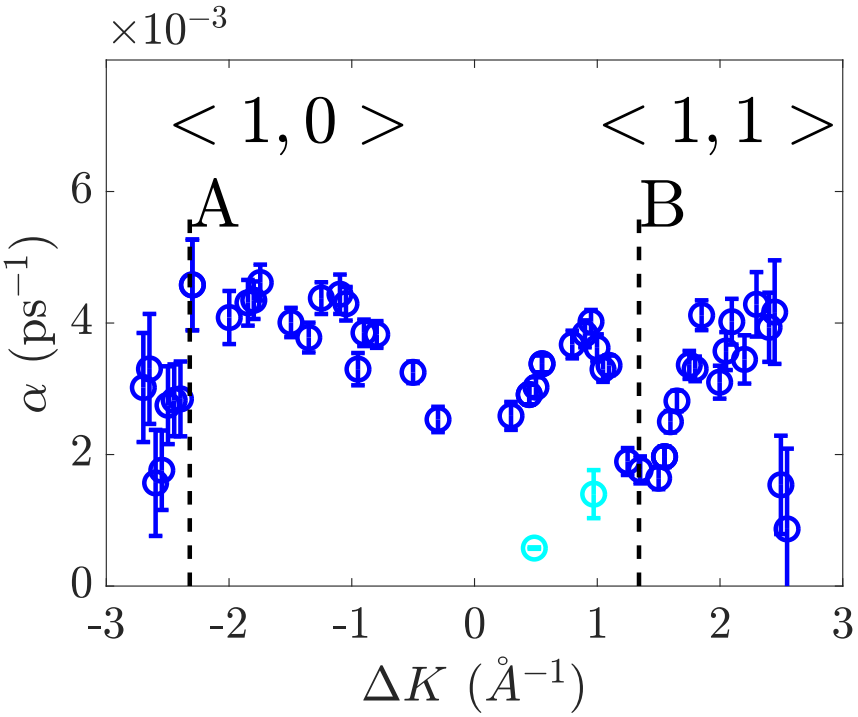

Figure 5.9: $\alpha(\Delta\mathbf{K})$ extracted from polarization scans of the oxygen-covered Ru(0001) surface at 800 K at an estimated coverage of 0.22 ML coverage (blue) and at the same temperature but at much lower coverage (cyan). The ideal half-order diffraction condition along $< 1, 1$ is shown as feature **A**. There is a pronounced dip in the dephasing rate near the half-order condition. The influences of inter-adsorbate interactions on the shape and absolute scale of the $\alpha(\Delta\mathbf{K})$ are discussed in the main text.

lar the data show that collective effects in the high coverage overlayer are crucial. Significant further theoretical work will be required to determine the precise role of interactions in the O/Ru(0001) system and how they relate to the models and surface systems just described. Further experimental clues would be provided by more extensive $\Delta\mathbf{K}$-dependent measurements at low and intermediate coverages.

The decay rate of the polarization is much slower at $T_s = 700$ K and so the lineshapes were fitted using the more sensitive marginalization method of Section 2.2.5 rather than the standard least-squares approach. The resulting $\alpha(\Delta\mathbf{K})$ along $< 1, 1 >$ at 700 K is shown in Figure 5.10, and shows a very well defined minimum in the decay rate at the half-order and first-order positions, as expected on the basis of the coverage and the considerations discussed in the previous paragraph concerning O-O interactions.

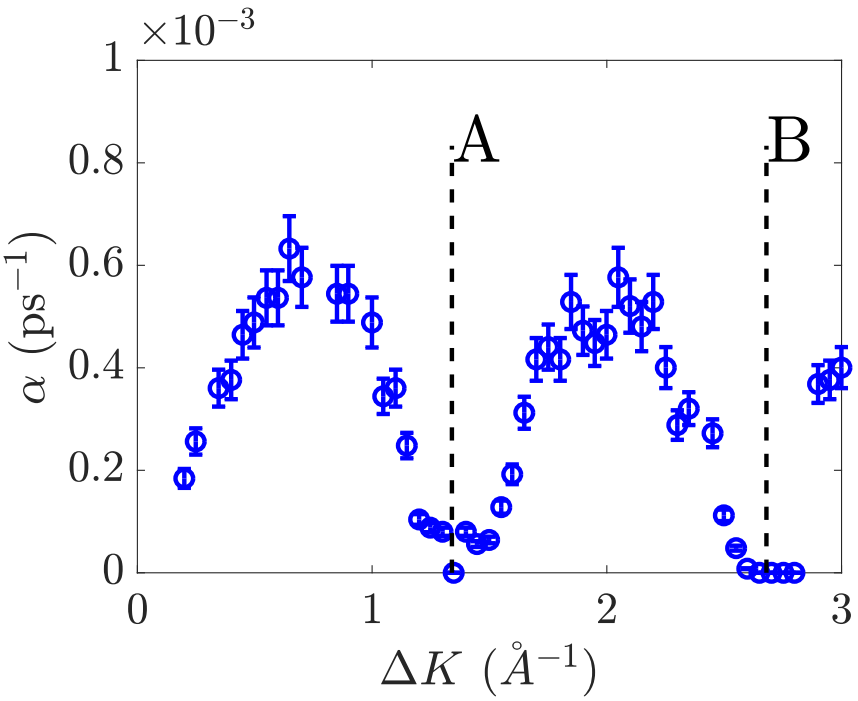

Figure 5.10: $\alpha(\Delta\mathbf{K})$ along $< 1, 1 >$ extracted from polarization scans of the oxygen-covered Ru(0001) surface at 700 K near 0.25 ML coverage (blue circles). To resolve the slow decays the marginalization method of Section 2.2.5 was used. The ideal half-order and first-order diffraction conditions are labelled as features **A** and **B**, and correlate perfectly with minima in the decay rate, as expected on the basis of the stability of (2×2)-like arrangements of interacting O atoms. The probability distributions $\rho(\alpha)$ inferred from each scan are significantly broader than the smooth trend which is closely followed by the dataset as a whole. However, the histograms of the best-fit parameter shown in Section 2.2.5 give an uncertainty compatible with the smooth trend, and therefore the plotted uncertainty has been estimated from those histograms.

5.2.2.2 Structure and dynamics of O/Cu(111)

Submonolayer O/Cu(111) was prepared by exposing the surface to molecular oxygen at 3×10^{-7} mbar up to a total exposure of 20 L with the surface held at 550 K. The dose was monitored via the helium specular reflected intensity $I(x)$ which fell to $I(0)/2$ over the course of c.1 min. $I(x)$ decreased monotonically. When the oxygen dose was stopped, there was no subsequent variation of the specular intensity over the timescale of minutes. Diffraction and polarization scans were then recorded for the system at $T_s = \{250, 300, 350, 450, 550, 650\}$ K, in which the temperature was ramped monotonically. The system was returned to 250 K with no further dosing, and the measurement sequence was repeated. All data were recorded along the $< 1, 0 >$ azimuth. At each temperature, the ΔK for polarization scans were visited in a different random order. In all cases the polarization scan was recorded over 4 loops and averaged.

The helium diffraction pattern along $< 1, 0 >$ at 250 K at the start of the first (blue) and second (red) measurement sequences is shown in Figure 5.11. A small relative scaling is applied between the scans for visual clarity, to separate the diffuse backgrounds. Different results were obtained on each run. The different results suggest that upon cooling to 250 K from high temperature, the system found itself in a kinetically limited state, on the first cycle if not both cycles. The blue curve displays several features above the diffuse background, which are labelled **A**-**F**. The red curve has lost features **A** and **C**, and gained feature **B**. The relatively prominent feature **E** of the first scan is much weaker in the second. Shown in the same figure are the corresponding scans at 650 K, at the end of the first (cyan) and the second (magenta) measurement sequences. A small relative scaling is applied to the high temperature scans too; without the scaling the curves do not exactly coincide for all ΔK but track each other closely. Neither scan shows any features to indicate ordered structures at 650 K. The diffraction scans will be discussed further in Section 5.2.3.

A typical polarization scan measured at 650 K is shown in Figure 5.12. The fitting procedure, exemplified by the red curve overlaid, is the same as used for the O/Ru(0001) polarization scans. In the particular example shown here, the deviation from single exponential behaviour is more significant. An important feature of the scan here compared to 5.8 is the absolute scale of $P(t_{SE})$. The amplitude of the exponential component shown is 0.05, which is significantly lower than the corresponding amplitude in the Ru(0001) data. Most of the decay amplitudes in the Cu(111) data are lower still. Because of the small decay amplitude, the polarization at $t_{SE} = 0$ is omitted because of the discrepancy in scale.

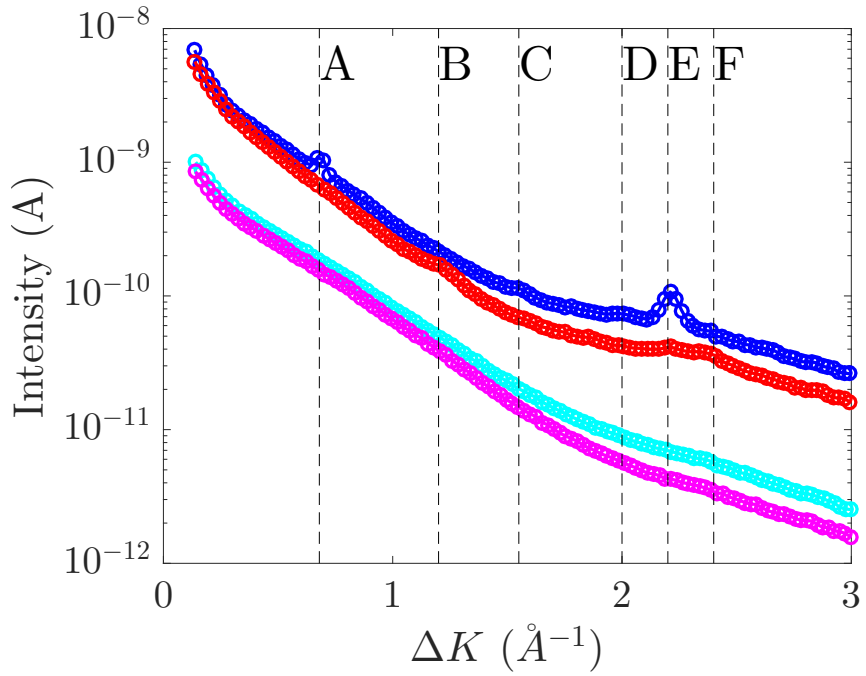

Figure 5.11: Helium diffraction scans along $< 1, 0 >$ of O/Cu(111) surface at an estimated coverage of 1/40 ML. Data were taken at 250 K during the first (blue) and second (red) measurement series, and at 650 K during the first (cyan) and second (magenta) series, interleaved with dynamics measurements as described in the main text. The second curve in each pair has been offset for clarity; without such an offset the diffuse components of each pair of curves would coincide almost exactly. Structural features visible by inspection are labelled **A** to **F**. The visible structural features at 250 K appear to have been changed by the first measurement cycle which involved an extended period of time at 650 K. However, the two scans taken at 650 K are qualitatively very similar and give no indication of any ordered structures.

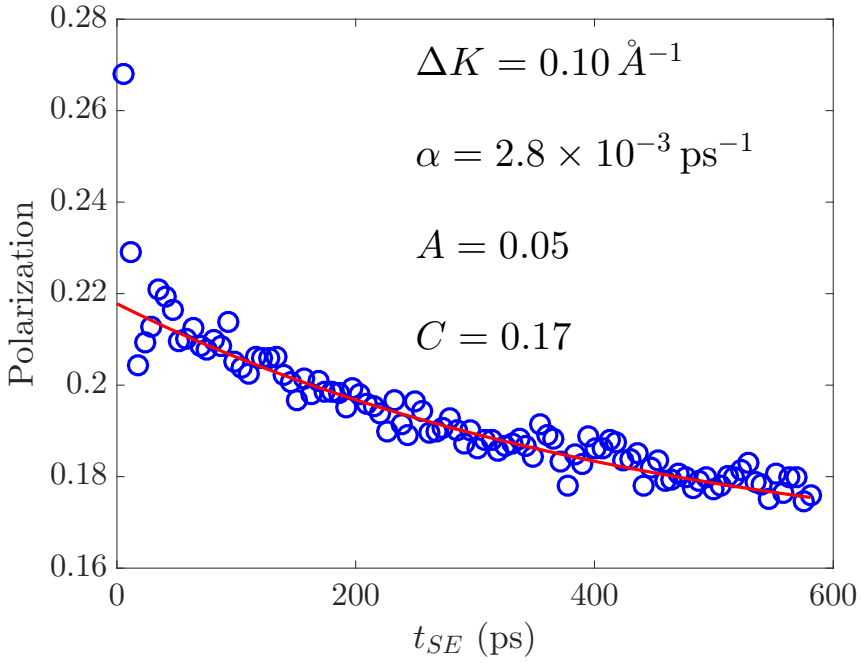

Figure 5.12: Polarization scan of the Cu(111) surface at $T_s = 650\,\mathrm{K}$, $\Delta K = 0.1\,\mathrm{\AA}{-}1$ during the first round of measurements. Only the real part of the polarization is plotted. The solid red curve is the best single exponential fit for $t_{SE} > 50\,\mathrm{ps}$, which is the start time applied consistently across all the scans. The amplitude of the decaying tail is much smaller than $P(t_{SE} = 0)$ and therefore the datum at $t_{SE} = 0$ is omitted for clarity. Fitted parameters are indicated on the plot.

The oscillations present in the polarization scan at short spin echo times are systematically present across the polarization scans at all temperatures. In most cases, the Fourier transform $S(\omega)$ of $P(t_{SE})$ contains a single broad peak. In other cases no peak is visible. As an example, the polarization scan of Figure 5.12 is shown in the frequency domain in Figure 5.13. The peak is dispersive, but the Nyquist frequency associated with the t_{SE} sampling is much lower than typical surface phonon or adsorbate mode frequencies. The apparent dispersion relation is not smooth, suggesting that in general the peak is aliased rather than being a very low frequency feature requiring a special explanation. Surface phonons on clean Cu(111) have been measured previously with inelastic helium atom scattering [62]. Figure 5.14 shows the experimental dispersion relation. The inelastic peak in the HeSE spectrum is consistent with the previous HAS measurements once aliasing is taken into account, as discussed in the Figure caption. The inelastic features are not analysed further. Although the Fourier representation is convenient for understanding the origin of the oscillations, the t_{SE} domain is more convenient for analysis of the slowly decaying tail.

The polarization scans at all temperatures were fitted to single exponential decays for $t_{SE} > 50\,\mathrm{ps}$. The exponential decay rate $\alpha(\Delta K)$ is shown in Figure 5.15.

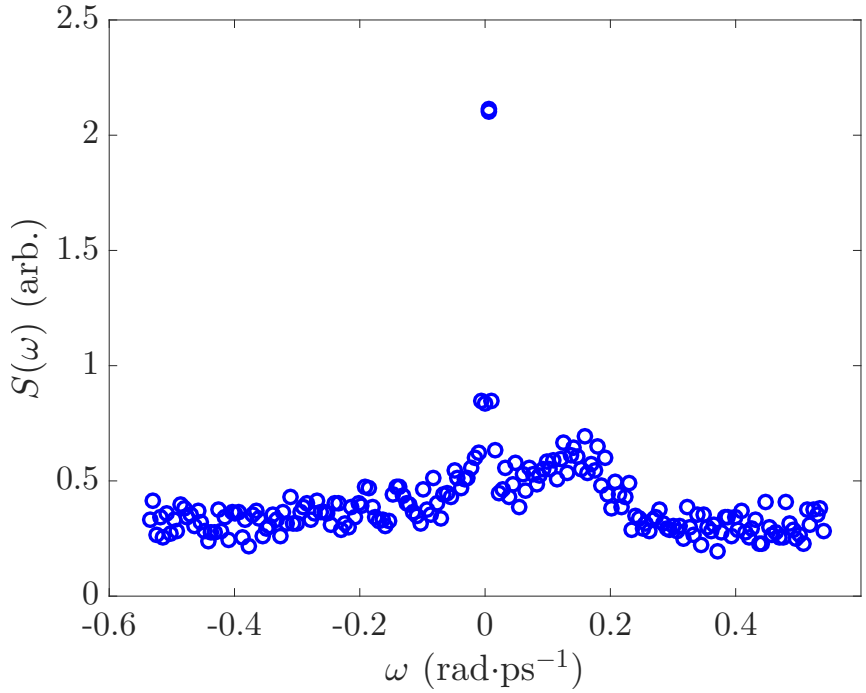

Figure 5.13: The polarization scan of Figure 5.12 shown in the frequency domain. The large peak at $\omega = 0$ has been removed for clarity. As well as the quasielastic peak, there is a broad inelastic peak at low frequency. The peak is dispersive but its dispersion is not smooth, implying that the peak is aliased at most ΔK.

Increasing the minimum t_{SE} further does not change the fitted rates. Results are shown only for fits whose decay amplitude A_1 is greater than 0.01 and whose adjusted R^2 parameter (Section 2.2) is greater than 0.8. The data from the first measurement series are shown on the negative horizontal axis; those from the second series (cooled to 250 K then all repeated) on the positive. $\alpha(\Delta K)$ is qualitatively repeatable between the first and second run. Because the amplitude of the decay decreases with increasing ΔK, only measurements in a small window of ΔK were feasible. The limited range of ΔK means that a detailed interpretation of the dynamics cannot be derived from the experiment as it stands. However, an Arrhenius plot can be made at a ΔK where fitted rates are available at all temperatures. At $\Delta K = 0.3$ the decays are well defined at all ΔK measured. Figure 5.16 shows the associated Arrhenius plot, which suggests that a single process with activation energy 86±15meV governs the diffusion at the lower temperatures, but that a different process dominates the dynamics at higher temperatures.

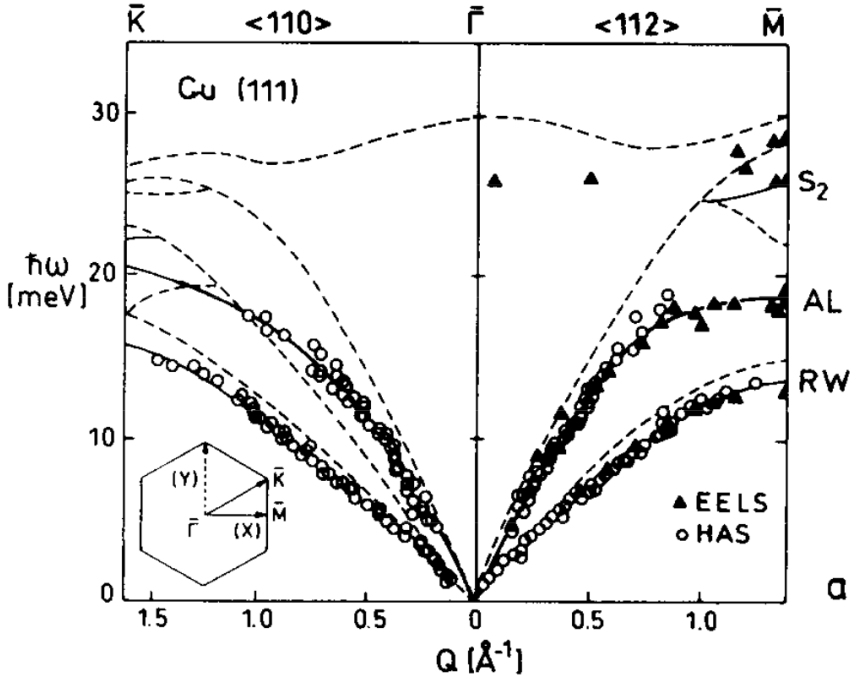

Figure 5.14: The surface phonon dispersions of clean Cu(111), measured with HAS. Reprinted from reference [62], Copyright (1994), with permission from Elsevier. The surface direction labels used in the previous work are related to the convention in the present Thesis by $\bar{\Gamma}\bar{K} \leftrightarrow < 1,0 >$ and $\bar{\Gamma}\bar{M} \leftrightarrow < 1,1 >$. The points $\bar{\Gamma}$, $\bar{K}$ and $\bar{M}$ represent special points in $\Delta\mathbf{K}$-space, namely the origin, a vertex of the first Brillouin zone (1BZ) and the midpoint of an edge of the 1BZ as illustrated in the figure inset. At $\Delta K = 0.1\,\text{Å}^{-1}$ the Rayleigh mode energy, as determined by linear interpolation of the dispersion down to $\Delta K \approx 0$, is about $\hbar\omega = 1.5\,\text{meV}$ (along either high symmetry direction). Although the energy resolution of the HAS experiment was around 0.5 meV, the uncertainty on $\omega(\Delta K)$ at small ΔK is made much smaller by linear interpolation of higher frequency data back to the origin. The associated frequency $\omega = E/\hbar$ at which we would expect an inelastic feature in $S(\omega)$ is $\Delta\omega = 2.3\,\text{rad}\cdot\text{ps}^{-1}$, assuming the Nyquist frequency is high enough. However, in the Fourier-transformed scan shown in Figure 5.13, the range of distinguishable frequencies is only $1.06\,\text{rad}\cdot\text{ps}^{-1}$. Wrapping $\Delta\omega$ back in to the principal range of allowed Fourier frequencies predicts an apparent $\Delta\omega \approx 0.2\,\text{rad}\cdot\text{ps}^{-1}$, in agreement with the HeSE result.

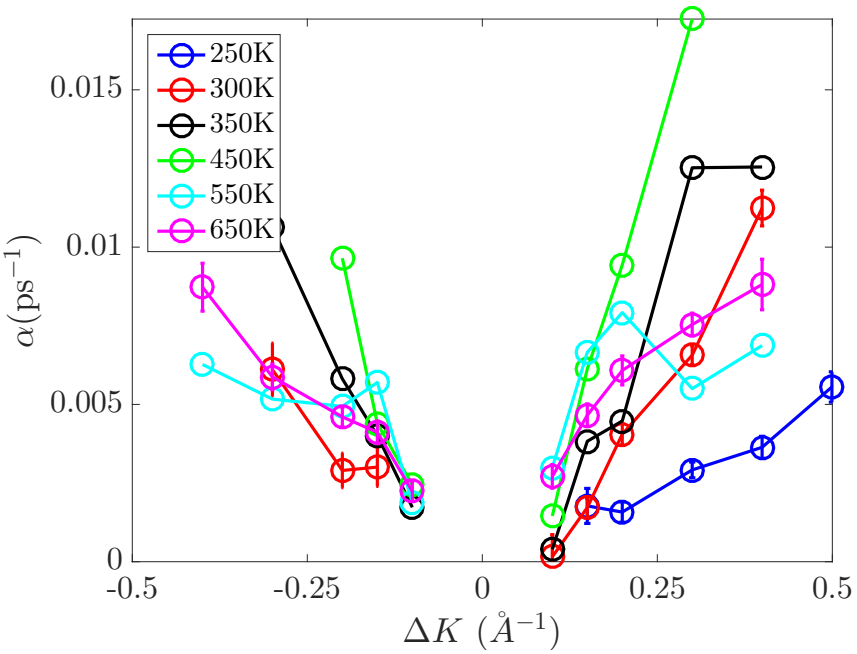

Figure 5.15: $\alpha(\Delta K)$ along $< 1, 0 >$ for O/Cu(111), at different temperatures during the first measurement series (shown as negative ΔK) and second series (shown as positive ΔK). On the whole the dephasing rates are reproducible despite structural shifts between the two series. Uncertainties are shown for a subset of data only for clarity; the uncertainties not shown are of comparable size.

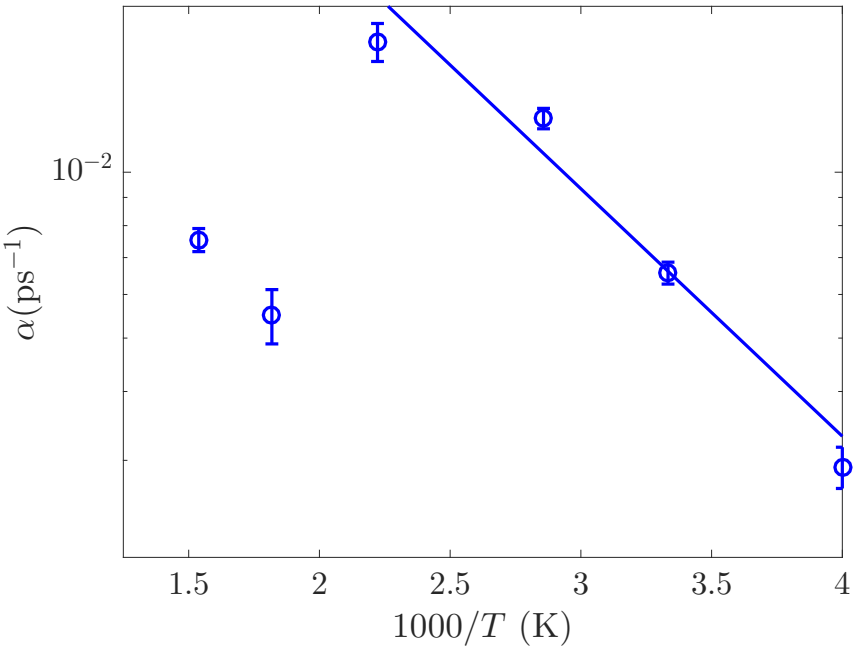

Figure 5.16: Temperature dependence of the decay rate shown in Figure 5.15 at $\Delta K = 0.3\,\mathrm{\AA}^{-1}$ (second run, shown at positive ΔK). The same fit start time of $t_{SE} > 50\,\mathrm{ps}$ was used at all temperatures. Between 250 K and 450 K the rate is described well by an activated rate law with activation energy $86 \pm 15\,\mathrm{meV}$. At the highest temperatures of 550 K and 650 K, the same activated process is not visible, but a slower process is still present which implies the nature of the diffusing species has changed.

5.2.3 Discussion

5.2.3.1 O/Ru(0001)

If we know the jump rates $\Gamma_{1,2}$, of isolated O atoms at two temperatures $T_{1,2}$, and the jump distribution can be assumed roughly constant, and we assume an Arrhenius rate law

$$\Gamma = \Gamma_0 \exp\Big(-\frac{E_A}{k_B T}\Big) \tag{5.10}$$

then the activation energy can be found as

$$E_A = \frac{k_B}{T_1^{-1} - T_2^{-1}} \ln\Big(\frac{\Gamma_2}{\Gamma_1}\Big), \tag{5.11}$$

and the prefactor as

$$\Gamma_0 = \exp\Big(\frac{T_1 \ln(\Gamma_1) - T_2 \ln(\Gamma_2)}{T_1 - T_2}\Big). \tag{5.12}$$

The values $T_1 = 293\,\mathrm{K}$, $\Gamma_1 = 16.6 \pm 0.9\,\mathrm{s}^{-1}$ are available from a low-coverage STM experiment [234]. The jump rate can be crudely estimated from HeSE data at only two ΔK, by assuming that the Chudley-Elliott (CE) model (Section 2.2.1) applies over the clean Ru(0001) lattice, with jumps to nearest neighbour sites only. The nearest-neighbour CE model is described by a single jump rate Γ, and the dephasing rate $\alpha(\Delta\mathbf{K})$ is given by

$$\alpha(\Delta\mathbf{K}) = 2\Gamma \sum_{\mathbf{j}} \sin^2\Big(\frac{\Delta\mathbf{K}\cdot\mathbf{j}}{2}\Big), \tag{5.13}$$

where $\mathbf{j}$ are six the nearest neighbour jump vectors. The jump rate at $T_2 = 800\,\mathrm{K}$ is fitted as $\Gamma_2 = (4.1 \pm 1.3) \times 10^8\,\mathrm{s}^{-1}$ from the spin echo data. From those values,

$$E_A = 680 \pm 15\,\mathrm{meV} \tag{5.14}$$

which is broadly in line with estimates in the literature based on either theory or experiment [253, 233, 234, 235]. The corresponding rate prefactor is:

$$\Gamma_0 = (8 \pm 4) \times 10^{12}\,\mathrm{s}^{-1}. \tag{5.15}$$

Assuming the jump process can be reasonably modelled using a one-dimensional transition path, the maximum possible value of the prefactor is the transition state

theory (TST) [161] attempt frequency

$$\Gamma_0 = \frac{\omega_0}{2\pi}\,. \tag{5.16}$$

where ω_0 is the frustrated translation (FT) frequency. The FT frequency has been determined from HREELS as approximately 53 meV for the disordered overlayer [254], and 51 meV at the origin in k-space for the 2×2 structure [255], which give a consistent estimate of

$$\frac{\omega_0}{2\pi} \approx 12 \times 10^{12}\,\mathrm{s}^{-1}\,. \tag{5.17}$$

ω_0 controls the maximum possible attempt frequency, but the actual attempt frequency depends on the friction γ. The friction can be estimated from vibrational linewidths. HREELS experiments with an energy resolution of 1 meV have been performed on the 2×2 structure [256, 257]. The high resolution studies do not treat the isolated-atom regime, and the intensity of the surface-parallel mode is very weak which makes the linewidth difficult to estimate. The linewidth of the surface-perpendicular mode of the 2×2 structure will have to serve for a ballpark estimate of the friction, which is a reasonable estimate of the friction governing isolated-atom frustrated translations as long as the friction is isotropic and not dominated by O-O interactions. Figure 5.17 shows data taken from [257] modelled with a friction of $2.5\,\mathrm{ps}^{-1}$ using a method explained in the caption. Good agreement is found, which suggests the actual friction is slightly lower than the value required to obtain the prefactor given in 5.15 within the one-dimensional rate theory. However, given the assumptions involved, a small disagreement is not surprising.

So far the metastable fcc sites have been treated as part of the diffusion barrier. A recent first-principles calculation of the hcp/fcc site energy difference ΔE states that ΔE is a decreasing function of coverage [236]. Linearly extrapolating the coverage-dependent result to the limit $\theta = 0$ gives $\Delta E = 570$ meV. Such a large ΔE is consistent with the fact that O atoms are never seen in fcc sites in the STM hopping measurements [233, 234]. However, the metastable site can still have an influence on the jump rate, depending on the depth of the metastable well, in other words the fcc energy relative to the bridge site energy. If the metastable well is shallow enough then treating the fcc site as the barrier is a reasonable approximation, in other words the process of trapping at fcc and hopping back to the original hcp site can be neglected. If the depth of the metastable well is large enough that trapping at fcc sites occurs with probability 1, followed by jumping to the original or neighbouring hcp site with equal probabilities, then the effective hcp-hcp jump rate will be halved compared to the case of no barrier recrossing. Trapping in the metastable site is more likely at low temperatures. Assuming the most extreme case,

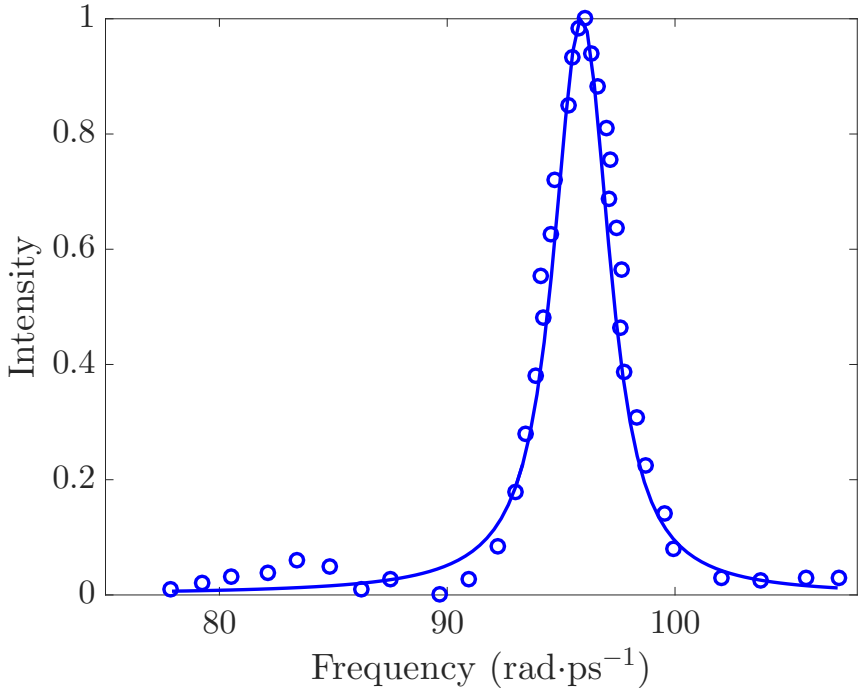

Figure 5.17: Extraction of an approximate dynamical friction for O/Ru(0001) from literature HREELS data. A full analysis of HREELS lineshapes depends on details such as the nature of the scattering [258]. However, here I provide a simple analysis of the peak by modelling it as the dynamical structure factor (DSF) of the adsorbate motion in order to gain a qualitative and comparative insight into the values of friction obtained respectively by HREELS and the dynamical measurements of HeSE HREELS data (blue points) for (2×2) O/Ru(0001) taken from [257]. Overlaid (solid curve) is the dynamical structure factor $S(\Delta k_z, \omega)$ for a scattering centre with the mass of atomic oxygen subject to a friction of $2.5\,\mathrm{ps}^{-1}$ in a well of frequency $\hbar\omega = 63\,\mathrm{meV}$. The solid curve was calculated using the experimental conditions $T_s = 90\,\mathrm{K}$ and $\Delta k_z = 2.0\,\mathrm{\AA}^{-1}$. However, the line width is not strongly sensitive to either T_s or Δk_z. $S(\Delta k_z, \omega)$ is calculated as the numerical Fourier transform of the analytical ISF 3.15. Convolution with the cited experimental resolution $\Delta E = 0.7\,\mathrm{meV}$ in the energy domain is achieved by multiplying $I(\Delta k_z, t)$ by a Gaussian function before the Fourier transform, where the Fourier transform of the Gaussian function is a Gaussian with 0.7 meV full width at half maximum.

where trapping occurs with certainty as 300 K and never occurs at 800 K, then the apparent jump rate from STM should be doubled. The new estimated activation energy and prefactor according to Equations 5.11 and 5.12 are then:

$$E_A = 650 \pm 10\,\text{meV}; \tag{5.18}$$

$$\Gamma_0 = (5 \pm 3) \times 10^{12}\,\text{s}^{-1}\,, \tag{5.19}$$

which brings the estimate closer to what is plausible based on the estimated friction γ.

5.2.3.2 O/Cu(111)

The O/Cu(111) measurements were performed at a relatively low coverage. Oxygen adsorption on Cu(111) is an activated process, with a low sticking coefficient $s(0) = 1 \times 10^{-3}$ at room temperature, increasing to 4×10^{-3} at our dosing temperature of 550 K [259]. At room temperature the exposure required to achieve the saturation coverage of 0.45 ML is around 1500 L based on a linear interpolation of the initial adsorption curve [259], and so at 550 K an exposure of 375 L is required. The exposure used in the present experiment was 20 L, so the coverage implying the coverage is approximately 1/20 of saturation coverage, or about 1/40 ML. An oxygen exposure of 300 L at 300 K reduces $I(x)$ to around $I(0)/500$, which is independent evidence that $I = I_0/2$ represents a small fraction of saturation.

The temperature-dependent structural data shown in Figure 5.11 is qualitatively in agreement with STM observations [248] in the following ways: firstly, no ordered structure was seen at the elevated temperatures, but emerged upon cooling; secondly, a period of annealing followed by cooling produced a different ordered structure. The most prominent feature in our scans is the feature **E** in the initial 250 K scan, which is expected for the '44' structure. This is expected since the '44' structure is the first to form under our dosing conditions. Unfortunately, the one dimensional helium diffraction scans cannot be reconciled in detail with the complex two-dimensional LEED patterns [248]. Very few of the LEED peaks lie exactly along the $< 1, 0 >$ azimuth, and therefore two-dimensional scans will be necessary to verify the structures present. The diffraction peaks of Figure 5.11 are weak and broad, suggesting that the order present is short-ranged. The features in the second scan at 250 K are weaker, which could be due to the heating and cooling cycle leading to smaller islands, or a mixture of island types.

The Arrhenius plot (Figure 5.16) at $\Delta K = 0.3\,\text{Å}^{-1}$ suggests that a change in the

dominant species could take place between 450 K and 550 K, which could be related to the structural changes apparent in the diffraction scans. Since the polarization decay is present at high temperature when there is no evidence for structured islands, there must be a contribution at high temperatures from a process that does not involve the islands, and can take place on the clean Cu surface. Certain species can be ruled by STM experiments in which they are seen to be static. For example, isolated oxygen atoms have been observed when the surface is in a disordered state during the initial stages of room temperature oxidation [260]. Small oxygen clusters were also observed, and were slightly more mobile, at least under the influence of tip effects, but the fact that they can be imaged at room temperature implies they are not our highly mobile species. Diffusion of Cu atoms at the higher temperatures is a possibility, and would be consistent with the increase in substrate mobility induced by adsorbed O on Cu(111) (and several other surfaces -"it appears in many cases to be the rule rather than the exception that the adsorbate mediates long-range mass transport of the substrate" [261]). Even if that was the case, the quantitative explanation of the $\alpha(\Delta K)$ is still an open problem. A further qualitative observation which could provide a hint to the solution is that diffusion is not seen at room temperature after dosing at room temperature, but is seen at room temperature after dosing at 550 K, and is also seen after dosing at room temperature and then annealing. Therefore, the species which diffuse at room temperature appear to be created in an activated process, and once created are either stable, or metastable but long-lived once the surface is cooled again.

5.2.4 Conclusions

The systems O/Cu(111) and especially O/Ru(0001) are amenable to detailed characterization via HeSE, since there is a surface temperature range in which oxygen remains adsorbed for long periods of time, and either diffuses rapidly or induces rapid diffusion of the substrate or composite surface species. There is much left to explore in both systems. The results so far suggest that oxygen diffusion on other transition metal surfaces could be a fruitful area for future HeSE investigations.

The diffusion of isolated O/Ru(0001) has been observed at 800 K at low coverage. The activation energy and rate prefactor have been estimated by assuming a Chudley-Elliott nearest-neighbour model, and comparing the jump rate to low-temperature STM data. Assuming a strictly activated rate law $\Gamma = \Gamma_0 \exp(-\beta E_A)$ leads to $E_A \approx 680 \pm 15$ meV in reasonable agreement with theoretical predictions in the literature. Allowing for trapping in the metastable fcc site at low temperatures, the activation energy is revised down to 650 meV, and the associated rate prefactor

is $5 \pm 3\text{ps}^{-1}$, which is realistic based on the vibrational frequency and friction implied by HREELS data. At a coverage approaching 0.25 ML, the $\alpha(\Delta K)$ is enhanced compared to the low-coverage result, at the ΔK where a comparison is available. At 800 K and the higher coverage, the adsorbate dynamics are strongly correlated, producing a very strong minimum in the $\alpha(\Delta K)$ which can be described as a de Gennes narrowing. At 800 K, correlated motion is clearly visible along the $< 1, 1 >$ high symmetry azimuth (an azimuth along which a principal diffraction peak of the clean surface lies), but not along $< 1, 0 >$ (along the Ru atomic rows), despite the expected structural features being present along both azimuths.

For O/Cu(111) a mobile species has been observed, which is present after a 20 L oxygen exposure at 550 K to a coverage of about 1/40 ML. The helium atom scattering cross section of the adsorbed species is large, probably due to locally induced surface roughening around the adsorbate. A degree of ordering is seen by helium diffraction at 250 K. The nature of the ordering is liable to change after annealing. At 650 K the surface is disordered. A diffusion process, as defined by the presence of a slow exponential decaying tail of HeSE polarization scans, is present on the disordered and partially ordered surface. Although the diffusion process might be required for the temperature-dependent structural changes, it is much too fast to be the rate-limiting step.

5.3 Summary and outlook

The diffusive surface dynamics of graphene precursors on Ru(0001) have been measured in the temperature range $550 \leq T_s \leq 1300\,\text{K}$. The lineshapes are consistent with hopping between inequivalent hollow sites, with an activation energy of $292 \pm 7\,\text{meV}$ and a prefactor of $2.45 \pm 0.25\,\text{ps}^{-1}$. The process is assigned to the diffusion of a small carbon cluster. The dynamics were modelled using a scaled atom/surface potential, but the evidence for cluster diffusion clearly motivates calculations of cluster energetics in terms of stability and diffusion.

The diffusion of O/Ru(0001) has been measured at low coverage, and in more detail at a coverage slightly below 0.25. The higher coverage data show strongly correlated adsorbate motion. An obvious extension of the experiment would be to record more extensive data at low coverage to determine the nature of the jump dynamics, the activation and prefactor within HeSE rather than relying on a comparison with STM data which requires assumptions about the dynamics over a very large temperature range. Another potentially interesting avenue of enquiry would be the nature of the diffusive dynamics at a coverage of exactly $\theta = 0.25$ ML, which

would reveal whether the mobility is dependent on the presence of vacancies in the (2×2) structure, or alternatively if the nearest-neighbour interaction energy or hcp-fcc site energy differences are small enough to be relevant in the dynamics.

There is scope for O/Cu(111) to be characterized much further with helium diffraction and spin echo. It would be useful to know how the complex structures observed in STM and LEED studies appear in helium diffraction when they are well defined. On the dynamics side, by adjusting the conditions of oxygen dosing and polarization measurements it might be possible to increase the coverage of the mobile surface species, and allow the fast diffusion process to be characterized in detail.

As far as reasonably possible, absolute jump rates and jump distributions have been rationalized in terms of a Langevin friction. In the case of carbon diffusion, the friction was estimated by simulating the Langevin equation on a physically realistic two-dimensional potential energy surface. In the case of oxygen diffusion, the broadening of high-frequency vibrations as observed in HREELS was analysed to provide an independent estimate of the friction. Similar methods will be used to rationalize the adsorbate/surface energy exchange rates in the final chapter, with the caveat that quantum mechanical effects are much more important.

Chapter 6

Surface diffusion of hydrogen

I present spin echo diffusion studies of three hydrogen/metal systems, which are analysed on a consistent footing. The key ingredients in the analysis of the jump rates are the rate theory of Chapter 4, and the first-principles potential energy surfaces described in Section 6.2.

Section 6.3 presents new measurements on Ru(0001), a system which has been measured with spin echo previously [23, 35] with a focus on the protium isotope. One of the unexpected and puzzling outcomes of the previous experiments was circumstantial evidence for a weak isotope effect in the tunneling rate of protium (^{1}H, H) versus deuterium (^{2}H, D) [35]. Because the suggested small isotope effect runs so contrary to theoretical predictions, there was a strong incentive to measure deuterium diffusion more extensively to confirm or refute the effect. The new measurements were motivated by awareness of potential H contamination in D measurements [35, 36], along with the improved detector installed in the interim which enables measurement times (number of loops) to be reduced, thereby reducing contamination effects. The new and more extensive deuterium results show that the jump rate of D at low temperatures is much slower than the H jump rate.

Section 6.4 presents the first HeSE measurements for H and D on Pd(111). From an applications point of view, palladium is a particularly interesting substrate on which to study hydrogen dynamics, because of the high solubility of hydrogen in the bulk. However, diffusion of adsorbed hydrogen down into the subsurface and bulk region is unfavourable except at high coverages where the barrier to subsurface diffusion is reduced by H-H interactions [262, 263], and so under UHV conditions surface diffusion can be studied in much the same way as on other transition metal surfaces. Pd(111) has recently been used as a test case for calculations of hydrogen diffusion rates, based on a phenomenological theory for the dynamical structure factor (DSF) broadening in terms of scattering rates [45]. The diffusive surface

dynamics can be measured in much the same way as for other surfaces, and have been analysed within the same framework.

Section 6.5 concerns the structure and diffusion of hydrogen on Cu(111). H/Cu(111) has been previously measured within HeSE, and displays more structural complexity at high temperatures, compared to Ru(0001) and Pd(111). H/Cu(111) has been used as a model test system for electronic friction calculations based on time-dependent density functional theory, which provides an independent line of reasoning in the discussion running through the present Chapter regarding the strength of friction.

For the three systems studied in the present Chapter, the semiclassical jump rate appears to be suppressed by the friction being too low rather than too high. In previous analyses of hydrogen diffusion data, evidence has been repeatedly found for multiple jumps [84, 35], and yet attempts to model the absolute rate in the semiclassical regime [43, 35] have yielded a very high friction (see Section 4.5.3), which would not be consistent with multiple jumps. The numerical results of the dissipative quantum rate theory implemented in Chapter 4 show that a very high friction is inconsistent with the fast tunneling rate seen at low temperatures on Ru(0001) (and more recently on Ni(111) [36]). Estimates of the friction from independent theoretical and experimental sources suggest that the low semiclassical rate seen in spin echo experiments is due to the friction being low rather than very high. The low friction interpretation explains the anomalously high crossover temperature to deep tunneling seen in spin echo experiments, since the reduction in rate caused by low friction is expected to be less severe at low absolute rates of hopping.

6.1 Hydrogen on metals

Hydrogen atoms adsorbed on metal surfaces are an experimental realisation of quantum particles diffusing in a dissipative periodic environment. As such, the surface diffusion displays a striking crossover from thermally activated behaviour to an approximately temperature-independent rate under conditions accessible by STM [41] or HeSE [23, 36] for example. Meanwhile, considerable theoretical work has led to a range of analytical and numerical methods for predicting quantum diffusion rates, subject to various assumptions or approximations. In some cases, diffusion in corrugated potentials has been modelled in terms of quantum escape rates, governed either by semiclassical theories such as the Wolynes model [42, 43] (Equation 4.91) or deep-tunneling extensions based on the analysis of bounces (Section 4.5), also referred to as instanton methods [23]. In other cases, a more direct modelling of the system dynamics has been attempted, for example through stochastic wavefunc-

tion evolution [44] or approximating the dynamical structure factor via Lorentzian broadening of the system energies [45].

HeSE has previously been applied to study hydrogen diffusion on the Pt(111) [43] and Ru(0001) [23] surfaces (published work) and also Cu(111) [84] and Ni(111) [36]. The results for Pt(111) were interpreted in the framework of the Chudley-Elliott jump diffusion model (Section 2.2.1), with rates governed by the semiclassical Wolynes theory [42]. The H/Ru(0001) data, interpreted in terms of a non-Bravais jump model (Section 2.2.1) were the first example of a transition to deep tunneling measured with HeSE. The difference in phenomenology between Ru(0001) and Pt(111) highlights the critical role of the precise static potential landscape, and the coupling to the heat bath, in quantum diffusion.

Isotope effects are a key aspect of any theoretical description of quantum rates. For hydrogen, the isotope effect has been shown experimentally to be very significant in surface diffusion at low temperature on some surfaces [41, 154], and in surface reactions [264, 265]. In the parameter regime that applies to H and D diffusion on typical metal surfaces, a range of methods predict a minor isotope effect in the semiclassical activated regime, but a very large effect at low temperatures. For the Cu(001) surface where tunneling takes place between degenerate sites, a WKB estimate for the tunneling matrix element Δ, combined with a rate expression that scales with Δ^2 consistent with incoherent tunneling as described in Section 4.5.6, predicts five orders of magnitude between the tunneling rates of H and D [266]. Close packed surfaces are the best candidates for surfaces that could display a small tunneling isotope effect. Indeed, for Ni(111) the tunneling isotope effect was originally determined to be much less than an order of magnitude [267], but subsequently corrected by the same investigators [268], revealing instead a Wolynes-like behaviour down to 65 K with a much more significant isotope effect. The original Ni(111) results were justified theoretically by phonon-induced mass renormalization [269] but relied on unrealistic tunneling matrix elements. The revision in interpretation illustrates the importance of both treating experimental results critically, and using realistic model parameters derived from first-principles calculations wherever possible.

6.2 First principles potential energy surfaces

A key ingredient in the comparison of HeSE data with first-principles theory is the hydrogen/metal potential energy surface (PES), as described in Section 4.5.5. Figure 6.1 shows the H/Ru(0001) PES as considered already in Section 4.5.5 and also the analogous potentials for Pd(111) and Cu(111). The potentials were calculated with

density functional theory (DFT). More details on the calculation parameters are given in the Figure caption. Figure 6.2 shows the potential as a function of reaction co-ordinate, evaluated along the transition paths drawn on the two dimensional potentials of Figure 6.1. The significance of the DFT potential energy surface, and its relationship to the model Hamiltonian used to predict jump rates, was discussed in Section 4.5.5.

As a broad consistency check on the accuracy of the first-principles potential energy surfaces, predicted vibrational frequencies are given in Table 6.1. The best theoretical estimate from the potential is given by the excitation energies probed in the relevant inelastic scattering experiments, corresponding to bandgaps in the H/surface bandstructure. The symmetry considerations underlying the choice of the relevant pair of bands is described in the Table caption. Estimates based on the harmonic expansion of the potential at the adsorption sites (hollows) and saddle points (bridges) are given for comparison. Anharmonic effects systematically reduce the bandgap below the harmonic estimate. The calculated bandgaps are in broad agreement with the measured vibrational frequencies, which verifies independently of any diffusion dynamics measurements that the overall scale and shape of the first principles potentials are reliable, although some further adjustment is necessary to achieve a consistent interpretation of diffusion data, as discussed in some detail in Section 4.5.5. The imaginary frequency ω_b, derived from the curvature of the barrier top, is a key parameter of the rate calculations performed later in the present Chapter.

6.3 Diffusion of hydrogen on Ru(0001)

The first detailed HeSE measurements of deuterium (D) diffusion on Ru(0001) are presented. Previous measurements [35] provided circumstantial evidence for D atoms diffusing by tunneling, at a surprisingly fast rate comparable to the tunneling rate of H. The more extensive measurements here, in which contamination by H was negligible, show that the diffusion of D by tunneling is extremely slow, in line with theoretical expectations. Coverage-dependent diffraction measurements suggest a form factor oscillation in the diffracted intensity, which contradicts the previous explanation of the diffuse diffraction feature in terms of repulsive H-H interactions.

6.3.1 Background

Molecular hydrogen adsorbs dissociatively on Ru(0001) with an initial sticking coefficient $s_0 = 0.4$ at $T_s = 100\,\mathrm{K}$ [275]. The sticking coefficient reduces with increasing

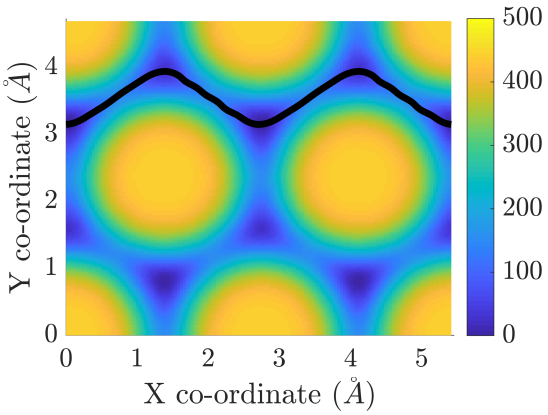

(a) $V(x, y)$ for H/Ru(0001).

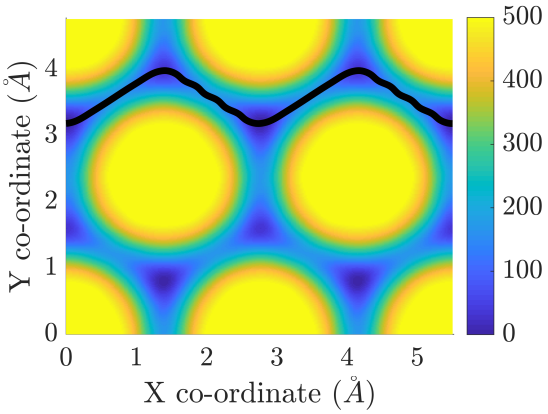

(b) $V(x, y)$ for H/Pd(111).

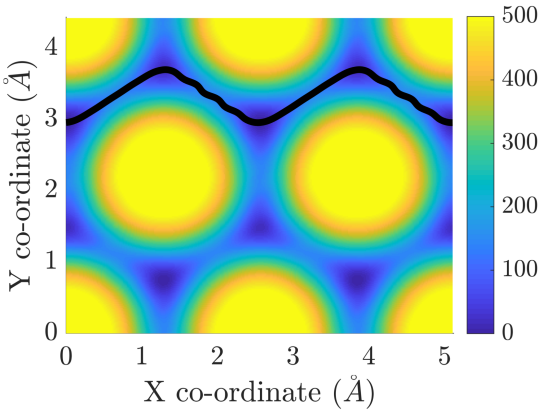

(c) $V(x, y)$ for H/Cu(111).

Figure 6.1: First principles potential energy surfaces calculated within DFT. The potential has been minimized in the z direction in each case, making a two-dimensional potential $V(x, y)$. The calculation of the H/Ru(0001) potential is described in Chapter 4 (Figure 4.7) where it is first introduced. The calculation The H/Pd(111) potential was computed by Dr Marco Sacchi using the CASTEP code [270], using ultrasoft pseudopotentials [271], a plane-wave cutoff energy of 360 eV, the PBE functional [181, 182] and a 3×3 supercell with 5 atomic layers. The Cu(111) calculation was performed with the PW91 functional [272] and a cutoff energy of 300 eV. Substrate atoms were frozen in their clean relaxed geometry. The centres of high potential (orange/yellow) are top sites. The transition path between adsorption sites is shown in black.

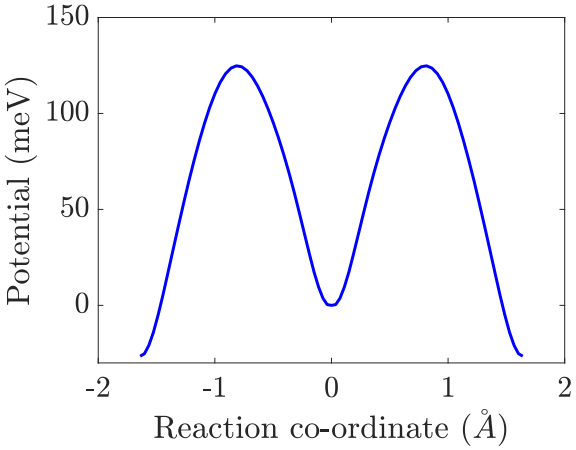

(a) Potential along the transition path, H/Ru(0001).

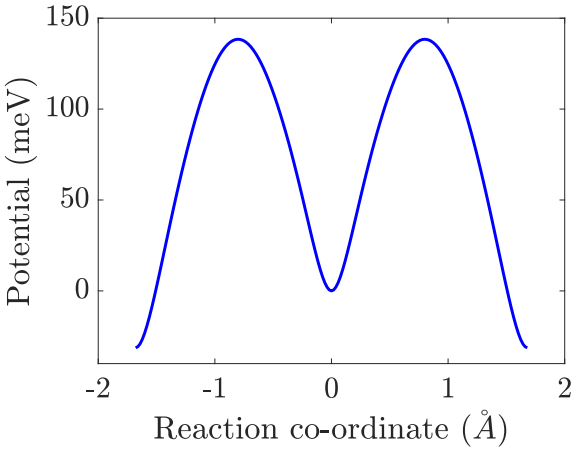

(b) Potential along the transition path, H/Pd(111).

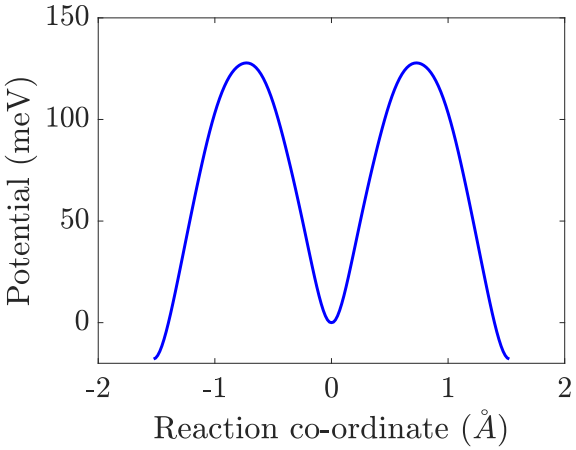

(c) Potential along the transition path, H/Cu(111).

Figure 6.2: The local potential along the transition paths extracted from the potential energy surfaces of Figure 6.2. The potentials have all been adjusted to reproduce the experimentally determined site energy differences, ΔE between fcc and hcp sites. The barrier heights are approximately $V_b = \{125, 140, 130\}$ meV for Ru, Pd and Cu respectively.

Table 6.1: Vibrational frequencies of adsorbed protium (H) atoms on Ru(0001), Pd(111) and Cu(111), derived from the theoretical potential energy surfaces shown in Figure 6.1. Curvature values are derived from the local harmonic expansion of the potential at the well (fcc) and saddle point (bridge). Bandgap values are read off from the H/surface bandstructure. The method for calculating the bandstructure from a three-dimensional atom/surface potential is given in [36], and the bandstructure for Cu(111) has been calculated using a code supplied by Dr John Ellis. Experimental values from vibrational spectroscopy are cited for comparison. In general the experimental frequencies are dependent on coverage θ, and the quoted values refer to the $\theta \to 0$ limit. All quantities are given in units of meV. The symbol $_{\parallel}$ indicates surface-parallel motion, $_{\perp}$ indicates z-motion, and † indicates the transition state. ω_b is the imaginary frequency at the saddle point along the transition path. Hollow sites possess threefold symmetry but only two surface-parallel frustrated translational classical eigenmodes. Therefore, the surface-parallel modes must be degenerate to avoid a conflict of symmetry. Numerically, the two surface-parallel frequencies derived using the curvature method are slightly non-degenerate, as indicated by the uncertainties on the theoretical values. In the bandgap method, the lowest pair of nearly-degenerate bands is associated with surface-parallel vibrations in fcc sites by analogy with the classical dynamics, and the lowest isolated band is assigned to surface-perpendicular excitation. The best theoretical estimates are broadly in agreement with the low-coverage experimental values.

Surface	**Energy**	**Theory (curvature)**	**Theory (bandgap)**	**Experiment**
Ru(0001)	$\hbar\omega_{\parallel}$	98 ± 1	79 [35]	85 [57]
	$\hbar\omega_{\perp}$	136 ± 1	117 [35]	125 [57]
	$\hbar\omega_b$	51	-	-
	$\hbar\omega^{\dagger}_{\parallel}$	92	-	-
	$\hbar\omega^{\dagger}_{\perp}$	166	-	-
Pd(111)	$\hbar\omega_{\parallel}$	119 ± 2	-	96[273]
	$\hbar\omega_{\perp}$	127 ± 1	-	124[273]
	$\hbar\omega_b$	45	-	-
	$\hbar\omega^{\dagger}_{\parallel}$	76	-	-
	$\hbar\omega^{\dagger}_{\perp}$	145	-	-
Cu(111))	$\hbar\omega_{\parallel}$	110 ± 1	80	88 [274]
	$\hbar\omega_{\perp}$	125	108	123 [274]
	$\hbar\omega_b$	57	-	-
	$\hbar\omega^{\dagger}_{\parallel}$	105	-	-
	$\hbar\omega^{\dagger}_{\perp}$	167	-	-

temperature. A very large exposure is needed to achieve saturation, which can be explained by the requirement of neighbouring vacancies in the H overlayer to dissociate an impinging molecule [276]. The desorption rate takes off at around 350 K [277], making constant-coverage experiments of a few hours' duration practical from cryogenic temperatures up to slightly above room temperature. The stable adsorption site can be assigned experimentally as a threefold hollow based on the symmetry of vibrational lineshapes in HREELS [278]. The saturation structure of the hydrogen overlayer is a commensurate (1×1) structure in which hydrogen atoms occupy exclusively fcc hollows [279], as determined by LEED and consistent with the previous HeSE work [35]. Below saturation coverage, no ordered structures are detectable with LEED unless the surface temperature is below 75 K [280, 281]. The fact that the ordered structures were observable at low temperatures suggests that the disordering at $T_s > 75\,\mathrm{K}$ is a genuine thermal effect rather than the result of electron-induced damage. Although the (1×1)-H overlayer has been observed with HAS [282], the phase diagram has not been systematically investigated with HAS. More recently, STM experiments at 50 K [276] have observed the ordering process upon increasing exposure. The first ordered structure to form is $(\sqrt{3} \times \sqrt{3})$-1H in fcc hollow sites when the coverage approaches 0.33, but there was no evidence for the formation of smaller islands upon initial exposure.

The H/Ru(0001) potential energy surface has been calculated independently several times with first-principles methods [283, 284, 23] and the results are broadly consistent. The fcc hollow is found as the most favourable adsorption site, and the relative energy ΔE of the hcp hollow site is small compared to the classical diffusion barrier of $120 - 140\,\mathrm{meV}$ over the bridge sites. ΔE is difficult to pin down theoretically to high relative precision because of its small value, but has been determined experimentally within HeSE as $22 \pm 1\,\mathrm{meV}$ [23]. Because $\Delta E \approx k_B T$ in the surface temperature range $100\,\mathrm{K} < T_s < 300\,\mathrm{K}$ applying to the present series of experiments, both types of hollow site play a role in the jump dynamics, so the non-Bravais model of Section 2.2 is appropriate for the analysis. HeSE data previously revealed an apparent activation energy of 95 meV in the quantum activated regime, which is substantially less than the classical barrier and more consistent with the inter-band activation energy in the H/surface bandstucture [35]. The macroscopic diffusion barrier as measured by optical methods (170 meV [285]) is even higher than the classical barrier for diffusion on terraces, since the macroscopic diffusion rate is limited by diffusion over step edges.

Some information on inter-adsorbate interactions can be obtained from variation of structural and dynamical information with coverage. Optical measurements of the global, collective diffusion rate show results constant with coverage [286]. HeSE

measurements [35] showed that reducing the coverage from 0.2 ML to 0.1 ML and increasing the coverage to 0.6 ML does not dramatically affect the mobility. However, simultaneous occupation of neighbouring fcc and hcp sites has been shown theoretically to be unfavourable [287], which could give rise to effective nearest-neighbour site blocking. Additionally, all ordered H structures are exclusively fcc-occupying [281], which suggests that the mean-field fcc/hcp site energy difference could systematically increase with coverage. Monte Carlo modelling of the LEED phase diagram showed that the experimental results could be well matched by a model where the pairwise component of H-H interactions is repulsive [288], but only weakly so in order to explain the low transition temperature of the sub-monolayer ordered phases. In the prior HeSE data there is some evidence for repulsive H-H interactions, namely:

- a diffuse feature in diffraction scans of the $\theta = 0.2\,\mathrm{ML}$ covered surface, and
- a dip in the $\alpha(\Delta K)$ at the same ΔK.

However, the best-fit $\alpha(\Delta K)$ produced by Monte-Carlo modelling of the dynamics of the interacting system [35] does not display the experimentally observed dip, so the interpretation is not entirely self-consistent. An alternative interpretation of the diffuse diffraction ring as a form factor effect will be explored in Section 6.3.3. The D diffusion measurements in the present Chapter were performed mostly at a constant coverage corresponding to the coverage used in the previous HeSE work. Some D measurements at low temperatures have been performed at different coverages to demonstrate that the absence of diffusion was not caused by site blocking.

6.3.2 Experimental methods

The single-crystal Ru(0001) sample was prepared according to the procedures given in Section 2.1.3, giving a typical reflectivity of 30% for the clean surface. Hydrogen was deposited on the surface by leaking H_2 (Air Liquide, 99.999%) into the scattering chamber. The majority of dynamics measurements were carried out after a dose of $1 \times 10^{-8}\,\mathrm{mbar}$ (gauge) for 45 s, corresponding to a dose of approximately 0.3 L (gauge) where $1\,\mathrm{L} = 1.33 \times 10^{-6}\,\mathrm{mbar{\cdot}s}$. All dosing was carried out either at a constant surface temperature $T_s = 250\,\mathrm{K}$, or during cooling through 250 K (typical temperature range 290 K to 210 K). Dosing during cooling rather than at constant T_s had no noticeable effect on the state of the dosed surface as determined by inspection of diffraction scans. The dosing conditions are summarized for Ru(0001), and also Pd(111) and Cu(111), in Table 6.2.

For D_2 experiments, the dosing procedure used was identical including the same uncorrected gauge pressure. H and D measurements were separated by several

Table 6.2: Typical dosing conditions for the three hydrogen/metal systems covered in the present Chapter, to prepare the surface in the state where the majority of dynamics measurements were carried out. Further details on the uptake characteristics of each system, and how the coverage has been estimated, are given in the respective sections on adsorption and structure (6.3.3, 6.4.3, 6.5.1.1).

Surface	**p(mbar)**	**T_s(K)**	**Time (s)**	**θ(ML)**	**I/I_0**
Ru(0001)	1.0×10^{-8}	250	45	0.2	0.65
Pd(111)	2.5×10^{-9}	350	Continuous	0.1	0.6
Cu(111)	1×10^{-8}	200	1000	0.1	0.75

days, a large D_2 dose (24 hours at 1×10^{-7} mbar), and several cleaning cycles, to minimize the possibility of H contamination. The separation time and dose of D_2 were adequate to prevent detectable contamination, as shown later in the present Chapter (see Figure 6.17). However, the exact details of the procedure were chosen by intuition and local experience based on how contamination was avoided in the study of D/Ni(111) [36], rather than by rigorous reasoning based on the properties of the sample and the vacuum system. Therefore it is possible that more relaxed measures would have been adequate to avoid contamination. Since there was no need to switch repeatedly between H and D measurements, the use of a relatively long and thorough anti-contamination period was not a significant inconvenience. During low temperature D measurements, only short measurement periods of less than 45 minutes were used, separated by flash anneals to $T_s > 600$ K to remove trace contaminants. Polarization scans were recorded using a uniformly spaced spin echo time base with $0 \leq t_{SE} \lesssim 600$ ps to observe relatively fast dynamics, and $0 \leq t_{SE} \lesssim 850$ ps to observe relatively slow dynamics.

6.3.3 Adsorption and structure

Figure 6.3 shows the variation in specular intensity upon exposure of the clean Ru(0001) surface to molecular hydrogen. The result exhibits the characteristic minimum seen in previous measurements of the system [35] but not the subsequent rise above the initial clean surface intensity.

Figure 6.4 shows the helium diffraction patterns from the clean surface, partially H-covered surface at 250 K and the H-saturated surface. The clean surface shows extremely weak and broad oscillatory features which were typical of clean surface scans even at high reflectivity. The small clean surface oscillations are visible in the previously reported helium diffraction measurements on the same instrument [35]. The diffraction pattern seen after dosing hydrogen is qualitatively consistent with the previous HeSE work, and is described in the Figure caption.

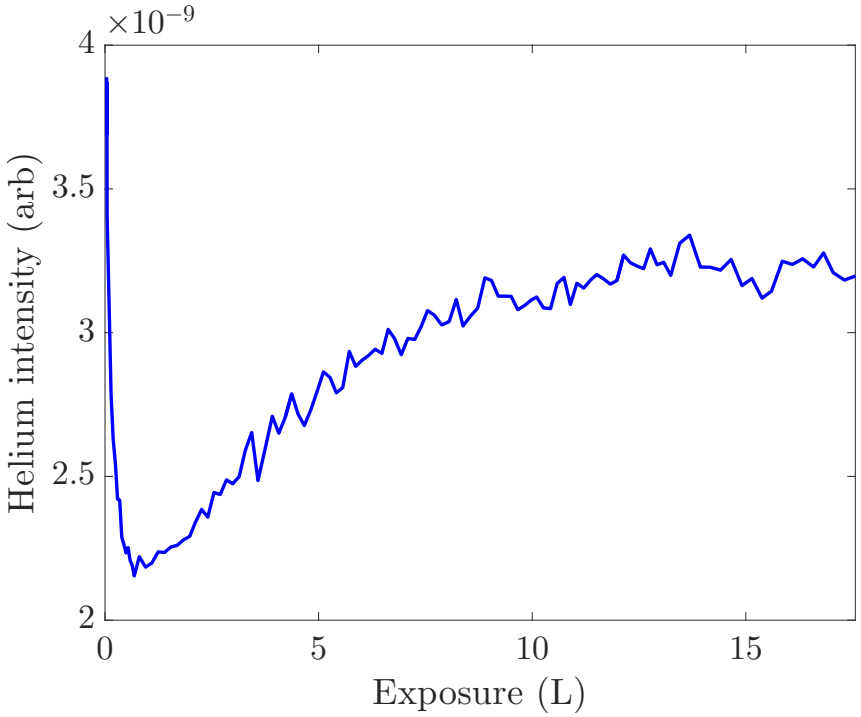

Figure 6.3: Variation of specular reflected intensity during exposure of Ru(0001) to molecular hydrogen, showing the characteristic minimum seen in previous measurements of the system [35] but not the subsequent rise above the clean surface intensity.

Previously [35] the diffuse feature seen at intermediate coverage in Figure 6.4 was ascribed to the structure factor of a repulsively interacting overlayer. However, separate measurements carried out with deuterium suggest a different interpretation. Figure 6.5 shows diffraction scans recorded at $T_s = 250\,\mathrm{K}$ after exposures of (0.0,0.1,0.2,0.3 and 0.75)$\times 10^{-6}\,\mathrm{L}$ (gauge) of molecular D_2. Unexpectedly, the position and shape of the diffuse feature is coverage-independent, which suggests it is related to the scattering form factor rather than the structure factor of the overlayer. At small exposures, there is a clear progression of the intensity of the broad peak with increasing exposure. However, the position of the peak barely changes, indicating that it its position does not define a coverage. Figure 6.6 shows the the peak intensity as a function of exposure. Continuing the dose past 0.75 L (gauge) reduces the intensity of the diffuse feature. The broad maximum in the intensity as a function of exposure explains why hardly any difference can be seen between the two highest coverage (magenta and red) curves of Figure 6.6. At high coverages the diffuse feature is suppressed by the structure factor of the overlayer, as seen in the high-coverage H diffraction pattern of Figure 6.4.

Because the diffuse diffraction feature occurs at or very near the half-order condition along $< 1, 1 >$, at first it seems plausible that small ordered islands could be responsible. The slight sharpening of the feature at lower temperatures [35] would

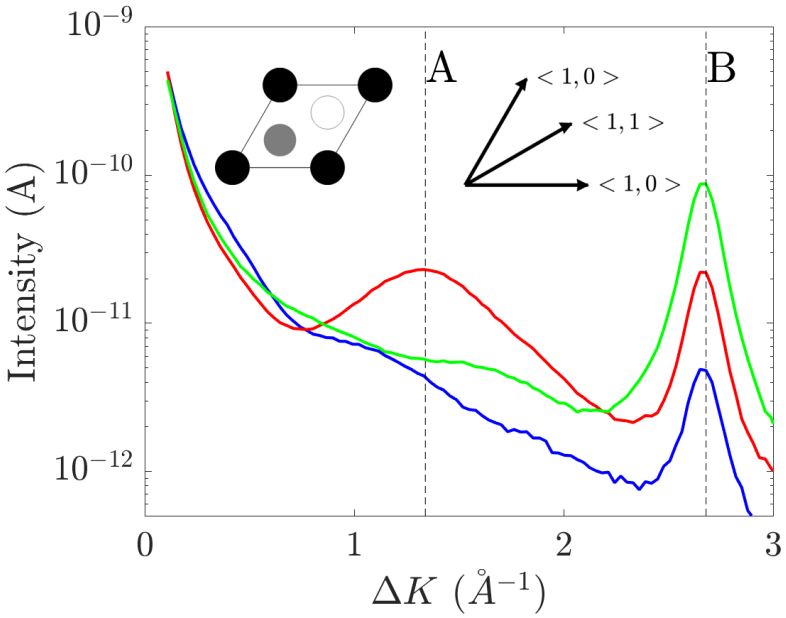

Figure 6.4: Helium diffraction scans along $< 1, 1 >$ of the clean Ru(0001) surface at 30 % reflectivity (blue), the partially H-covered surface at $T_s = 250\,\mathrm{K}$ after dosing to the point of minimum intensity shown in Figure 6.3 (red) and after a large dose leading to approximate saturation (green). The clean surface scan shows the expected first-order diffraction peak at **B**, and very weak oscillatory features that are typically present even after intensive cleaning. The partially covered surface shows a diffuse maximum at the position labelled **A**. The first-order diffraction feature from the saturated surface is enhanced over the clean surface value due to the increased corrugation of the hydrogen overlayer.

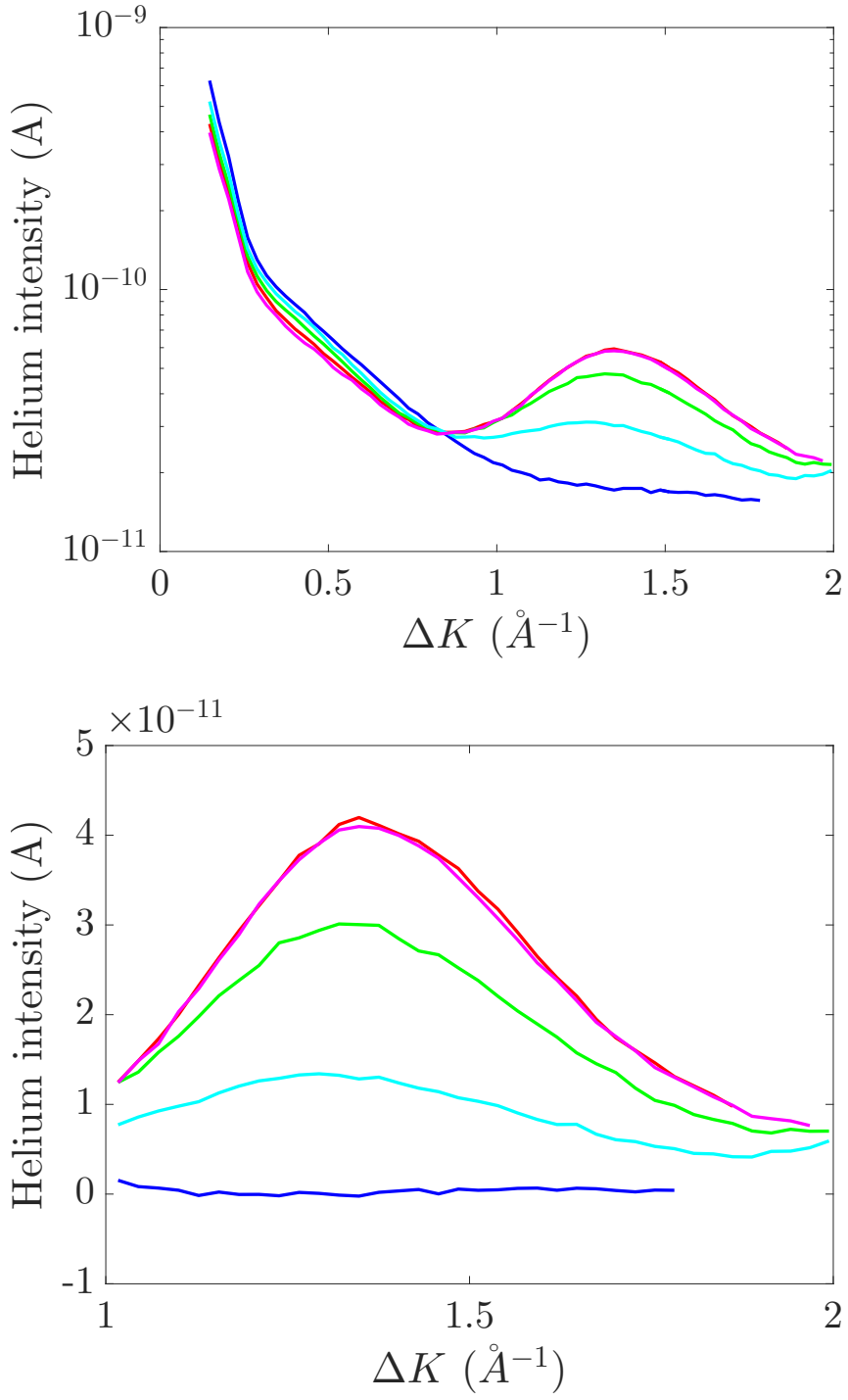

Figure 6.5: Diffraction scan along $< 1, 1 >$ of Ru(0001) at $T_s = 250\,\mathrm{K}$ after exposure to (0.0,0.1,0.2,0.3 and 0.75)$\times 10^{-6}\,\mathrm{L}$ (gauge) of molecular deuterium, showing the development of a feature related to the form factor of adsorbed deuterium atoms. The diffuse peak is absent in the clean surface scan. The upper plot shows the raw data (log scale). The lower plot (linear scale) shows the data after subtraction of the smooth background of the clean surface.

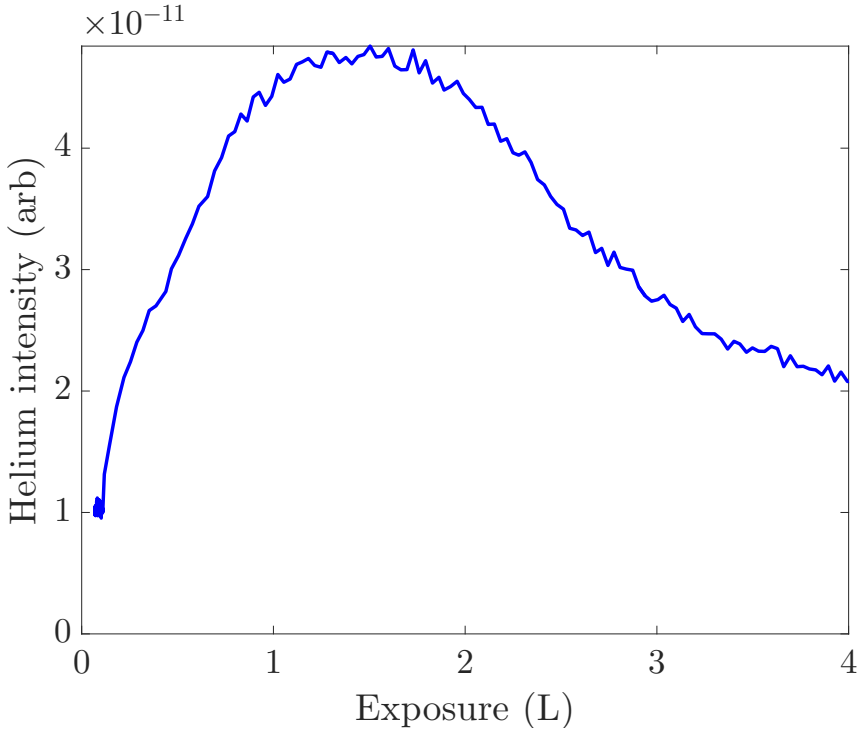

Figure 6.6: Variation of the scattered intensity at $\Delta K = 1.3\text{Å}^{-1}$ along $< 1, 1 >$ on Ru(0001) at $T_s = 250\,\text{K}$, as a function of exposure to molecular deuterium. The maximum intensity occurs at about 1.5L (gauge).

be consistent with that picture. However, there is no obvious shift of the feature's mean ΔK between the two high symmetry azimuths [35] which would be expected for islands with a simple internal structure commensurate with the substrate. Additionally, the measurements at 250 K are so far above the temperature at which disordering is observed in LEED (72 K) that the formation of significant local order at low coverage seems inherently unlikely. HREELS measurements at $T_s = 170\,\text{K}$ suggest that islanding does not occur to any significant extent below $\theta = 0.5\,\text{ML}$ above which the vibrational lineshapes show evidence for multiple distinct environments [57]. The structural data in the present Section is very limited in scope, being projected along a single high symmetry azimuth and referring to a single surface temperature. A more thorough and systematic HAS investigation would be desirable to resolve the relative contributions of form factor effects, repulsive interactions and local ordering.

6.3.4 Nature of jump dynamics

Polarization scans for protium (H) at two temperatures are shown in Figure 6.7. The scan at 270 K has completely decayed to a static value, and is unambiguously described by a biexponential fit rather than a single exponential. A biexponential

fit is overlaid (solid red curve). The scan at 145 K has not fully decayed, and two exponential components cannot be clearly resolved: a single exponential fit is overlaid.

Figure 6.8 shows the fitted fast and slow exponential decay rates of the polarization scans of H/Ru(0001), at temperatures from $T_s = 150\,\mathrm{K}$ to $T_s = 300\,\mathrm{K}$. The fitting methods are described in the Figure caption. The results are broadly consistent with the previous HeSE data, illustrated at $T_s = 250\,\mathrm{K}$ with black circles. The approximately symmetric rise from $\alpha \to 0$ at $\Delta K = 0$ to a maximum and back to $\alpha \to 0$ at the diffraction condition is the expected form for diffusion proceeding by jumps, even if the jump model involves two adsorption sites per unit cell [84]. Solid curves overlaid to guide the eye are best fits to the Chudley-Elliott jump model (Section 2.2.1), but the quantitative analysis will be performed with the Bayesian method (Section 2.2.6) and so the fitted parameters of the Chudley-Elliott model will not be analysed here.

Analogous data were measured for deuterium (D). Two sample D/Ru(0001) polarization scans are shown at $\Delta K = 1.5\,\mathrm{\AA}^{-1}$ along $< 1, 1 >$ at $T_s = 300\,\mathrm{K}$ and $T_s = 150\,\mathrm{K}$, in Figure 6.9. Qualitatively the hopping dynamics are broadly the same for D as H. The slow $\alpha(\Delta K)$ functions are shown in Figure 6.10.

Figure 6.11 compares more closely the $\alpha(\Delta K)$ at $T_s = 150\,\mathrm{K}$ for the two isotopes. The fitting methods are discussed in the Figure caption. The $\alpha(\Delta K)$ for D is around $20\times$ slower than that for H in overall scale. The $\alpha(\Delta K)$ for H does not have a single central peak but has a local maximum at $\Delta K \approx 1.0\,\mathrm{\AA}^{-1}$.

Although the $\alpha(\Delta K)$ confirms the hopping nature of the dynamics, and gives an indication of relative rates, it is not a completely satisfactory reduction of the data because the previous theoretical and experimental evidence points to both the fcc and hcp threefold sites being acting as adsorption sites for the hopping dynamics. To quantify the dynamics in detail, the Bayesian analysis technique set out in Section 2.2 has been applied to the different datasets. Table 6.3 shows the results of fitting constant-temperature datasets to the non-Bravais triple jumps model detailed in Section 2.2.1.

6.3.5 Temperature dependence of jump dynamics

Figure 6.12 shows a selection of polarization scans at $\Delta K = 1.5\,\mathrm{\AA}^{-1}$ along $< 1, 1 >$ from intermediate to low temperature, at the usual coverage of deuterium. The condition $\Delta K = 1.5\,\mathrm{\AA}^{-1}$ was chosen for extensive temperature-dependent measurements for deuterium because of the indication from the $\alpha(\Delta K)$ at $T_s = 150\,\mathrm{K}$ (Figure

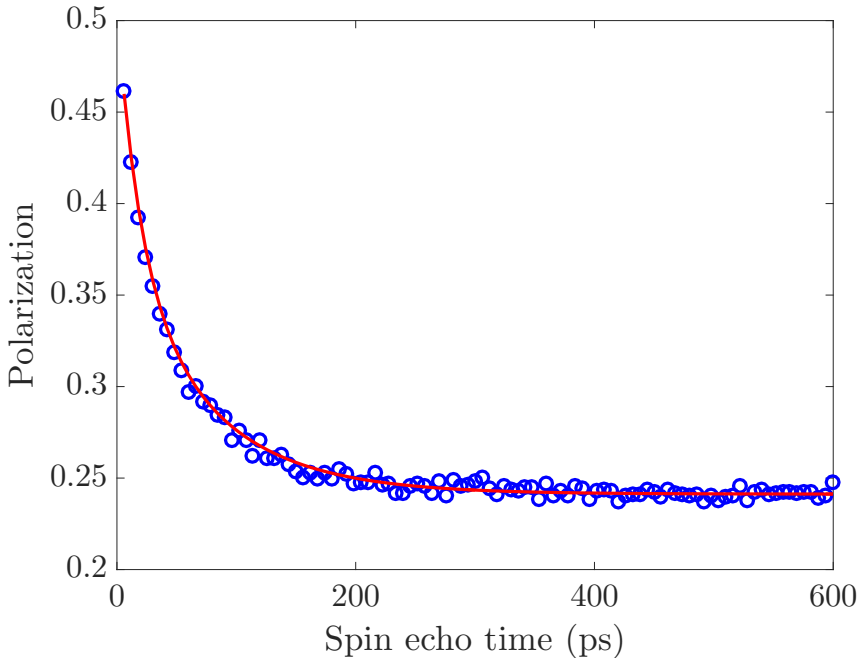

(a) Polarization scans of H/Ru(0001) at 270 K.

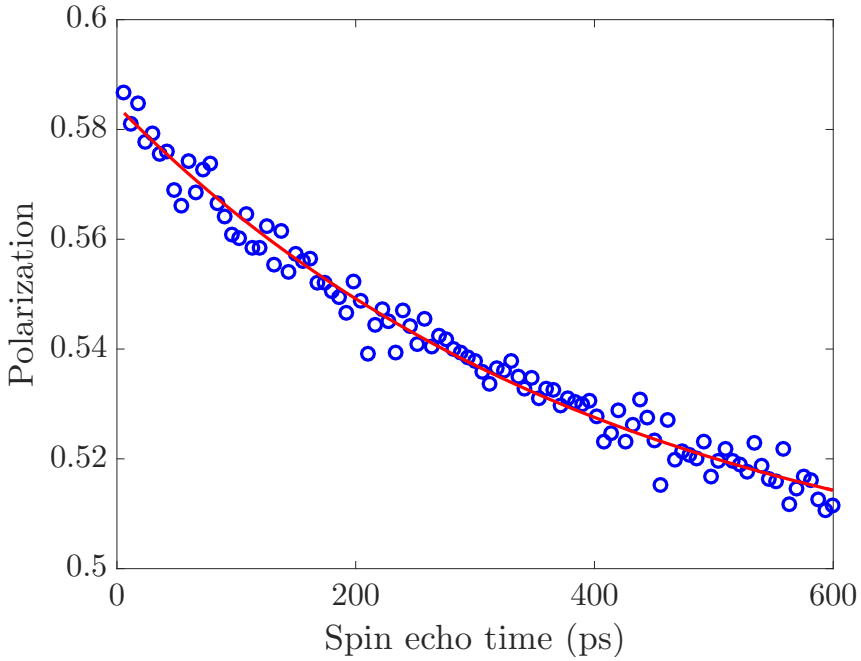

(b) Polarization scan of H/Ru(0001) at 145 K.

Figure 6.7: Polarization scans of Ru(0001) at $\Delta K = 1.0\,\text{Å}^{-1}$ along $< 1, 1 >$ at $T_s =$ 270 K (upper) and 145 K (lower), after dosing 0.3 L (gauge) molecular hydrogen, which corresponds to $I = 0.6 I_0$ specular attenuation, the minimum of the specular uptake curve shown in Figure 6.3. The solid red curve in the upper plot shows the best biexponential fit. In the lower plot, the best mono-exponential fit is shown as there is insufficient curvature in the lineshape to perform a biexponential fit. The solid curves are best regarded as guides to the eye, since the quantitative analysis proceeds through the Bayesian method of Section 2.2.6 which involves analysing many scans at once.

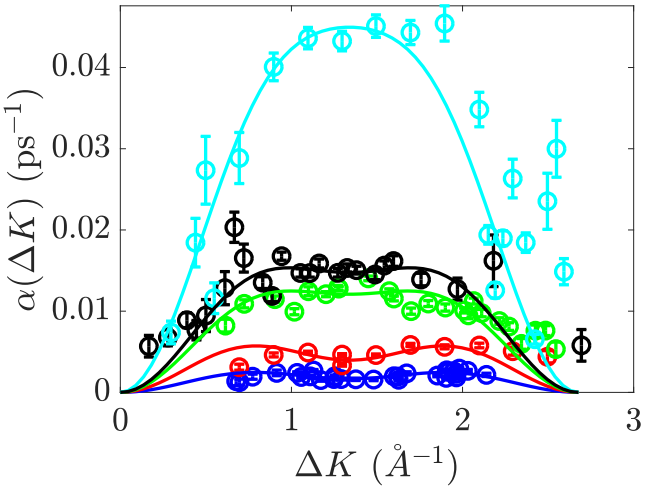

(a) Slow dephasing rates, H/Ru(0001).

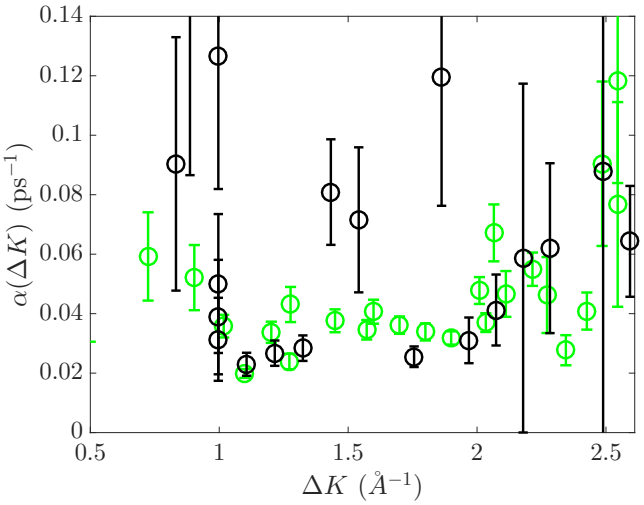

(b) Fast dephasing rates at 250 K, H/Ru(0001).

Figure 6.8: The ΔK-dependence of the fitted decay rates of polarization scans of H/Ru(0001) after dosing 0.3 L (gauge) molecular hydrogen (deposition temperature 250 K). ΔK is oriented along along the $< 1, 1 >$ azimuth. Results are shown at temperatures $T_s = 150$ K (blue), 200 K (red), 250 K (green) and 300 K (cyan). Prior HeSE data at 250 K [23, 35] is shown in black. Figure 6.8a shows the slower exponential component, fitted by varying the start time of a single exponential fit (Section 2.2.3) until the $\alpha(\Delta K)$ longer changes with increasing start time. The fast decay rates at 250 K are shown in Figure 6.8b, where again the prior data is shown in black. The rates were extracted from a free biexponential fit with an optimized start time corresponding to the first datum at $t_{SE} > 0$. The agreement in the fast decay rates is reasonable between points with small statistical errors. The amplitude of the faster exponential component vanishes $\Delta K \to 0$ in non-Bravais hopping models [84], with the consequence that the faster component cannot be reliably fitted at small ΔK.

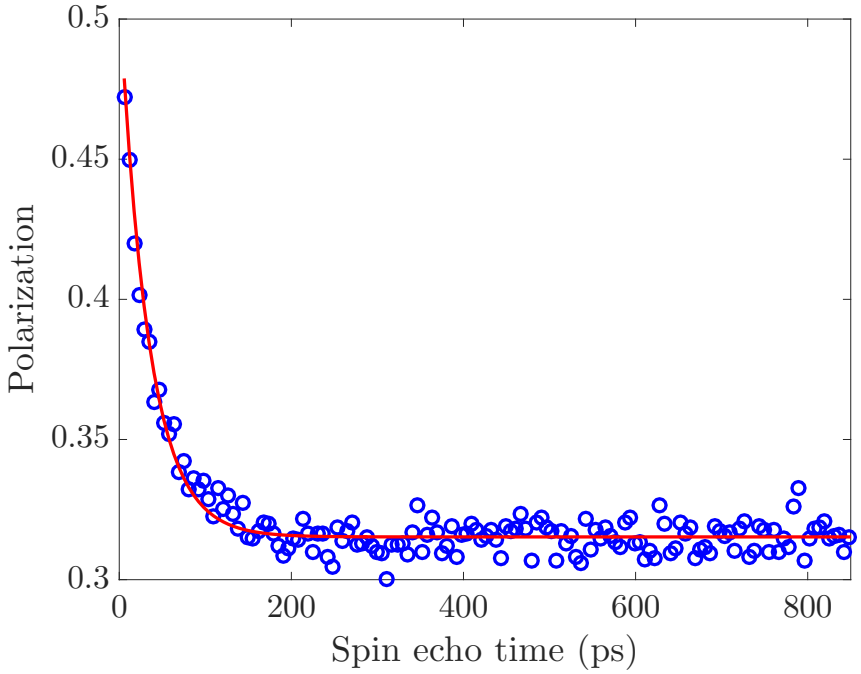

(a) D/Ru(0001) polarization scan at $T_s = 300\,\mathrm{K}$.

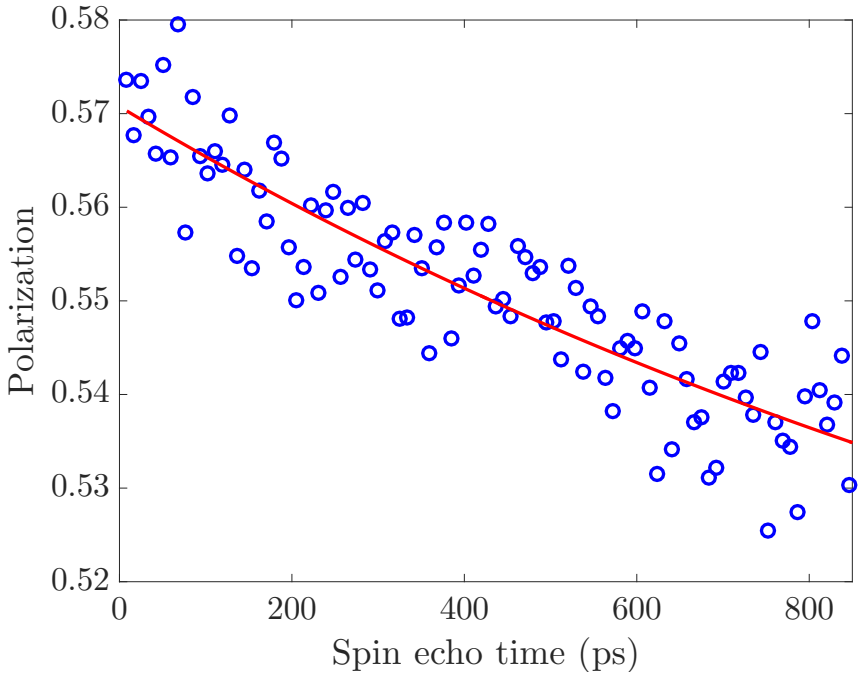

(b) D/Ru(0001) polarization scan at $T_s = 150\,\mathrm{K}$.

Figure 6.9: Polarization scans of Ru(0001) at $\Delta K = 1.5\,\mathrm{\AA}^{-1}$ after dosing 0.3 L (gauge) molecular deuterium. ΔK is oriented along $< 1, 1 >$. Results are presented for temperatures $T_s = 300\,\mathrm{K}$ (Figure 6.9a and 150 K (6.9b).

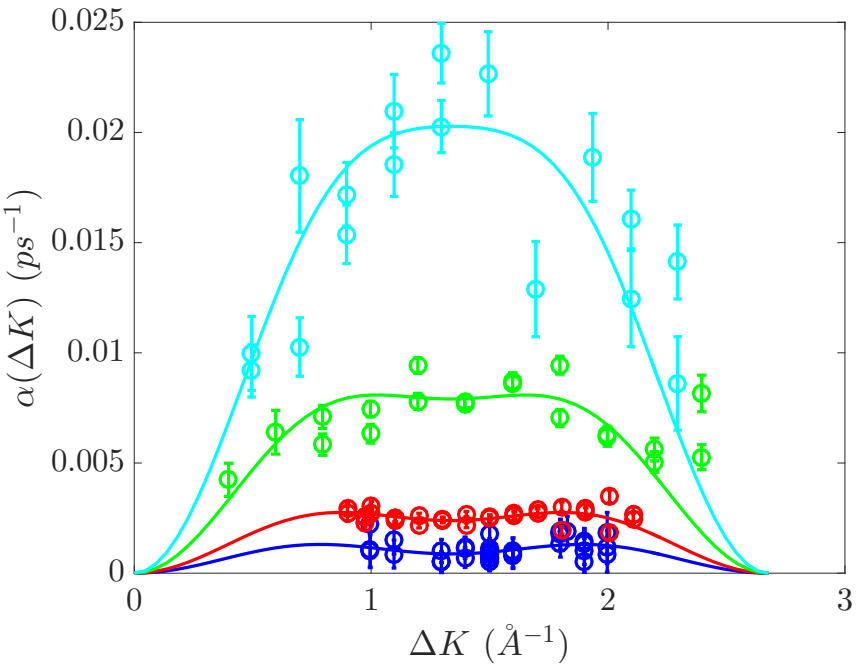

Figure 6.10: The ΔK-dependence of the slow dephasing rate $\alpha(\Delta K)$ fitted from polarization scans of Ru(0001) after dosing 0.3 L (gauge) molecular deuterium. ΔK is oriented along the $< 1, 1 >$ azimuth. Results are shown for temperatures $T_s =$ 150 K (blue), 200 K (red), 250 K (green) and 300 K (cyan). As with Figure 6.8a, the solid lines are guides to the eye based on the Chudley-Elliott model (Section 2.2.1), but the quantitative analysis of jump dynamics will proceed through the global Bayesian analysis method (Section 2.2.6 assuming the non-Bravais hopping model described in Section 2.2.1). Measurements at low temperature and small ΔK were not performed as no measurable polarization decay was expected. At the higher temperatures shown, measurements were recorded at ΔK smaller than shown, but the slow dephasing rate cannot be reliably extracted because of a high static polarization, in other words a high fraction of the detected helium atoms have been scattered elastically from static defects. High static polarization at small ΔK was also reported in the prior HeSE work [35]. According to the observations Chapter 5, carbon clusters are a persistent contaminant, i.e. difficult to remove completely, and are therefore a plausible source of a substantial static level in ranges of ΔK where they scatter He atoms more strongly than do hydrogen atoms. From Figure 6.4 we can see that upon dosing hydrogen the reflected He intensity in the range $0.1 \lesssim \Delta K \lesssim 1.0 \mathring{\text{A}}^{-1}$ decreases, and therefore the origin of the static at small ΔK is unlikely to be due to static hydrogen.

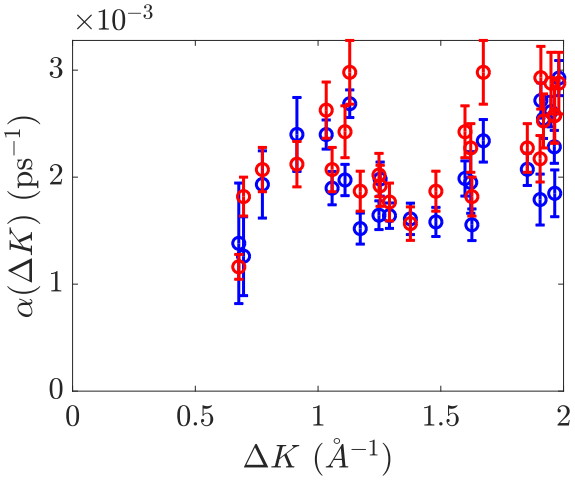

(a) $\alpha(\Delta K)$ for H/Ru(0001) at $T_s = 150\,\mathrm{K}$.

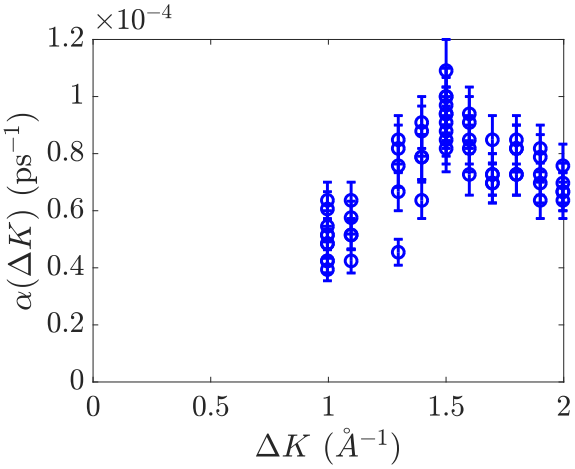

(b) $\alpha(\Delta K)$ for H/Ru(0001) at $T_s = 150\,\mathrm{K}$.

Figure 6.11: $\alpha(\Delta K)$ along $< 1, 1 >$ for Ru(0001) after dosing 0.3 L (gauge) molecular protium (Figure 6.11a) and deuterium (Figure 6.11b) respectively. The $\alpha(\Delta K)$ represented in Figure 6.11a was obtained by fitting polarization scans to a single exponential function for $t_{SE} > 50\,\mathrm{ps}$ using standard least-squares fitting (blue points) and the marginalization method of Section 2.2.5 (red points). The results obtained by either method are in close agreement. The $\alpha(\Delta K)$ shows a local maximum around $\Delta K = 1.0\,AA^{-1}$ and a dip at $\Delta \approx 1.5\mathrm{Å}^{-1}$, in qualitative agreement with previous measurements on the system [35]. The deuterium $\alpha(\Delta K)$ was fitted using the marginalized approach as the standard least squares method is unreliable for such slow decays. The results for the two isotopes differ in two major respects: firstly, the maximum measured α is slower for D than H by a factor of around 20, which is much greater than any expected classical isotope effect. Secondly, the maximum of the $\alpha(\Delta K)$ for D is at $\Delta K \approx 1.5$ rather than $\Delta K \approx 1.0$.

Table 6.3: Parameters of the non-Bravais, triple jumps model of Section 2.2.1 fitted for different H/Ru(0001) and D/Ru(0001) datasets using the Bayesian method of Section 2.2.6. The hopping rate as measured by τ^{-1} is strongly temperature dependent as the data lie in the quantum activated regime. The hopping rate is systematically faster for protium than for deuterium at the same temperature. Multiple jumps are significant for the higher temperature data. The concentration ratio λ defines a site energy difference via detailed balance, $\Delta E = k_B T \ln(\lambda)$. λ systematically increases as the temperature decreases, as expected. However, the site energy difference appears to be consistently underestimated at 300 K. The survival parameter systematically increases as the temperature increases.

Isotope	$\mathbf{T_s(K)}$	τ**(ps)**	λ	**s**	**ΔE (meV)**
H	300	16 ± 3	1.7 ± 0.25	0.5 ± 0.1	14 ± 4
H	250	31 ± 1	2.4 ± 0.05	0.25 ± 0.2	18.9 ± 0.4
H	200	63 ± 6	3.7 ± 0.04	0.14 ± 0.02	22.6 ± 0.2
H	150	76 ± 4	6.0 ± 0.1	0.05 ± 0.01	23.2 ± 0.2
D	300	38 ± 3	1.3 ± 0.1	0.43 ± 0.04	7 ± 2
D	250	54 ± 2	2.5 ± 0.1	0.28 ± 0.02	19.8 ± 0.8

6.11b) that $\Delta K = 1.5\,\text{Å}^{-1}$ offers the best chance of observing a finite polarization decay rate down to low temperatures. The lowest measurement temperature was $T_s = 110\,\text{K}$. Qualitatively, the scans in Figure 6.12 demonstrate that as the temperature is lowered to $T_s \approx 110\,\text{K}$ the hopping dynamics of D atoms, as monitored via the decay of polarization scans, appears to be completely frozen out, in contrast to what is seen for H atoms in the previous and the present work.

Figure 6.13 illustrates the temperature dependence of the H atom hopping rate as measured at $\Delta K = 1.0\,\text{Å}^{-1}$ via measurement of α the apparent exponential decay rate of polarization scans, and the inverse residence time $1/\tau$ in hcp sites (as discussed in Section 2.2.1 and the previous Subsection) as a function of surface temperature. The inverse residence time was determined by fitting polarization scans at different temperatures to the model used in the Bayesian analysis, assuming a constant ΔE (as done in Section 5.1.2.4 for C/Ru(0001) data), and assuming a survival ratio that varies smoothly between the values given in Table 6.3 and tends to zero at low temperatures. By either measure of the hopping rate, the rate undergoes a clear transition from a strongly temperature dependent (quantum activated) regime to an approximately temperature-independent (quantum tunneling) regime.

The solid curves in Figure 6.13b are fits to an activated rate law with constant prefactor, using the data at $T_s \geq 200\,\text{K}$. The apparent activation energies are $E_A = 85 \pm 25\,\text{meV}$ (H) and $101 \pm 10\,\text{meV}$ (D), both of which are much smaller than the classical barrier height. The same trend, where the quantum activation energy for D is reduced below the classical activation energy and the activation energy for H diffusion is reduced further still, will also be seen in the Pd(111) and Cu(111)

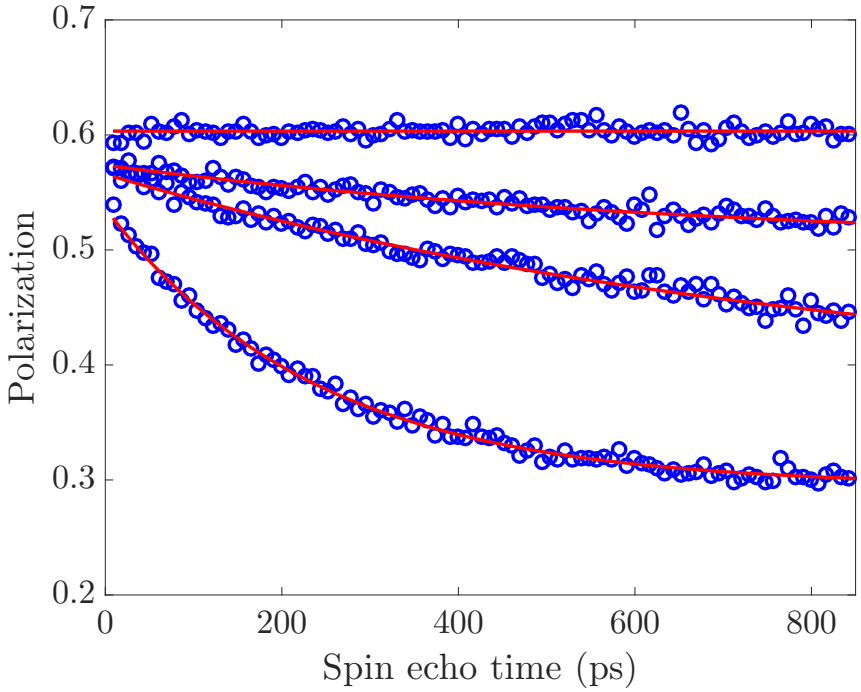

Figure 6.12: Polarization scans of Ru(0001) after dosing 0.3 L (gauge) molecular deuterium, at $\Delta K = 1.5\,\text{Å}^{-1}$ along $< 1, 1 >$ at $T_s = (200, 160, 140, 111)\,\text{K}$.

high-temperature dynamics (Sections 6.4 and 6.5).

The temperature-dependent D/Ru(0001) scans were fitted using the marginalized method of Section 2.2.5 in an attempt to extract very slow decay rates. Figure 2.12 shows examples of the inferred distribution of $\rho(\alpha)$ for three different scans.

Maxima from distribution like those shown in Figure 6.14 across the whole temperature range were used to construct the rate curve shown in Figure 6.15. The rate is expressed as $1/\tau(T)$ where τ is the residence time in the metastable (hcp) adsorption sites. Unlike for H/Ru(0001) where a temperature-independent regime is easily within the resolution limit, there is no systematic evidence for such fast decays at low temperature for D/Ru(0001), and instead the rate appears to follow an activated law down to low temperatures. The lack of any clear positive evidence for a fast temperature-independent diffusion rate demonstrates that the D/Ru(0001) system does not undergo the same activated/tunneling crossover as H/Ru(0001), i.e. the D/Ru(0001) jump rate does not closely track the H/Ru(0001) rate at low temperatures. The large isotope effect at low temperatures is the central experimental result of the present Section. A large isotope effect in the deep tunneling regime is the theoretical expectation, whereas the small isotope effect tentatively proposed experimentally [35] would be anomalous.

It is plausible *a priori* that a moderate coverage of deuterium could result in a suppression of hopping rates. However, measurements recorded at $T_s = 115\,\text{K}$ after

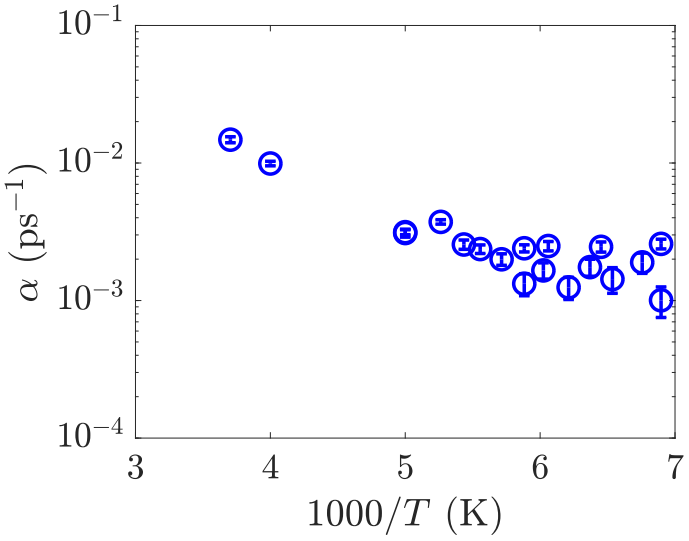

(a) Temperature dependence of α for H/Ru(0001).

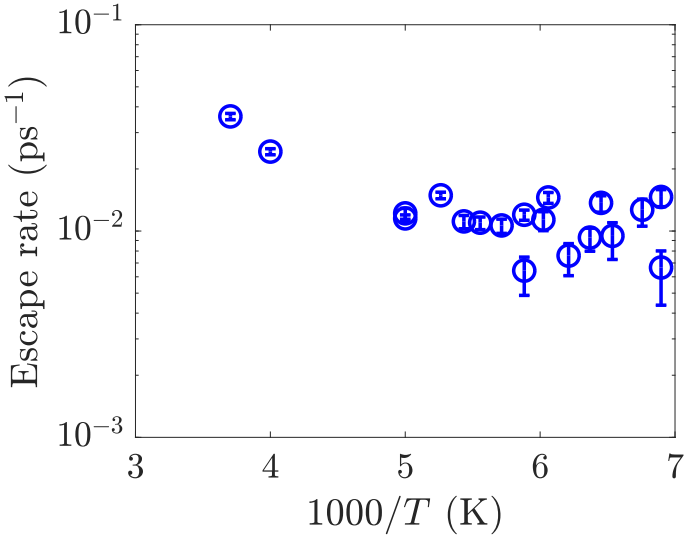

(b) Temperature dependence of $1/\tau$ for H/Ru(0001).

Figure 6.13: Temperature dependence of the diffusion rate of H/Ru(0001) (0.3 L (gauge) exposure at $T_s = 250\,\mathrm{K}$) by two different measures, the fitted exponential decay rate α at $\Delta K = 1.0\,\mathrm{\AA}^{-1}$ along $< 1, 1 >$, and the inverse residence time $1/\tau$ in hcp sites fitted from the same set of polarization scans. $1/\tau$ was obtained by freely fitting polarization scans at different temperatures to the non-Bravais triple jumps model of Section 2.2.1, assuming a constant site energy difference ΔE. The survival parameter s was interpolated from the data in Table 6.3 using an activated rate law to represent a smooth function satisfying $s \to 0$ as $T \to 0$. Both measures of the hopping rate exhibit a distinctive flattening at low temperatures. There is no material difference between the results obtained by least squares fitting (Section 2.2.2) and marginalized fitting (Section 2.2.5).

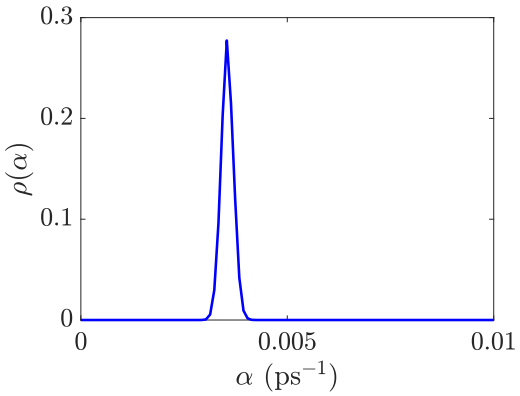

(a) The marginalized relative probability $\rho(\alpha)$ derived from a D/Ru(0001) polarization scan at $\Delta K = 1.5\,\text{Å}^{-1}$, $T_s = 200\,\text{K}$.

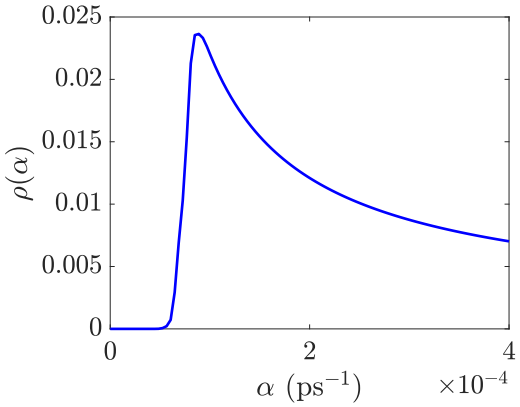

(b) As above, except $T_s = 150\,\text{K}$.

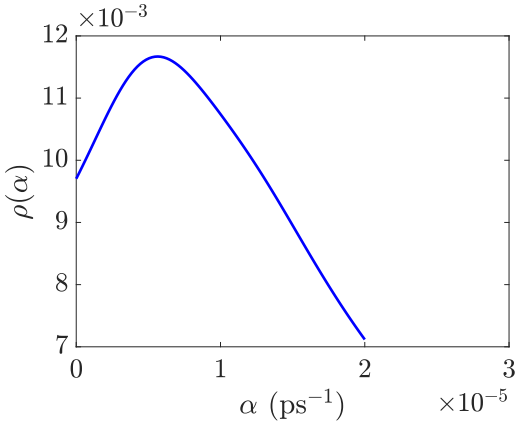

(c) As above, except $T_s = 110\,\text{K}$.

Figure 6.14: Inferred distribution $\rho(\alpha)$ derived from three D/Ru(0001) experimental polarization scans, using the methods applied to generate Figure 2.12 from simulated data. Each distribution contributes one point to the rate curve in Figure 6.15. At low temperatures, where there is no visible curvature in the polarization scans, $\rho(\alpha)$ becomes very broad, reflecting an unavoidably large statistical uncertainty. However, the histograms of the argmax of $\rho(\alpha)$ for simulated data in Section 2.2.5 suggests that the α that maximizes $\rho(\alpha)$ is a reliable estimate of the true underlying decay rate, down to rates as low as about $1 \times 10^{-5}\,\text{ps}^{-1}$, as long as the decay amplitude remains large at low temperatures.

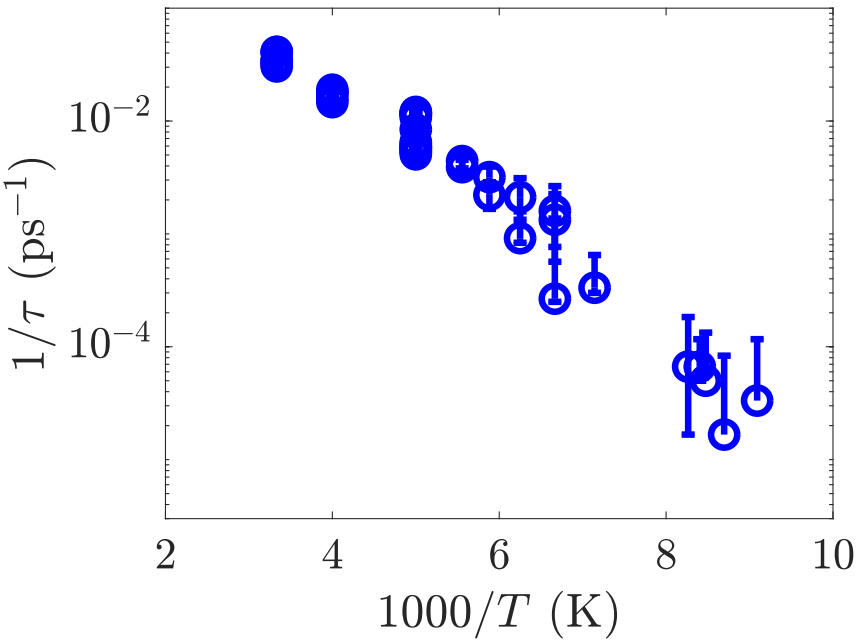

Figure 6.15: Temperature dependence of the jump rate of D/Ru(0001) (0.3 L (gauge) exposure at $T_s = 250\,\mathrm{K}$) quantified by the inverse residence time $1/\tau$ in hcp sites. Lineshape fitting was carried out by marginalizing over amplitude and static as described in Section 2.2.5 but using a model function given by the non-Bravais triple jumps model of Section 2.2.1 informed by the parameters in Table 6.3 fitted from high temperature data. The concentration ratio has been assumed to vary as $\lambda = e^{\Delta E/(k_B T)}$ where $\Delta E = 20\,\mathrm{meV}$. The survival parameter s was interpolated from the data in Table 6.3 using an activated rate law to represent a smooth function satisfying $s \to 0$ as $T \to 0$. The quoted uncertainties are the full width at half maximum of the marginalized distribution in $1/\tau$. Unlike in the H/Ru(0001) data, there is no evidence for a fast temperature-independent diffusion rate at low temperatures, and the progression of the marginalized best-fit parameter appears to follow an activated rate law.

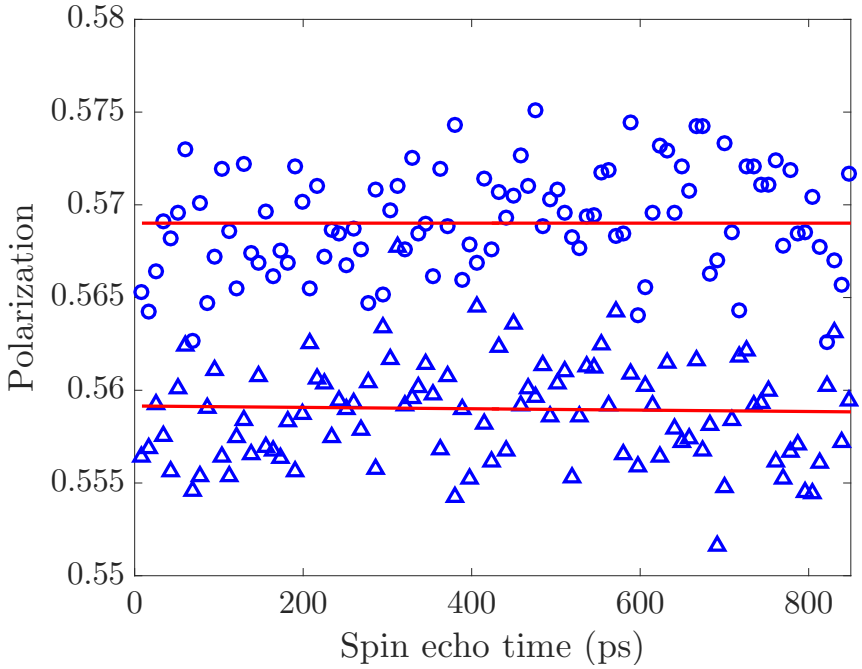

Figure 6.16: Polarization scans of Ru(0001), at $\Delta K = 1.5\,\text{Å}^{-1}$ along $< 1, 1 >$ at $T_s = 116\,\text{K}$ (upper, circles) and 114 K (lower, triangles), after exposures of 0.2 L and 0.1 L (gauge) molecular deuterium. The consistent flatness confirms that the lack of diffusion at the lowest temperature in Figure 6.12 is not due to the coverage being excessively high.

reduced deuterium exposures of 0.2 L and 0.1 L (2/3 and 1/3 of the usual exposure) show no evidence for increased adsorbate mobility. The scans at reduced coverage are shown in Figure 6.16.

6.3.6 Extent of contamination effects

Contamination of the surface can potentially affect measurements of $P(t_{SE})$ in two distinct ways:

1. the dynamics of a fast-moving contaminant species (H, for example) could introduce spurious decays, even if the coverage of the contaminating species is constant;

2. a systematic increase in the coverage of any species, regardless of its dynamics, can introduce a systematic variation of P at fixed t_{SE}, which can give a spurious variation of P as t_{SE} is scanned.

The first point above can be addressed by studying thermal desorption spectra, as described in the HeSE studies of H and D/Ni(111) [36]. It has been emphasized earlier in the present Chapter that previous measurements of D/Ru(0001) suffered

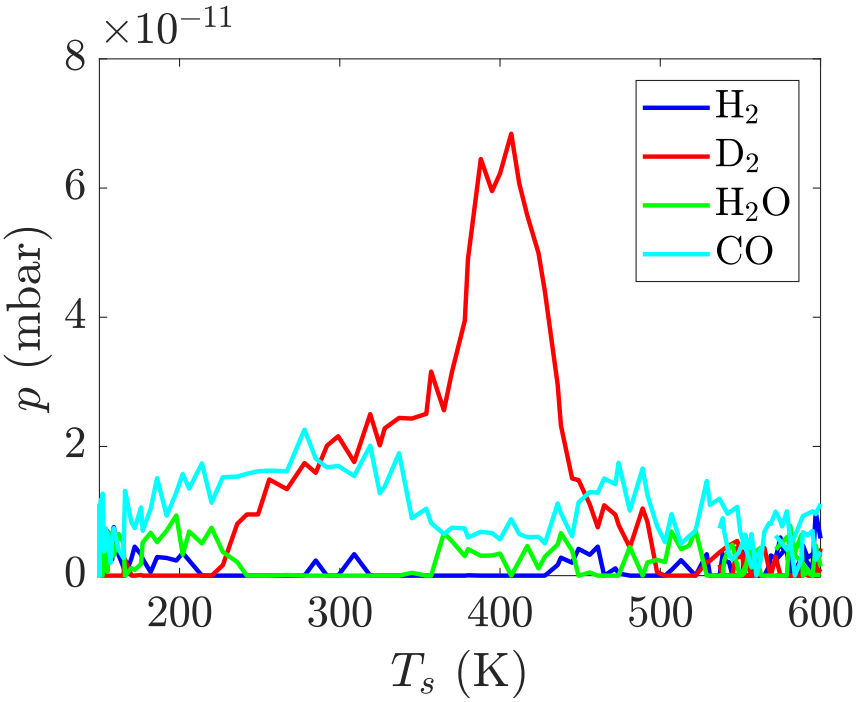

Figure 6.17: Simultaneous thermal desorption spectra from Ru(0001) during heating from 150 K after dosing 0.3 L (gauge) D_2 and performing dynamics measurements for 45 minutes. The (uncorrected) partial pressure on the m/z conditions shown was measured with a commercial quadrupole mass spectrometer (VG, model SX200). The mass spectrum of the desorbed gas is dominated by deuterium, D_2 with $m/z = 4$. There is no discernible rise in the $m/z = 2$ intensity, demonstrating that contamination by H_2 was insignificant under the conditions used to measure the deuterium dynamics reported in the present Chapter.

from likely contamination of the surface by H, possibly leading to a spurious signature of quantum diffusion, and that in the present work measures were taken specifically to avoid H contamination of the D experiments. Figure 6.17 shows thermal desorption spectra during sample heating, after dosing D_2 in the normal way and performing 45 minutes of dynamics measurements at $T_s = 150$ K. The quantities plotted as a function of temperature are the m/z-resolved partial pressures of key background gas components in the scattering chamber, measured with a commercial quadrupole mass spectrometer (VG, model SX200). The only species for which a clear peak in intensity is observed is D_2 ($m/z = 4$), and in particular no discernible H_2 contribution is detected, which demonstrates that the measures taken to avoid H contamination were effective. A mass spectrum taken during D_2 dosing (not shown) separately demonstrates that the $m/z = 2$ peak arising from cracking of D_2 is insignificant compared to the molecular $m/z = 4$ (D_2^+) mass peak. Therefore if the $m/z = 2$ peak in Figure 6.17 did show a significant rise in parallel with the $m/z = 4$ peak it would have to be attributed to molecular H_2, but no such rise is observed.

Given the low background pressure in the scattering chamber and the relatively

high differential He-scattering cross-section of hydrogen atoms at moderate ΔK, the second point above does not normally present a significant problem when attempting to measure not-too-small and not-too-slow decays, where the total decay in polarization from small t_{SE} to the maximum t_{SE} considered is large compared to any time-dependent drift caused by slow adsorption of trace background contaminants. However, because in the previous subsection an attempt is made to extract quantitative information about very slow decays at low temperature, it is important to estimate bounds on the possible influence of time-dependent contamination. To do so, a series of polarization scans at $T_s = 150\,\mathrm{K}$ and $\Delta K = 1.5\,\mathrm{\AA}^{-1}$ is analysed in Figure 6.18. There is a systematic but small change in the polarization over a fixed range of t_{SE}. The changes in polarization over time as the system contaminates can be related to an apparent decay of polarization with t_{SE}. The apparent decay rate estimated from Figure 6.18 is $\alpha = 7 \times 10^{-6}$, which is comparable to the slowest decay rates fitted for D/Ru(0001) polarization scans in Section 6.3.5, but orders of magnitude slower than the slowest decay observed for H/Ru(0001).

To provide an alternative perspective on the effects of contamination, a series of temperature-dependent measurements of the nominally clean surface was performed for 45 minutes at $T_s < 200\,\mathrm{K}$, to isolate the effect of adsorbing background species that could also adsorb during measurements of the D-covered surface. Two comparisons between measurements of the clean and D-covered surface are shown in Figure 6.19. The results are phrased in terms of the polarized intensity, which for a real-valued polarization is simply the parameter A of Equation 2.30 rather than the normalized polarization $A/(C - \mathrm{bkg})$. At the higher temperature of $T_s = 190\,\mathrm{K}$, the effects of contamination are insignificant compared to the polarization decay due to deuterium dynamics. At the lower temperature of 140 K there is no discernible polarization decay on the clean surface, whereas the decay on the D-covered surface is slow but significant.

6.3.7 Theoretical discussion

A key outcome of the Bayesian analyses at different temperatures is the systematic presence of multiple jumps. A classical picture of multiple jumps is provided by the Langevin or Generalized Langevin framework, as discussed in 5.1.2.4. When a classical particle crosses a barrier, there is a finite chance it will rollercoast straight through the subsequent well region and perform a double jump or longer. The likelihood of successively longer jumps is controlled by the friction, where strong friction suppresses multiple jumps. In the quantum activated regime, the picture can be rephrased in terms of excitation and de-excitation to and from mobile bands [36].

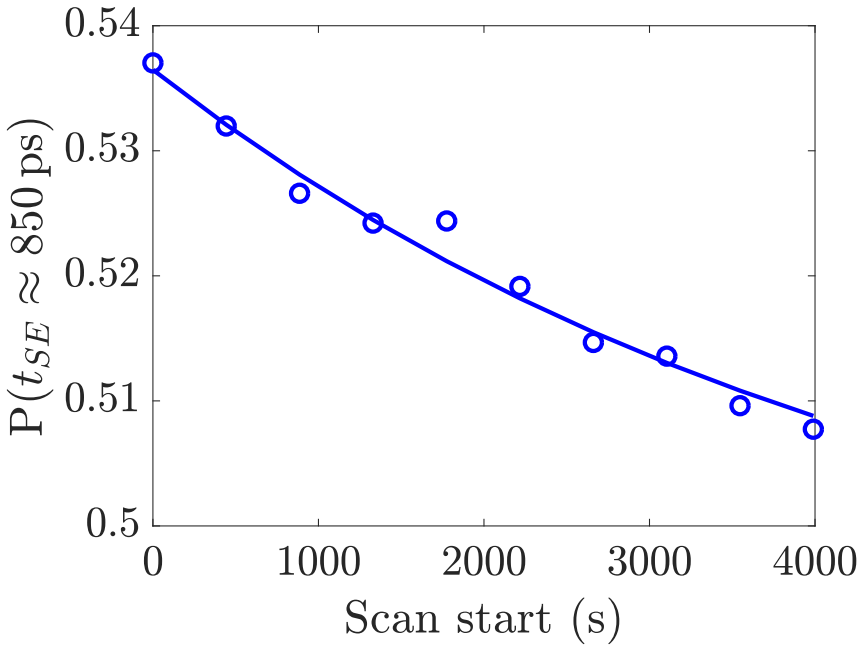

Figure 6.18: The variation of the polarization at $t_{SE} \approx 850\,\text{ps}$, $\Delta K = 1.5\,\text{Å}^{-1}$ along $< 1, 1 >$ for D/Ru(0001) at 150 K, from 10 polarization scans performed in direct succession. Specifically, the plotted quantity is the mean of the last 20 points in each polarization scan, as a function of the time at which the scan was begun. The polarization varies with time in a systematic but small way. An exponential fit through the data is shown as a solid blue curve, which appears to be a reasonable description of the variation with time. The exponential fit implies a ratio r between the polarization in successive scans of $r = 0.994$. If the same ratio was applied between the beginning and end of a polarization scan over $0 \leq t_{SE} \leq 850\,\text{ps}$ then a spurious exponential lineshape would be measured with $\alpha = 7 \times 10^{-6}\,\text{ps}^{-1}$. Therefore in Figure 6.15, the slowest fitted decay rates could be influenced by polarization drift. However, an effect of the scale $\alpha = 7 \times 10^{-6}\,\text{ps}^{-1}$ does not affect the qualitative conclusion about a crossover to fast deep tunneling being observed for H/Ru(0001) and not for D/Ru(0001).

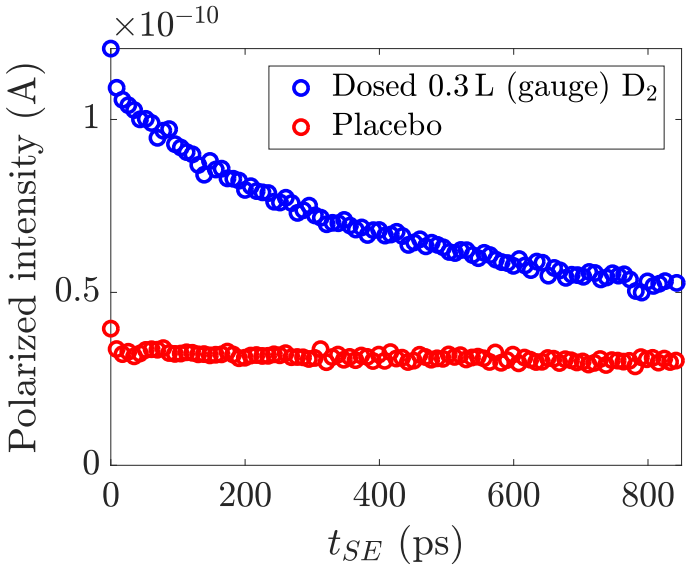

(a) Scans of clean and D-covered Ru(0001) contrasted at $T_s = 190\,\mathrm{K}$.

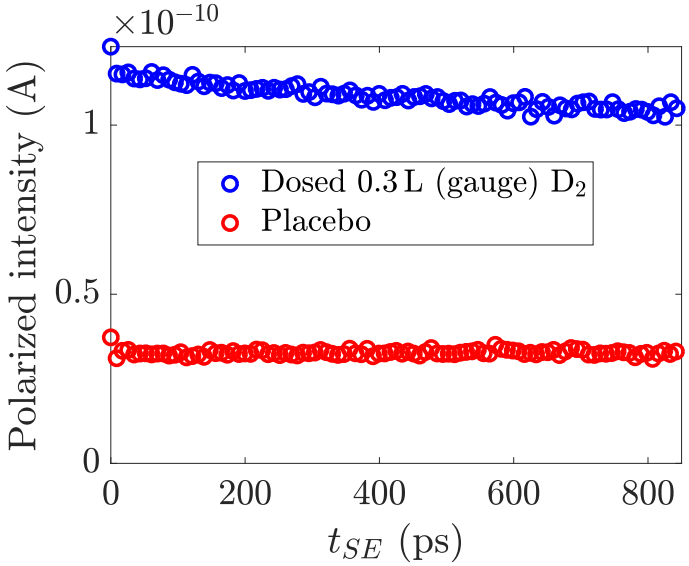

(b) Scans of clean and D-covered Ru(0001) contrasted at $T_s = 140\,\mathrm{K}$.

Figure 6.19: Comparison of polarization scans of clean Ru(0001) and D-covered Ru(0001) at two temperatures, at $\Delta K = 1.5\,AA^{-1}$ along $< 1.1 >$. At the higher temperature $T_s = 190\,\mathrm{K}$, the decay in polarized intensity due to contamination is completely insignificant compared to the decay caused by the deuterium dynamics. At the lower temperature $T_s = 140\,\mathrm{K}$, there is negligible polarization decay due to contamination, and the decay of polarization seen when deuterium has been dosed is easily detectable by comparison.

In either the classical or quantum case, the parameter that controls the proportion of multiple jumps describes a rate of energy exchange between the adsorbate and surface, whether it is a classical Langevin friction or an inter-band transition rate. Estimates of the energy exchange rate can be derived from the literature either through experimental data (vibrational linewidths) or first-principles calculations of electronic friction. First-principles literature estimates of electronic friction are available for Cu(111) and will be discussed in Section 6.5. For Ru(0001) the friction will be estimated here from HREELS data using the method applied to O/Ru(0001) vibrational lineshapes in Section 5.2.3.1.

HREELS spectra have been measured for H/Ru(0001) at a series of coverages at $T_s = 170\,\mathrm{K}$ [57]. Figure 6.20 shows a surface-parallel (85 meV) feature, at a probe energy of 4 eV using an off-specular scattering angle of 20°. The nominal resolution of the experiment at coverages $\leq 0.5\,\mathrm{ML}$ was $4-6\,\mathrm{meV}$. The experimental lineshape is consistent with a friction $\gamma = 4\,\mathrm{ps}^{-1}$, assuming that the dynamical structure factor $S(\Delta k, \Delta\omega)$ (solid blue curve in the Figure) is an appropriate model for the lineshape, and that there are no significant sources of lineshape broadening apart from the friction and the fundamental experimental resolution. Additional sources of broadening such as inhomogeneous broadening and the relatively high bandwidth of excited vibrational states will only increase the linewidth, so $4\,\mathrm{ps}^{-1}$ is an upper bound on γ.

The one-dimensional classical rate prefactor (cf. Section 4.5.1) is strongly suppressed when $\gamma << \omega_0$ where ω_0 is the free oscillation frequency in the well region. Although the correction will not be quantitatively the same in the semiclassical regime, because γ estimated from HREELS is so much smaller than ω_0 a strong suppression of the rate compared to the quantum TST prediction is expected, and consistent with the absolute rate calculations using the bounce method in Chapter 4. The high rate of deep tunneling for the H isotope, and the large isotope effect between H and D in the deep tunneling regime, are both consistent with a low friction.

6.3.8 Consistency with previous HAS/HeSE results

At face value there are quantitative discrepancies of the results in the current Section when compared with previous results of helium scattering and HeSE experiments on the same system [35]. I therefore clarify to what extent the previous and new data on adsorption, structure and dynamics are consistent, using unpublished data from the previous investigations ([35]) when necessary to establish the full picture.

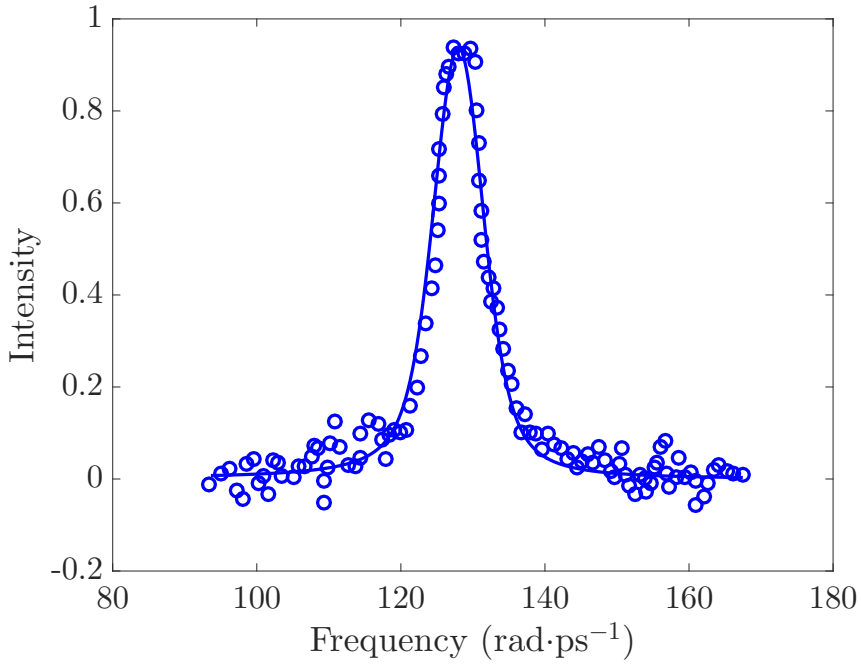

Figure 6.20: HREELS data (blue points) for $\theta = 0.2\,\mathrm{ML}$ H/Ru(0001) taken from [57]. Overlaid is the dynamical structure factor $S(\Delta k_z, \omega)$ for a scattering centre with the mass of atomic oxygen subject to a friction of $4\,\mathrm{ps}^{-1}$ in a well of frequency $\hbar\omega = 84.5\,\mathrm{meV}$ at the experimental temperature of 170 K and $\Delta k_z = 2.0\,\mathrm{Å}^{-1}$. $S(\Delta k_z, \omega)$ is calculated as the numerical Fourier transform of the analytical ISF 3.15. Convolution with the cited experimental resolution $\Delta E = 5\,\mathrm{meV}$ in the energy domain is achieved by multiplying $I(\Delta k_z, t)$ by a Gaussian function before the Fourier transform, where the Fourier transform of the Gaussian function is a Gaussian with 5 meV full width at half maximum. The energy resolution of the experiment accounts for most of the broadening of the central peak. If $\gamma \gtrsim 5\,\mathrm{ps}^{-1}$ then the central peak of the simulated lineshape becomes much broader than the experimental peak. If $\gamma \lesssim 3\,\mathrm{ps}$ the foot of the simulated lineshape is visually much sharper than the data. If other sources of lineshape broadening, such as the distribution of local environments caused by H-H interactions, are significant, then the value of $4\,\mathrm{ps}^{-1}$ is a significant over-estimate.

6.3.8.1 Adsorption

As shown in the previous investigations, there are circumstances where the specular reflected helium intensity from Ru(0001) can be increased by a large hydrogen exposure. In principle, such an effect is plausible for a very clean initial surface if there is a large attenuation of specular on the clean surface due to phonon exchange and the Debye-Waller factor (attenuation due to effective static disorder associated with vibrations [60]). However, an increase in specular intensity above the initial value when dosing hydrogen was not seen in any of the uptake curves in the present investigation. Closer inspection of the previous dataset shows that uptake curves where the final intensity is higher than the initial intensity were recorded from a starting point of low reflectivity (i.e. before the surface was fully clean). Uptake curves recorded from a state of high initial reflectivity have the same form as shown in Figure 6.3 in which the specular reflected intensity reaches a minimum before increasing to a plateau value lower than the original clean-surface value.

Figure 6.21 shows the difference in form between an uptake measurement from a low-reflectivity initial state and a high-reflectivity initial state. The measurements from a highly reflective initial state are consistent with the measurements presented in Figure 6.3.

6.3.8.2 Structure

One of the puzzling experimental facts demonstrated in Section 6.3.3 was that helium diffraction scans of the partially covered surface show a broad peak along $< 1, 1 >$ which does not appear to move as the exposure (and hence coverage) varies, although its intensity changes. Previously, the broad feature in diffraction scans was interpreted as a signature of repulsive H-H interactions, since the feature arises in lattice Monte Carlo simulations of the diffraction pattern [35] within the kinematic scattering approximation (Section 2.1.4.2, using a radially repulsive H-H interaction. In other words, the origin of the feature was proposed as inter-adsorbate correlations which lead to a broad peak in the structure factor $S(\Delta\mathbf{K})$. However, according to the interpretation just put forward, the position of the feature should vary with coverage, which is inconsistent with the experimental observations for variable-temperature deuterium exposure in Section 6.3.3. The new experimental data overturns an apparently uncontroversial previous finding, and therefore I put the experimental observation on firmer ground by showing that it was recorded in the original investigation but not presented.

Figure 6.22a shows diffraction scans along $< 1, 1 >$ recorded after dosing H/Ru(0001) to the minimum of specular intensity, which was previously associated with a nomi-

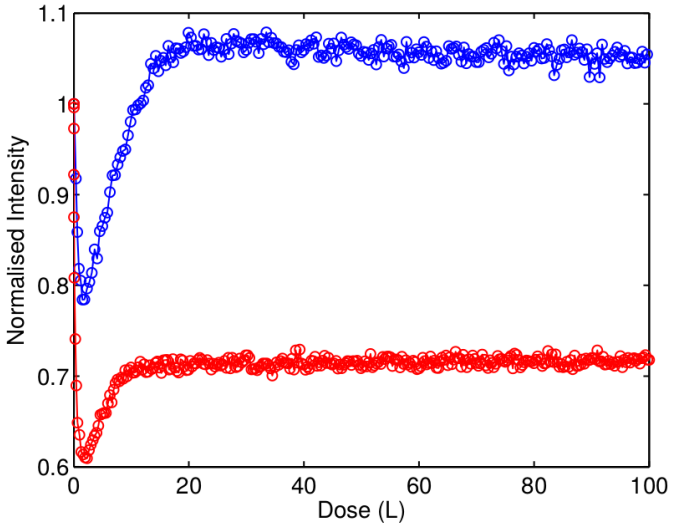

(a) Uptake curves for H and D/Ru(0001) reproduced from [35].

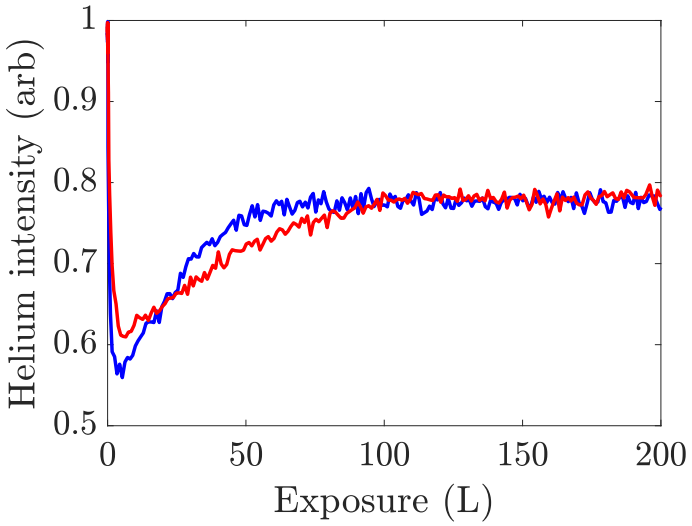

(b) Uptake curves recorded during the same investigation but starting from a highly reflective $R \approx 35\,\%$ initial surface.

Figure 6.21: Uptake curves recorded at $T_s = 250\,\mathrm{K}$ during the prior HeSE investigation of the H/Ru(0001) system [35]. Figure 6.21a is reproduced directly from [35] and shows the helium specular reflected intensity of the Ru(0001) surface increasing upon a large H dose (blue), and decreasing upon a large D dose (red). However, the H uptake curve shown is typical of uptake curves recorded from a low starting reflectivity, before the sample was fully clean. Uptake curves recorded once the surface was fully clean did not show the same effect. Instead, the final intensity was always lower than the initial intensity, regardless of isotope, as shown in Figure 6.21b (same colour scheme) where the uptake curves for both isotopes were recorded from a starting state of $R \approx 35\,\%$. The effect of the initial surface cleanliness on the shape of the uptake curve resolves the apparent discrepancy between the uptake curves in Figures 6.21a and 6.3.

nal coverage of 0.2 ML [35]. In agreement with the results presented in the previous work, there is a broad peak at $\Delta K \approx 1.35\,\text{Å}^{-1}$. However, in the course of the same investigation, diffraction scans were recorded at 150 K after a much larger hydrogen exposure corresponding to a nominal coverage of 0.6 ML. The broad peak does not change its position.

Given that the position of the diffuse feature is insensitive to coverage, the coverage cannot be deduced from the position of the feature. Therefore the previous assignment of $\theta = 0.2$ ML at the minimum of intensity in the uptake curve is not justifiable on the basis of the position of the feature, although the estimate was argued independently based on the exposure and the known initial sticking coefficient and could therefore still be correct.

The scans shown at higher coverage in Figure 6.22 are the only ones available at the higher coverage, so although they confirm the variable-coverage diffraction data from Section 6.3.3, the scope of the coverage-dependent structural measurements remains limited. Further coverage-dependent measurements including two-dimensional diffraction scans would be desirable in order to confirm the interpretation of the diffuse feature.

6.3.8.3 Dynamics

Without reiterating the arguments in detail, there are a few differences in the interpretation of the protium dynamics to emerge between the previous ([35]) and present studies, which I summarize side-by-side.

1. Previously, the relatively low jump rate in the quantum activated regime was attributed to high friction, but the evidence for multiple jumps at high temperatures in the present work suggests the rate is suppressed by low friction.

2. Previously, the shape of the $\alpha(\Delta K)$ for H at $T_s = 150$ K was interpreted as revealing a high proportion of multiple jumps, implying a low friction at low temperatures and therefore a large variation of the friction with temperature. However, the Bayesian analysis of $T_s = 150$ K data in the present Section indicates a low proportion of multiple jumps. The discrepancy could be due to α being an imperfect data reduction measure for underlying lineshapes associated with fcc/hcp hopping dynamics.

3. Previously, the inverse residence time in the stable adsorption sites (fcc) was characterized as becoming approximately temperature-independent at low temperatures; in the present work the inverse residence time in the metastable sites (hcp) is found to be approximately constant at low temperatures. The

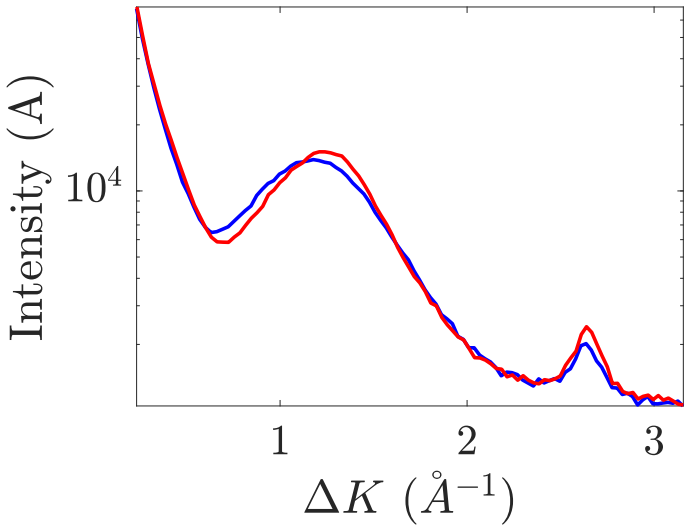

(a) .

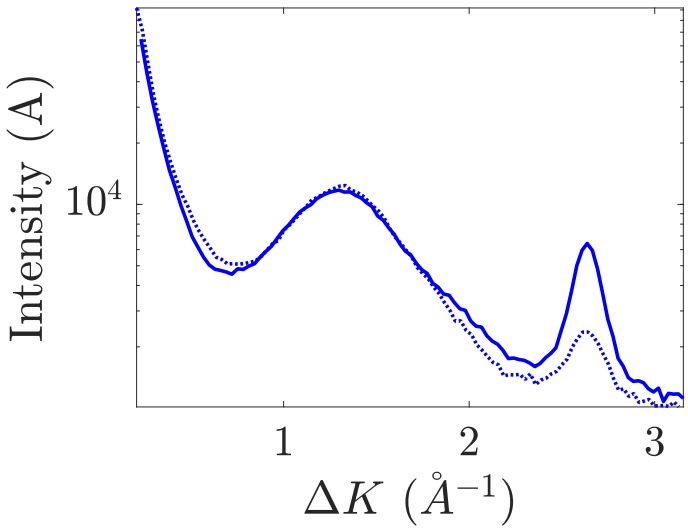

(b)

Figure 6.22: Diffraction scans of H/Ru(0001) from the previous investigation [35], recorded at different hydrogen exposures and therefore different coverages. Figure 6.22a shows results at 250 K (red) and 150 K (blue) after H was dosed to the minimum in specular intensity, which was how the surface was prepared for most dynamics measurements. As well as the first-order diffraction peak at $\Delta K = 2.68\,\text{Å}^{-1}$, a broad peak is seen at $\Delta K \approx 1.3\,\text{Å}^{-1}$ which was previously interpreted as a peak in the structure factor (Section 2.1.4.2) caused by repulsive H-H interactions. Figure 6.22b shows further data from the same experimental series, consisting of scans taken along the same azimuth after a much larger dose of hydrogen. Both scans were recorded at $T_s = 150\,\text{K}$, but on different sides of the specular condition: on the solid curve, $\Delta\mathbf{K}$ is opposite in sign to the initial surface-resolved momentum $\mathbf{K}_i$, whereas on the dotted curve $\Delta\mathbf{K}$ and $\mathbf{K}_i$ have the same sign. The scans shown here confirm that the broad feature does not migrate towards $\Delta K = 0$ as the coverage increases. The data are therefore not consistent with the previous interpretation of the diffuse peak as a de Gennes feature. For clarity: all data in the present Figure were recorded during the experiments associated with the prior published work on H/Ru(0001) [35, 23, 180].

two rates are assumed to be related by detailed balance (with a factor of $\exp(\Delta E/k_B T)$), and so a constant residence time in the stable site would imply that the escape rate from metastable sites increases with decreasing temperature. A trend of that kind cannot realistically persist down to very low temperatures, otherwise the metastable escape rate would become very large. However, the temperature-dependent measurements for protium in the present study were not extended down to very low temperatures where the difference in the two measures of the rate becomes very large. At some low temperature, diffusion dynamics will be dominated instead by fcc-fcc tunneling, whose rate is not calculated in the present work but is assumed to be significantly slower than inelastic fcc-hcp tunneling due to the double-barrier separating equivalent sites. STM experiments on Cu(111) [154] and Pd(111) [289] suggest that the elastic incoherent tunneling rate (fcc-fcc) is significantly slower than the plateau in the metastable escape rate. However, the analogous measurements are not available for Ru(0001).

6.3.9 Conclusions

The diffusion of hydrogen on Ru(0001) has been revisited, and D/Ru(0001) has been investigated in detail. Jump distributions obtained with the Bayesian analysis method of Section 2.2 systematically contain multiple jumps for both H and D, with a survival parameter for long jumps of $s = 0.5$ at $T_s = 250\,\mathrm{K}$. Helium diffraction patterns along $< 1, 1 >$ show a diffuse feature whose position and width in ΔK is constant with coverage, and therefore cannot be simply assigned to repulsive interactions as previously assumed, which invites both a more detailed structural investigation, and form factor calculations. The evidence is largely in favour of the incoherent deep tunneling rate being much slower for D than for H, in line with theoretical expectations.

6.4 Diffusion of hydrogen on Pd(111)

The first HeSE measurements of H and D diffusion on Pd(111) are presented. The results are analysed within broadly the same framework set out for Ru(0001) in the previous Section. Additionally, explicit comparison is made between the experimental data and recent theoretical diffusion-rate calculations for H/Pd(111).

6.4.1 Background

Palladium (Pd) is a promising material for applications in hydrogen technologies including purification, sensing and storage [290]. Applications rely on the surface properties as well as bulk properties, and therefore the interaction of hydrogen with Pd surfaces is a very significant topic. Helium atom scattering can make a valuable contribution to the field thanks to the unique features summarized in Chapter 2, and HeSE diffusion measurements provide a sensitive test of the lateral H/surface interaction.

H_2 chemisorbs dissociatively on Pd(111) with an adsorption energy of 460 meV [291], which is roughly double the bulk adsorption energy [292], and therefore surface sites are more stable than bulk sites at low coverage. Molecular beam experiments show that both non-activated and activated pathways are available [293], and the initial molecular dissociative sticking coefficient falls from 0.6 at low incident energies to 0.4 at high incident energies, at a surface temperature $T_s = 220\,\mathrm{K}$. Whether isolated or in ordered phases, hydrogen prefers to adsorb at the fcc hollow sites, as seen by LEED [294], STM [289] and consistent with almost all first-principles theoretical studies. At room temperature and 1×10^{-7} Torr H_2, H forms a (1×1) ordered structure while at the same time dissolution in the near-surface region causes a 2% expansion of the interlayer spacing [295]. Helium diffraction [296] showed that below 270 K the rotational symmetry of the (1×1) phase breaks from sixfold to threefold, a fact that the investigators attributed to quantum delocalization of the H atoms at the higher temperature. Two more ordered phases are known: at a coverage $\theta = \frac{1}{3}$ a $(\sqrt{3} \times \sqrt{3})R30°$ phase is stable up to 85 K and at $\theta = \frac{2}{3}$ another $(\sqrt{3} \times \sqrt{3})R30°$ phase is stable up to 105 K [297]. The existence of two separate $\sqrt{3}$ phases is illustrated by the behaviour of the intensity of a $\sqrt{3}$ diffraction peak upon dosing, which shows a double maximum. The phenomenology was independent of the electron beam energy, but dependent on temperature, implying that the lack of ordered phases at $T \gtrsim 105\,\mathrm{K}$ except for the (1×1) at $\theta \to 1$ is a genuine thermal effect. Thermal desorption profiles show two peaks in the hydrogen evolution rate [298, 299]. The peak at $T_s = 310\,\mathrm{K}$, referred to as the β peak, corresponds to desorption from surface sites. Therefore, above $T \approx 300\,\mathrm{K}$, an overpressure of H_2 (D_2) is required to maintain a long-term coverage of surface hydrogen.

The microscopic surface diffusion of H/Pd(111) has been studied experimentally and theoretically, but theoretical studies have been more focussed on the quantum activated regime while experimental (STM) measurements have been performed at much lower temperatures. On the theoretical side, Rick *et al.* used quantum transition state theory (QTST) in conjunction with embedded atom model (EAM)

potentials to calculate jump rates between neighbouring fcc and hcp hollow sites [300]. At 300 K the H jump rate was predicted to be $16\,\mathrm{ns}^{-1}$. The EAM method was justified on the basis that it reproduces the phase diagram to good accuracy [297], but it does produce a rather high barrier over the bridge site of 202 meV, and the method has been superseded by GGA-DFT which predicts a significantly lower fcc-bridge barrier of 140 meV [283]-150 meV [301], [302]. Recently the $\alpha(\Delta K)$ has been predicted directly using a formalism in which the $\delta(\omega, \omega_m - \omega_n)$ functions in the microscopic expression for $S(\Delta K, \Delta\omega)$ in Section 4.1 are replaced by Lorentzian functions. The Lorentzians represent scattering rates induced by coupling to excitations in the substrate. At 250 K the maximum predicted dephasing rate is about $130\,\mathrm{ns}^{-1}$. The Lorentzian-broadening method,at least as implemented in published work [45], largely overestimates the rate and underestimates the activation energy, which will be discussed in Section 6.4.6. On the experimental side, H/Pd(111) diffusion has been observed with STM [289] at $T_s = 37\,\mathrm{K}$, at a jump rate of $6\,\mathrm{s}^{-1}$. Given only a single low-temperature datum for the rate, it is not straightforward to relate the low-temperature rate to the high-temperature rate because the STM experiment does not distinguish between direct fcc-fcc tunneling, and tunneling via a real but short-lived transitions to the metastable hcp sites.

In some contexts, subsurface sites play an important role in the behaviour of hydrogen atoms on Pd surfaces. Helium diffraction data relating to subsurface migration of hydrogen on Pd(311) [303] is consistent with subsurface hydrogen being essentially invisible to helium scattering, as expected from the surface sensitivity of the technique. The influence of subsurface sites on the diffusion data can therefore only be indirect. If hydrogen atoms disappear and reappear at the surface on a timescale comparable to the lateral hopping, then the effect of the subsurface sites should be quantified through a surface/subsurface jump rate, which is sensitive to the surface/subsurface barrier. The very large theoretical barrier to subsurface diffusion from DFT calculations (420 meV [302] - $>$ 500 meV [304]) suggests that the timescale of hopping between the surface and subsurface is much slower than the timescale of surface diffusion by jumps.

6.4.2 Experimental methods

The single crystal sample was prepared as described in Section 2.1.3, giving a clean surface with a reflectivity of 45%. Hydrogen was introduced onto the surface by leaking H_2 (Air Liquide, 99.999%) into the scattering chamber at a controlled overpressure maintained by an automatic leak valve. All measurements reported in detail in the present work, were carried out with the sample in equilibrium with

the applied UHV atmosphere. The majority of the data presented are associated with an uncorrected overpressure of 2.5×10^{-9}mbar on the extractor gauge before accounting for scattered helium or sensitivity corrections. For practical reasons the hydrogen was introduced through a retractable dosing arm. When the dosing arm is close to the sample surface, the local pressure in front of the sample is enhanced above the background pressure by up to a factor of 20 [28]. However, the dosing arm was kept retracted a significant distance from the surface. Direct comparison of uptake curves in which dosing was carried out using the dosing arm, and the manual leak valve far from the sample, showed no difference in uptake as a function of background pressure, and therefore the enhancement of the local pressure in front of the crystal was negligible when using the dosing arm. Between each polarization scan the crystal was flashed to 500 K to avoid a build-up of CO on the surface. Repeated flashing of this kind in a 2.5×10^{-9} mbar hydrogen atmosphere maintained a stable, repeatable specular intensity throughout the measurement series. In a separate series of measurements, D_2 was dosed through the same method. H/D dynamics measurement series were separated by a dose of D_2 followed by six cycles of sputtering and annealing, and around 36 hours. No H dynamics measurements were performed after the D measurements were finished. Most polarization scans were taken with a uniform spin echo time base $-60\,\text{ps} \lesssim t_{SE} \lesssim 60\,\text{ps}$, symmetrically distributed around $t_{SE} = 0$ with an odd number of points (usually 301) such that $t_{SE} = 0$ is included in the measurements.

All previous HeSE studies of hydrogen diffusion at metal surfaces have been conducted in a regime where the desorption rate is negligible. For the closest possible comparison with theoretical calculations of surface diffusion it would have been preferable to work in the same regime with Pd(111). Working in the overpressure regime was motivated by the tendency of the specular intensity to fall rapidly at temperatures of around 300 K and below. Residual CO could be responsible due to its high sticking coefficient, high desorption temperature, and large helium scattering cross section. The nature of the contamination could be revealed by careful comparison of the desorption profile compared to reference measurements for plausible candidates including hydrogen and CO. However, in the present work contamination was avoided by the choice of measurement regime.

6.4.3 Adsorption and structure

Figure 6.23, shows the change in specular reflected helium intensity when introducing 2.5×10^{-9} mbar (gauge) H_2 into the scattering chamber with the surface at $T_s = 350\,\text{K}$. A stepwise introduction of a hydrogen overpressure leads to a rapid re-

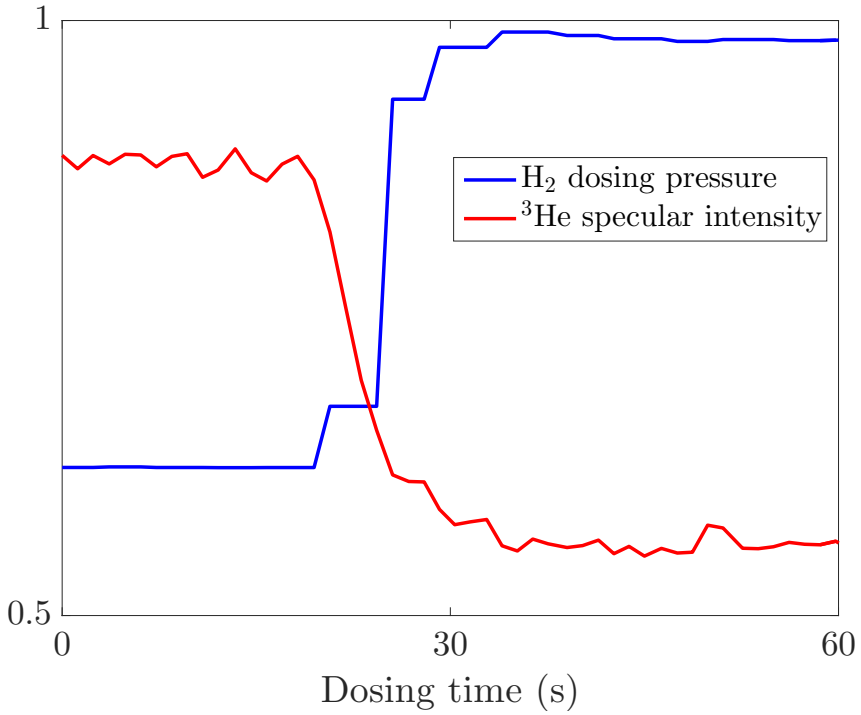

Figure 6.23: The rapid equilibration of the specular intensity (red) as a function of dosing time, when the dosing pressure of 2.5×10^{-9} mbar (gauge) is applied stepwise (blue curve) at a surface temperature of $T_s = 350\,\mathrm{K}$. The intensity and pressure curves are given an arbitrary relative scaling to show them on the same axes. The response of the specular intensity appears to be over in about 15s, and is difficult to distinguish from finite response of the pressure reading. We can use the fast equilibration response to place a fairly restrictive upper bound on the equilibrium coverage, as discussed in the main text.

equilibration of the specular reflectivity. Considering the rate of atmosphere/surface equilibration during uptake we can estimate an upper bound on the coverage by assuming an initial sticking coefficient of 1 and neglecting desorption during equilibration. The coverage is given by $2\times$ the integrated molecule number flux over the equilibration period, divided by the area of a primitive unit cell ($6.5\,\mathrm{\AA}^2$). The integrated number flux over time t of hydrogen molecules of mass m at pressure p is given by kinetic theory [11] as

$$N = \frac{pt}{\sqrt{2\pi m k_B T}}\,. \tag{6.1}$$

At $p = 2.5 \times 10^{-9}$ (gauge) the equilibration period takes approximately 10 s. After applying a gauge correction factor of 0.46 the estimated upper limit on the coverage is 0.1. The initial sticking coefficient has been measured at lower temperatures [291], [305] and was found to be < 1.

The progression of the uptake behaviour on specular at different temperatures is shown in Figure 6.24a. At the lowest temperature $T_s = 240\,\mathrm{K}$ (blue), the specular

intensity falls rapidly upon the initial dose, and then recovers with increasing dose. At intermediate temperatures ($T_s = 300\,\mathrm{K}$, green curve) the specular intensity falls monotically before levelling off at about $I_0/4$, showing that the surface has taken up considerably more hydrogen at 300 K than at 350 K. A different perspective on the same behaviour is provided by uptake curves on the first order diffraction condition of the clean surface. Two representative diffraction uptakes are shown in Figure 6.24b. The important contrast between the two curves is in the final diffracted intensity, which at $T_s = 280\,\mathrm{K}$ is a factor of 40 higher than the clean surface value, but at $T_s = 350\,\mathrm{K}$ is a factor of 2 lower than the clean surface value, implying negligible ordering of surface hydrogen at 350 K. A more detailed discussion of the uptake curves is provided in the Figure caption.

The behaviour of the system when the dosing pressure is removed is illustrated in Figure 6.25. In all cases the intensity relaxes once the overpressure is removed, implying that hydrogen leaves the surface at a non-negligible rate even at 300 K.

Figure 6.26 shows diffraction scans along $< 1, 1 >$ recorded with an overpressure of 2.5×10^{-9} mbar H_2 (gauge) at temperatures from 240 K to 350 K, and additionally a scan at 350 K recorded without an overpressure. Subtracting the background intensity consisting of the scan without any overpressure, leads to the Figure 6.26a in which the peak position is plotted as a function of temperature. Approximating the mutually repelling overlayer as a quasi-hexagonal arrangement, the coverage can be estimated from the position of the diffuse feature by [307]

$$\theta = \left(\frac{\Delta K}{\Delta K_{diff}}\right)^2, \tag{6.2}$$

where ΔK_{diff} is the position of the first-order diffraction peak along $< 1, 1 >$. The results of applying Equation 6.2 are shown in Figure 6.26c. The results are consistent with the pressure-based estimate derived from Figure 6.24. Finally, as an independent check that the coverage estimates make sense, the specular intensity as a function of temperature during the constant-pressure, variable-temperature deuterium measurements (Section 6.4.5) is converted into specular intensity as a function of inferred coverage, and shown in Figure 6.26d.

6.4.4 Nature of jump dynamics

Figure 6.27 shows two typical polarization scans recorded sequentially at 350 K and a constant overpressure of 2.5×10^{-9} mbar (gauge) H_2, which corresponds to a specular intensity of $I = 2I_0/3$ as seen in Figure 6.23.

The short-time oscillations can be studied more conveniently in the Fourier do-

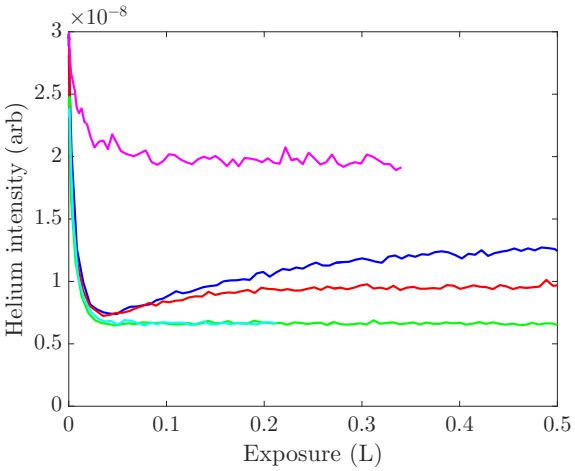

(a) H/Pd(111) uptake curves on specular.

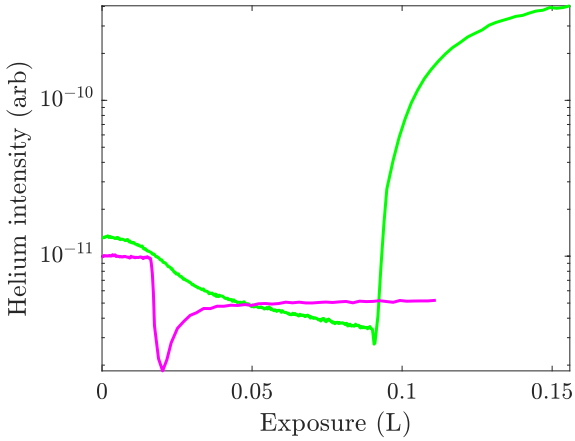

(b) H/Pd(111) uptake curves on a first-order clean surface diffraction peak.

Figure 6.24: Uptake curves on specular (Figure 6.24a, linear vertical axis) and the first-order diffraction condition along $< 1,1 >$ (Figure 6.24b, logarithmic vertical axis) of H/Pd(111) at temperatures $240\,\mathrm{K} \leq T_s \leq 350\,\mathrm{K}$, dosing H_2 at 2.5×10^{-9} mbar (gauge). The uppermost curve (magenta) corresponds to 350 K, the same conditions represented in Figure 6.23. The curves at the lowest temperatures (240 K blue, 260 K red) show a minimum in specular intensity followed by an approach to equilibrium which is much slower than the initial drop. At intermediate temperatures of 280 K and 300 K (green, cyan), the specular intensity does not recover with increasing exposure. At $240\,\mathrm{K} \leq T_s \leq 300\,\mathrm{K}$, the minimum specular intensity is about $I_0/4$. The diffraction uptakes shown are at $T_s = 280\,\mathrm{K}$ (green) and $T_s = 350\,\mathrm{K}$ (magenta). At the lower temperature the final diffracted intensity, when equilibrium has been reached, is approximately 40× higher than the clean surface diffracted intensity. Before the hydrogen dose was commenced, the diffracted intensity decreased smoothly due to the low-temperature contamination described at the end of Section 6.4.2. At the higher temperature where the extensive dynamics measurements are reported in the present Chapter, the final diffracted intensity is a factor of 2 below the initial intensity, implying there is negligible ordering of hydrogen atoms on the surface. The minor recovery of intensity before equilibration at 350 K can be ascribed to an increase in the amount of diffuse scattering, as demonstrated by the blue curve in Figure 6.26a where the diffraction peak is very shallow. In general the clean surface diffracted intensity between 280 K and 350 K showed negligible temperature dependence, which is unsurprising since the specular peak in He/Pd(111) scattering has been shown to vary approximately as a decaying exponential function of surface temperature, $I(T_s) \propto \exp(-WT_s)$ $(T_s \geq 300\,\mathrm{K})$ where $W = 0.0035\,\mathrm{K}^{-1}$ [306], which predicts only a 20% decrease in intensity over a 70 K interval, which can be compensated for by small changes in adsorbate coverage.

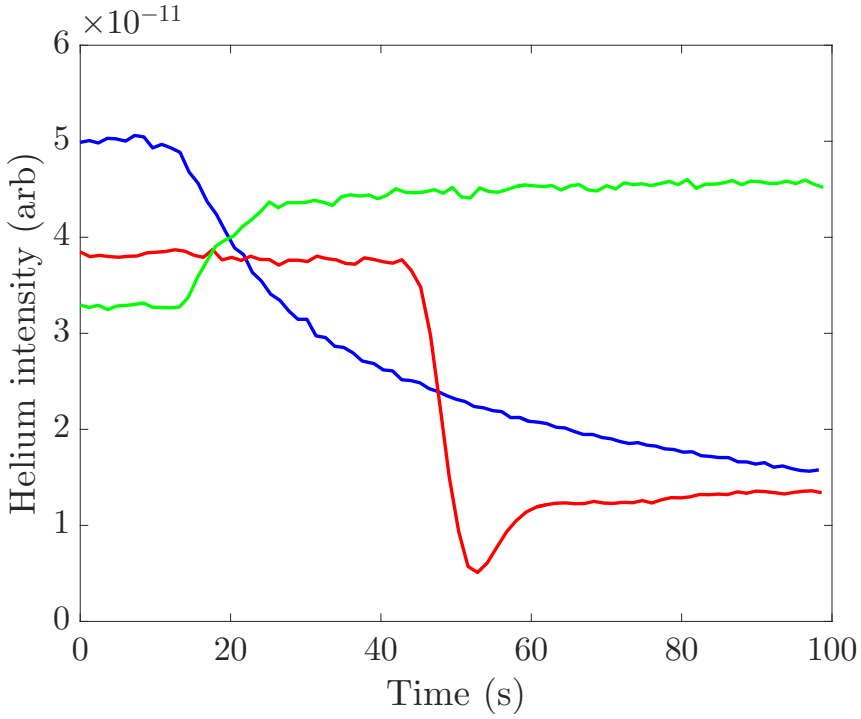

Figure 6.25: The response of the Pd(111) diffracted helium intensity ($< 1, 1 >$ first-order) to a stepwise removal of a 2.5×10^{-9} (gauge) overpressure of H_2 at three different temperatures: 300 K (blue), 350 K (red) and 400 K (green). The surface was initially in equilibrium with the applied overpressure. In all three cases, the diffracted intensity starts recovering immediately upon removal of the overpressure.

main, as described in Section 2.2. In general the polarization scans in the Fourier domain have the qualitative form illustrated in Figure 2.9, with a quasielastic and inelastic peak. Figure 6.28 shows the apparent dispersion relation $\omega(\Delta K)$ as a function of the momentum transfer calculated from equation 2.15. Although it is not a quantitatively accurate representation of the inelastic frequencies, the shape and scale of the dispersion relation suggest that surface phonons are responsible. To provide a better estimate of the phonon frequencies being probed, we can convert the apparent energy exchanges $\hbar\Delta\omega_{app}$ into wavelength exchanges. The way the spin-echo time (Equation 2.6) is defined means that an inelastic feature at energy $E = \hbar\omega$ gives an inelastic peak at frequency ω in the Fourier transform when ω is small, such that changes in energy and changes in wavelength are linearly related by

$$\Delta\lambda = \frac{m\lambda_i^3}{\hbar}\Delta\omega\,. \tag{6.3}$$

When the energy exchanges are relatively large, the oscillation frequency in the time domain depends on the wavelength change rather than the energy exchange, because the time a helium atom spends in a solenoid in the beamline is linearly proportional to its wavelength. So if we have extracted an apparent peak frequency ω_{app} by Fourier transforming a polarization scan, then the dominant wavelength

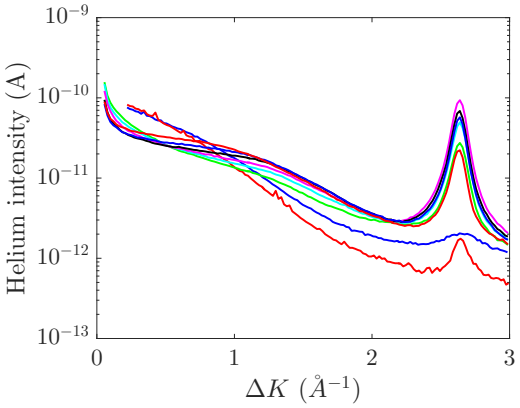

(a) Diffraction scans at varying coverage.

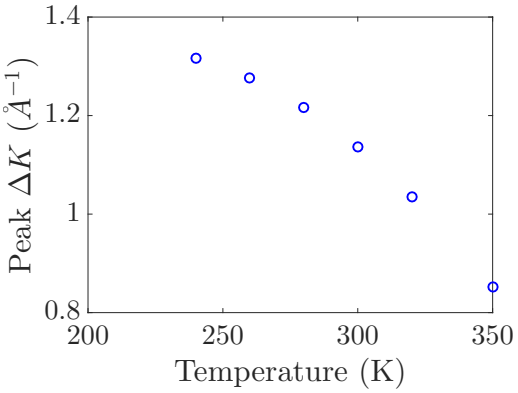

(b) Position of the diffuse shoulder for different scans.

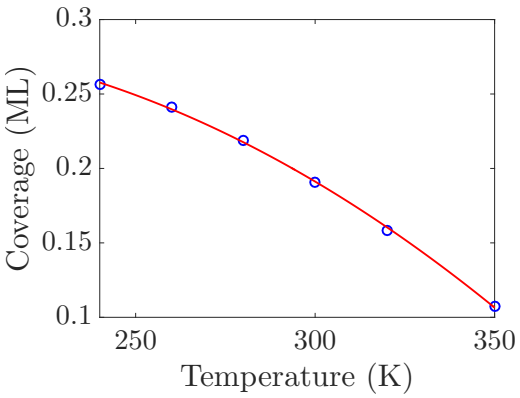

(c) Coverage estimated from shoulder position.

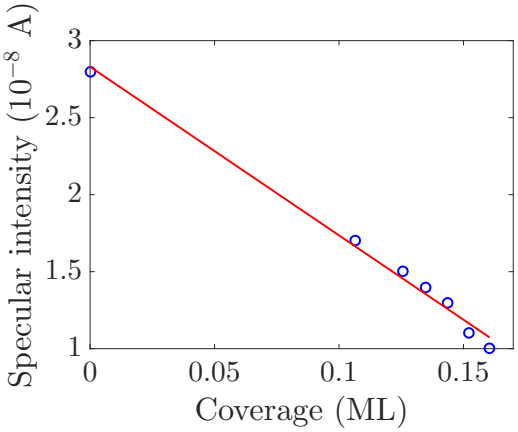

(d) Coverage as a function of temperature at constant pressure, deuterium.

Figure 6.26: Hydrogen coverage inferred from helium diffraction scans of Pd(111) along $< 1, 1 >$. Figure 6.26a shows diffraction scans at variable temperature $240\,\mathrm{K} \leq T_s \leq 350\,\mathrm{K}$ in equilibrium with 2.5×10^{-9}mbar (gauge) H_2 (blue), and also a scan at 350 K in the absence of the overpressure (red). The scans with constant overpressure show a broad feature which becomes more pronounced as the temperature decreases. To estimate the position of the broad feature as a function of temperature, the scan recorded without an overpressure was used as a background intensity. The position in ΔK of the maximum in residual intensity is plotted as a function of temperature in Figure 6.26b. The associated coverages calculated using Equation 6.2 are shown in Figure 6.26c. Finally, Figure 6.26d shows the specular intensity as a function of $\theta(p, T)$ measured during the variable-temperature, constant pressure ($p = 2.5 \times 10^{-9}\,\mathrm{mbar}$) deuterium measurements of Section 6.4.5, where $\theta(p, T)$ is assumed to have the same dependence on p and T for both isotopes.

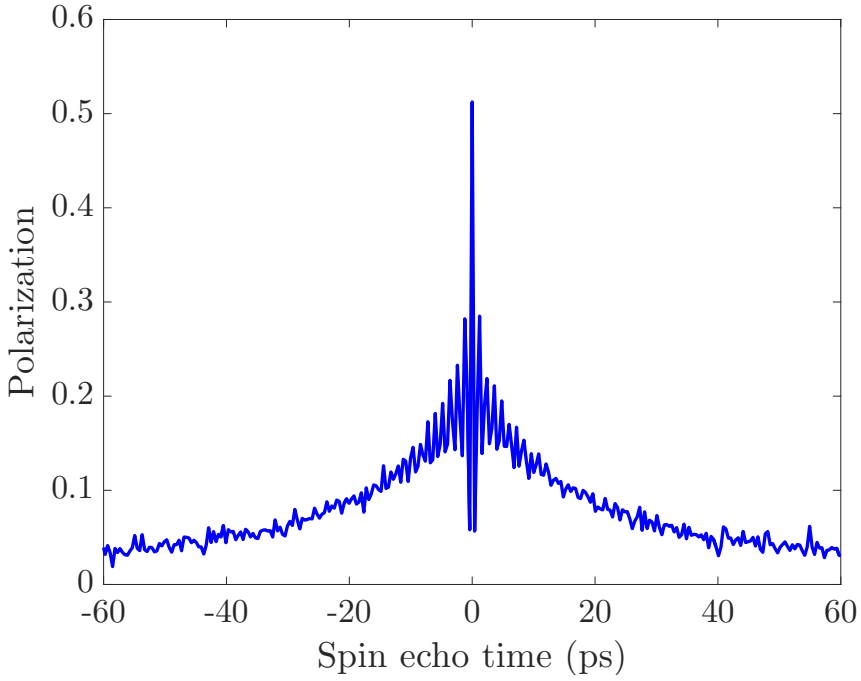

(a) Polarization scan

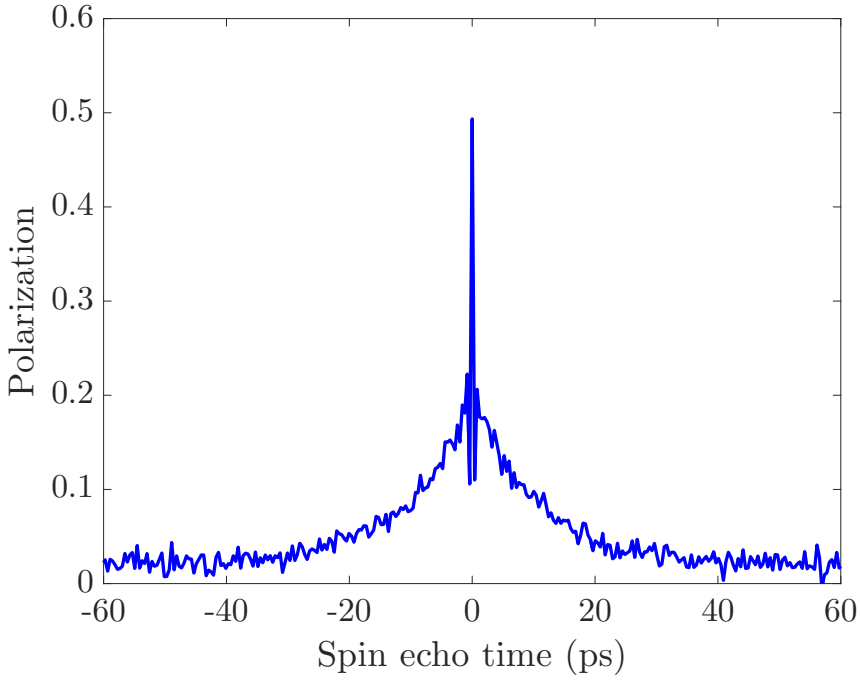

(b) Polarization scan

Figure 6.27: Polarization scans of Pd(111) at 350 K while an overpressure of 2.5×10^{-9} mbar (gauge) H_2 is applied, corresponding to a specular attenuation $I = 2I_0/3$ and an estimated coverage of 0.1 as described in Section 6.4.3. Upper plot: $\Delta K = 0.7\text{Å}^{-1}$, $< 1,1 >$ azimuth. At short times there are many oscillations visible. Lower plot: $\Delta K = 1.3\text{Å}^{-1}$, $< 1,1 >$ azimuth. Oscillations are confined to the first few points.

change probed by the measurement was

$$\Delta\lambda = \frac{m\lambda_i^3}{\hbar}\Delta\omega_{app}\,. \tag{6.4}$$

The wavelength exchange is related nonlinearly to the initial and final probe energies by

$$\Delta\lambda = \sqrt{\frac{\hbar^2}{2m}}\Big(\frac{1}{E_f} - \frac{1}{E_i}\Big)\,. \tag{6.5}$$

The real energy exchange can therefore be calculated as $E_f - E_i$, where

$$E_f = \frac{E_i}{(1 + \sqrt{2mE_i/\hbar^2}\Delta\lambda)^2}\,. \tag{6.6}$$

The momentum transfer should also be corrected for the energy exchange using the inelastic version of Equation 2.15 with an initial and final wavevector:

$$\Delta K = k_f \sin(\delta - \gamma) - k_i \sin(\gamma)\,. \tag{6.7}$$

The corrected dispersion relation is shown in the middle plot of Figure 6.28. A theoretical dispersion relation from an 30-layer normal modes calculation in the literature [308] is overlaid for comparison. The full set of theoretical surface phonon dispersion relations for the 30-layer slab is reproduced in the lower plot. The points K and M in reciprocal space were defined in Figure 5.14. M lies halfway be between the origin and the first-order diffraction peak along $< 1, 1 >$, and K is related to M by a 30° rotation and a $2/\sqrt{3}$ scaling. The branch overlaid on the experimental data is the Rayleigh mode. The interatomic forces were calculated with the embedded atom method which is no longer the state of the art in first principles calculations. However, the calculation was considered reliable at the time since it reproduced the experimental Rayleigh mode at the K point [309].

The quasielastic and inelastic features are strongly separated in the Fourier domain, so the inelastic features have been removed by the Fourier method illustrated in Section 2, using the peak frequencies and widths determined on a scan-by-scan basis by inspection of the Fourier transforms. The Fourier filtering method is illustrated for an experimental scan in Figure 6.29.

After Fourier filtering, the slowest exponential decaying component of the polarization scans were extracted by varying the fitting start time until the result does not vary in any meaningful way. The resulting $\alpha(\Delta K)$ for H (red) and D (blue) at 350 K is shown in Figure 6.30. The solid curves are fits to the Chudley-Elliott model (Equation 2.33). The fit describes the data well up to around $|\Delta K| = 1.5\,\text{Å}^{-1}$. At larger momentum transfers there is a systematic deviation from the fit, which sug-

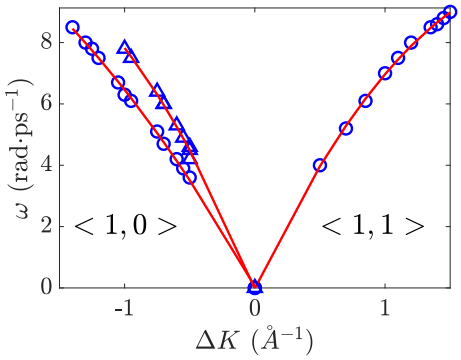

(a) Apparent $\Delta\omega(\Delta\mathbf{K})$, treating $\Delta\omega$ and t_{SE} as Fourier-conjgate t variables.

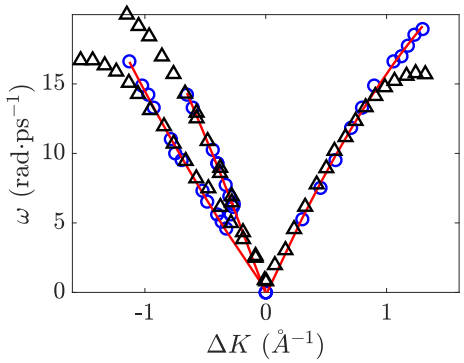

(b) Dispersion relation corrected via relations 6.6 and 6.7.

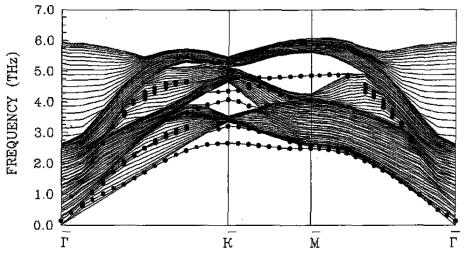

(c) Theoretical dispersion relations [308].

Figure 6.28: Analysis of the dispersive inelastic feature seen in polarization scans of H/Pd(111). In Figure 6.28a, the apparent inelastic frequency is plotted as a function of the quasielastic surface-parallel momentum transfer. The smooth dispersion tending to the origin indicates that the inelastic features are due to surface phonons. Along $< 1,0 >$ a second sharp inelastic feature is visibile at certain ΔK. In Figure 6.28b, the wavelength-based correction 6.6 with 6.7 is applied to estimate the true phonon dispersion relation. The theoretical Rayleigh mode dispersion [308] is overlaid as black triangles, where the points are taken from the full spaghetti diagram in Figure 6.28c, reprinted from reference [308], Copyright (1997), with permission from Elsevier. The mode frequencies were derived from a normal modes calculation on a 30-layer slab where the total energy is evaluated with the embedded atom method [308]. As noted in the previous Chapter in Figure 5.14, the surface direction labels in the present Thesis are related to those in the reproduced surface phonon plots by $\bar{\Gamma}\bar{K} \leftrightarrow < 1,0 >$ and $\bar{\Gamma}\bar{M} \leftrightarrow < 1,1 >$. The experimental data is in reasonable agreement with the theoretical prediction (including both branches along $< 1,0 >$) except near the zone boundary. The discrepancy could potentially be due to probing other surface modes, or due to the presence of surface hydrogen.

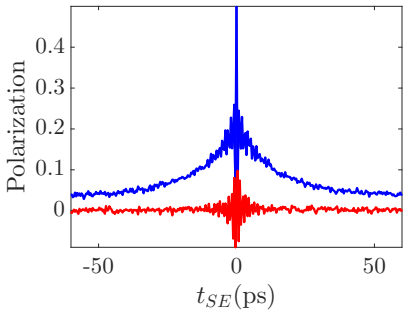

(a) Polarization scan in the time domain

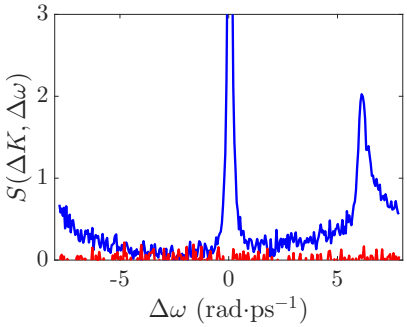

(b) Polarization scan in the Fourier domain

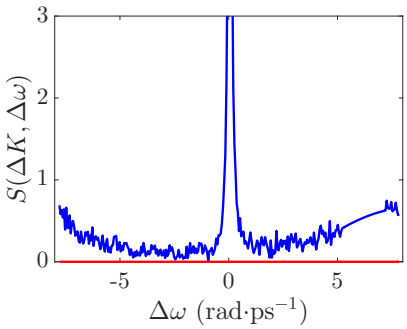

(c) Polarization in the Fourier domain after applying window

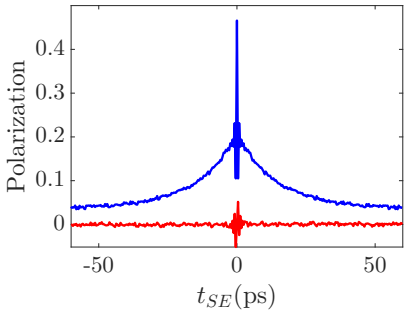

(d) Polarization scan transformed back to the time domain

Figure 6.29: The inelastic filtering procedure for a typical experimental scan. The filtering algorithm was explained in Section 2.2, and applied to simulated data in Figure 2.9.

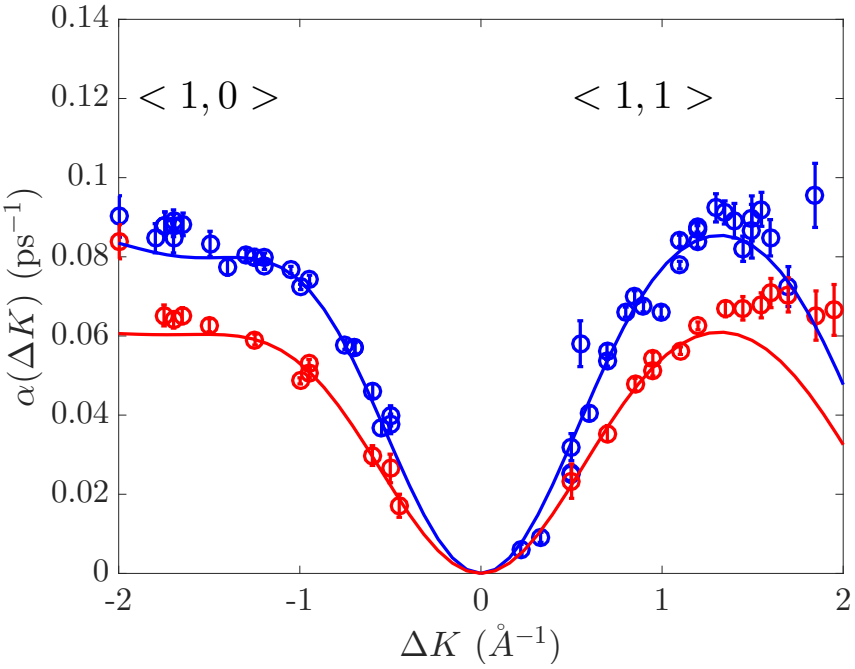

Figure 6.30: The dephasing rate $\alpha(\Delta K)$ of the slowest exponential decay of polarization scans of Pd(111) at $T_s = 350\,\mathrm{K}$ in equilibrium with an overpressure of $2.5 \times 10^{-9}\,\mathrm{mbar}$ (gauge) of H_2 (blue) and D_2 (red), which corresponds to a specular attenuation of $I = 2I_0/3$ and an estimated coverage of $\theta \lesssim 0.1$ as argued in Section 6.4.3. The start time for the exponential fits was increased until $\alpha(\Delta K)$ does not vary with the start time. The smooth curves are best fits of $\alpha(\Delta K)$ to the Chudley-Elliott model (Section 2.2.1) and should be considered as guides to the eye. The Chudley-Elliott best fit parameters are not analysed quantitatively because the dynamics are more appropriately described by the non-Bravais hollow-hollow diffusion model, fitted using the Bayesian method of Section 2.2.6. However, the behaviour of the slow dephasing rate alone does demonstrate jump diffusion, as $\alpha(\Delta K)$ rises quadratically from the origin and turns over at larger ΔK.

gests a faster-decaying second exponential component whose amplitude is too small to directly distinguish. The Chudley-Elliott model is used here to produce a guide to the eye but will not be used to quantitatively analyse the jump rates here since the non-Bravais model (as applied to the H/Ru(0001) data) is more appropriate.

A free biexponential fit for the scans represented in Figure 6.30 does not give meaningful results. In order to extract information about the dynamics on the non-Bravais lattice, the Bayesian analysis routine of Sections 2.2 and 6.3.4 has been applied. The results are shown in Table 6.4. The fcc/hcp occupation ratio λ is very similar for both isotopes. Notably, the survival ratio s for long jumps is much lower for D than H, which was not a feature of the Ru(0001) data. Possible interpretations in terms of the isotope dependence of friction will be discussed after analysis of the temperature dependence of the dynamics.

Table 6.4: Parameters of the non-Bravais, triple jumps model applied to H/Pd(111) and D/Pd(111) datasets at 350 K. The fcc/hcp occupation ratio λ is very similar for both isotopes, as expected. The survival ratio s for long jumps is much lower for D than H, which was not a feature of the Ru(0001) data.

Isotope	$\mathbf{T_s(K)}$	τ**(ps)**	λ	**s**	**ΔE (meV)**
H	350	4.9 ± 0.5	2.9 ± 0.2	0.40 ± 0.05	32 ± 2
D	350	6.3 ± 0.3	3.0 ± 0.1	0.23 ± 0.01	33 ± 1

6.4.5 Temperature dependence of jump dynamics

The temperature-dependent slow dephasing rate, extracted from polarization scans by fitting a single exponential decay from a start time of 20 ps, is shown in Figure 6.31. The temperature-dependent data was measured at $\Delta K = 0.95\,\text{Å}^{-1}$ along $< 1, 1 >$ at $300\,\text{K} \leq T_s \leq 400\,\text{K}$ for H, and $300\,\text{K} < T_s < 360\,\text{K}$ for D. For H, the overpressure was adjusted to maintain a constant attenuation of specular $(2I_0/3)$. For D, a constant overpressure was used out of concern that for very low D_2 overpressures residual H in the crystal could replace surface D and contaminate the measurements. The variation of specular intensity as the temperature was lowered at constant overpressure of D_2 was shown in Figure 6.26, along with estimated coverages which remain low. At 400 K the overpressure required to achieve $2I_0/3$ was 7.5×10^{-8} mbar, which is 30× higher than at 350 K. The relatively high overpressure induced gradual changes in the surface which require a sputter cycle to reverse, which could be due to a build-up of trace impurities from the dosed gas. However, the changes are very slow compared to the time required to record a polarization scan, and the single datum at 400 K is in qualitative agreement with the data recorded under stable conditions. Additionally, a datum for H was recorded at 250 K after dosing to $I_0/2$ and removing the overpressure. The solid lines in the Figure are fits to an Arrhenius rate law. The best-fit parameters and their uncertainties are given in Table 6.5.

In Figure 6.31, the temperature-dependent data is presented in two different ways. In the upper plot, the dephasing rate is presented in its raw form, which enables a straightforward comparison with a theoretical prediction in Section 6.4.6. In the lower plot, a temperature-dependent τ is extracted using the method stated in 6.3.5, where λ varies according to detailed balance and s is assumed constant.

6.4.6 Theoretical discussion

As a straightforward, preliminary piece of analysis I compare the experimental dephasing rates in Figure 6.31 with recent published theoretical predictions which are

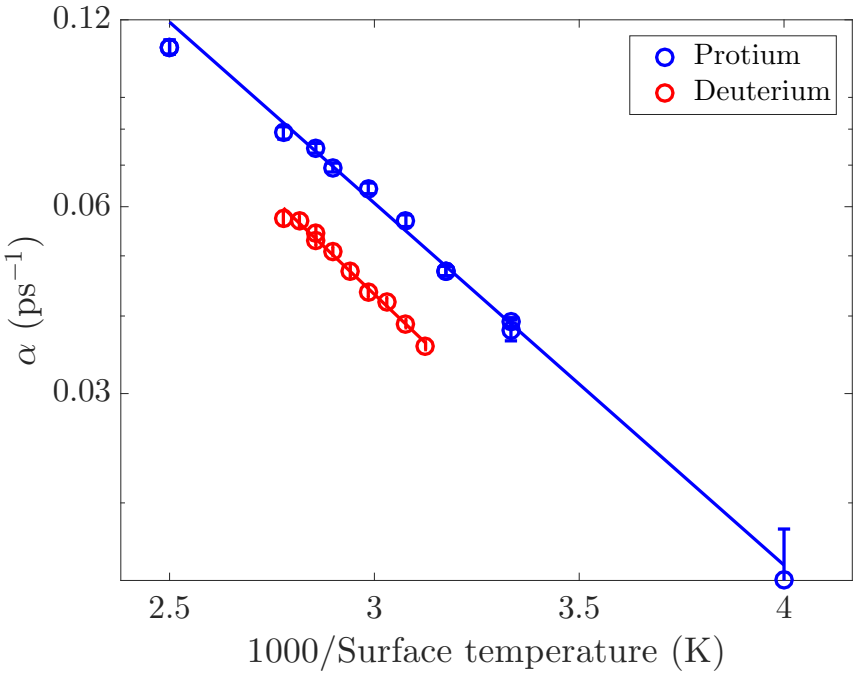

(a) Temperature dependence of the jump rate measured via the dephasing rate $\alpha(T)$.

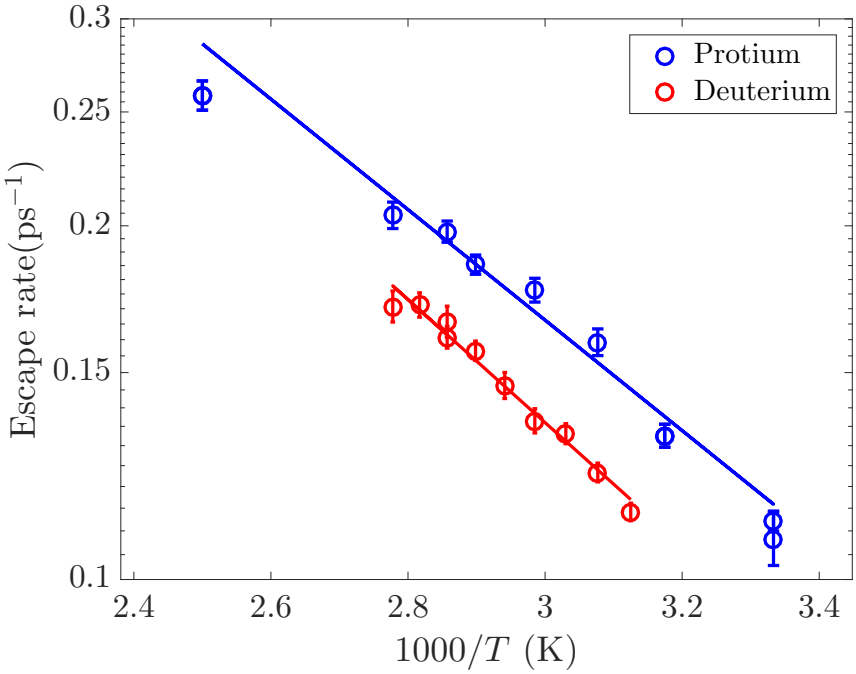

(b) Temperature dependence of the jump rate measured via the jump model parameter τ^{-1}.

Figure 6.31: Temperature dependence of two different measures of the diffusion rate at $\Delta K = 0.95\text{Å}^{-1}$ along $< 1, 1 >$ for H (blue) and D (red) at a coverage of $2I_0/3$ on Pd(111). In Figure 6.31a, the rate is presented as the fitted single-exponential decay rate of the ISF. In Figure 6.31b the rate is presented as the escape rate τ^{-1} from the metastable hollow sites, derived from fitting the non-Bravais triple jumps model at different temperatures assuming a constant site energy difference ΔE and survival probability s as given at $T_s = 350\,\text{K}$ in Table 6.4.

Table 6.5: Activation energy and prefactor derived from the temperature-dependent data cast as $\alpha(T)$ and $\tau(T)$, as shown in Figure 6.31. The uncertainties indicated are 66% confidence intervals from the Arrhenius law fits. The 400 K datum is excluded from the fits due to the compromised surface quality during the measurement. In general the Arrhenius representation $\ln(\Gamma)(1/T)$ is expected to have a curved form over a wide temperature range, but over the limited temperature range of the measurements an effective activated rate law holds. The apparent activation energy is the local slope of the Arrhenius curve. The interpretation of the derived parameters will be discussed further in Section 6.4.6.

Isotope	**Rate measure**	**Activation energy (meV)**	**Prefactor (ps^{-1})**
H	$\alpha(T)$	116 ± 3	3.4 ± 0.4
D	$\alpha(T)$	124 ± 4	3.3 ± 0.4
H	$\tau^{-1}(T)$	93 ± 7	4.3 ± 1.0
D	$\tau^{-1}(T)$	104 ± 6	5.1 ± 1.0

nominally based on a direct calculation of $S(\Delta K, \Delta\omega)$ [45]. The theoretical predictions are focussed on the low temperature regime and the transition to deep tunneling. However, they overlap with the experimental data at $T = 250\,\mathrm{K}$ where the experimental dephasing rate is $0.015\,\mathrm{ps}^{-1}$. The published theoretical results (black circles) are compared with experimental data (blue) in Figure 6.32. The theoretical activation energy is implausibly low. In the semiclassical activated regime, the activation energy is mostly governed by the energy required to promote the diffusing particle from one of the low-lying bands (associated with ground state tunneling) to the lowest band with a significant bandwidth. In other words the hopping (or diffusion) rate is strongly suppressed by the fact that the diffusing particle spends only a small fraction of its time in mobile states. The treatment of the lowest energy bands in the published calculation [45] misses the dominant source of the activation energy. Preliminary calculations [310] in which the method is adjusted to take account of the energy gap from the lowest lying bands are shown on the same plot (black triangles), and show an activation energy in closer agreement with the experimental data. The discrepancy in the prefactor will not be pursued further here.

The experimental rates in the form of τ^{-1} can be compared with results from the thermodynamic rate method of Chapter 4 in much the same way as the Ru(0001) data was analysed in Section 6.3.7. Firstly, the site-levelling correction is applied to the DFT potential motivated by the experimentally determined site energy difference. The site energy difference before the experimentally-motivated adjustment is approximately 60 meV, whereas the experimental site energy difference determined by the Bayesian analysis in Section 6.4.5 was approximately 32 meV for both isotopes. A slightly lower site energy difference is consistent with some previous DFT calculations in the literature [311, 302, 301]. The hcp-bridge barrier predicted by

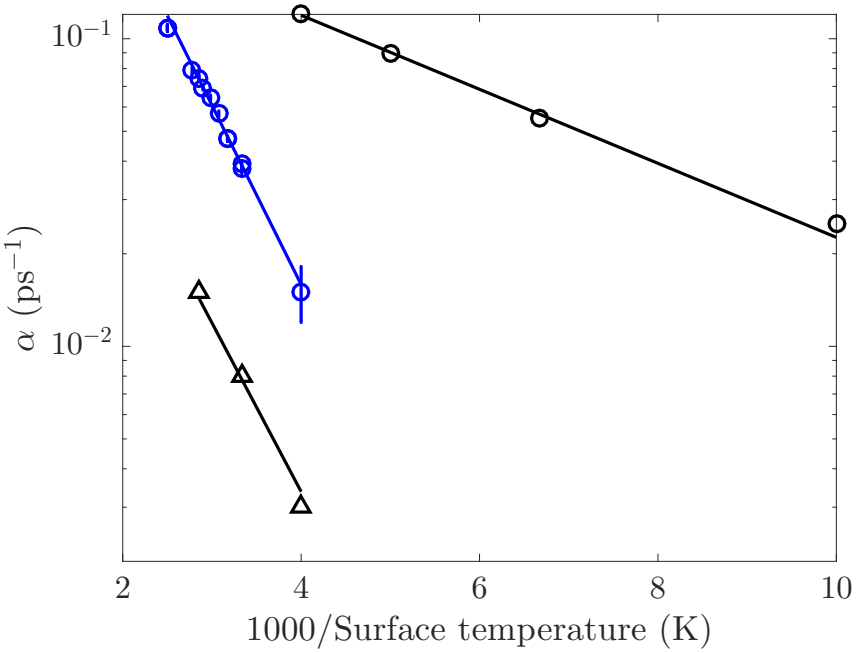

Figure 6.32: Temperature dependence of the dephasing rate for H/Pd(111) according to the Lorentzian broadening method [45] described in the main text (black circles), the Lorentzian broadening method adjusted [310] to incorporate the leading source of the activation energy in the experiment (black triangles) and the HeSE experimental data reproduced from Figure 6.31a. When the theoretical method is adjusted on physical grounds to accommodate the Boltzmann factor associated with excitation from the lowest lying bands to excited bands, the activation energy of the theoretical rate agrees with experiment. However, the absolute rate is significantly lower than the experimentally measured rate. Although the possibility of obtaining scattering functions for a dissipative system from the matrix elements in the closed system modified by a simple broadening is an intriguing direction of enquiry, the current ability of the method to quantitatively predict adsorbate hopping rates appears to be limited. The method will not be analysed further in the present work.

Table 6.6: Effective activation energy of the rate $\tau^{-1}(T)$ calculated from the Wolynes model, using the one-dimensional site-levelled transition path. The classical activation energy is 140 meV. The effective activation energy is significantly reduced for both isotopes, and is significantly smaller for H than D, in agreement with the trend in the experimental values reproduced from Table 6.5. There is a small but systematic discrepancy in the apparent activation energy of about 15 meV, which could originate in the original potential, the site-levelling correction and neglected zero-point energy corrections. The small overall discrepancy of the energetics with experiment implies that the errors in those separate sources are either small or compensating.

Isotope	E_A **(Theory)**	E_A **(Expt)**
H	108	93 ± 7
D	123	104 ± 6

those calculations lies in the range $90 - 110$ meV, whereas after applying the site-levelling correction to the PES in Section 6.2 the classical barrier to escape from bridge sites is approximately 140 meV. However, the activation energies calculated from the local gradient of the semiclassical Wolynes rate formula (Section 4.5.1) in the experimental temperature range $300\,\mathrm{K} \leq T_s \leq 350\,\mathrm{K}$ are significantly lower than the classical barrier. The effective activation energies are shown in Table 6.6.

As expected from previous HeSE experiments, and the theoretical discussion in Section 6.3.7, the absolute rate computed from the Wolynes model at low friction is much higher than the experimental value. In Section 6.3.7, HREELS data from the literature was used to argue that the friction cannot be greater than $10\,\mathrm{ps}^{-1}$, and is more likely $\mathcal{O}(4)\,\mathrm{ps}^{-1}$. The analogous HREELS data is not available for H/Pd(111). However, it would be surprising if the friction was enormously different on Pd(111). In a theoretical study [312], electronically-induced H-atom transition rates between different vibrational states on the surface have been calculated using numerical nuclear eigenstates and a jellium model for the electron gas. The typical transition rates are around $2\,\mathrm{ps}^{-1}$, which qualitatively supports the assumption of a similar friction for Pd(111) as for Ru(0001). As in the case of Ru(0001), the corollary is that the experimental rate is far below the theoretical TST rate due to low friction, as further evidenced by the multiple jumps required to fit the data. As further evidence that a low friction suppresses the rate, Figure 6.33 shows the escape rate and survival probability derived from classical simulations on the D/Pd(111) potential energy surface at 350 K. The rate and survival probability are consistent with a friction in the range of $2 - 3\,\mathrm{ps}^{-1}$. The experimental system does not obey classical mechanics, but for deuterium at 350 K the difference between the classical TST rate and the quantum TST rate is minor, so classical mechanics is likely to give a reasonable estimate of the rate as a function of the friction.

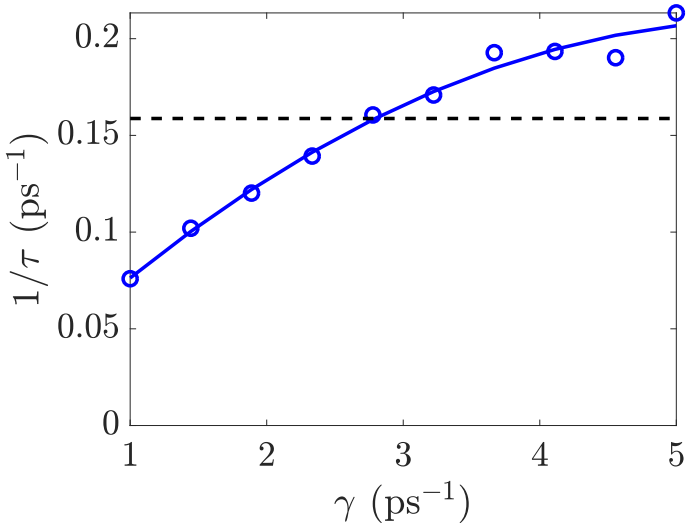

(a) γ-dependence of τ^{-1} in classical D/Pd(111) simulations.

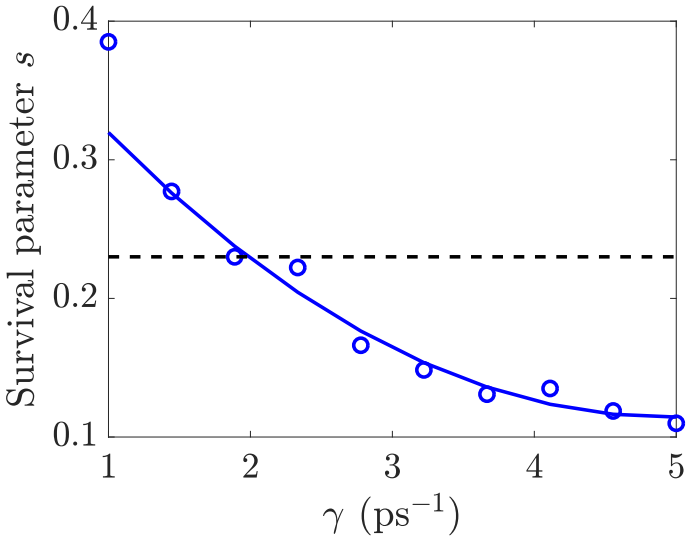

(b) γ-dependence of the survival parameter s.

Figure 6.33: Dependence of the inverse residence time of D/Pd(111), computed from classical Langevin simulations at $T_s = 350\,\mathrm{K}$ on the two-dimensional adjusted first-principles potential, with a timestep of 0.5 fs for 100 independent runs of length 1000 ps. The three-dimensional potential was minimized in z and then adjusted using the site-levelling operation (Section 4.5.5) to produce a fcc/hcp site energy difference of 30 meV as implied by the experimental data. Solid blue lines indicate the trends in the simulation results. τ and s were fitted using the same Bayesian method applied to the experimental data. The experimental values of τ and s are overlaid as dashed lines.

A feature of the Pd(111) data which was not seen for Ru(0001) is the significantly lower proportion of multiple jumps for D compared to H. It is straightforward to show within the Caldeira-Leggett model of Sections 3 and 4 that the isotopic dependence of a Langevin friction is $\gamma_H = 2\gamma_D$ (for example, that constraint was used in the published analysis of H/Pt(111) and D/Pt(111) rates [43]). In other words, if the same Caldeira-Leggett Hamiltonian 4.12 applies to both isotopes with the only change being the isotopic mass, then classically H and D obey precisely the same GLE except for the scaling of the friction kernel. However, it is possible that the rate of energy exchange [1] between adsorbate and surface does not follow the same isotopic scaling, if for example the cutoff frequency ω_c of the friction kernel (Section 3.2) is comparable to, or less than, the vibration frequencies in adsorption wells. Within the Caldeira-Leggett Hamiltonian approach, the cutoff frequency does not scale with isotopic mass, but the vibrational frequencies (or in the bandstructure picture, inter-band separation) reduce with increasing mass, and therefore the rate of energy exchange (rate of inter-band transitions) could be faster for D than H even though the Langevin friction coefficient is lower.

6.4.7 Conclusions

The first HeSE measurements of H and D diffusion on Pd(111) are presented. The data were largely recorded in an overpressure regime at elevated temperature $300\,\mathrm{K} \leq T_s \leq 400\,\mathrm{K}$. A Bayesian analysis of H data at 350 K indicates a mean residence time of $\tau = 4.9 \pm 0.5\,\mathrm{ps}$ in hcp sites, a site energy difference of 32 ± 2 meV between fcc and hcp sites, and multiple jumps occurring with a long-jump survival ratio of 0.4. The equivalent analysis of the D data finds the same site energy difference, a residence time $\tau = 6.3 \pm 0.3\,\mathrm{ps}$, and a lower survival ratio $s = 0.2$, suggestive of more effective frictional coupling to the surface for D, which was a phenomenon not apparent in the Ru(0001) data. Comparison of the temperature-dependent residence time with semiclassical rate calculations using the first principles PES of Section 6.2 suggests a low friction regime. Separately, a dispersive inelastic feature is observable in the data in the range $0 \lesssim \Delta K \lesssim 1.5\,\mathrm{\AA}^{-1}$ whose frequency is largely consistent with the theoretical dispersion of the Rayleigh mode.

There are some obvious directions for further work on the system. It would be desirable to perform measurements at lower temperatures. In order to do so, the source of the contamination present at low temperatures should be more thoroughly characterized so that it can be eliminated, for example by reduction of the trace CO background pressure or extensive bulk cleaning of the sample. A serious study

[1] As distinct from γ, which is a parameter appearing in the GLE and not an energy exchange rate *per se*

of the surface phonons would benefit from measuring the polarization along a more favourable tilted projection, and from performing measurements of the perfectly clean surface as well as the partially hydrogen-covered surface.

6.5 Diffusion of hydrogen on Cu(111)

6.5.1 Background

The adsorption and structure of hydrogen on Cu(111) has been studied with a wide range of techniques. Although some aspects of the system are well established, many hard numbers remain unclear or controversial. In the present work we are concerned with the behaviour of chemisorbed hydrogen. Ambient molecular hydrogen adsorbs at a negligibly low rate [313], due to a high dissociation energy barrier. The barrier is given by state of-the-art Diffusion Monte Carlo methods as 560 ± 40meV [314], in reasonable agreement with semi-empirical density functional theory calculations [315]. Dissociation can therefore be enhanced by using an incident beam of high kinetic energy, as demonstrated by a number of molecular beam studies [316, 317]. Alternatively, atomic hydrogen can be introduced directly to the surface via cracking methods. The dosing method affects the state of the surface at saturation, as evidenced by variation in the flash desorption spectra taken after dosing with atomic hydrogen as opposed to a molecular beam [316, 318]. It is well established that incident hydrogen atoms can efficiently abstract atoms already chemisorbed on the surface [319] and it has been shown that the abstraction process leads to a reduced saturation coverage compared to dosing via high-energy molecular species, because of the adsorption/abstraction equilibrium [318]. The saturation coverage after dosing atomic H, measured by integration of the portion of flash desorption spectra assigned to surface species, has been determined as $\theta_{sat} = 0.34\,\mathrm{ML}$ [318], where 1 ML means one H atom per surface Cu atom. The value 0.34 ML is in contrast to an earlier determination by nuclear reactive analysis (NRA) for D adsorption [320]. The discrepancy could be attributed to the acknowledged depth-insensitivity of NRA, but the qualitative form of the desorption spectra at low temperatures was quite different in each case [320, 318], implying that the precise conditions under which dosing was carried out likely played a role in the discrepancy too.

Although the absolute coverage should be treated with scepticism, Lee *et al*'s combined NRA/LEED study [320] at least tells us what to expect in terms of the development of surface structure with increasing relative coverage. When dosing at a surface temperature of 100 K, the first ordered superstructure to develop has a (2×2) LEED pattern, nominally at a coverage of 0.5 ML. Upon further exposure,

a mixture of (2×2) and (3×3) patterns were reported, and at saturation only the (3×3) pattern was reported. No changes were seen upon annealing to 230 K and cooling, suggesting that the structures formed when dosing at 120 K are the thermodynamically stable ones. That conclusion is again subject to disagreement. Earlier LEED measurements [321] showed that the structure of the saturated surface prepared at 150 K changes when modestly annealed to 186 K. The isotope used could be a factor in the disagreement.

More recently, helium atom scattering (HAS) methods have been applied to the system. Compared to LEED, HAS provides a complementary view of hydrogen chemisorption systems because of its delicacy, surface specificity, and significant hydrogen cross-section. In the first HAS investigation of the system, the helium diffraction patterns after dosing at 130 K were found to be consistent with LEED results, but the behaviour of the helium specular reflected intensity during desorption indicated that subsurface sites are more stable than surface sites [74]. The conclusion about subsurface stability has not been supported by theoretical investigations [304, 322, 323], but has been supported by further HAS data [324] in which the loss of H atoms from the surface at $210 - 245$ K was shown to follow first-order kinetics, in contrast to the second-order kinetics of associative desorption.

Previous published experimental data concerning H/Cu(111) surface diffusion is either macroscopic [325] or microscopic but at very low temperatures [154]. The macroscopic diffusion rates are not relevant here as they are limited by the rate of crossing step edges, which we do not measure. In contrast, high-rate STM imaging has been used to measure the jump diffusion of H and D atoms on terraces, during the self-assembly of hydrogen clusters [154]. H/Cu(111) is one of a handful of jump diffusion systems for which both STM and HeSE data is available. For systems where the jump rate is well described by a single activated rate law which joins the STM and HeSE regimes, HeSE measurements have been valuable in providing accurate measurements of the rate prefactor [250]. However, comparison of STM and HeSE data is far less straightforward when the two regimes are separated by up to two regime changes, from activated diffusion to inelastic tunneling to elastic tunneling, as described in Section 6.4.1.

By definition, jump dynamics take place between preferred adsorption sites. Previous DFT calculations of the H/Cu(111) potential energy landscape [322, 283, 154] unanimously favour adsorption at threefold hollow sites, with a diffusion barrier in the region of 130 meV over bridge sites. The relative stability ΔE of the inequivalent fcc and hcp hollow sites has important consequences for the dynamics. Independent DFT calculations from the literature do not provide a consistent estimate of ΔE, but suggest that it could be small, of the order of $k_B T$ or less at

200 K. Therefore both hollow sites can potentially play a role in the jump dynamics. By allowing for a site energy difference ΔE as a fitting parameter in the analysis of spin echo diffusion data, fcc/hcp site energy differences have previously been determined to high accuracy within HeSE, exemplified by published results [23, 89] and other HeSE studies of hydrogen diffusion [36, 84]. For H/Cu(111), by analysing effective single-exponential dephasing rates over the experimental t_{SE} window, the diffusion was found to be consistent with hops between approximately degenerate hollow sites ($\Delta E = 0$) with a small fraction of multiple jumps. Expressed in terms of the survival parameter s describing the jump distribution, the HeSE data implied $s = 0.075$. The new features of the data and analysis presented here are a lower coverage, the application of the Bayesian analysis method (Section 2.2.6) and comparison with quantum rate theory making use of the first-principles potential energy surface.

6.5.1.1 Recent background: prior HeSE

Figure 6.34 shows the changes in specular and diffracted intensities upon exposure of the clean Cu(111) surface to atomic hydrogen at 200 K [84]. The curves are arbitrarily scaled for clarity. From the top curve downwards at 400 L, the peaks monitored are $n = \frac{1}{2}$ (green), $n = \frac{1}{3}$ (cyan), $n = 1$ (red) and specular (blue) respectively. The specular intensity falls monotonically from its initial value of I_0 to about $I_0/10$, and levels off at about 300 L. The fractional order diffraction peaks increase in intensity immediately upon exposure, which is expected because of the increased diffuse scattering from a disordered H overlayer. Meanwhile, the $n = 1$ peak rises only after a small initial exposure. The late rise of the $n = 1$ intensity compared to the fractional order intensities is not surprising because the diffuse scattering amplitude at the $n = 1$ position is much lower, and the effect of the hydrogen initially deposited is to reduce the degree of surface order, which will reduce the intensity of the $n = 1$ peak until the deposited hydrogen starts to assemble itself into ordered structures. At the largest exposures there is a very slow decline in the specular and $n = 1$ intensities which could be caused by a slow migration of some hydrogen to the subsurface region, reducing the degree of surface order. The fractional order intensities, however, fully saturate.

The full deposition curve can be used to derive an upper bound on the coverage at sub-saturation doses. The highest possible saturation coverage known from the literature is 0.67 ML. During dosing, the specular intensity decreases monotonically from I_0 to about $I_0/10$. Assuming that the decay of specular is described by the exponential function

$$I(\theta) = I_0 e^{-a\theta}\,, \tag{6.8}$$

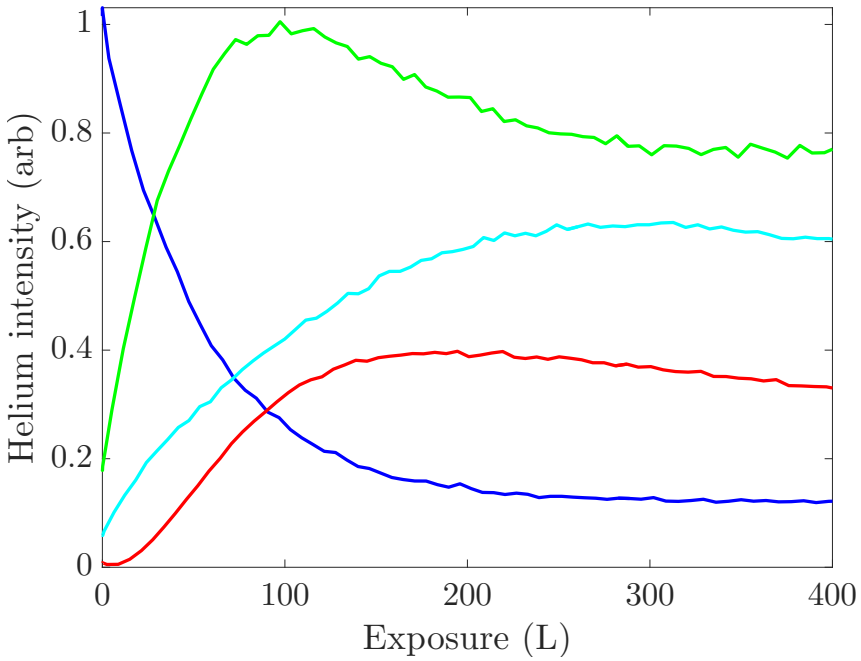

Figure 6.34: Variation in specular reflected ^{3}He intensity, and intensity of selected diffraction peaks along the $< 1, 1 >$ direction, as a function of exposure of Cu(111) to molecular hydrogen. The exposure to atomic hydrogen depends on the cracking efficiency of the nearby tungsten cracking filament, and is assumed to be linearly proportional to the molecular exposure. The result for specular intensity has been presented in prior work [84]; the diffraction peak uptakes were recorded as part of the same measurement series. The exposure is given in L where $1L = 1.33 \times 10^{-6}$mbar·s. Adsorption is dominated by the uptake of atomic H produced by a tungsten cracking filament. The form of the uptake curves is discussed in the main text.

and associating the coverage $\theta = 0.67$ with $I = I_0/10$ gives $a \approx 3.44$, and

$$\theta \leq \frac{\ln(I/I_0)}{3.44}\,. \tag{6.9}$$

The estimate is an upper bound for three reasons. Firstly, the saturation coverage of 0.67 ML from the literature was measured using a method that does not distinguish between the surface and near-surface regions [320]. Secondly, the surface structure at saturation does not consist of independent scatters but ordered structures, which increases the reflectivity compared to the exponential extrapolation of the initial deposition of disordered scatterers. Thirdly, the helium diffraction scans of the surface after dosing at 200 K (Figure 6.35) show both two- and three-fold structure, whereas the completely saturated surface is expected to show only threefold structure, and therefore the surface is not truly saturated after dosing at 200 K even though the specular intensity does not change appreciably with further dosing. From the upper bound on coverage we can conclude that when $I = I_0/2$, $\theta \leq 0.2$ and when $I = 3I_0/4$, $\theta \leq 0.08$.

Figure 6.35 shows the helium diffraction pattern of the surface after dosing to saturation (exposure $>$ 400 L) at 200 K, along the two high-symmetry azimuths $< 1,1 >$ (right) and $< 1,0 >$ (left). The upper scans (blue) displaying sharp features were recorded with the surface cooled to 125 K after dosing was completed, and held at that lower temperature. The lower scans (red) displaying highly broadened features were taken with the surface held at the dosing temperature of 200 K. The prominent features are labelled **A**-**H**. The mixture of $\frac{1}{2}$ and $\frac{1}{3}$ order structural features is expected based on previous structural studies. However, the fact that both two-fold and three-fold structural features are present implies that even after $>$ 400 L dosing the surface is not completely saturated, because then only threefold structure would be expected [320].

6.5.2 Experimental methods

The single crystal sample was prepared as described in 2.1.3, giving a clean surface with a typical reflectivity of 50%. Molecular hydrogen (Air Liquide, 99.999 % pure) was introduced into the clean vacuum via a leak valve, with the surface held at 200 K. The dosing pressure was varied between 1×10^{-8} mbar and 3×10^{-7}mbar (uncorrected extractor gauge reading) depending on the intended total exposure. Atomic hydrogen was generated during dosing via a tungsten cracking filament in the scattering chamber, approximately 130 mm from the sample with line of sight to the surface and run at 1000 K.

Dynamics measurements were interleaved with structural measurements, so the sample preparation and dosing methods described in Section 6.5.2 also apply here. Doses of different hydrogen isotopes were separated by at least 24 hours, annealing the surface to 800 K, and flushing the dosing lines with the new isotope at least once.

6.5.3 Islanding

Previous published studies of the H/Cu(111) phase diagram, whether carried out with LEED [320] or HAS [74], do not make explicit reference to coexistence of islands and a mobile lattice gas. The diffracted intensity from small hydrogen islands will be lower than from long-range hydrogen overlayers, and will be detected more readily within HAS than within LEED. However, ^{3}He diffraction measurements at a hydrogen coverage corresponding to $I_0/5$ showed broad features that correspond to the two- and three-fold features seen near saturation [84]. Recently the growth of hydrogen clusters has been observed with STM in real time, under conditions

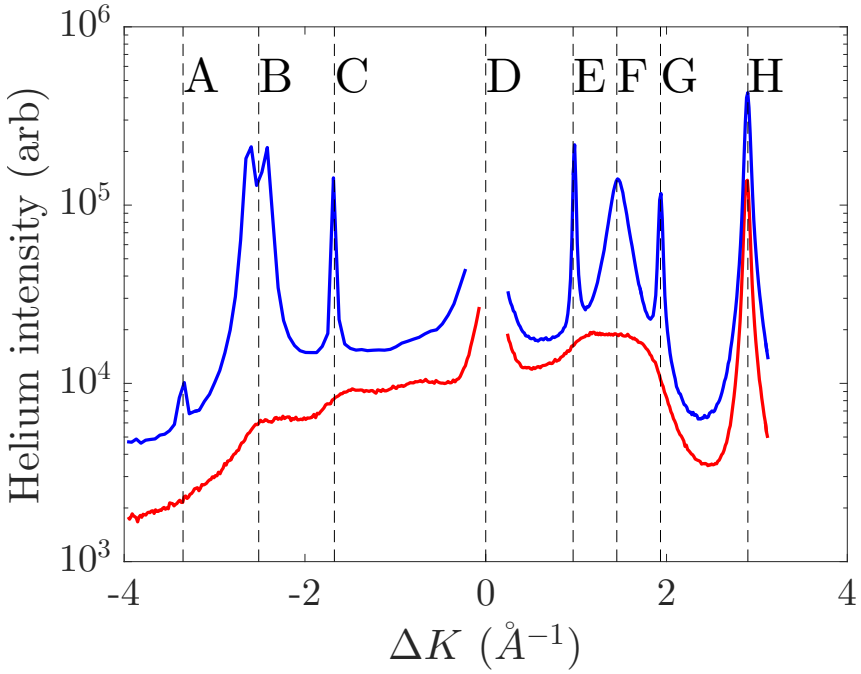

Figure 6.35: Helium diffraction patterns of Cu(111) along $< 1, 1 >$ (right) and $< 1, 0 >$ (left) after dosing atomic hydrogen to saturation ($> 400\,\mathrm{L}$ molecular exposure) at deposition temperature $T = 200\,\mathrm{K}$ [84]. Vertical dashed lines indicate the position of key diffraction features. The upper scans (blue) displaying sharp features was taken with the surface cooled to 125 K after dosing was completed, and held at that lower temperature. The lower scans (red) displaying highly broadened features were taken with the surface held at the dosing temperature of 200 K. The prominent features are labelled **A**-**H**. **A**,**C**, **E** and **G** are sharp $n = \frac{k}{3}$ features. **B** and **F** are $n = \frac{1}{2}$ features. Along $< 1, 0 >$ the half-order feature has a distinctive split structure, as seen previously with LEED [321]. The split peak could be due to a long-range superstructure which can be described in terms of antiphase domains of locally twofold structure. **D** and **H** are the specular and $n = 1$ peaks, which are present on the clean surface. Due to the small corrugation of the He-Cu(111) interaction potential, on the clean surface **D** is many orders of magnitude larger than **G**. After dosing hydrogen to saturation, **D** loses around 90 % of its intensity to diffuse scattering and diffraction, while **H** is enhanced by a factor of 50 due to increased corrugation of the hydrogen-covered surface. **H** contains contributions from all structures commensurate with the clean surface. The temperature dependence of **H** is markedly different to the behaviour of the fractional order peaks. **H** remains bright and sharp even when the fractional order features are enormously broadened.

($T_s = 5\,\mathrm{K}$) where the establishment of equilibrium could take a very long time [154]. In contrast, we would expect that at medium to low coverage, and temperatures of 125 K and above, equilibrium within the overlayer is established rapidly, at least within terraces. The existence of small islands in equilibrium with a lattice gas places certain constraints on the inter-adsorbate interactions, which must have an attractive region at short range but island ripening must be suppressed by a long range repulsion. Although H-H interactions are not guaranteed to be well described by a sum of pairwise potentials, qualitatively the form of the interaction just described is consistent with the attractive-repulsive interaction proposed in the STM study [154] on the basis of DFT calculations and observed dimer motion.

Figure 6.36 shows helium diffraction patterns after dosing to coverages less than saturation, and at different temperatures, along the two high-symmetry azimuths $< 1,1 >$ (right) and $< 1,0 >$ (left). The positions of the features observed at high coverage are shown so that they can be correlated with the broad features seen at low coverage. The scans are represented in clusters of equal exposure and varying temperature, with the highest exposures shown uppermost. The top scan along $< 1,0 >$ was taken at a coverage $I_0/5$ and a temperature of 125 K, and has been presented in prior work [84]. The top scans along $< 1,1 >$ were taken at $I_0/4$ and at temperatures $150 - 250\,\mathrm{K}$. The lowest pair of scans along $< 1,1 >$ correspond to a coverage of $3I_0/4$ and temperatures of 150 K and 200 K. The general trend to emerge is that structural features smoothly shrink and broaden with either increasing temperature or decreasing coverage, which suggests that island size is a smooth function of θ and T. Meanwhile, the coexistence of a mobile lattice gas is demonstrated by interleaved surface diffusion measurements (polarization scans).

The structural measurements were not affected by desorption or diffusion into the subsurface region, as evidenced by repeat measurements. However, in principle we can only ever establish a quasi-equilibrium with respect to desorption or diffusion into the subsurface and bulk. At 250 K it was possible to perform dynamics measurements for several hours from a starting coverage of $I_0/4$, although by the end the coverage was reduced to around $I_0/2$. It is not possible to say from our measurements whether the hydrogen was lost to the vacuum or to the subsurface. Either way, the long-term presence of surface hydrogen at 250 K sharply contradicts previous HAS studies [74],[324] which suggested that adsorbed H atoms rapidly migrate to the subsurface by 250 K and become invisible to the helium probe. The disagreement could perhaps be related to a difference in the density and nature of surface defects.

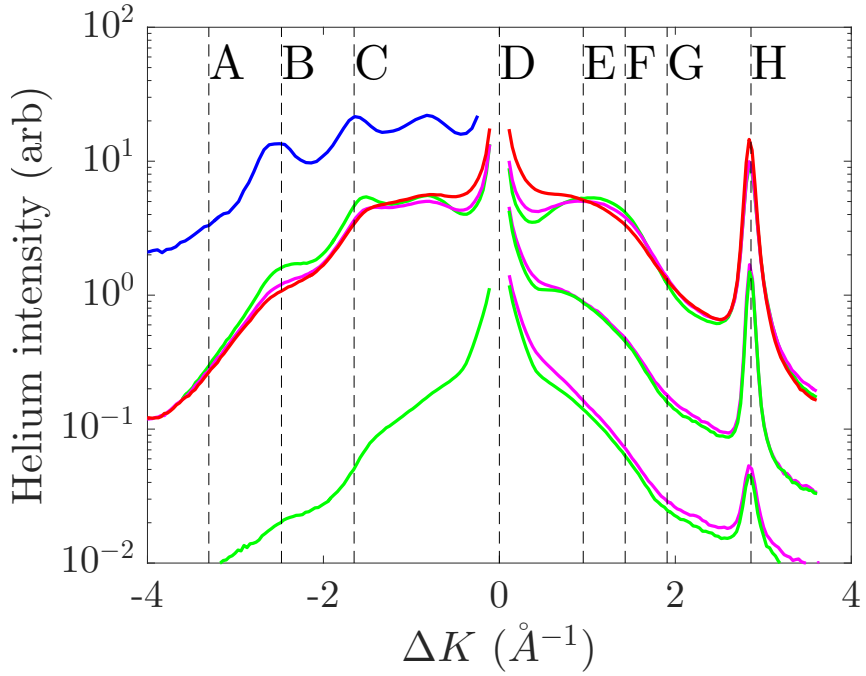

Figure 6.36: Helium diffraction patterns of Cu(111) along $< 1,1 >$ (right) and $< 1,0 >$ (left) after dosing atomic hydrogen at a deposition temperature of 200 K to less than saturation. The scans are given an arbitrary scaling for clarity, and clustered according to coverage. The position of the features **A**-**H** of Figure 6.35 are shown so that they can be correlated with the position of broad features at low coverage. The results will be discussed from highest to lowest coverage, top to bottom on the plot. The blue curve was recorded at a coverage of $I_0/5$ and $T_s = 125$ K [84] and shows the most well-defined features as it corresponds to the highest coverage and lowest temperature. The rest of the scans are new data, all at lower coverage. The topmost cluster of scans shown along $< 1,1 >$ was recorded at $I_0/4$ and $T_s = 150$ K (green), 200 K (magenta) and 250 K (blue). All three scans show a strong first order diffraction peak **H**. A broad feature is spread over the range occupied by features **E**-**G** in Figure 6.35. The corresponding set of scans along $< 1,0 >$ show broad peaks at **B** and **C** which are more well defined at lower temperatures. The next pair of scans down along $< 1,1 >$ (150 K green, 200 K magenta) were taken at $I_0/2$ and show the same broad feature seen at $I_0/4$. Finally, even at the lowest coverage shown of $3I_0/4$, diffuse features are present in the same locations, suggesting that islanding occurs even at low coverage. The formation of islands at low coverages is consistent with the monotonic nature of the uptake curves in Figure 6.34.

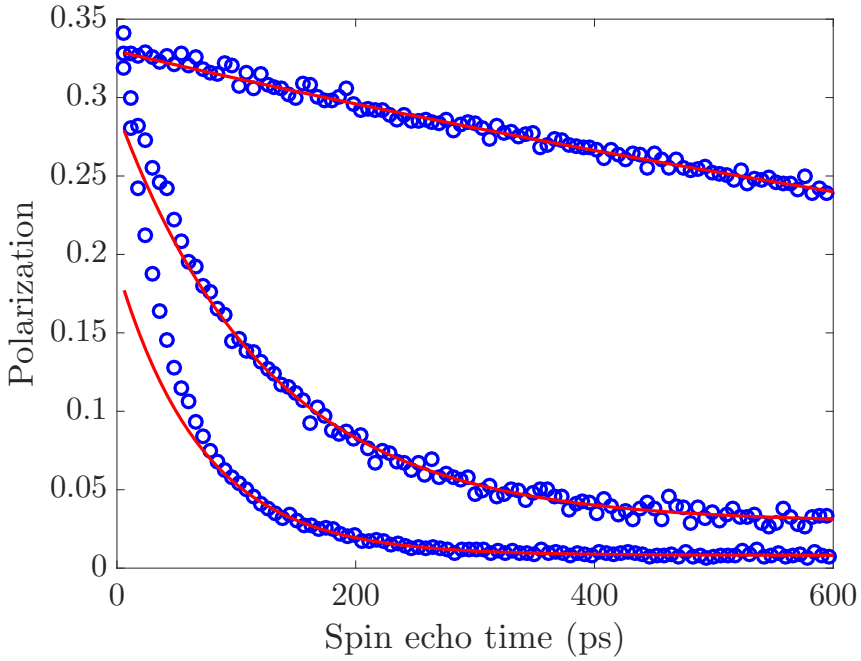

Figure 6.37: Typical polarization scans of the Cu(111) surface after dosing atomic hydrogen to $I = 3I_0/4$ at a deposition temperature $T = 200\,\mathrm{K}$, corresponding to a coverage of $\theta \leq 0.08$. The polarization scans were measured at $T_s = 150\,\mathrm{K}$, $200\,\mathrm{K}$ and $250\,\mathrm{K}$. The scans at $200\,\mathrm{K}$ and $250\,\mathrm{K}$ are qualitatively similar in that they possess a well-defined curvature and static level. The scan at $150\,\mathrm{K}$ is effectively straight on the measurement timescale. Each scan contains 101 points, uniformly sampled in t_{SE} with a sampling interval of approximately 6 ps. A single exponential fit for $t_{SE} > 50\,\mathrm{ps}$ is overlaid which reveals a systematic second exponential component due to the non-Bravais hopping dynamics.

6.5.4 Nature of jump dynamics

Figure 6.37 shows typical polarization scans near $\Delta K = 1.5\,\mathrm{Å}^{-1}$ along $< 1, 1 >$ at $250\,\mathrm{K}$, $200\,\mathrm{K}$ and $150\,\mathrm{K}$. Each scan contains 101 points, uniformly sampled in t_{SE} with a sampling interval of approximately 6 ps. Exponential fits for $t_{SE} > 100\,\mathrm{ps}$ are overlaid as solid red curves, which shows a strong systematic deviation at shorter t_{SE}, characteristic of the underlying non-Bravais hopping model with a small site energy difference. As expected in the quantum activated regime, the decay rate is strongly temperature dependent.

Although some scans show clear double-exponential behaviour, reliable double decay rates cannot be systematically determined for arbitrary ΔK. Therefore, as with Pd(111) in Section 6.4.4 I will present the dynamics data in terms of the slowest measurable decay, and then a Bayesian analysis (Section 2.2.6) which gives the best fit parameters of the non-Bravais hollow-hollow triple jumps model. Figure 6.38 shows the dynamics data analysed in terms of the decay rate $\alpha(\Delta K)$ of the slowest decaying component of the ISF. The apparent difference in phenomenology in the

Table 6.7: Best fit parameters of the non-Bravais, triple jumps model of Section 2.2.1 to H/Cu(111) and D/Cu(111) dynamics at 200 K and a coverage of $3I_0/4$. The site energy difference is given in terms of the concentration ratio λ between sublattices, by $\Delta E = k_B T \ln(\lambda)$. The relatively small site energy difference ΔE, compared to the result for H/Pd(111) with the same surface structure (Sections 6.4) is consistent with the trend seen in DFT calculations, and can be loosely justified in terms of the size of the ion cores in the substrate compared to the lattice parameter, i.e. the relatively small core radius in Cu means that the second and third Cu layers at the close-packed surface have a weaker localized effect on the adsorbate, resulting in a small the fcc/hcp site energy difference [304]. The survival parameter is of the magnitude expected on the basis of the Ru and Pd measurements earlier in the chapter, assuming a similar strength of friction. It is also approximately consistent with the value obtained in the previous HeSE study by inspection of the effective $\alpha(\Delta K)$ over the finite experimental t_{SE} window. The friction and the absolute hopping rates τ^{-1} will be discussed further in Section 6.5.6.

Parameter	τ **(ps)**	λ	ΔE **(meV)**	**s**
H, 200 K	60 ± 4	2.3 ± 0.18	14 ± 2	0.11 ± 0.02
D, 200 K	129 ± 6	2.5 ± 0.14	16 ± 2	0.14 ± 0.01

two plots is discussed in the figure caption.

The low coverage ($3I_0/4$) data at $T_s = 200$ K has been analysed in terms of the hollow-hollow triple jump model of Section 2.2.1, using the Bayesian fitting method of Section 2.2.6. The best fit parameters at $T_s = 200$ K for H and D are given in Table 6.7. The residence time of H atoms is significantly shorter than that of D atoms, as expected. The site energy difference ΔE is calculated via $\Delta E = k_B T \ln(\lambda)$. It is reasonable for ΔE to take lightly different values for H and D.

6.5.5 Temperature dependence of jump dynamics

At each temperature, a single ISF at $\Delta K = 1.2\,\text{Å}^{-1}$ along $< 1, 1 >$ was measured, and fitted assuming that only τ varies over the temperature range concerned, while s is constant and λ is extrapolated using $\lambda = \exp(\Delta E/k_B T)$. Although setting s constant is an approximation, it is reasonable to expect the vast majority of the temperature dependence of the dynamics to be associated with the overall escape rate $\Gamma(T) = 1/\tau(T)$, rather than the jump distribution (the same procedure was applied in Sections 6.3.5, 6.4.5, 5.1.2.4). Figure 6.39 shows the temperature dependence of the escape rate $\Gamma(T)$ between 140 K and 250 K for both isotopes, measured at the same low coverage of $3I_0/4$ that was analysed to obtain τ, λ and s at $T_s = 200$ K. The fits shown as solid lines are to an effective activated rate law

$$\Gamma(T) = \Gamma_0 e^{-E_a/k_B T}\,. \tag{6.10}$$

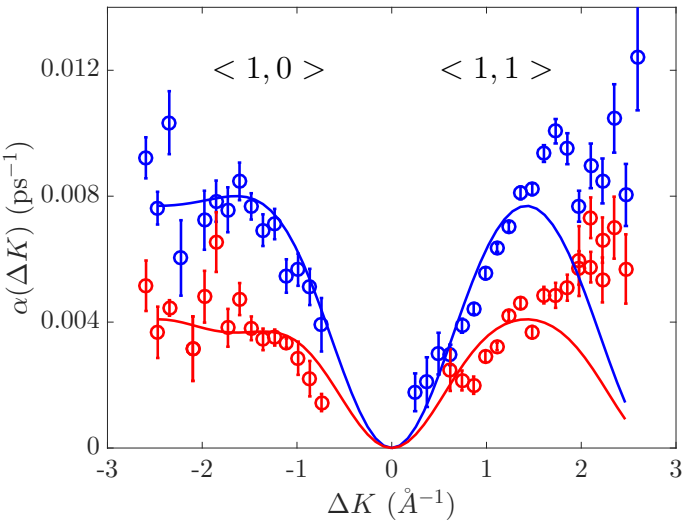

(a) H/Cu(111) $\alpha(\Delta K)$ at low coverage at 200 K.

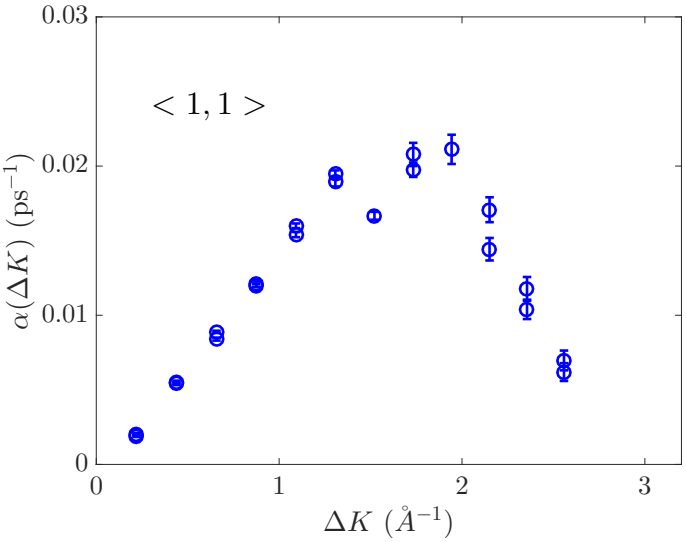

(b) H/Cu(111) $\alpha(\Delta K)$ at intermediate coverage at 250 K.

Figure 6.38: Decay rates $\alpha(\Delta K)$ obtained by fitting H/Cu(111) and D/Cu(111) polarization scans from $t_{SE} > 50$ ps. The measurements represented in Figure 6.38a were taken at low coverage $I = 3I_0/4$. H measurements are shown in blue and D measurements in red. The best fit to the Chudley-Elliott model (Section 2.2.1) is overlaid to guide the eye. Even though the measurements extend to the first diffraction condition along $< 1, 1 >$, the decay rate of the slowest component extracted by the fit does not return towards the origin, suggesting that the amplitude of that component is too small to be reliably distinguished. Figure 6.38b shows the results of a measurement series starting at a higher coverage $I_0/4$. A better signal to noise was available because of the higher coverage giving more off-specular scattering, and also due to running the detector multiplier at a higher gain (Section 2.3). Under the conditions of Figure 6.38b a clear return of $\alpha(\Delta K)$ to the origin can be seen. During the measurement series, which took several hours, the coverage decreased from $I_0/4$ to $I_0/2$ as determined by the comparison of specular intensity at the start of the measurement, the end of the measurement, and after annealing the hydrogen from the surface. However, the measurements were performed in a random order and the repeat points show no significant change in the dynamical signatures.

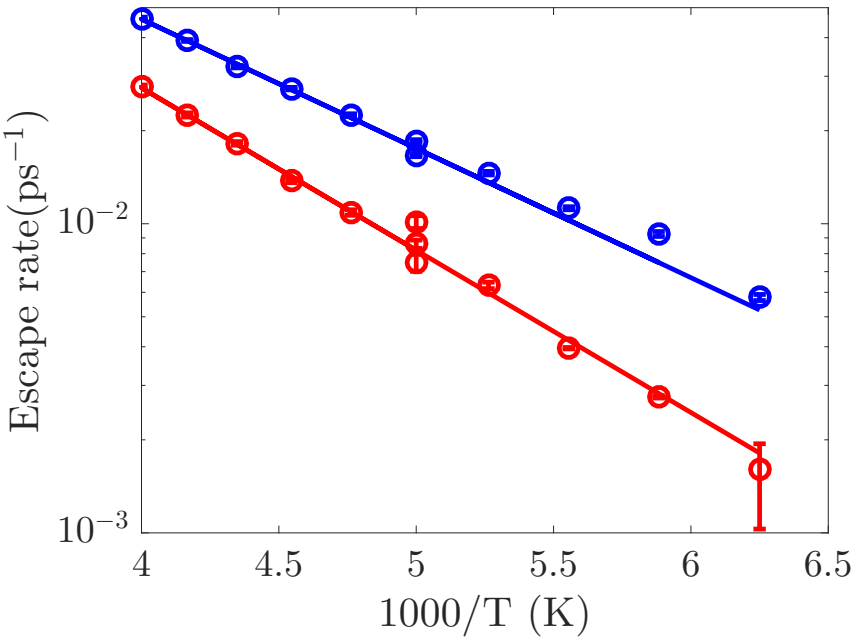

Figure 6.39: Temperature dependence of the escape rate, defined as $1/\tau$ where τ is the residence time of the jump model. The solid lines are a fit to the effective activated rate law 6.10. The effective activation energies are 83 ± 2 meV (H) and 105 ± 2 meV (D). In the quantum activated regime we expect the effective activation energy to be lower for H than for D, as seen for the Pd(111) data (Section 6.4.5). From the Wolynes formula the reduced effective activation energy is caused by the reduced local gradient of the Arrhenius plot induced by the temperature-dependent quantum prefactor, which is more significant for H than D over the same temperature range as illustrated in Figure 6.40. Alternatively, within the bandstructure approach to the quantum rate [36], the higher activation energy for D results because even though the first excited band is lower in energy, its mobility is very low so that promotion to the second excited band of even higher energy contributes heavily to the rate.

The fitting parameters are discussed in the Figure caption, and comparison with the theoretical absolute hopping rates is drawn in the following Section (6.5.6) in light of theoretical and experimental handles on the friction.

At lower temperatures still, we expect in principle to see a transition to deep tunneling as seen on Ru(0001), because the site energy difference ΔE between neighbouring inequivalent threefold sites is small. However, in the present case, at low temperatures it becomes impossible to reliably fit the lineshapes because the concentration of the mobile lattice gas is reduced as islands form.

6.5.6 Theoretical discussion

Figure 6.40 shows the quantum escape rate calculated using the one-dimensional bounce method of Chapter 4 applied to the first-principles potential energy surface

of Section 6.2. Above the crossover regime the method is equivalent to the Wolynes formula.

As for H/Ru(0001) and H/Pd(111), the large over-estimation of the semiclassical rate by the thermodynamic method can be assigned to low friction. The width of the parallel vibrational mode has been measured at low coverage within HREELS [274] and is substantially broader than the measurements discussed in Section 6.3.7. Applying the same analysis method (modelling the lineshape as the dynamical structure factor) therefore leads to a much higher friction of $\approx 15\,\mathrm{ps}^{-1}$. However, given the low temperature of the measurements (100 K), we know that hydrogen islands must be present on the surface, and so a substantial contribution to the measured broadening could arise from the distribution of different local environments. The parallel vibrational lineshape has also been measured at high coverage (3×3 structure) by infra-red absorption [326], with a fit to the lineshape producing a friction of $\mathcal{O}(1)\mathrm{ps}^{-1}$. From the theoretical side, using time-dependent density functional theory to model the response of the electron gas the friction acting on surface-perpendicular vibrations at the hcp hollow site has been computed as 0.8 ps [327]. The unanimous prediction is for electronic friction at the hollow sites to be much smaller than the hollow site vibrational frequencies, a situation which classically would place the jump dynamics in the low-friction, energy-diffusion limited regime. Therefore, H/Cu(111) provides a third example of a quantum diffusion system in which the hopping rate in the quantum activated regime is greatly reduced from its TST value by low friction.

6.5.7 Conclusions

At medium coverages, H/Cu(111) exhibits a coexistence phase in which islands equilibriate with a lattice gas. The islands have been observed by helium atom scattering (HAS) and their presence is deduced by correlating sharp features of the near-saturation H overlayer with broad features that weaken as the temperature increases and the coverage decreases. At surface temperatures $140\,\mathrm{K} \leq T_s \leq 250\,\mathrm{K}$, the diffusion mechanism for atoms in the lattice gas phase involves both fcc and hcp hollow sites which are symmetrically inequivalent. The hcp site is metastable by 15 meV. Bayesian analysis of H and D diffusion at low coverage ($\theta \leq 0.08\,\mathrm{ML}$) at $T_s = 200\,\mathrm{K}$ reveals a small but nonzero proportion of multiple jumps in the diffusion mechanism, parameterised by the triple jumps survival parameter (Section 2.2.1) $0.1 < s < 0.15$. The absolute hopping rate is much lower than predicted by the bounce method (Section 4.5.4) on a first-principles potential energy surface computed with density functional theory. The combination of multiple jumps and

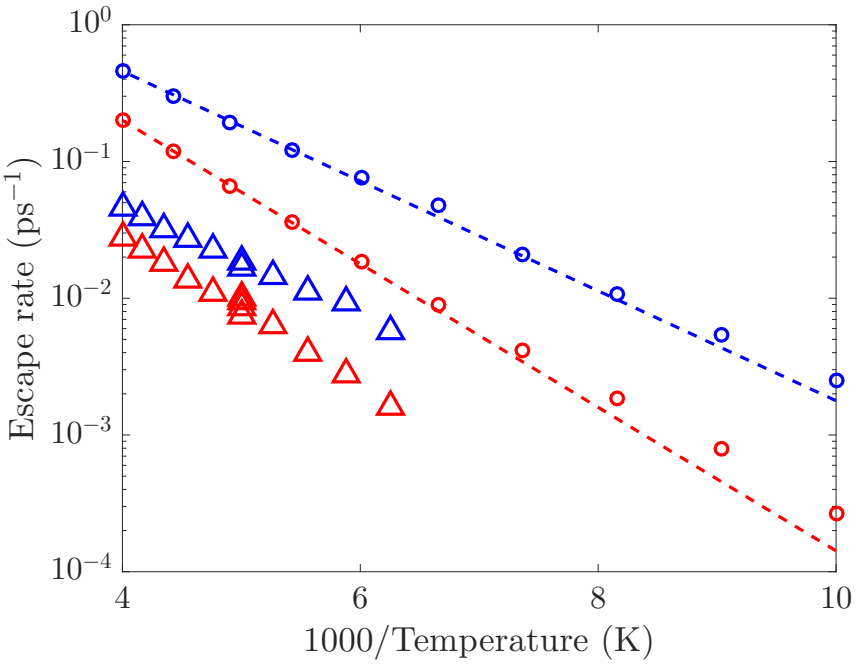

Figure 6.40: The thermal escape rate of a H atom (blue) or D atom (red) from the metastable hcp site on Cu(111), calculated by applying the bounce method of Chapter 4 applied to the first-principles potential energy surface of Section 6.2. The site energy difference of the raw first-principles potential (18 meV) is in good agreement with the experimental value derived in Section 6.5.4, and therefore no site-levelling operation is applied before performing the rate calculation. The rates shown are given at a friction of $1\,ps^{-1}$. The crossover temperature T_0 (Section 4.5.1) is 110 K (H) and 78 K (D). Far above the crossover temperature, the Wolynes formula overestimates the experimental rate (triangles) by an order of magnitude, consistent with the findings for Ru(0001) and Pd(111). The fit of the $T > 150$ theoretical data to the same effective rate law applied to the experimental data is shown as dashed lines. The classical barrier height is 128 meV, but the effective activation energies are 80 meV (H) and 104 meV (D), in remarkably good agreement with the experimental values (Figure 6.39). Therefore, although no zero-point energy correction has been applied to obtain the effective one-dimensional potential, the results suggest that zero-point effects are either insignificant or compensate a different source of error. The predicted deep tunneling rate at low friction (not shown on the plot) is $3 \times 10^{-3} ps^{-1}$, which suggests that deep tunneling would be easily detectable for H/Cu(111) if island formation at low temperatures was not an issue. It is possible that deep tunneling effects would be easily visible at higher absolute coverages, as long as the concentration of the lattice gas phase increases does not plateau too strongly as a function of the mean coverage.

low absolute hopping rate suggests that the jump dynamics are in a low-friction regime. The potential energy surface and the evidence for low friction together suggest that deep tunneling would be easily accessible if islanding did not occur at low temperatures.

6.6 Summary and outlook

The diffusion of chemisorbed atomic hydrogen has been measured on three close-packed hexagonal surfaces, Ru(0001), Pd(111) and Cu(111), with HeSE. Most of the dynamics are in the quantum activated regime, but the transition to deep tunneling is seen on Ru(0001) in agreement with prior data. The dynamics in the three systems have been analysed in terms of the fcc/hcp hollow non-Bravais jump model of Section 2.2.1. There is systematic evidence for multiple jumps in all cases. The absolute hopping rates have been modelled using the bounce method of Chapter 4, applied to the one-dimensional transition path between hcp and fcc sites on the first-principles potential energy surfaces computed with DFT. A frictional coupling γ in the region of $\mathcal{O}(1-5)\text{ps}^{-1}$ for all three systems is broadly consistent with the non-negligible fraction of multiple jumps, the absolute rates in the activated regime, the high tunneling rate observed for H/Ru(0001), and independent measures of the friction from the literature including HREELS measurements and first-principles calculations. The original tentative observations of fast D/Ru(0001) deep tunneling [35] which were a key motivating factor in performing the Ru(0001) experiments, have not been reproduced.

The picture provided by the analysis of three hydrogen diffusion systems on the same footing, in which a relatively low friction ($\gamma << \omega_0$) qualitatively explains a large amount of experimental data simultaneously, has a bearing on past and future measurements on other metallic surfaces. The original proposal of a high friction in H/Pt(111) diffusion [43] based on the Wolynes model, should be re-examined. By working with Pt(111) in the regime explored in Section 6.4 for Pd(111), at high temperatures with an overpressure of hydrogen maintaining a constant coverage, the relatively high fcc/hcp site energy difference on Pt(111) could be measured directly, and by applying the Bayesian method the jump distribution could then be inferred, which would reveal which of the diametrically opposed interpretations (low friction *vs* very high friction) applies to the system. Separately, recent experiments on D/Ni(111) in which H contamination was carefully considered and eliminated, showed fast deep tunneling [36], which remains an open theoretical puzzle. The lack of evidence for fast D tunneling on Ru(0001) suggests the fast tunneling result for D/Ni(111) might be facilitated by a qualitatively unexpected physical mechanism,

leading to a diffusion pathway on Ni(111) which is not captured by the standard "PES and friction" modelling used throughout the present Thesis.

Chapter 7

Outlook

7.1 Outlook

HERE I summarize what has been learned in Chapters 2-6, and discuss the future directions in which the work could be taken.

7.1.1 Instrumentation

In Chapter 2 I presented measurements of the efficiency, background and $\mathcal{O}(1)$ Hz signal-to-noise characteristics of the solenoidal detector on the Cambridge HeSE spectrometer. The measured ionisation efficiency $\eta = 2 \times 10^{-3}$ is consistent with the measurement at commission-time, and a 100× improvement on the previous (pre-2011) detector. The $m/z = 3$ background ion current of 2×10^{-14} A is a 10−fold improvement compared to the old design. The main components of detector noise are a constant term of electrical origin, a term originating in shot noise, and a term linear in the helium-3 signal with a signal-to-noise ratio of 1% when measuring with a 1 s integration time. Most of the data presented in Chapters 5-6 was limited in SNR by the linear term. In principle beam source fluctuations could be responsible, but the apparent m/z-dependence of the ultimate SNR when detecting the background gas (Section 2.3.2.2) suggests that the 1 % linear noise could well originate in the detector.

The 1% noise is an absolute limit on the SNR, no matter how high the signal. Because the 1% noise is the limiting factor for so many spectra its global effect on the average quality of data is enormous. If the linear noise originates in the detector, as suggested by the m/z-resolved measurements in the absence of a beam, then more detailed measurements on the isolated detector, including the frequency dependence

of the noise would shed further light on the origin. In the longer term, the transfer of developments in detector modelling and implementation from the ongoing helium microscope project to the spin echo spectrometer can be expected to lead to a more stable system with better sensitivity and fewer inefficiencies.

7.1.2 Classical molecular dynamics

In Chapter 3 I derived analytical expressions for the intermediate scattering function (ISF) of an adsorbate on a flat surface subject to the generalized Langevin equation (GLE) with exponential memory friction. The results contribute to the understanding of the HeSE lineshape at short times and the relative amplitudes of different components in the lineshape. The methods generalize straightforwardly to GLE dynamics in a harmonic potential, and could therefore be used to model vibrational lineshapes in the presence of memory friction.

Another aspect of the Chapter was the estimation of the short and long-time lineshape amplitudes via simple thermodynamic considerations, including the effect of lateral corrugation, surface-perpendicular vibrations and k_z transfer. Experimentally, additional effects such as inelastic scattering from substrate phonons, tend to further decrease the relative intensity of the long-time tail of the lineshape. Additionally the simple ISF-based estimate would need to be combined with instrumental factors to predict the corresponding amplitudes in the experimental lineshape.

The connection between the GLE and many-body three-dimensional MD simulations is a rich source of further work. A microcanonical (constant energy) many-body simulation was analysed to extract an effective two-dimensional potential energy $V(x, y)$ and a measure of the effective GLE friction kernel governing the dynamics. On metallic surfaces, a component of the friction originates in electron-hole pair creation and annihilation, which can be reasonably assumed to be a Langevin-like contribution to the friction because of the wide energy range of the accessible excitations. Therefore, nonmetallic substrates could be better test systems in general for drawing comparisons between experimental data and theoretical phonon-driven surface diffusion.

7.1.3 Quantum dynamics and rate theory

In Chapter 4, I presented a derivation of the quantum ISF from its definition as a quantum correlation function, using an analytically solvable model whose classical limit is the GLE of Chapter 3. The generality of the results for arbitrary memory friction makes the model a potentially useful test case for approximate numerical

methods. However, the calculations with more immediate application to the interpretation of HeSE data were the dissipative quantum rate calculations of Section 4.5, performed using the so-called $\mathrm{Im}(F)$ or bounce method. The theoretical results are not consistent with high friction ($\gamma \gtrsim \omega_0$), which suggests that unless the friction has an extreme temperature dependence (cf. the suggestion in [35]), the low and high temperature regimes can be rationalized with a friction which is too low to realize the semiclassical TST rate at high temperatures. The low friction interpretation is consistent with the multiple jumps observed experimentally in Chapter 6 and in past works [35, 84]. However, the argument that a low friction leads to a rate significantly lower than that given by semiclassical TST is currently a qualitative argument and should be explored further now that it has been established that low-friction is the regime of interest. Semiclassical turnover theory in a periodic potential [328] provides one sensible starting point for calculating the dynamical corrections due to low friction in the quantum activated regime, and applying the method in the present context could give additional insight into the significance of the bandstructure (ASTST) method. Additional further directions of work to refine the combined theoretical and experimental picture derived so far could include:

- use input from methods expected to be systematically more accurate than DFT (e.g. DMC, see Section 7.1.5);
- given a sufficiently accurate potential, incorporate transverse degrees of freedom into the rate calculation;
- incorporate factors within the bounce method that not been explored due to the lack of corresponding first-principles input, including memory friction, position-dependent and nonlinear friction;
- clarify the relative importance of elastic incoherent tunneling and inelastic incoherent tunneling;
- compute higher order corrections to the Gaussian expansion of the path integral within the bounce method;

In classical Langevin simulations (for example), the limitations of transition state theory (or any rate theory at all) are bypassed by direct calculation of the ISF whose long time limit defines the jump dynamics via comparison with jump models (Section 2.2.1). The classical ISF can be simulated to high numerical accuracy relatively cheaply. The equivalent quantum mechanical calculation in a continuous potential for a dissipative system is not feasible. However, comparable dissipative calculations for model truncated systems, in which the Hilbert space of the diffusing

particle is reduced to a few states, are possible. Two promising methods which have been applied to calculate long-time dynamics of low-dimensional dissipative systems are:

- tensor propagators [329, 139];
- stochastic unraveling [140].

A detailed mathematical description of the methods and how they deal with the quantum environment is not relevant to the present argument. In the broadest terms, the environmental degrees of freedom are reduced to an implicit influence using methods comparable to the path integral techniques leading to the effective action used in the dissipative theory of Section 4.5, albeit with extra complications arising from considering the product of operators at different times as required for correlation function evaluation. Figure 7.1 illustrates the simulation of the dissipative two-state system for times much longer than an oscillation period of the undamped coherent motion.

The fully dynamical techniques bypass the approximations of rate theory. However, they rely on being able to accurately construct the model truncated system from the full continuous system, whereas the semiclassical rate theory uses the continuous potential. The dynamics of two-state biased and unbiased systems has been worked out in some detail using both analytic approximations and numerically exact simulations, but to apply the methods to quantum diffusion in the experimentally relevant regime near the crossover temperature, at least the lowest excited states would need to be included in the model. The minimum requirement for a model to display multiple jumps is that it includes at least three sites; however, it would be desirable to include enough sites that the length of the longest jump is not limited by the total extent of the system.

7.1.4 Diffusion of carbon and oxygen

In Chapter 5 I presented the first HeSE studies of carbon and oxygen diffusion on surfaces. Carbon was precipitated to the surface by annealing Ru(0001). Extensive annealing produced the moiré diffraction peaks indicative of well-ordered graphene patches. In parallel with the formation of graphene patches, a steady state 292 meV-activated diffusion process takes place. The diffusion is too fast to be residual oxygen which was measured independently, and the diffusion barrier is too small for atomic carbon according to first-principles calculations in the literature. The process was assigned to the diffusion of a small carbon cluster. Therefore, the surface carbon

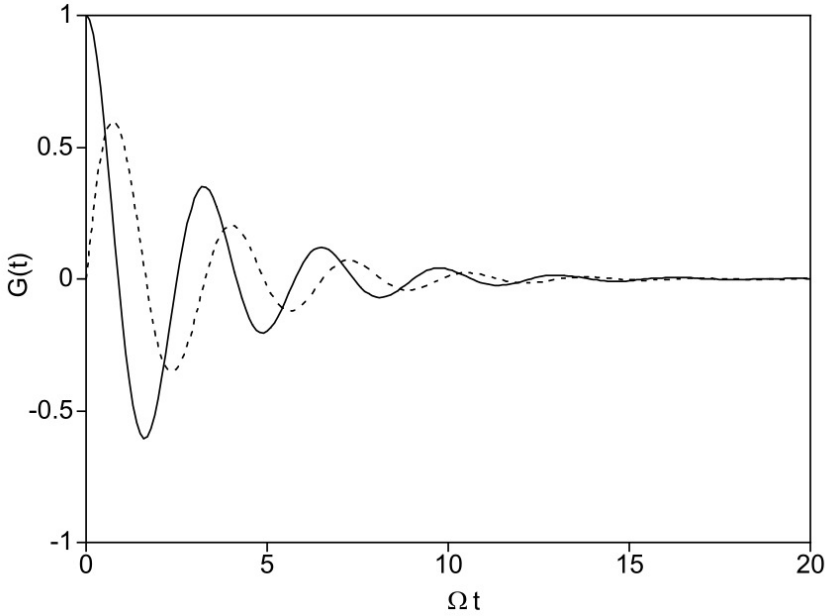

(a) Position correlation function in the dissipative two-state system simulated with the tensor propagator method [329].

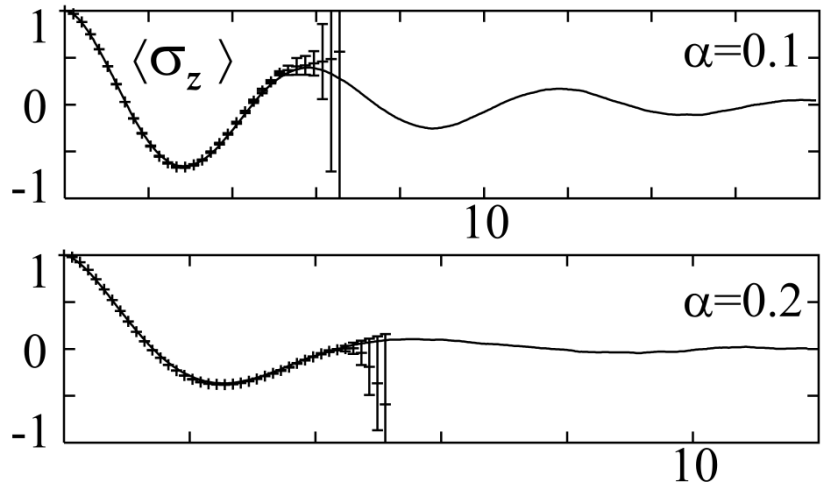

(b) Expectation of the position operator in the dissipative two-state system simulated with the stochastic unraveling method [330].

Figure 7.1: Illustration of the use of path integral techniques to calculate numerically exact dynamical properties of an open two-state quantum system over time scales long compared to the intrinsic dynamics of the system. The fact that such calculations are possible is significant because it allows direct dynamical calculation of incoherent tunneling rates, including regimes not known to be accessible by fully analytical theory. For example, a small number of additional system basis states could be introduced to model activated tunneling or additional sites that would allow in principle for multiple jumps. Damped oscillations are simulated over many cycles of the coherent motion, using the tensor propagator method (Figure 7.1a, reprinted from reference [329], Copyright (2001), with permission from Elsevier) and stochastic unraveling (Figure 7.1b, reprinted from reference [330], Copyright (2004), with permission from Elsevier). The stochastic unraveling results are compared with straightforward Monte Carlo evaluation of the path integrals, which becomes statistically meaningless after only a short propagation time, due to the well-known quantum dynamical sign problem. In the unraveled representation, the incoherent sum over independent quantum time evolutions bypasses the sign problem.

is not completely tied up in graphene patches, and yet the graphene islands must grow to large sizes as evidenced by the well-defined moiré features and the non-appearance of high-order "convolution peaks" (Section 2.1.4.2). The likely state of the surface would seem to be large graphene patches in a quasi-equilibrium with a lattice gas of diffusing clusters on the clean Ru patches. If the dominant mechanism for attaching at the island edges involves temporary formation of larger clusters, then a low concentration lattice gas of the diffusing species could exist alongside very slowly growing graphene islands for a very long time. At high temperatures it is possible that some carbon returns to the bulk on thermodynamic grounds.

Usually in spin echo diffusion measurements the diffusing species is known, and the coverage is known at least approximately. In the carbon diffusion experiments so far, the nature of the diffusion species is inferred only by indirect arguments, and there is no simple handle on the coverage. The fact that the data are explained well by a non-interacting jump diffusion model suggests that the coverage of diffusing species is low. To some extent, the difficulty in interpretation arises because of the growth method, from an unknown concentration of bulk carbon. An obvious candidate for future work on the system would be to explore the diffusion signatures produced after carbon dosing by deposition from the vacuum rather than precipitation from the bulk. The nature of the diffusing species could potentially be settled entirely on theoretical grounds, based on the stability and diffusion pathways of different carbon clusters. Available STM data already quite strongly restricts the possible sizes of the mobile species, but a search for the mobile species, suitably informed by the HeSE data, could confirm the proposed interpretation directly.

The picture of O/Ru(0001) diffusion developed so far on the basis of relatively preliminary data, can be readily extended with straightforward measurements of the low coverage regime. Low-coverage data can probably be measured without significant desorption at slightly higher temperatures (e.g. 900 K rather than 800 K which should increase the basic hopping rate about a factor of 3 based on the activation energy of 650 meV 5.18) and make extraction of absolute rates and jump distributions more accurate. The effect of the metastable fcc site would still not be directly detectable if the site energy difference is roughly as predicted by DFT (570 meV) since $\exp(\Delta E/k_B T)$ is still vanishingly small even when $T \approx 1000$ K. However, if the true value of ΔE is substantially smaller than predicted by DFT, then a detailed low-coverage study would be able to quantify ΔE using the same methodology applied to the carbon and hydrogen studies (Sections 2.2.6, 5.1.2.3, 6.3.4). A second major direction for future investigation is the high coverage regime, where the preliminary data can be extended and improved by measuring at an exact coverage rather than an approximate coverage slightly below 0.25 ML. A recipe for

achieving $\theta = 0.25\,\mathrm{ML}$ has been established previously [255], and could be used in future to prepare an oxygen overlayer at a well-defined ideal coverage, in order to study the dynamics of the structure in the absence of vacancies.

7.1.5 Hydrogen systems

In Chapter 6, HeSE studies of hydrogen diffusing on Ru(0001), Pd(111) and Cu(111) were presented. When analysed using the Bayesian technique described in Chapter 2, all three systems showed evidence for a jump rate significantly below the semi-classical TST prediction in the quantum activated regime, using the first principles potential energy surfaces derived from DFT. The data also consistently show multiple jumps at elevated temperatures, suggesting that the rate is suppressed by low friction rather than high friction. Independent evidence was gathered from alternative experimental and theoretical sources which supports the low friction hypothesis. Deuterium measurements on Ru(0001) are consistent with a slow deep tunneling rate, as distinct from the anomalously fast rate suggested by circumstantial data, and which appears to be present on Ni(111).

Each system studied has its own idiosyncratic open questions and obvious channels of further work, for example,

- if the broad diffraction feature on Ru(0001) is a form factor effect, why is it so much more noticeable on Ru(0001) than on the other surfaces?
- is the contamination of Pd(111) at low temperature due to adsorption from the gas phase or resurfacing of subsurface species?

However, here I will concentrate on general issues to do with the connection between theory and experiment.

Theoretical modelling of hydrogen diffusion data can be usefully divided into three parts-

1. calculation of the static hydrogen/surface interaction (PES) from first principles;
2. obtaining a handle on the dissipation (either from first principles or from jump distributions or other experimental sources);
3. legitimate use of the PES to calculate either rates or, ideally, full dynamical properties.

Item 2 is generally very difficult to address rigorously within first-principles theory. Item 3 has been discussed at length above (Section 7.1.3). In the context of HeSE interpretation, item 1 has been dominated by density functional theory (DFT). The quantitative predictive power of DFT is well known to be limited in certain cases such as systems where van der Waals interactions are important, and chemisorption systems such as CO on transition metals [331]. In the context of hydrogen dynamics on close-packed surfaces, a major difficulty of theoretical modelling with DFT is the sensitivity of the dynamics to the very small relative energy of non-degenerate adsorption sites. An emerging candidate for practical calculations with accuracy beyond DFT which could be applied to calculating surface diffusion potentials is fermionic diffusion Monte Carlo (DMC) [332]. DMC is systematically more accurate than DFT, and although it is more computationally expensive it is being applied to real systems including hydrogen/transition metal systems [314]. Application to atomic hydrogen diffusion would be a valuable test case. However, some aspects of the comparison between first principles calculations and experimental results present difficulties even if the total electronic energy calculation is beyond reproach. For example, H-H interactions cannot be properly quantified without using a large periodic calculation cell, and averaging over many adsorbate configurations. Although the qualitative effect of on-site interaction terms on correlated dynamics can be modelled effectively by kinetic Monte Carlo methods [35], the precise effect on absolute hopping rates via modification of local barriers needs first-principles input.

One of the major unresolved questions in the understanding of hydrogen diffusion is why the diffusion rate of deuterium on Ni(111) appears to be similar to the protium diffusion rate, even though the isotope is expected to be orders of magnitude [36]. One of the directions explored in the present Thesis for rationalizing small isotope effects has been the effect of dissipation on quantum rates. However, we saw in Chapter 4 that the dissipation required for the theory to predict comparable rates for H and D is so large that the absolute rate becomes inconsistent with experiment. The relative tunneling efficiency of H and D out of their adsorption sites is so different that any theoretical explanation in those terms appears to be impossible, at least when the PES is modelled as a low dimensional function. Some previous attempts to explain apparently very similar H and D tunneling rates have essentially relied on strong dissipation coupled with an unrealistically high bare tunneling matrix element.

A slow, temperature-independent diffusion process whose rate is only weakly dependent on the isotope in question, could be caused by a diffusion path which is essentially non-activated but which is very narrow in the multi-dimensional potential

energy landscape. In that case, a break in the Arrhenius behaviour will be seen even when the dynamics are completely classical. For a concrete illustration, consider the model potential energy

$$V(x,y) = \frac{1}{2}\Omega^2(x)y^2\,, \tag{7.1}$$

where $\Omega(x)$ is a positive periodic function. Dynamics in the model potential will consist of jump diffusion along the x direction coupled to vibrations in the y direction. If we assume that the dynamics are governed by a GLE or similar dissipative equation, and that the role of perpendicular vibrations is essentially to contribute to the friction and random force while renormalizing the potential along the x axis, then the effective potential governing the jump dynamics is the free energy

$$V(x) = -k_B \ln Z(x) = k_B T \Omega(x)\,. \tag{7.2}$$

Since the effective barrier height scales with $k_B T$, $\exp(-\beta V_b)$ is a constant, and therefore the motion is not activated, even classically. However, the absolute rate could be small if the perpendicular constriction at the barrier is narrow, and therefore if an alternative, activated path is available then an Arrhenius plot of the rate will show a classical break. Given that experimentally the activated/non-activated transition is at approximately the expected temperature on the basis of quantum rate theory on a low-dimensional potential energy surface, it seems unlikely that the effect described here is responsible for the anomalous isotope effect observed on Ni(111).

7.1.6 Final comments

In the opening Section I highlighted some major applications where an understanding of microscopic surface processes is vital, and argued that building fundamental understanding through a bottom-up experimental approach and a close comparison with theory is an indispensable part of the same ecosystem from which headline technological advances arise. By providing a very detailed perspective on atom/surface interactions, the HeSE experiment makes a unique and vital contribution.

Bibliography

[1] G. Ertl. Nobel lecture: Reactions at surfaces: From atoms to complexity, 2007.

[2] Y. Cui, Q. Fu, H. Zhang, and X. Bao. Formation of identical-size graphene nanoclusters on Ru(0001). *Chemical Communications*, **47**(5):1470–2, 2011.

[3] S. Hofmann, G. Csányi, A.C. Ferrari, M.C. Payne, and J. Robertson. Surface diffusion: The low activation energy path for nanotube growth. *Physical Review Letters*, **95**(3):036101, 2005.

[4] G. Pawin, L.K. Wong, K.-Y. Kwon, and L. Bartels. A homomolecular porous network at a Cu(111) surface. *Science*, **313**(5789):961–2, 2006.

[5] E.C. Tyo and S. Vajda. Catalysis by clusters with precise numbers of atoms. *Nature Nanotechnology*, **10**(7):577–88, 2015. Review.

[6] A.H. Castro Neto, F. Guinea, N.M.R. Peres, K.S. Novoselov, and A.K. Geim. The electronic properties of graphene. *Reviews of Modern Physics*, **81**(1):109–62, 2009.

[7] J. Bardeen. Surface states and rectification at a metal semi-conductor contact. *Physical Review*, **71**(10):717–27, 1947.

[8] S. Nakamura, M. Senoh, S. Nagahama, N. Iwasa, T. Yamada, T. Matsushita, H. Kiyoku, and Y. Sugimoto. InGaN-based multi-quantum-well-structure laser diodes. *Japanese Journal of Applied Physics*, **35**(1B):L74–6, 1996.

[9] M.D. Tikekar, S. Choudhury, Z. Tu, and L.A. Archer. Design principles for electrolytes and interfaces for stable lithium-metal batteries. *Nature Energy*, **1**(16114):1–7, 2016.

[10] J.T.S. Irvine, D. Neagu, M.C. Verbraeken, C. Chatzichristodoulou, C. Graves, and M.B. Mogensen. Evolution of the electrochemical interface in high-temperature fuel cells and electrolysers. *Nature Energy*, **1**(15014):1–13, 2016.

[11] I. Langmuir. The mechanism of the catalytic action of platinum in the reactions 2CO+O2=2CO2 and 2H2+O2=2H2O. *Transactions of the Faraday Society*, **17**(2):621–54, 1922.

[12] K.-H. Bernhardt. *Vacuum Technology Compendium*. Pfeiffer Vacuum GmbH, 2010.

[13] R.T. Bayard and D. Alpert. Extension of the low pressure range of the ionization gauge. *Review of Scientific Instruments*, **21**(6):571–2, 1950.

[14] C.B. Duke. The birth and evolution of surface science: Child of the union of science and technology. *Proceedings of the National Academy of Sciences*, **100**(7):3858–64, 2003.

[15] G. Binnig and H. Rohrer. Scanning tunneling microscopy. *Helvetica Physica Acta*, **55**(6):726–35, 1982.

[16] R. Campargue. Progress in overexpanded supersonic jets and skimmed molecular beams in free-jet zones of silence. *Journal of Physical Chemistry*, **88**(20):4466–74, 1984.

[17] X. Su, P.S. Cremer, Y.R. Shen, and G.A. Somorjai. High-pressure CO oxidation on Pt(111) monitored with infrared-visible sum frequency generation (SFG). *Journal of the American Chemical Society*, **119**(17):3994–4000, 1997.

[18] G. Rupprechter and C. Weilach. Spectroscopic studies of surfacegas interactions and catalyst restructuring at ambient pressure: mind the gap! *Journal of Physics: Condensed Matter*, **20**(18):184019, 2008.

[19] S. Kaya, H. Ogasawara, L.-Å Näslund, J.-O. Forsell, H. Sanchez Casalongue, D.J. Miller, and A. Nilsson. Ambient-pressure photoelectron spectroscopy for heterogeneous catalysis and electrochemistry. *Catalysis Today*, **205**(Supplement C):101–5, 2013. Operando IV: The 4th International Congress on Operando Spectroscopy.

[20] B. Eren, D. Zherebetskyy, L.L. Patera, C.H. Wu, H. Bluhm, C. Africh, L.-W. Wang, G.A. Somorjai, and M. Salmeron. Activation of Cu(111) surface by decomposition into nanoclusters driven by CO adsorption. *Science*, **351**(6272):475–8, 2016.

[21] W. Kohn and J.L. Sham. Self-consistent equations including exchange and correlation effects. *Physical Review*, **140**(4A):A1133–8, 1965.

[22] H. Hedgeland, B.A.J. Lechner, F.E. Tuddenham, A.P. Jardine, W. Allison, J. Ellis, M. Sacchi, S.J. Jenkins, and B.J. Hinch. Weak intermolecular interactions in an ionically bound molecular adsorbate: Cyclopentadienyl/Cu(111). *Physical Review Letters*, **106**(18):6–9, 2011.

[23] E.M. McIntosh, K.T. Wikfeldt, J. Ellis, A. Michaelides, and W. Allison. Quantum Effects in the Diffusion of Hydrogen on Ru(0001). *Journal of Physical Chemistry Letters*, **4**(9):1565–9, 2013.

[24] B.A.J. Lechner, M. Sacchi, A.P. Jardine, H. Hedgeland, W. Allison, J. Ellis, S.J. Jenkins, P.C. Dastoor, and B. J. Hinch. Jumping, rotating, and flapping: The atomic-scale motion of thiophene on Cu(111). *Journal of Physical Chemistry Letters*, **4**(11):1953–8, 2013.

[25] S.P. Rittmeyer, D.J. Ward, P. Gütlein, J. Ellis, W. Allison, and K. Reuter. Energy dissipation during diffusion at metal surfaces: Disentangling the role of phonons versus electron-hole pairs. *Physical Review Letters*, **117**(19):196001, 2016.

[26] S. Miret-Artés and E. Pollak. The dynamics of activated surface diffusion. *Journal of Physics: Condensed Matter*, **17**(49):S4133–50, 2005.

[27] P. Fouquet, M.R. Johnson, H. Hedgeland, A.P. Jardine, J. Ellis, and W. Allison. Molecular dynamics simulations of the diffusion of benzene sub-monolayer films on graphite basal plane surfaces. *Carbon*, **47**(11):2627–39, 2009.

[28] D.J. Ward. *A study of spin-echo lineshapes in helium atom scattering from adsorbates*. PhD thesis, University of Cambridge, 2013.

[29] H.-P. Breuer and F. Petruccione. *Open Quantum Systems*. Oxford University Press, 2002.

[30] U. Weiss. *Quantum Dissipative Systems*, volume 13 of *Series in Modern Condensed Matter Physics*. World Scientific, fourth edition, 2012.

[31] J. Ankerhold. *Quantum Tunneling in Complex Systems: the Semiclassical Approach*, volume 224 of *Springer Tracts in Modern Physics*. Springer, 2007.

[32] T.D. Ladd, F. Jelezko, R. Laflamme, Y. Nakamura, C. Monroe, and J.L. O'Brien. Quantum computers. *Nature*, **464**(7285):45–53, 2010.

[33] R. A. Marcus and Norman Sutin. Electron transfers in chemistry and biology. *BBA Reviews On Bioenergetics*, **811**(3):265–322, 1985.

[34] W. Zurek. Decoherence and the transition from quantum to classical. *Physics Today*, **44**(10):36–44, 1991.

[35] E.M. Mcintosh. *Adsorption and Dynamics of Interacting Surface Systems*. PhD thesis, University of Cambridge, 2013.

[36] J. Zhu. *Study of Quantum Effects in Adsorbate Diffusion*. PhD thesis, University of Cambridge, 2015.

[37] S. Hofmann, P. Braeuninger-Weimer, and R.S. Weatherup. CVD-enabled graphene manufacture and technology. *Journal of Physical Chemistry Letters*, **6**(14):2714–21, 2015.

[38] A. Trovarelli. Catalytic properties of Ceria and CeO2-containing materials. *Catalysis Reviews*, **38**(4):439–520, 1996.

[39] H. Over, D.Y. Kim, P.A. Seitsonen, S. Wendt, E. Lundgren, M. Schmid, P. Varga, A. Morgante, and G. Ertl. Atomic-scale structure and catalytic reactivity of the RuO2(110) surface. *Science*, **287**(5457):1474–6, 2000.

[40] T. Luttrell, S. Halpegamage, J. Tao, A. Kramer, E. Sutter, and M. Matzill. Why is anatase a better photocatalyst than rutile? - model studies on epitaxial TiO2 films. *Scientific Reports*, **4**(4043):1–8, 2014.

[41] L.J. Lauhon and W. Ho. Direct observation of the quantum tunneling of single hydrogen atoms with a scanning tunneling microscope. *Physical Review Letters*, **85**(21):4566–9, 2000.

[42] P.G. Wolynes. Quantum theory of activated events in condensed phases. *Physical Review Letters*, **47**(13):968–71, 1981.

[43] A.P. Jardine, E.Y.M. Lee, D.J. Ward, G. Alexandrowicz, H. Hedgeland, W. Allison, J. Ellis, and E. Pollak. Determination of the quantum contribution to the activated motion of hydrogen on a metal surface: H/Pt(111). *Physical Review Letters*, **105**(13):136101, 2010.

[44] S.C. Badescu, S.C. Ying, and T. Ala-Nissila. Quantum diffusion of H/Ni(111) through a Monte Carlo wave function formalism. *Physical Review Letters*, **86**(22):5092–5, 2001.

[45] T. Firmino, R. Marquardt, F. Gatti, and W. Dong. Diffusion Rates for Hydrogen on Pd(111) from Molecular Quantum Dynamics Calculations. *Journal of Physical Chemistry Letters*, **5**(24):4270–4, 2014.

[46] H. Haberland, U. Buck, and M. Tolle. Velocity distribution of supersonic nozzle beams. *Review of Scientific Instruments*, **56**(9):1712–6, 1985.

[47] N. Esbjerg and J.K. Nørskov. Dependence of the He-scattering potential at surfaces on the surface-electron-density profile. *Physical Review Letters*, **45**(10):807–10, 1980.

[48] D. Farías and K.-H. Rieder. Atomic beam diffraction from solid surfaces. *Reports on Progress in Physics*, **61**(12):1575–664, 1998.

[49] A.G. Fedorus, E.V. Klimenko, A.G. Naumovets, E.M. Zasimovich, and I.N. Zasimovich. Electron-stimulated mobility of adsorbed particles. *Nuclear Instruments and Methods in Physics Research Section B*, **101**(1–2):207–15, 1995.

[50] J.T. Yates, P.A. Thiel, and W.H. Weinberg. The chemisorption of hydrogen on Rh(111). *Surface Science*, **84**(2):427–39, 1979.

[51] G. Witte, J.P. Toennies, and C. Wöll. Comparison of surface phonon dispersion curves for clean and hydrogen covered Rh (111) surfaces. *Surface Science*, **323**(3):228–40, 1995.

[52] M. Gallagher, A. Omer, G.R. Darling, and A. Hodgson. Order and disorder in the wetting layer on Ru(0001). *Faraday Discussions*, **141**(0):231–49, 2008.

[53] N. Avidor and W. Allison. Helium diffraction as a probe of structure and proton order on model ice surfaces. *Journal of Physical Chemistry Letters*, **7**:4520–3, 2016.

[54] G. Held, H. Pfnür, and D. Menzel. A LEED-IV investigation of the Ru(001)-p(2×1)-H structure. *Surface Science*, **271**(1–2):21–31, 1992.

[55] P. Fouquet, H. Hedgeland, A.P. Jardine, G. Alexandrowicz, W. Allison, and J. Ellis. Measurements of molecule diffusion on surfaces using neutron and helium spin echo. *Physica B: Condensed Matter*, **385–386**:269–71, 2006.

[56] K. Heinz. LEED and DLEED as modern tools for quantitative surface structure determination. *Reports on Progress in Physics*, **58**(6):637–704, 1995.

[57] K.L. Kostov, W. Widdra, and D. Menzel. Hydrogen on Ru(001) revisited: Vibrational structure, adsorption states, and lateral coupling. *Surface Science*, **560**(1–3):130–44, 2004.

[58] D. Martoccia, P.R. Willmott, T. Brugger, M. Björck, S. Günther, C.M. Schlepütz, A. Cervellino, S.A. Pauli, B.D. Patterson, S. Marchini, J. Wintterlin, W. Moritz, and T. Greber. Graphene on Ru(0001): A 25×25 Supercell. *Physical Review Letters*, **101**(12):126102, 2008.

[59] I.K. Robinson and D.J. Tweet. Surface x-ray diffraction. *Reports on Progress in Physics*, **55**(5):599–651, 1992.

[60] G.L. Squires. *Introduction to the Theory of Thermal Neutron Scattering*. Dover, 1996.

[61] A.P. Jardine, H. Hedgeland, G. Alexandrowicz, W. Allison, and J. Ellis. Helium-3 spin-echo: Principles and application to dynamics at surfaces. *Progress in Surface Science*, **84**(11-12):323–79, 2009.

[62] G. Benedek and J.P. Toennies. Helium atom scattering spectroscopy of surface phonons: genesis and achievements. *Surface Science*, **299–300**(1-3):587–611, 1994.

[63] A.P. Graham. The low energy dynamics of adsorbates on metal surfaces investigated with helium atom scattering. *Surface Science Reports*, **49**(4–5):115–68, 2003.

[64] F. Mezei. Neutron spin echo: A new concept in polarized thermal neutron techniques. *Zeitschrift für Physik*, **255**(2):146–60, 1972.

[65] A.P. Jardine, G. Alexandrowicz, H. Hedgeland, W. Allison, and J. Ellis. Studying the microscopic nature of diffusion with helium-3 spin-echo. *Physical Chemistry Chemical Physics*, **11**(18):3355–74, 2009.

[66] J.J. Sakurai and J. Napolitano. *Modern Quantum Mechanics*. Addison-Wesley, second edition, 2011.

[67] L. Van Hove. Correlations in space and time and Born approximation scattering in systems of interacting particles. *Physical Review*, **95**(1):249–62, 1954.

[68] S.W. Lovesey. *Theory of neutron scattering from condensed matter*, volume 1 of *International Series of Monographs on Physics (no. 72)*. Oxford University Press, 1984.

[69] G. Alexandrowicz and A.P. Jardine. Helium spin-echo spectroscopy: studying surface dynamics with ultra-high-energy resolution. *Journal of Physics: Condensed Matter*, **19**(30):305001, 2007.

[70] P. Fouquet, A.P. Jardine, S. Dworski, G. Alexandrowicz, W. Allison, and J. Ellis. Thermal energy He 3 spin-echo spectrometer for ultrahigh resolution surface dynamics measurements. *Review of Scientific Instruments*, **76**(5):053109, 2005.

[71] P.R. Kole. *Dynamics and morphology of metal and metal oxide surfaces*. PhD thesis, University of Cambridge, 2011.

[72] B.A.J. Lechner. *Studying complex surface dynamical systems using helium-3 spin-echo spectroscopy*. PhD thesis, University of Cambridge, 2012.

[73] N. Avidor, H. Hedgeland, G. Held, A.P. Jardine, W. Allison, J. Ellis, T. Kravchuk, and G. Alexandrowicz. Highly proton-ordered water structures on oxygen precovered Ru{0001}. *Journal of Physical Chemistry A*, **115**(25):7205–9, 2011.

[74] M.F. Luo, D.A. MacLaren, I.G. Shuttleworth, and W. Allison. Preferential sub-surface occupation of atomic hydrogen on Cu(111). *Chemical Physics Letters*, **381**(5–6):654–9, 2003.

[75] H. Ohtani, M.A. van Hove, and G.A. Somorjai. LEED Intensity Analysis of the Surface Structures of Pd(111) in a $(\sqrt{3}\times\sqrt{3})-R30^\circ$ Arrangement. *Surface Science*, **187**(2):372–86, 1987.

[76] K.A. Stoerzinger. *Nanoscale Dynamics of Benzene and Naphthalene on Ru and Graphene*. PhD thesis, University of Cambridge, 2011.

[77] U. Garibaldi, A.C. Levi, R. Spadacini, and G.E. Tommei. Quantum theory of atom-surface scattering: Diffraction and rainbow. *Surface Science*, **48**(2):649–75, 1975.

[78] J.A. Lau, I. Calvo Almazán, P.S.M. Townsend, D.J. Ward, A.P. Jardine, W. Allison, J. Ellis, B.J. Hinch, and N. Avidor. Structural evolution of a cyclooctatetraene adlayer on Cu(111) during isothermal desorption. Submitted to Journal of Physics Chemistry C.

[79] R. Martínez-Casado, B. Meyer, S. Miret-Artés, F. Traeger, and Ch. Wöll. Diffraction patterns of he atoms from the MgO(100) surface calculated by the close-coupling method. *Journal of Physics: Condensed Matter*, **19**(30):305006, 2007.

[80] A.M. Lahee, J.R. Manson, J.P. Toennies, and Ch. Wöll. Helium atom differential cross sections for scattering from single adsorbed co molecules on a Pt(111) surface. *Journal of Chemical Physics*, **86**(12):7194–203, 1987.

[81] C.T. Chudley and R.J. Elliott. Neutron scattering from a liquid on a jump diffusion model. *Proceedings of the Physical Society of London*, **77**(2):353–61, 1961.

[82] J.M. Rowe, K. Sköld, H.E. Flotow, and J.J. Rush. Quasielastic neutron scattering by hydrogen in the α and β phases of vanadium hydride. *Journal of Physics and Chemistry of Solids*, **32**(1):41–54, 1971.

[83] F.E. Tuddenham, H. Hedgeland, A.P. Jardine, B.A.J. Lechner, B.J. Hinch, and W. Allison. Lineshapes in quasi-elastic scattering from species hopping between non-equivalent surface sites. *Surface Science*, **604**(17-18):1459–75, 2010.

[84] F.E. Tuddenham. *Helium Atom Scattering as a Probe of Hydrogen Adsorption and Dynamics*. PhD thesis, University of Cambridge, 2011.

[85] The Mathworks Inc. fit, 2017. [Online; accessed 27 November 2017].

[86] The Mathworks Inc. fft, 2017. [Online; accessed 27 November 2017].

[87] D.S. Sivia and J. Skilling. *Data Analysis: A Bayesian Tutorial*. Oxford University Press, second edition, 2005.

[88] Wolfram Research, Inc. Mathematica, Version 11.2. Champaign, IL, 2017.

[89] B.A.J. Lechner, P.R. Kole, H. Hedgeland, A.P. Jardine, W. Allison, B.J. Hinch, and J. Ellis. Ultra-high precision determination of site energy differences using a Bayesian method. *Physical Review B - Condensed Matter and Materials Physics*, **89**(12):1–5, 2014.

[90] Irene Calvo-Almazán, Marco Sacchi, A. Tamtögl, E. Bahn, M.M. Koza, S. Miret-Artés, and P. Fouquet. Ballistic diffusion in polyaromatic hydrocarbons on graphite. *The Journal of Physical Chemistry Letters*, **7**(24):5285–5290, 2016.

[91] M. DeKieviet, D. Dubbers, M. Klein, U. Pieles, and C. Schmidt. Design and performance of a highly efficient mass spectrometer for molecular beams. *Review of Scientific Instruments*, **71**(5):2015–8, 2000.

[92] M. DeKieviet, D. Dubbers, C. Schmidt, D. Scholz, and U. Spinola. 3He spin echo: New atomic beam technique for probing phenomena in the neV range. *Physical Review Letters*, **75**(10):1919–22, 1995.

[93] M. DeKieviet, D. Dubbers, M. Klein, C. Schmidt, and M. Skrzipczyk. Surface science using molecular beam spin echo. *Surface Science*, **377–9**(97):1112–17, 1997.

[94] A.P. Jardine. Ultrahigh-Resolution Spin-Echo Measurement of Surface Potential Energy Landscapes. *Science*, **304**(5678):1790–3, 2004.

[95] H. Hedgeland, P.R. Kole, W. Allison, J. Ellis, and A.P. Jardine. An improved high intensity recycling helium-3 beam source. *Review of Scientific Instruments*, **80**(7):076110, 2009.

[96] H. Hedgeland. *The Development of Quasi-Elastic Helium-3 Spin-Echo Spectroscopy as a Tool for the Study of Surface Dynamics*. PhD thesis, University of Cambridge, 2006.

[97] A.R. Alderwick. *Instrumental and Analysis Tools for Atom Scattering from Surfaces*. PhD thesis, University of Cambridge, 2009.

[98] A.R. Alderwick, A.P. Jardine, H. Hedgeland, D.A. MacLaren, W. Allison, and J. Ellis. Simulation and analysis of solenoidal ion sources. *Review of Scientific Instruments*, **79**(12):123301, 2008.

[99] D.M. Chisnall. *A High Sensitivity Detector for Helium Atom Scattering*. PhD thesis, University of Cambridge, 2012.

[100] M. Koch, S. Rehbein, G. Schmahl, T. Reisinger, G. Bracco, E.W. Ernst, and B. Holst. Imaging with neutral atoms—a new matter-wave microscope. *Journal of Microscopy*, **229**(1):1–5, 2008.

[101] M. Barr, A. Fahy, A.P. Jardine, J. Ellis, D.J. Ward, D.A. MacLaren, W. Allison, and P.C. Dastoor. A design for a pinhole scanning helium microscope. *Nuclear Instruments and Methods in Physics Research Section B Beam Interactions with Materials and Atoms*, **340**:76–80, 2014. 20th International Workshop on Inelastic Ion-Surface Collisions (IISC-20).

[102] M. Bergin. Verbal communication.

[103] B.A.J. Lechner, H. Hedgeland, W. Allison, J. Ellis, and A.P. Jardine. Note: A new design for a low-temperature high-intensity helium beam source. *Review of Scientific Instruments*, **84**(2):8–11, 2013.

[104] J. Ellis, A.P. Graham, and J.P. Toennies. Quasielastic helium atom scattering from a two-dimensional gas of Xe atoms on Pt(111). *Physical Review Letters*, **82**(82):5072–5, 1999.

[105] H. Hedgeland, P. Fouquet, A.P. Jardine, G. Alexandrowicz, W. Allison, and J. Ellis. Measurement of single-molecule frictional dissipation in a prototypical nanoscale system. *Nature Physics*, **5**(8):561–4, 2009.

[106] K.F. Riley, M.P. Hobson, and S.J. Bence. *Mathematical Methods for Physics and Engineering*. Cambridge University Press, 3 edition, 2006.

[107] L. Onsager. Reciprocal relations in irreversible processes. i. *Physical Review*, **37**(4):405–26, 1931.

[108] R. Martínez-Casado, J.L. Vega, A.S. Sanz, and S. Miret-Artés. Generalized Chudley-Elliott vibration-jump model in activated atom surface diffusion. *Journal of Chemical Physics*, **126**(194711):1–5, 2007.

[109] H. Hedgeland, P.R. Kole, H.R. Davies, A.P. Jardine, G. Alexandrowicz, W. Allison, J. Ellis, G. Fratesi, and G.P. Brivio. Surface dynamics and friction of K/Cu(001) characterized by helium-3 spin-echo and density functional theory. *Physical Review B - Condensed Matter and Materials Physics*, **80**(12):1–7, 2009.

[110] B.A.J. Lechner, A.S. De Wijn, H. Hedgeland, A.P. Jardine, B.J. Hinch, W. Allison, and J. Ellis. Atomic scale friction of molecular adsorbates during diffusion. *Journal of Chemical Physics*, **138**(19):194710, 2013.

[111] L. Verlet. Computer "experiments" on classical fluids. I. Thermodynamical properties of Lennard-Jones molecules. *Physical Review*, **159**(1):98–103, 1967.

[112] J. Ellis and J.P. Toennies. A molecular dynamics simulation of the diffusion of sodium on a Cu(001) surface. *Surface Science*, **317**(94):99–108, 1994.

[113] J.I. Juaristi, M. Alducin, R. Díez Muiño, H.F. Busnengo, and A. Salin. Role of electron-hole pair excitations in the dissociative adsorption of diatomic molecules on metal surfaces. *Physical Review Letters*, **100**(11):116102, 2008.

[114] G. Gershinsky, Y. Georgievskii, E. Pollak, and G. Betz. Microscopic and macroscopic estimates of friction: Application to surface diffusion of copper. *Surface Science*, **365**(1):159–67, 1996.

[115] R. Kubo. The fluctuation-dissipation theorem. *Reports on Progress in Physics*, **29**(1):255–84, 1966.

[116] R.F. Grote and J.T. Hynes. The stable states picture of chemical reactions. II. Rate constants for condensed and gas phase reaction models. *Journal of Chemical Physics*, **73**(6):2715–32, 1980.

[117] E. Hershkovitz, P. Talkner, E. Pollak, and Y. Georgievskii. Multiple hops in multidimensional activated surface diffusion. *Surface Science*, **421**(1-2):73–88, 1999.

[118] R. Huang, I. Chavez, K.M. Taute, B. Lukic, S. Jeney, M.G. Raizen, and E.-L. Florin. Direct observation of the full transition from ballistic to diffusive brownian motion in a liquid. *Nature Physics*, **7**:576–80, 2011.

[119] P.N. Pusey. Brownian motion goes ballistic. *Science*, **332**(6031):802–3, 2011.

[120] B.A.J. Lechner, H. Hedgeland, A.P. Jardine, W. Allison, and J. Ellis. Vibrational lifetimes and friction in adsorbate motion determined from quasi-elastic scattering. *Physical Chemistry Chemical Physics*, **17**(34):1–5, 2015.

[121] A.O. Caldeira and A.J. Leggett. Path integral approach to quantum Brownian motion. *Physica A: Statistical Mechanics and its Applications*, **121**(3):587–616, 1983.

[122] A. O. Caldeira and A. J. Leggett. Quantum tunnelling in a dissipative system. *Annals of Physics*, **149**(2):374–456, 1983.

[123] E. Pollak, J.M. Moix, and S. Miret-Artés. Classical theory for asymmetric in-plane atom surface scattering. *Physical Review B*, **80**:165420, 2009.

[124] E. Pollak and S. Miret-Artés. Classical theory for the in-plane scattering of atoms from corrugated surfaces: Application to the arag(111) system. *The Journal of Chemical Physics*, **130**(19):194710, 2009.

[125] J.L. Vega, R. Guantes, and S. Miret-Artés. Quasielastic and low vibrational lineshapes in atomsurface diffusion. *Journal of Physics: Condensed Matter*, **16**(29):S2879–94, 2004.

[126] G. Caratti, R. Ferrando, R. Spadacini, G.E. Tommei, and I. Zelenskaya. Resonant diffusion in periodic systems with memory. *Chemical Physics Letters*, **290**(4–6):509–13, 1998.

[127] M. Ottobre and G.A. Pavliotis. Asymptotic analysis for the generalized Langevin equation. *Nonlinearity*, **24**(5):1629–53, 2011.

[128] M. Ceriotti. *A novel framework for enhanced molecular dynamics based on the generalized Langevin equation*. PhD thesis, ETH Zurich, 2010.

[129] M. Ceriotti, D.E. Manolopoulos, and M. Parrinello. Accelerating the convergence of path integral dynamics with a generalized Langevin equation. *Journal of Chemical Physics*, **134**(8):084104, 2011.

[130] R. Ianconescu, E. Pollak, R. Ianconescu, and E. Pollak. A study of Kramers' turnover theory in the presence of exponential memory friction. *Journal of Chemical Physics*, **143**(10):104104, 2015.

[131] M. Diamant, S. Rahav, R. Ferrando, and G. Alexandrowicz. Interpretation of surface diffusion data with Langevin simulations: a quantitative assessment. *Journal of Physics: Condensed Matter*, **27**(12):125008, 2015.

[132] A. Bakan, L.M. Meireles, and I. Bahar. Prody: Protein dynamics inferred from theory and experiments. *Bioinformatics*, **27**(11):1575–7, 2011.

[133] E. Jones, T. Oliphant, P. Peterson, et al. SciPy: Open source scientific tools for Python, 2001. [Online; accessed 28 September 2017].

[134] J.A. Anderson, C.D. Lorenz, and A. Travesset. General purpose molecular dynamics simulations fully implemented on graphics processing units. *Journal of Computational Physics*, **227**(10):5342–59, 2008.

[135] The Wilkes Cluster at the University of Cambridge. Provided by Dell Inc., NVIDIA and Mellanox, and part funded by STFC with industrial sponsorship from Rolls Royce and Mitsubishi Heavy Industries.

[136] W. Humphrey, A. Dalke, and K. Schulten. VMD – Visual Molecular Dynamics. *Journal of Molecular Graphics*, **14**(1):33–8, 1996.

[137] H. Li, J. Shao, A. Azuri, E. Pollak, and R. Alicki. Quantum markovian master equation for scattering from surfaces. *The Journal of Chemical Physics*, **140**(1):014104, 2014.

[138] A.V. Mokshin, R.M. Yulmetyev, and P. Hänggi. Diffusion processes and memory effects. *New Journal of Physics*, **7**(9):1–9, 2005.

[139] J. Shao and N. Makri. Iterative path integral formulation of equilibrium correlation functions for quantum dissipative systems. *Journal of Chemical Physics*, **116**(2):507–14, 2002.

[140] J.T. Stockburger and H. Grabert. Exact c-number representation of non-Markovian quantum dissipation. *Physical Review Letters*, **88**(17):1–4, 2002.

[141] R. Martínez-Casado, A.S. Sanz, and S. Miret-Artés. Quantum Markovian activated surface diffusion of interacting adsorbates. *Journal of Chemical Physics*, **129**(18):184704, 2008.

[142] N. Makri. The linear response approximation and its lowest order corrections: an influence functional approach. *J. Phys. Chem. B*, **103**(15):2823–9, 1999.

[143] J.T. Stockburger. Stochastic and numerical approaches to dissipative quantum mechanics: path integrals and beyond. *Physica Status Solidi (b)*, **237**(1):146–58, 2003.

[144] R. Martínez-Casado, A.S. Sanz, J.L. Vega, G. Rojas-Lorenzo, and S. Miret-Artés. Linear response theory of activated surface diffusion with interacting adsorbates. *Chemical Physics*, **370**(1-3):180–93, 2010.

[145] R. Martínez-Casado, A.S. Sanz, and S. Miret-Artés. Phonon lineshapes in atom–surface scattering. *Journal of Physics: Condensed Matter*, **22**(30):304017, 2010.

[146] Neil W. Ashscroft and David N. Mermin. *Solid State Physics*. First edition, 2003.

[147] E. Pollak. Theory of activated rate processes: A new derivation of Kramers' expression. *Journal of Chemical Physics*, **85**(2):865–7, 1986.

[148] A.J. Leggett, S. Chakravarty, A.T. Dorsey, M.P.A. Fisher, A. Garg, and W. Zwerger. Dynamics of the dissipative two-state system. *Reviews of Modern Physics*, **59**(1):1–85, 1987.

[149] G. Gamow. Zur Quantentheorie des Atomkernes. *Zeitschrift für Physik*, **51**(3–4):204–12, 1928.

[150] A. B. Balantekin and N. Takigawa. Quantum tunneling in nuclear fusion. *Reviews of Modern Physics*, **70**(1):77–100, 1998.

[151] A. Heuer and U. Haeberlen. The dynamics of hydrogens in double well potentials: The transition of the jump rate from the low temperature quantum-mechanical to the high temperature activated regime. *Journal of Chemical Physics*, **95**(6):4201–14, 1991.

[152] S. Andersson, G. Nyman, A. Arnaldsson, U. Manthe, and H. Jónsson. Comparison of quantum dynamics and quantum transition state theory estimates of the H + CH_4 reaction rate. *Journal of Physical Chemistry A*, **113**(16):4468–78, 2009.

[153] S. Washburn, R.A. Webb, R.F. Voss, and S.M. Faris. Effects of dissipation and temperature on macroscopic quantum tunneling. *Physical Review Letters*, **54**(25):2712–5, 1985.

[154] A.D. Jewell, G. Peng, M.F.G. Mattera, E.A. Lewis, C.J. Murphy, G. Kyriakou, M. Mavrikakis, and E.C.H. Sykes. Quantum tunneling enabled self-assembly of hydrogen atoms on Cu(111). *ACS Nano*, **6**(11):10115–21, 2012.

[155] J. Singleton. *Band Theory and Electronic Properties of Solids*. Oxford Master Series in Condensed Matter Physics. Oxford University Press, 2001.

[156] S. Dattagupta, H. Grabert, and R. Jung. The structure factor for neutron scattering from a two-state system in metals. *Journal of Phyics: Condensed Matter*, **1**(8):1405–22, 1989.

[157] A.S. Sanz, R. Martínez-Casado, and S. Miret-Artés. Adsorbate surface diffusion: The role of incoherent tunneling in light particle motion. *Surface Science*, **617**:229–32, 2013.

[158] A. Van-Brunt and M. Visser. Special-case closed form of the Baker-Campbell-Hausdorff formula. *Journal of Physics A: Mathematical and Theoretical*, **48**(22):225207, 2015.

[159] H. Grabert, P. Olschowski, and U. Weiss. Quantum decay rates for dissipative systems at finite temperatures. *Physical Review B*, **36**(4):1931–51, 1987, doi:https://doi.org/10.1103/PhysRevB.36.1931.

[160] A. Altland and B. Simons. *Condensed Matter Field Theory*. Cambridge University Press, 2007.

[161] P. Hänggi, P. Talkner, and M. Borkovec. Reaction-rate theory: fifty years after Kramers. *Reviews of Modern Physics*, **62**(2):251–341, 1990, doi:https://doi.org/10.1103/RevModPhys.62.251.

[162] H.A. Kramers. Brownian motion in a field of force and the diffusion model of chemical reactions. *Physica*, **7**(4):284–304, 1940.

[163] T. Ala-Nissila, R. Ferrando, and S.C. Ying. Collective and single particle diffusion on surfaces. *Advances in Physics*, **51**(3):949–1078, 2002.

[164] S.H. Northrup and J.T. Hynes. The stable states picture of chemical reactions. I. Formulation for rate constants and initial condition effects. *Journal of Chemical Physics*, **73**(6):2700–14, 1980.

[165] V.I. Mel'nikov and S.V. Meshkov. Theory of activated rate processes: Exact solution of the Kramers problem. *Journal of Chemical Physics*, **85**(2):1018–27, 1986.

[166] E. Pollak, H. Grabert, and P. Hänggi. Theory of activated rate processes for arbitrary frequency dependent friction: Solution of the turnover problem. *The Journal of Chemical Physics*, **91**(7):4073–87, 1989.

[167] Sidney Coleman. Fate of the false vacuum: Semiclassical theory. *Physical Review D*, **15**(10):2929–36, 1977.

[168] T. Nakamura, A. Ottewill, and S. Takagi. The Bounce Method in the Theory of Quantum Decay. *Annals of Physics*, **260**(1):9–26, 1997.

[169] I. Affleck. Quantum statistical metastability. *Physical Review Letters*, **46**(6):388–91, 1981.

[170] W.H. Miller. Semiclassical limit of quantum mechanical transition state theory for nonseparable systems. *Journal of Chemical Physics*, **62**(5):1899–1906, 1975.

[171] P. Haänggi and W. Hontscha. Unified approach to the quantum-Kramers reaction rate. *Journal of Chemical Physics*, **88**(6):4094–5, 1988.

[172] E. Pollak. Transition state theory for quantum decay rates in dissipative systems: the high-temperature limit. *Chemical Physics Letters*, **127**(2):178–82, 1986.

[173] A.I.M. Rae. *Quantum Mechanics*. Institute of Physics, fourth edition, 2002.

[174] G. Alexandrowicz, A.P. Jardine, H. Hedgeland, W. Allison, and J. Ellis. Onset of 3D collective surface diffusion in the presence of lateral interactions: Na/Cu(001). *Physical Review Letters*, **97**(15):1–4, 2006.

[175] A P Jardine, G Alexandrowicz, H Hedgeland, R D Diehl, W Allison, and J Ellis. Vibration and diffusion of Cs atoms on Cu(001). *Journal of Physics: Condensed Matter*, **19**(30):305010, 2007.

[176] S. Paterson. *Elucidating surface dynamics in systems of atomic and molecular adsorbates*. PhD thesis, University of Cambridge, 2012.

[177] U. Weiss and H. Grabert. Quantum diffusion of a particle in a periodic potential with ohmic dissipation. *Physics Letters A*, **108**(2):63–67, 1985.

[178] P.G. Sundell and G. Wahnström. Quantum motion of hydrogen on Cu(001) using first-principles calculations. *Physical Review B*, **70**:081403, 2004.

[179] M. Born and R. Oppenheimer. Zur quantentheorie der molekeln. *Annalen der Physik*, **389**(20):457–84, 1927.

[180] E.M. McIntosh, K.T. Wikfeldt, J. Ellis, A. Michaelides, and W. Allison. Supporting Information for: Quantum Effects in the Diffusion of Hydrogen on Ru(0001). *Journal of Physical Chemistry Letters*, **4**:S1–16, 2013.

[181] J.P. Perdew, K. Burke, and M. Ernzerhof. Generalized gradient approximation made simple. *Physical Review Letters*, **77**(18):3865–8, 1996.

[182] J.P. Perdew, K. Burke, and M. Ernzerhof. Generalized gradient approximation made simple [Phys. Rev. Lett. 77, 3865 (1996)]. *Physical Review Letters*, **78**(7):1396, 1997. Erratum.

[183] G. Kresse and D. Joubert. From ultrasoft pseudopotentials to the projector augmented-wave method. *Physical Review B*, **59**(3):1758–75, 1999.

[184] G. Kresse and J. Furthmüller. Efficiency of ab-initio total energy calculations for metals and semiconductors using a plane-wave basis set. *Computational Materials Science*, **6**(1):15–50, 1996.

[185] C.D. Schwieters and G.A. Voth. The semiclassical calculation of nonadiabatic tunneling rates. *Journal of Chemical Physics*, **108**(3):1055–62, 1998.

[186] V.A. Benderskii, D.E. Makarov, D.L. Pastur, and P.G. Grinevich. Preexponential factor of the rate constant of low-temperature chemical reactions. fluctuational width of tunneling channels and stability frequencies. *Chemical Physics*, **161**(1–2):51–61, 1992.

[187] H. Grabert and U. Weiss. Quantum tunneling rates for asymmetric double-well systems with ohmic dissipation. *Physical Review Letters*, **54**:1605–8, 1985.

[188] A.T. Dorsey, M.P.A. Fisher, and M.S. Wartak. Truncation scheme for double-well systems with Ohmic dissipation. *Physical Review A*, **33**(2):1117–21, 1986.

[189] M.A.P. Fisher and A.T. Dorsey. Dissipative quantum tunneling in a biased double-well system at finite temperatures. *Physical Review Letters*, **54**(15):1609–12, 1985.

[190] J. Kondo. The non-adiabatic effect for heavy particles in metals. *Journal of the Physical Society of Japan*, **56**(5):1638–41, 1987.

[191] H. Grabert. Dissipative quantum tunneling of two-state systems in metals. *Physical Review B*, **46**:12753–6, 1992.

[192] J. H. Van Vleck. The correspondence principle in the statistical interpretation of quantum mechanics. *Proceedings of the National Academy of Sciences of the United States of America*, **14**(2):178–88, 1928.

[193] T.J.H. Hele and S.C. Althorpe. Derivation of a true ($t \to 0_+$) quantum transition-state theory. i. uniqueness and equivalence to ring-polymer molecular dynamics transition-state-theory. *Journal of Chemical Physics*, **138**(8):084108, 2013.

[194] Stuart C. Althorpe and Timothy J H Hele. Derivation of a true ($t \to 0_+$) quantum transition-state theory. II. Recovery of the exact quantum rate in the absence of recrossing. *Journal of Chemical Physics*, **139**(8):084115, 2013.

[195] D. Emin. *Polarons*. Cambridge University Press, 2013.

[196] J.T. Grant and T.W. Haas. A study of Ru(0001) and Rh(111) surfaces using LEED and Auger electron spectroscopy. *Surface Science*, **21**(1):76–85, 1970.

[197] S. Marchini, S. Günther, and J. Wintterlin. Scanning tunneling microscopy of graphene on Ru(0001). *Physical Review B*, **76**(7):075429, 2007.

[198] P.W. Sutter, J.-I. Flege, and E.A. Sutter. Epitaxial graphene on ruthenium. *Nature Materials*, **7**(5):406–11, 2008.

[199] E. Starodub, S. Maier, I. Stass, N. C. Bartelt, P. J. Feibelman, M. Salmeron, and K. F. McCarty. Graphene growth by metal etching on Ru(0001). *Physical Review B*, **80**(23):235422, 2009.

[200] A.K. Engstfeld, H.E. Hoster, R.J. Behm, L.D. Roelofs, X. Liu, C.-Z. Wang, Y. Han, and J.W. Evans. Directed assembly of Ru nanoclusters on Ru(0001)-supported graphene: STM studies and atomistic modeling. *Physical Review B*, **86**(8):085442, 2012.

[201] E. Sutter, P. Albrecht, B. Wang, M.-L. Bocquet, L. Wu, Y. Zhu, and P. Sutter. Arrays of Ru nanoclusters with narrow size distribution templated by monolayer graphene on Ru. *Surface Science*, **605**(17–18):1676–84, 2011.

[202] A. Politano, B. Borca, M. Minniti, J.J. Hinarejos, A.L. Vázquez de Parga, D. Farías, and R. Miranda. Helium reflectivity and Debye temperature of graphene grown epitaxially on Ru(0001). *Physical Review B*, **84**(3):035450, 2011.

[203] A. Politano. Probing growth dynamics of graphene/Ru(0001) and the effects of air exposure by means of helium atom scattering. *Surface Science*, **634**(SI):44–8, 2015.

[204] P. Sutter, M. Minniti, P. Albrecht, D. Farías, R. Miranda, and E. Sutter. A high-reflectivity, ambient-stable graphene mirror for neutral atomic and molecular beams. *Applied Physics Letters*, **99**(21):211907, 2011.

[205] M. Iannuzzi, I. Kalichava, H. Ma, S.J. Leake, H. Zhou, G. Li, Y. Zhang, O. Bunk, H. Gao, J. Hutter, P.R. Willmott, and T. Greber. Moiré beatings in graphene on Ru(0001). *Physical Review B*, **88**(12):125433, 2013.

[206] D. Maccariello, D. Campi, A. Al Taleb, G. Benedek, D. Farías, M. Bernasconi, and R. Miranda. Low-energy excitations of graphene on Ru(0001). *Carbon*, **93**:1–10, 2015.

[207] E. Loginova, N.C. Bartelt, P.J. Feibelman, and K.F. McCarty. Evidence for graphene growth by C cluster attachment. *New Journal of Physics*, **10**(9):093026, 2008.

[208] H. Chen, W. Zhu, and Z. Zhang. Contrasting behavior of carbon nucleation in the initial stages of graphene epitaxial growth on stepped metal surfaces. *Physical Review Letters*, **104**(18):186101, 2010.

[209] J. Li, E. Croiset, and L. Ricardez-Sandoval. Carbon clusters on the Ni(111) surface: a density functional theory study. *Physical Chemistry Chemical Physics*, **16**(7):2954–61, 2014.

[210] H. Tetlow, I.J. Ford, and L. Kantorovich. A free energy study of carbon clusters on Ir(111): Precursors to graphene growth. *Journal of Chemical Physics*, **146**(4):044702, 2017.

[211] M. Gao, Y.-F. Zhang, L. Huang, Y. Pan, Y. Wang, F. Ding, Y. Lin, S.-X. Du, and H.-J. Gao. Unveiling carbon dimers and their chains as precursor of graphene growth on Ru(0001). *Applied Physics Letters*, **109**(13):131604, 2016.

[212] J. Gao, Q. Yuan, H. Hu, J. Zhao, and F. Ding. Formation of carbon clusters in the initial stage of chemical vapor deposition graphene growth on Ni(111) surface. *Journal of Physical Chemistry C*, **115**(36):17695–703, 2011.

[213] R.G. Van Wesep, H. Chen, W. Zhu, and Z. Zhang. Communication: Stable carbon nanoarches in the initial stages of epitaxial growth of graphene on Cu(111). *Journal of Chemical Physics*, **134**(17):171105, 2011.

[214] L. Zhong, J. Li, Y. Li, H. Lu, H. Du, L. Gan, C. Xu, W.S. Chiang, and F. Kang. Unraveling the influence of metal substrates on graphene nucleation from first-principles study. *Journal of Physical Chemistry C*, **120**(40):23239–45, 2016.

[215] Q. Yuan, J. Gao, H. Shu, J. Zhao, X. Chen, and F. Ding. Magic carbon clusters in the chemical vapor deposition growth of graphene. *Journal of the American Chemical Society*, **134**(6):2970–75, 2012.

[216] J. Gao and F. Ding. The study on the medium-sized carbon islands on Ru(0001) surface. *Journal of Cluster Science*, **26**(2):347–60, 2015.

[217] K.F. McCarty, P.J. Feibelman, E. Loginova, and N.C. Bartelt. Kinetics and thermodynamics of carbon segregation and graphene growth on Ru(0001). *Carbon*, **47**(7):1806–13, 2009.

[218] S. Günther, S. Dänhardt, M. Ehrensperger, P. Zeller, S. Schmitt, and J. Wintterlin. High-Temperature Scanning Tunneling Microscopy Study of the Ordering Transition of an Amorphous Carbon Layer into Graphene on Ruthenium(0001). *ACS Nano*, **7**(1):154–64, 2013.

[219] R. Blume, H. Niehus, H. Conrad, A. Böttcher, L. Aballe, L. Gregoratti, A. Barinov, and M. Kiskinova. Identification of Subsurface Oxygen Species Created during Oxidation of Ru(0001). *Journal of Physical Chemistry B*, **109**(29):14052–58, 2005.

[220] Y. Georgievskii, M.A. Kozhushner, and E. Pollak. Activated surface diffusion: Are correlated hops the rule or the exception? *The Journal of Chemical Physics*, **102**(17):6908–18, 1995.

[221] H. Hedgeland, B.A.J. Lechner, F.E. Tuddenham, A.P. Jardine, W. Allison, J. Ellis, M. Sacchi, S.J. Jenkins, and B.J. Hinch. Weak intermolecular interactions in an ionically bound molecular adsorbate: cyclopentadienyl/Cu(111). *Physical Review Letters*, **106**:186101, 2011.

[222] F. Calleja, H. Ochoa, M. Garnica, S. Barja, J. Jesús Navarro, A. Black, M.M. Otrokov, V.E. Chulkov, A. Arnau, L.A. Vazquez de Parga, F. Guinea, and R. Miranda. Spatial variation of a giant spin-orbit effect induces electron confinement in graphene on Pb islands. *Nature Physics*, **11**(1):43–7, 2015.

[223] L.K. Wagner and D. Ceperley. Discovering correlated fermions using quantum Monte Carlo. *Reports on Progress in Physics*, **79**(9):94501, 2016.

[224] V.I. Anisimov, F. Aryasetiawan, and A.I. Lichtenstein. First-principles calculations of the electronic structure and spectra of strongly correlated systems: the LDA+ U method. *Journal of Physics: Condensed Matter*, **9**(4):767–808, 1997.

[225] G. Zhou and J.C. Yang. Initial oxidation kinetics of Cu(100), (110), and (111) thin films investigated by in situ ultra-high-vacuum transmission electron microscopy. *Journal of Materials Research*, **20**(7):1684–94, 2005.

[226] L. Luo, Y. Kang, J.C. Yang, and G. Zhou. Effect of oxygen gas pressure on orientations of Cu_2O nuclei during the initial oxidation of Cu(100), (110) and (111). *Surface Science*, **606**(23–24):1790–7, 2012.

[227] S.H. Kim and J. Wintterlin. Morphology of RuO_2(110) oxide films on Ru(0001) studied by scanning tunneling microscopy. *Journal of Chemical Physics*, **131**(6):064705, 2009.

[228] J.C. Goritzka, B. Herd, P.P.T. Krause, J. Falta, J.-I. Flege, and H. Over. Insights into the gas phase oxidation of Ru(0001) on the mesoscopic scale using molecular oxygen. *Physical Chemistry Chemical Physics*, **17**(21):13895–903, 2015.

[229] M.M. Thiam, T. Kondo, N. Horimoto, H.S. Kato, and M. Kawai. Initial growth of the water layer on (1× 1)-oxygen-covered Ru(0001) in comparison with that on bare Ru(0001). *Journal of Physical Chemistry B*, **109**(33):16024–9, 2005.

[230] T.E. Madey, H.A. Engelhart, and D. Menzel. Adsorption of oxygen and oxidation of CO on the ruthenium (001) surface. *Surface Science*, **48**(2):304–28, 1975.

[231] A. Böttcher and H. Niehus. Formation of subsurface oxygen at Ru(0001). *Journal of Chemical Physics*, **110**(6):3186–95, 1999.

[232] C. Stampfl and M. Scheffler. Theoretical study of O adlayers on Ru(0001). *Physical Review B*, **54**(4):2868–72, 1996.

[233] J. Wintterlin, J. Trost, R. Schuster, T. Zambelli, and G. Ertl. Real-time STM observations of atomic equilibrium fluctuations in an adsorbate system: O/Ru(0001). *Surface Science*, **394**(1–3):159–69, 1997.

[234] S. Renisch, R. Schuster, J. Wintterlin, and G. Ertl. Dynamics of adatom motion under the influence of mutual interactions: O/Ru(0001). *Physical Review Letters*, **82**(19):3839–42, 1999.

[235] B. Hammer. Adsorption, diffusion, and dissociation of NO, N and O on flat and stepped Ru(0001). *Surface Science*, **459**(3):323–48, 2000.

[236] J.-Q. Cai, H.-J. Luo, X.-M. Tao, and M.-Q. Tan. Initial subsurface incorporation of oxygen into Ru(0001): A density functional theory study. *ChemPhysChem*, **16**(18):3937–48, 2015.

[237] H. Pfnür and P. Piercy. Critical behavior of p(2×2) oxygen on Ru(001): An example of four-state Potts critical exponents. *Physical Review B*, **40**(4):2515–22, 1989.

[238] P. Piercy, K. De'Bell, and H. Pfnür. Phase diagram and critical behavior of the adsorption system O/Ru(001): Comparison with lattice-gas models. *Physical Review B*, **45**(4):1869–77, 1992.

[239] P. G. De Gennes. Liquid dynamics and inelastic scattering of neutrons. *Physica*, **25**(7–12):825–39, 1959.

[240] C. Gattinoni and A. Michaelides. Atomistic details of oxide surfaces and surface oxidation: the example of copper and its oxides. *Surface Science Reports*, **70**(3):424–47, 2015.

[241] F.C. Elam and H.G. Tipper. The etching of copper by oxygen. *Transactions of the Faraday Society*, **32**(0):1604–14, 1936.

[242] E. Menzel, B. Schichler, and U. Jeschkowski. Thermal faceting of copper and structures of oxygen adsorption. *Surface Science*, **7**(3):482–5, 1967.

[243] L.H Dubois. Oxygen chemisorption and cuprous oxide formation on Cu(111): A high resolution EELS study. *Surface Science*, **119**(2–3):399–410, 1982.

[244] A. Spitzer and H. Luth. The adsorption of oxygen on copper surfaces: Ii. Cu(111). *Surface Science*, **118**(1–2):136–44, 1982.

[245] H. Niehus. Surface reconstruction of Cu(111) upon oxygen adsorption. *Surface Science*, **130**(1):41–9, 1983.

[246] J. Haase and H.-J. Kuhr. Reconstruction and relaxation of the oxygen-covered Cu(111) surface: A SEXAFS study. *Surface Science Letters*, **203**(3):695–9, 1988.

[247] F. Jensen, F. Besenbacher, E. Laegsgaard, and I. Stensgaard. Oxidation of Cu(111): two new oxygen induced reconstructions. *Surface Science Letters*, **259**(3):774–80, 1991.

[248] T. Matsumoto, A.R. Bennett, P. Stone, T. Yamada, K. Domen, and M. Bowker. Scanning tunneling microscopy studies of oxygen adsorption on Cu(111). *Surface Science*, **471**(1–3):225–45, 2001.

[249] G. Alexandrowicz, P.R. Kole, E.Y.M. Lee, H. Hedgeland, R. Ferrando, A.P. Jardine, W. Allison, and J. Ellis. Observation of uncorrelated microscopic motion in a strongly interacting adsorbate system. *Journal of the American Chemical Society*, **130**(21):6789–94, 2008.

[250] P.R. Kole, H. Hedgeland, A.P. Jardine, W. Allison, J. Ellis, and G. Alexandrowicz. Probing the non-pairwise interactions between CO molecules moving on a Cu(111) surface. *Journal of Physics: Condensed Matter*, **24**(10):104016, 2012.

[251] I. Calvo-Almazán, E. Bahn, M.M. Koza, M. Zbiri, M. Maccarini, M.T.F. Telling, S. Miret-Art'es, and P. Fouquet. Benzene diffusion on graphite described by a rough hard disk model. *Carbon*, **79**:183 – 191, 2014.

[252] R. Martínez-Casado, A.S. Sanz, G. Rojas-Lorenzo, and S. Miret-Artés. Two-bath model for activated surface diffusion of interacting adsorbates. *The Journal of Chemical Physics*, **132**(5):054704, 2010.

[253] A.B. Anderson and M.K. Awad. Binding of Ru, O, and RuO_n (n=1-4) to the Ru(001) surface: Structures, stabilities, and diffusion barriers. *Surface Science*, **183**(1-2):289–301, 1987.

[254] T.S. Rahman, A.B. Anton, N.R. Avery, and W.H. Weinberg. Electron-energy-loss spectroscopy of ordered oxygen overlayers on Ru(001). *Physical Review Letters*, **51**(21):1979–82, 1983.

[255] K.L. Kostov, W. Widdra, and D. Menzel. Vibrational properties and lateral interactions of the (2×2)-(O+CO) coadsorbate layer on Ru(001). *Journal of Physical Chemistry B*, **108**(38):14324–31, 2004.

[256] K.L. Kostov, M. Gsell, P. Jakob, R. Moritz, W. Widdra, and D. Menzel. Observation of a novel high density 3O(2 × 2) structure on Ru(001). *Surface Science*, **394**(1–3):L138–44, 1997.

[257] T. Moritz, D. Menzel, and W. Widdra. Collective vibrational modes of the high-density (1 × 1)-O phase on Ru(001). *Surface Science*, **427–428**:64–8, 1999.

[258] H. Ibach. Electron energy loss spectroscopy: the vibration spectroscopy of surfaces. *Surface Science*, **299–300**(1-3):116–28, 1994.

[259] F.H.P.M. Habraken, E. Ph. Kieffer, and G.A. Bootsma. A study of the kinetics of the interactions of O_2 and N_2O with a Cu(111) surface and of the reaction of CO with adsorbed oxygen using AES, LEED and ellipsometry. *Surface Science*, **83**(1):45–59, 1979.

[260] F. Wiame, V. Maurice, and P. Marcus. Initial stages of oxidation of Cu(111). *Surface Science*, **601**(5):1193–1204, 2007.

[261] F. Besenbacher and J.K. Nørskov. Oxygen chemisorption on metal surfaces: General trends for Cu, Ni and Ag. *Progress in Surface Science*, **44**(1):5–66, 1993.

[262] J.-F. Paul and P. Sautet. Density-functional periodic study of the adsorption of hydrogen on a palladium (111) surface. *Physical Review B*, **53**(12):8015–27, 1996.

[263] R. Löber and D. Hennig. Interaction of hydrogen with transition metal fcc(111) surfaces. *Physical Review B*, **55**(7):4761–5, 1997.

[264] I. Waluyo, Y. Ren, and M. Trenary. Observation of tunneling in the hydrogenation of atomic nitrogen on the Ru(001) surface to form nh. *Journal of Physical Chemistry Letters*, **4**(21):3779–86, 2013.

[265] G. Kyriakou, E.R.M. Davidson, G. Peng, L.T. Roling, S. Singh, M.B. Boucher, M.D. Marcinkowski, M. Mavrikakis, A. Michaelides, and E.C.H. Sykes. Significant Quantum Effects in Hydrogen Activation. *ACS Nano*, **8**(5):4827–35, 2014.

[266] J. Kua, L.J. Lauhon, W. Ho, and W.A. Goddard. Direct comparisons of rates for low temperature diffusion of hydrogen and deuterium on Cu(001) from quantum mechanical calculations and scanning tunneling microscopy experiments. *Journal of Chemical Physics*, **115**(12):5620–4, 2001.

[267] A. Lee, X.D. Zhu, A. Wong, L. Deng, and U. Linke. Observation of diffusion of H and D on Ni(111) from over-barrier hopping to nonactivated tunneling. *Physical Review B*, **48**(15):11256–9, 1993.

[268] G. Cao, E. Nabighian, and X. Zhu. Diffusion of Hydrogen on Ni(111) over a Wide Range of Temperature: Exploring Quantum Diffusion on Metals. *Physical Review Letters*, **79**(19):3696–9, 1997.

[269] J.P. Sethna. Phonon coupling in tunneling systems at zero temperature: An instanton approach. *Physical Review B*, **24**(2):698–713, 1981.

[270] S.J. Clark, M.D. Segall, C.-J. Pickard, P.J. Hasnip, M.I.J. Probert, K. Refson, and M.C. Payne. First principles methods using CASTEP. *Zeitschrift für Kristallographie*, **220**(5-6):567–70, 2005.

[271] D. Vanderbilt. Soft self-consistent pseudopotentials in a generalized eigenvalue formalism. *Physical Review B*, **41**(11):7892–5, 1990.

[272] J.P. Perdew, J.A. Chevary, S.H. Vosko, K.A. Jackson, M.R. Pederson, D.J. Singh, and C. Fiolhais. Atoms, molecules, solids, and surfaces: Applications of the generalized gradient approximation for exchange and correlation. *Physical Review B*, **46**(11):6671–87, 1992.

[273] H. Conrad, M.E. Kordesch, R. Scala, and W. Stenzel. Surface resonances on Pd(111)/H observed with HREELS. *Journal of Electron Spectroscopy and Related Phenomena*, **38**(1–4):289–98, 1986.

[274] G. Lee and E.W. Plummer. High-resolution electron energy loss spectroscopy study on chemisorption of hydrogen on Cu(111). *Surface Science*, **498**(3):229–236, 2002.

[275] L.R. Danielson, M.J. Dresser, E.E. Donaldson, and J.T. Dickinson. Adsorption and desorption of ammonia, hydrogen, and nitrogen on ruthenium (0001). *Surface Science*, **71**(3):599–614, 1978.

[276] M. Tatarkhanov, F. Rose, E. Fomin, F.D. Ogletree, and M. Salmeron. Hydrogen adsorption on Ru(001) studied by scanning tunneling microscopy. *Surface Science*, **602**(2):487–92, 2008.

[277] P. Feulner and D. Menzel. The adsorption of hydrogen on ruthenium (001): Adsorption states, dipole moments and kinetics of adsorption and desorption. *Surface Science*, **154**(2–3):465–88, 1985.

[278] M.A. Barteau, J.Q. Broughton, and D. Menzel. Determination of hydrogen atom binding sites on Ru(001) by HREELS. *Surface Science*, **133**(2–3):443–52, 1983.

[279] M. Lindroos, H. Pfnür, P. Feulner, and D. Menzel. A study of the adsorption sites of hydrogen on Ru(001) at saturation coverage by electron reflection. *Surface Science*, **180**(1):237–51, 1987.

[280] M. Lindroos, H. Pfnür, and D. Menzel. Investigation of a disordered adsorption system by electron reflection: H/Ru(001) at intermediate coverages. *Surface Science*, **192**(2–3):421–37, 1987.

[281] M. Sokolowski, T. Koch, and H. Pfnür. Ordered structures and phase diagram of atomic hydrogen chemisorbed on ruthenium (001). *Surface Science*, **243**(1–3):261–72, 1991.

[282] J. Braun, K.L. Kostov, G. Witte, L. Surnev, J.G. Skofronick, S.A. Safron, and Ch. Wöll. Surface phonon dispersion curves for a hexagonally close packed metal surface: Ru(0001). *Surface Science*, **372**(1–3):132–44, 1997.

[283] L. Kristinsdóttir and E. Skúlason. A systematic DFT study of hydrogen diffusion on transition metal surfaces. *Surface Science*, **606**(17–18):1400–4, 2012.

[284] J.A. Herron, S. Tonelli, and M. Mavrikakis. Atomic and molecular adsorption on Ru(0001). *Surface Science*, **614**:64–74, 2013.

[285] C.H. Mak, J.L. Brand, A.A. Deckert, and S.M. George. Surface diffusion of hydrogen on Ru(001) studied using laserinduced thermal desorption. *Journal of Chemical Physics*, **85**(3):1676–80, 1986.

[286] C.H. Mak, J.L. Brand, B.G. Koehler, and S.M. George. Coverage dependence of the surface diffusion coefficient for hydrogen on Ru(001). *Surface Science*, **191**(1–2):108–20, 1987.

[287] M.Y. Chou and J.R. Chelikowsky. First-principles study of hydrogen adsorption on Ru(0001): Possible occupation of subsurface sites. *Physical Review Letters*, **59**(15):1737–40, 1987.

[288] M. Sandhoff, H. Pfnür, and H.-U. Everts. Phase diagram and phase transitions in the system H/Ru(0001): a Monte Carlo study. *Surface Science*, **280**(1-2):185–96, 1993.

[289] T. Mitsui, M.K. Rose, E. Fomin, D.F. Ogletree, and M. Salmerón. Hydrogen adsorption and diffusion on Pd(111). *Surface Science*, **540**(1):5–11, 2003.

[290] B.D. Adams and A. Chen. The role of palladium in a hydrogen economy. *Materials Today*, **14**(6):282–9, 2011.

[291] H. Conrad, G. Ertl, and E.E. Latta. Adsorption of hydrogen on palladium single crystal surfaces. *Surface Science*, **41**(2):435–46, 1974.

[292] D.M. Nace and J.G. Aston. Palladium hydride. I. the thermodynamic properties of Pd_2H between 273 and 345°K. *Journal of the American Chemical Society*, **79**(14):3619–23, 1957.

[293] Ch. Resch, H.F. Berger, K.D. Rendulic, and E. Bertel. Adsorption dynamics for the system hydrogen/palladium and its relation to the surface electronic structure. *Surface Science*, **316**(3):L1105–9, 1994.

[294] T.E. Felter, E.C. Sowa, and M.A. Van Hove. Location of hydrogen adsorbed on palladium (111) studied by low-energy electron diffraction. *Physical Review B*, **40**(2):891–9, 1989.

[295] K. Christmann, G. Ertl, and O. Schober. LEED intensities from clean and hydrogen covered Ni(100) and Pd(111) surfaces. *Surface Science*, **40**(1):61–70, 1973.

[296] C.-H. Hsu, B.E. Larson, M. El-Batanouny, C.R. Willis, and K.M. Martini. Evidence of quantum motion of hydrogen on Pd(111) in helium-diffraction data. *Physical Review Letters*, **66**(24):3164–7, 1991.

[297] T.E. Felter, S.M. Foiles, M.S. Daw, and R.H. Stulen. Order-disorder transitions and subsurface occupation for hydrogen on Pd(111). *Surface Science*, **171**(1):L379–86, 1986.

[298] G.E. Gdowski, T.E. Felter, and R.H. Stulen. Effect of surface temperature on the sorption of hydrogen by Pd(111). *Surface Science*, **181**(3):L147–55, 1987.

[299] A. Tamtögl, M. Kratzer, J. Killman, and A. Winkler. Adsorption/desorption of H2 and CO on Zn-modified Pd(111). *Journal of Chemical Physics*, **129**(22):1–7, 2008.

[300] S.W. Rick, D.L. Lynch, and J.D. Doll. The quantum dynamics of hydrogen and deuterium on the Pd(111) surface: A path integral transition state theory study. *Journal of Chemical Physics*, **99**(10):8183–93, 1993.

[301] N. Ozawa, T.A. Roman, H. Nakanishi, H. Kasai, N.B. Arboleda, and W.A. Diño. Potential energy of hydrogen atom motion on Pd(111) surface and in subsurface: A first principles calculation. *Journal of Applied Physics*, **101**(12):123530, 2007.

[302] S. Hong and T.S. Rahman. Adsorption and diffusion of hydrogen on Pd(211) and Pd(111): Results from first-principles electronic structure calculations. *Physical Review B*, **75**(15):155405, 2007.

[303] D. Farías, M. Patting, and K.H. Rieder. Helium diffraction investigations of the transition of chemisorbed hydrogen into subsurface sites on palladium surfaces. *Physica Status Solidi (a)*, **159**(1):255–62, 1997.

[304] K. Nobuhara, H. Nakanishi, H. Kasai, and A. Okiji. Interactions of atomic hydrogen with Cu(111), Pt(111), and Pd(111). *Journal of Applied Physics*, **88**(11):6897–901, 2000.

[305] T. Engel and H. Kuipers. A molecular-beam investigation of the scattering, adsorption and absorption of H2 and D2 from/on/in Pd(111). *Surface Science*, **90**(1):162–80, 1979.

[306] T. Engel. A molecular beam investigation of He, CO, and O_2 scattering from Pd(111). *The Journal of Chemical Physics*, **69**(1):373–85, 1978.

[307] G. Witte. Probing metallization transitions in two-dimensional alkali metal films by metastable He-atom scattering. *Journal of Physics: Condensed Matter*, **16**(29):S2937–52, 2004.

[308] I.Y. Sklyadneva, G.G. Rusina, and E.V. Chulkov. Vibrational states on Pd surfaces. *Surface Science*, **377–379**(1–3):313–16, 1997.

[309] C.H. Hsu. As cited in [308].

[310] R. Marquardt. Re: high T figure. Private Communication.

[311] O.M. Lövvik and R.A. Olsen. Adsorption energies and ordered structures of hydrogen on Pd(111) from density-functional periodic calculations. *Physical Review B*, **58**(16):10890–8, 1998.

[312] J.C. Tremblay. A unifying model for non-adiabatic coupling at metallic surfaces beyond the local harmonic approximation: From vibrational relaxation to scanning tunneling microscopy. *Journal of Chemical Physics*, **138**(24):244106, 2013.

[313] F. Greuter and E.W. Plummer. Chemisorption of atomic hydrogen on Cu(111). *Solid State Communications*, **48**(1):37–41, 1983.

[314] K. Doblhoff-Dier, J. Meyer, P.E. Hoggan, and G.-J. Kroes. Quantum Monte Carlo calculations on a benchmark molecule–metal surface reaction: H_2 + Cu(111). *Journal of Chemical Theory and Computation*, **13**(7):3208–19, 2017.

[315] C. Díaz, E. Pijper, R.A. Olsen, H.F. Busnengo, D.J. Auerbach, and G.-J. Kroes. Chemically accurate simulation of a prototypical surface reaction: H2 dissociation on Cu(111). *Science*, **326**(5954):832–4, 2009.

[316] G. Anger, A. Winkler, and K.D. Rendulic. Adsorption and desorption kinetics in the systems H2/Cu(111), H2/Cu(110) and H2/Cu(100). *Surface Science*, **220**(1):1–17, 1989.

[317] C.T. Rettner, D.J. Auerbach, and H.A. Michelsen. Role of vibrational and translational energy in the activated dissociative adsorption of D2 on Cu(111). *Physical Review Letters*, **68**(8):1164–7, 1992.

[318] Th. Kammler and J. Küppers. Interaction of H atoms with Cu(111) surfaces: Adsorption, absorption, and abstraction. *Journal of Chemical Physics*, **111**(17):8115–23, 1999.

[319] C.T. Rettner. Dynamics of the direct reaction of hydrogen atoms adsorbed on Cu(111) with hydrogen atoms incident from the gas phase. *Physical Review Letters*, **69**(2):383–6, 1992.

[320] G. Lee, D.B. Poker, D.M. Zehner, and E.W. Plummer. Coverage and structure of deuterium on Cu(111). *Surface Science*, **357–358**(100):717–20, 1996.

[321] E.M. McCash, S.F. Parker, J. Pritchard, and M.A. Chesters. The adsorption of atomic hydrogen on Cu(111) investigated by reflection-absorption infrared spectroscopy, electron energy loss spectroscopy and low energy electron diffraction. *Surface Science*, **215**(3):363–77, 1989.

[322] J.L. Nie, H.Y. Xiao, and X.T. Zu. First-principles study of H adsorption on and absorption in Cu(111) surface. *Chemical Physics*, **321**(1–2):48–54, 2006.

[323] M.F. Luo, G.R. Hu, and M.H. Lee. Surface structures of atomic hydrogen adsorbed on Cu(111) surface studied by density-functional-theory calculations. *Surface Science*, **601**(6):1461–6, 2007.

[324] M.F. Luo, D.A. MacLaren, and W. Allison. Migration and abstraction of H-atoms from the Cu(111) surface. *Surface Science*, **586**(1):109–14, 2005.

[325] X. Wang, Y.Y. Fei, and X.D. Zhu. Classical and quantum diffusion of hydrogen atoms on Cu(111). *Chemical Physics Letters*, **481**(1–3):58–61, 2009.

[326] C.L.A. Lamont, B.N.J. Persson, and G.P. Williams. Dynamics of atomic adsorbates: hydrogen on Cu(111). *Chemical Physics Letters*, **243**(5–6):429–34, 1995.

[327] J.R. Trail, D.M. Bird, M. Persson, and S. Holloway. Electron–hole pair creation by atoms incident on a metal surface. *Journal of Chemical Physics*, **119**(8):4539–49, 2003.

[328] Y. Georgievskii and E. Pollak. Semiclassical theory of activated diffusion. *Physical Review E*, **49**(6):5098–102, 1994.

[329] J. Shao and N. Makri. Iterative path integral calculation of quantum correlation functions for dissipative systems. *Chemical Physics*, **268**(1):1–10, 2001.

[330] J.T. Stockburger. Simulating spin-boson dynamics with stochastic Liouville-von Neumann equations. *Chemical Physics*, **296**(2–3):159–69, 2004.

[331] P.J. Feibelman, B. Hammer, J.K. Nørskov, F. Wagner, M. Scheffler, R. Stumpf, R. Watwe, and J. Dumesic. The CO/Pt(111) puzzle. *Journal of Physical Chemistry B*, **105**(18):4018–25, 2001.

[332] R.J. Needs, M.D. Towler, N.D. Drummond, and P. López Ríos. Continuum variational and diffusion quantum Monte Carlo calculations. *Journal of Physics: Condensed Matter*, **22**(2):023201, 2010.